UNIVERSITÉ DU QUÉBEC À MONTRÉAL

OPTIMIZATION OF CERAMIC MATERIALS FOR APPLICATION AS SOLID-STATE ELECTROLYTES IN LITHIUM BATTERIES

DISSERTATION
PRESENTED
AS PARTIAL FULFILLMENT
OF THE DOCTORATE IN CHEMISTRY

BY
DANIELE CAMPANELLA

OCTOBER 2023

UNIVERSITÉ DU QUÉBEC À MONTRÉAL

OPTIMISATION DE MATÉRIAUX CÉRAMIQUES POUR UTILISATION, EN TANT QU'ÉLECTROLYTE À L'ÉTAT SOLIDE, DANS LES BATTERIES AU LITHIUM

THÈSE
PRÉSENTÉE
COMME EXIGENCE PARTIELLE
DU DOCTORAT EN CHIMIE

PAR
DANIELE CAMPANELLA

OCTOBRE 2023

RÉSUMÉ

L’intérêt pour les batteries à l'état solide en tant que technologie post-lithium-ion a sensiblement augmenté dans la recherche moderne, en raison de la variété des nouvelles chimies d'électrolytes, permettant des performances élevées, et de leur sécurité améliorée par suite de l'élimination des électrolytes inflammables. Les caractéristiques de l'électrolyte solide jouent un rôle crucial dans la détermination de l'efficacité de la cellule. Aujourd’hui, les oxydes inorganiques, y compris les NASICONs et les grenats, représentent la classe des électrolytes solides la plus explorée. Ces matériaux présentent une conductivité élevée à température ambiante et une stabilité chimique notable vis-à-vis du lithium métallique. La synthèse des oxydes est généralement effectuée selon des méthodes à l'état solide à haute température, qui nécessitent de longs temps de réaction et des températures très élevées, par conséquent, de sérieux efforts doivent être entrepris pour améliorer le processus de fabrication.

L'objet de cette thèse est la modification des conditions de synthèse d'une série de matériaux oxydes, dont le $Li_{1+x}Al_xTi_{1-x}(PO_4)_3$ (LATP) de type NASICON et les grenats $Li_5La_3Bi_2O_{12}$ (LLBO) et $Li_7La_3Zr_2O_{12}$ (LLZO). Le traitement de tous ces composés implique l'utilisation de la technique de pressage à chaud pour le frittage thermique. Diverses approches de fabrication ont été utilisées, y compris la substitution élémentaire et l'application d'auxiliaires de frittage pour diminuer la température de formation des structures finales. La formation des électrolytes est étudiée par diffraction de rayons-X (DRX) *in situ* pour identifier le mécanisme d'évolution des phases du produit en fonction de la température. L'optimisation de la taille des particules peut être obtenue en modifiant correctement les conditions de travail, comme montré pour le LATP qui réalise le meilleur compromis entre la distribution des particules et la concentration des impuretés après un traitement thermique à 700 °C. La variation des paramètres externes peut également contribuer à rendre la phase souhaitée plus stable à température ambiante: un tel comportement est observé pour le LLBO qui se stabilise en choisissant judicieusement la température de frittage entre 600 et 650 °C, alors qu'une température plus élevée conduit à une décomposition thermique.

L'ajout d'un agent externe a démontré un impact positif sur l'évolution et le frittage thermique des pastilles céramiques, et ceci est observé pour le LLZO, qui présente une température de formation plus faible après l'incorporation de matériaux carbonés dans le mélange de recuit. Un

comportement semblable peut pareillement être observé après dopage aliovalent de la structure avec des ions tellure. Ces deux approches se sont avérées efficaces pour obtenir une phase stabilisée à des températures de travail remarquablement inférieures à celles généralement requises pour la synthèse à l'état solide des grenats. En plus de cela, les matériaux modifiés présentent des dimensions de particules plus homogènes qui permettent une meilleure densification et l'atteinte d'une densité plus élevée.

Tous les matériaux étudiés, à la fois les NASICONs et les grenats, rapportent des valeurs de conductivité particulièrement élevées compte tenu du traitement thermique à basse température, souvent comparables à celles rapportées dans les précédentes études sur la synthèse conventionnelle à haute température. L'amélioration des propriétés électrochimiques dévoile les avantages du pressage à chaud pour produire des électrolytes solides plus performants et confirme l'efficacité des modifications à l'état solide étudiées dans ce travail.

Mots Clés:

Batteries au lithium, Électrolytes solides, Matériaux céramiques, Pressage à chaud, Frittage à basse température

ABSTRACT

The interest in solid-state batteries as a post-lithium-ion battery technology has sensibly increased in modern research, owing to the variety of new electrolyte chemistries, enabling high performance, and their improved safety following the removal of flammable electrolytes. The inherent features of the solid electrolyte play a crucial role in determining cell efficiency, and the most explored class of solid electrolytes consists of inorganic oxides, including NASICONs and garnets. These materials display a high room temperature conductivity and a notable chemical stability against metallic lithium. The synthesis of oxides is typically conducted following high-temperature solid-state methods, which require long reaction times and high working temperatures, therefore serious efforts should be undertaken to improve the fabrication process.

The focus of this thesis is the modification of the synthesis conditions for a series of oxide materials, which include NASICON-type $Li_{1+x}Al_xTi_{1-x}(PO_4)_3$ (LATP) and garnets $Li_5La_3Bi_2O_{12}$ (LLBO) and $Li_7La_3Zr_2O_{12}$ (LLZO), and the treatment of all these compounds involves the use of the hot-pressing technique for the thermal sintering. Diverse approaches for manufacturing are attempted, including elemental substitution and application of sintering aids to decrease the formation temperature of the final structures. The formation of the electrolytes is investigated via *in situ* XRD to identify the evolution mechanism of the product phases based on temperature. Optimization of the particle size can be obtained by properly altering the working conditions, as shown for LATP which achieves the best compromise between particle distribution and concentration of impurities after a thermal treatment at 700 °C. Acting on the external parameters can also help render the desired phase more stable at room temperature: such a behavior is observed for LLBO which is stabilized by aptly choosing the sintering temperature between 600 and 650 °C, whereas an excessive temperature leads to thermal decomposition.

The addition of external agents has a positive impact on the evolution and the thermal sintering of ceramic pellets. This is observed for LLZO which exhibits a lower formation temperature after incorporating carbon materials in the annealing mix. An analogous behavior can be also seen after aliovalent doping of the structure with tellurium ions. Both these approaches are proven effective in obtaining a stabilized phase at working temperatures remarkably lower than the ones typically required for the solid-state synthesis of garnets. In addition, the modified

materials present more homogeneous particle dimensions which permit better densification and the attainment of higher densities.

The investigated materials, both NASICONs and garnets, exhibit notably high values of conductivity considering the low-temperature thermal treatment, often comparable with the ones reported in the literature for conventional high-temperature synthesis. The amelioration in the electrochemical outputs unveils the advantages of hot-pressing to produce more performant solid electrolytes and is a clear confirmation of the effectiveness of the solid-state modifications investigated in this work.

Keywords:
Lithium batteries, Solid Electrolytes, Ceramic Materials, Hot-Pressing, Low-temperature Sintering

ACKNOWLEDGEMENTS

My sincere thanks are due to Professor Daniel Bélanger for helping me in the realization of this thesis and for his oversight and assistance in every step of the project. I would also like to thank the direction of the Hydro-Québec Center of Excellence, in particular Dr. Karim Zaghib and Dr. Chisu Kim, for the economic contribution to the research project and their supervision of the activities.

I would like to acknowledge all the researchers and technicians at CEETSE for their direct help in my laboratory experiences. In particular, I want to thank the members of the oxide research team – Gabriel Girard, Sylvio Savoie, Alina Gheorghe Nita, and Vincent Gariepy – for their help in my training and their active involvement in laboratory practices. I am thankful for all the time they spent on discussions and experiments. The possibility to work in such an active group of people deepened my experience and allowed me to empower myself and express my abilities to the fullest. I would also thank Dr. Andrea La Monaca for the enriching discussions and collaborations in the activities at Hydro-Québec.

I want to equally thank Professors Joshua Byers and Ali Nazemi of Université du Québec a Montréal for accompanying me through the academic exams of my PhD at the university and for their comments, which allowed the evolution of my research project and helped me become confident in the exposition of my results.

I want to give my most special thanks to Dr Andrea Paolella of the Austrian Institute of Technology (AIT) for his continuous guidance throughout my period at Hydro-Québec and his help in the setting and publication of my experimental results. His invaluable feedback and his continuous support even outside the working environment have made my life as a Ph.D. student easier, especially during the hardships of living through the pandemic. I am grateful for having worked with him and I am honored to consider him a mentor and a friend.

Additional thanks go to Professor Jusef Hassoun of University of Ferrara for allowing me to begin this doctorate experience years ago, providing me with the information I needed, and

supporting me in my academic journey. His knowledge and experience fueled my interest in this discipline and his detailed explanations ignited my passion for research and new discoveries.

Finally, I want to thank my family for their enduring support during all these years far from home. They have always believed in me and supported my decisions and in the hardest moments, when I was on the verge of giving up, they were always there when I needed them. I wouldn't be here if it wasn't for them. I love you all and I hope I made you proud of me, but knowing you all, you have always been.

LIST OF ABBREVIATIONS

ASR	Area-Specific Resistance
ASSLIB	All-Solid-State Lithium-Ion Battery
DFT	Density Functional Theory
DTA	Differential Thermal Analysis
EDS	Energy Dispersion Spectroscopy
EIS`	Electrochemical Impedance Spectroscopy
Emf	Electromotive force
EV	Electric Vehicle
f.u.	Formula Unit
LAGP	$Li_{1+x}Al_xGe_{1-x}(PO_4)_3$
LATP	$Li_{1+x}Al_xTi_{1-x}(PO_4)_3$
LCO	Li_xCoO_2
LIB	Lithium-Ion Battery
LLBO	$Li_5La_3Bi_2O_{12}$
LLTO	$Li_{3x}La_{2/3-x}TiO_3$
LLZO	$Li_7La_3Zr_2O_{12}$
NASICON	Sodium (NA) Super-Ionic CONductor
NMC	$LiNi_xMn_yCo_zO$
NMR	Nuclear Magnetic Resonance
OCV	Open Circuit Voltage
PEO	Polyethylene Oxide
SEM	Scanning Electron Microscopy
TEM	Transmission Electron Microscopy
TGA	Thermogravimetric Analysis
XRD	X-Ray Diffraction

TABLE OF CONTENTS

LIST OF FIGURES

LIST OF TABLES

INTRODUCTION

The evolution of the human population has been characterized by a slow and constant growth during the last millennia, until the beginning of the 19th century, when an ever-increasing trend has led the global population to an increase of about 7 billion in a period of 200 years (Sadigov, 2022). According to the United Nations, the population has crossed the 8 billion people threshold on 15 November 2022 (UN, n.d.). The fundamental causes behind the acceleration of humans' growth rate lie in the overall improval in health conditions and life quality, because of the scientific discoveries and technological advancements following the first industrial revolution. Changes in public health and sanitation as well as development of proper sewage disposal in cities have significantly bettered health in developed countries. In addition, medical innovations such as vaccines, antibiotics and food preservation have reduced the impact of epidemics and infective diseases and decreased the global mortality rates (Van Bavel, 2013). At the dawn of the 20th century, the development of the Haber-Bosch industrial process for the fixation of nitrogen permitted a simpler and more economical pathway for the mass production of ammonia (Haber, 1905). This allowed for the industrial synthesis of nitrogen fertilizers and, after WWI, contributed to the expansion of intensive agriculture, providing ulterior support for global population growth. Nowadays, nitrogen based synthetic products are main staples of modern farming and are vital to the nourishment of billions of people around the globe (Smil, 2000). Future projections by the UN declare that the world population is foreseen to increase until we cross the 10 billion people threshold before the end of the current century (Roser & Rodés-Guirao, 2014; Sadigov, 2022), as reported in **Figure I1**, before reaching a stationary phase when the population growth will halt and stabilize.

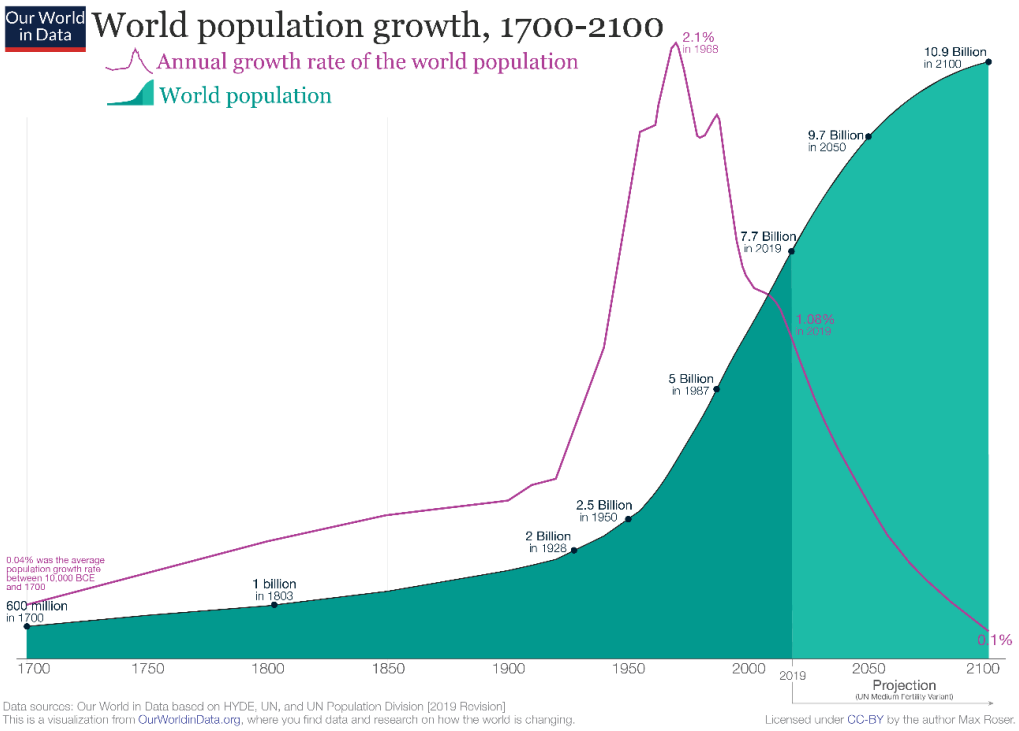

Figure I1. Human population growth and annual growth rate in the period from 1700 to 2100 (future projections). Significant milestones highlighted: 1 billion (1803), two billion (1928), 2.5 billion (1950), 5 billion (1987). The population growth rate reached its peak in 1968 at 2.1%. Image by Max Roser and Lucas Rodés-Guirao (2013) - "Future Population Growth". Published online at OurWorldInData.org(Roser & Rodés-Guirao, 2014).

The technological advances have indeed improved the carrying capacity of human environment but, at the same time, this unprecedented increment vastly inflated the impact of humanity on the Earth's natural environment, leading numerous ecosystems to the brink of irreparable collapse. Impactful changes on a global scale caused by human activities include the depletion of the ozone layer, spread desertification and topsoil loss, as well as global climate change (EPA, n.d.; IPCC, 2022). The latter, in particular, can find its roots in the rapid pace of economic growth in most countries. This phenomenon has been followed by a significant increase in energy consumption which caused the massive exploitation of fossil energy sources, namely coal, petroleum, and natural gas (IEA, 2021). Currently, worldwide energy production still relies heavily on fossil fuels, as observed in **Figure I2a-b**, showing the evolution of global energy sources, from 1971 to modern days. It can be seen that, from 1970 to 2021, the use of renewable

sources as a main source of energy has shown an increment (**Figure I2a**). However, they still represent only about 2% of global production.

All non-fossil sources combined (including hydroelectric and nuclear) provide about 20% of the global production, as shown in **Figure I2c**, whereas the contribution of all fossil fuels amounts to 23.2, 26.8 and 30.9% for natural gas, coal, and oil respectively. In particular, considering the three main fossil fuels, in 2019 oil provided the greatest contribution to the consumed energy, with more than 4000 Mtoe (**Figure I2b**), covering about 40% of global consumption. On the other hand, renewable sources (represented by the thin red area) account for only 3.6% of global energy consumption. Fossil fuels are a non-renewable energy source and that means that the continuous exploitation of the reserves will cause their rapid depletion, until they are totally consumed. At the same time, the combustion of fossil fuels contributes to the production of copious amounts of greenhouse gases (CO_2, NO_x), with a strong impact on climate alteration around the globe. Consumption of fossil fuels, and more specifically oil, is currently dominated by the field of transport which accounts for more than 60% of the energy produced (**Figure I2d**), and this massive consumption is the cause for the majority of CO_2 emissions. As exposed in **Figure I2e**, all fossil fuels combined make up for more than 99% of CO_2 emissions, amounting to more than 30 billion tons of CO_2 released. For this reason, the transition from these polluting sources towards green renewable sources in the fields of heavy industry and transportation is of crucial importance to limiting human impact on the environment. According to prospects, the demand for energy is not going to diminish in the immediate future and the green transition is far from an easy and fast process. In fact, energy request has more than doubled in less than 50 years following the explosion of the human population in the earlier decades. This phenomenon can partly be explained taking into account the recent economic growth of the so-called “emerging world” (O’ Neill, 2021). In the beginning of the 21st century, the raise of fast-growing economies, such as the BRICS countries (Brazil, Russia, India, China, South Africa) (O’ Neill, 2001), and, more recently, the rampant raise of south-east Asia (Fox, 2023) countries like Indonesia and Vietnam, has tottered the power balance of the western world.

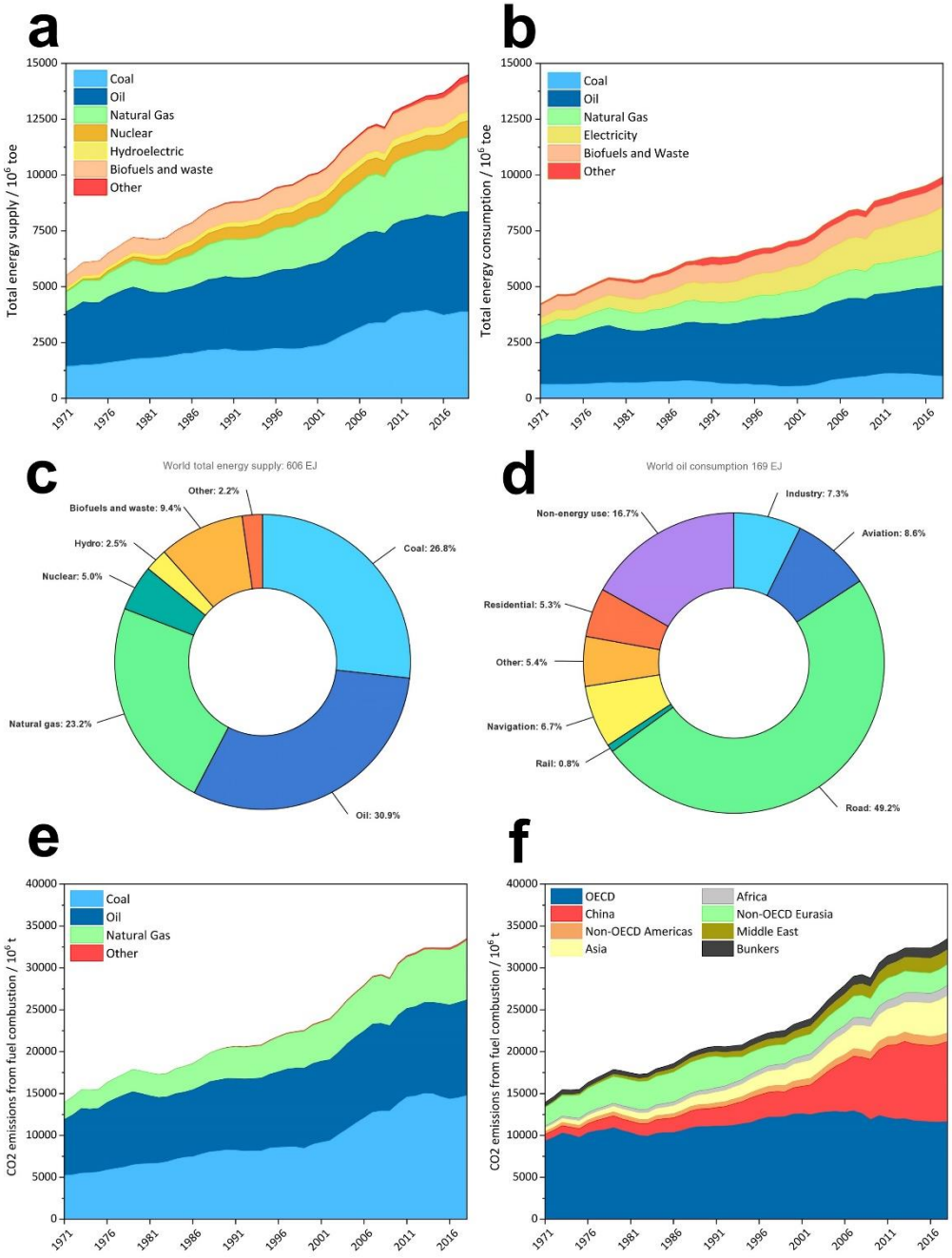

Figure I2. a) World total energy supply and b) total energy consumption per energy source, from 1971 to 2019, in million of toe ("Other" includes solar, geothermal and wind plants; "Electricity" is comprehensive of nuclear plants and electricity-only productors); c) relative world energy supply per source, 2019; d) share of oil final consumption by sector, 2019; e) total CO_2 emissions per energy source and f) per region, in million of tons of CO_2. "Bunkers" is referred to the contribution of international aviation and marine bunkers.

The most relevant example can be found in the blooming of China as a global superpower in the second half of the 20th century. The adoption of social market economy in the late seventies led to a 10-fold increment of Chinese GDP in less than 30 years, and the economic boom reflected on the environmental impact of the country (X. Zhou, 2021). The sudden development of these regions in different times and ways has brought different approaches in dealing with the environmental issue. The aim of the growing economies to reach a higher quality of life, akin to that of Western countries, made for a burgeoning demand for energy. This led to a frantic consumption of fossil fuels to accelerate the industrial expansion, with the direct support of exporting countries, eager to sell massive amounts of oil and forage this vicious circle, exploiting the situation as much as possible, instead of looking for new greener solutions. The development of Asian countries is paradoxical by itself, considering the vast extent of rural areas punctuated by polluted industrial megalopolis populated by millions of people.

This is reflected by the future outlooks of population growth for the Asian continent (Roser & Rodés-Guirao, 2014). Over the past 50 years Asia manifested a booming expansion. Nowadays, its population stands at 4.7 billion, which are expected to rise to more than 5 billion by 2050, China and India accounting for 3 billion by themselves. The impact of this situation is displayed in Figure I2f, showing the evolution of CO_2 emissions per region and union of countries from 1971 to 2019. The graph shows that the emissions of the Asian giant have exploded in the last 30 years, from about 2000 Mt in 1990 to 10000 Mt in 2019, just 10% less than all the OECD countries combined (amounting at 11300 Mt), The amount of emitted CO_2 has not stopped increasing in the last decades and, according to current prospects for the next decades, a bleak outlook awaits us, since the emissions are not going to decrease in the immediate future despite the conjoint efforts of countries around the world ratified in the Paris Agreement in 2015 (Savaresi, 2016). The primary aim of the treaty is to have a more resolute response to the consequences of climate change and it covers a wide range of topics including climate mitigation and financial actions (UNFCCC, 2015). Its main course of action concerns the limitation of world temperature increase to 1.5 °C above pre-industrial levels, encouraging the parties to the adaptation towards negative effects of climate change and the development of low greenhouse gas alternatives.

As previously described, the sector of transports is still one of the major actors in the use of fossil sources and the production of CO_2, hence the replacement of internal combustion engines

with new technologies working with renewable resources is crucial. Numerous efforts have been taken to evolve the concept and application of electric vehicles (Wakefield, 1994), since the mid-19th century with the assembly of the first electric motors following Michael Faraday's work (Larminie & Lowry, 2012). Prime examples of electric propulsion were typically limited to public transportation, such as Davidson's electric locomotive (1837) or the first prototypical electric trams in Europe in 1880. Development of experimental vehicles carried on during the second half of the century, and a fundamental step in the evolution of the technology was the first invention of lead-acid batteries by Gaston Planté in 1859 and the amelioration by Camille Alphonse Faure in 1881, providing more feasible means for energy storage. Interest in this technology increased in the late 1800s to the early 1900s, leading to the engineering of the first full-scale electric cars by the end of the century. The first full-electric taxis were introduced in London in 1897 and in 1899 the Jamais Contente was the first vehicle to reach a speed of 100 km/h.

The beginning of the 20th century was the golden age of electric vehicles but, despite their visible advantages, the next decades saw an important halt in this technology due to a series of reasons. Betterment of infrastructures after WWI and the discoveries of new reserves of oil helped the diffusion of IC engines and rendered gas-powered vehicles cheaper for use over longer distances, while electric vehicles remained limited to urban transport due to their lower autonomy and top speed. Comparing IC engines and lead-acid batteries in terms of specific energy shows for the former a typical value of about 9000 Wh kg^{-1}, whereas the value for the latter is around 30 Wh kg^{-1}. Considering the average efficiency of IC engines ($\sim$ 20%) leads ot a value of 1800 Wh kg^{-1} of available energy from petrol. The same available energy would require a 70 kg lead-acid battery for each kg of fuel, without considering the volume of the battery itself and the energy for moving the additional mass. Gasoline vehicles overcame numerous technological limitations compared to their electric counterparts, such as the invention of the engine self-starter in 1911, and the introduction of industrial mass production by Henry Ford in 1908 brought the prices down, whereas the price of electric vehicles kept increasing in the following years, leading to their decline. The revival of interest in this technology started in the 1960s and a series of battery-electric prototypes were presented, but none of them reached production. An explosion in commercial vehicles happened in the 1990s, when automakers started the development of electric models such as the GM EV1 or the Toyota Prius, and the early 2000s saw the appearance of a major actor in the scene in Tesla Motors, with the development and commercialization of the

Roadster in 2008. Several automakers followed in the footsteps of Tesla and, from the early 2010s, the global production of electric vehicles showed an ever-increasing trend, as can be seen in Figure I3. Japanese automakers such as Nissan and Mitsubishi covered a spot in the market by introducing electric hatchback and city car models, which furtherly helped the worldwide diffusion of the technology.

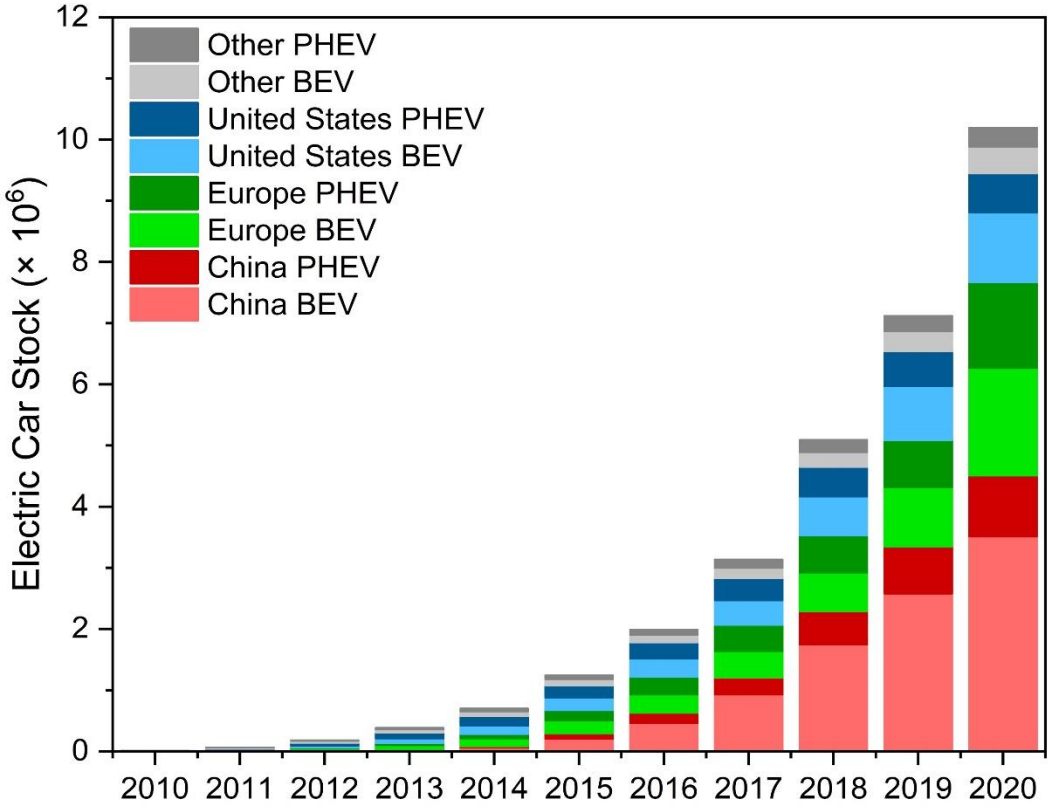

Figure I3. Global stock of electric vehicles during the 2010s per region, in million of vehicles. BEV = Battery electric vehicles; PHEV = Plug-in hybrid electric vehicles. © *Images reproduced from IEA. Licence: CC BY 4.0*

Despite these undoubted efforts, the shift towards a full electric propulsion faces the same main challenges of a century ago, including the relative low cost of fossil fuels and the low autonomy range of current storage systems. From a technical standpoint, the battery pack in the electric vehicle should yield as much energy as possible in a continuous way. Therefore, energy density is a vital feature for battery technology to be applied in the automotive field. Energy density represents the amount of energy stored in a given unit of volume or weight and, as reported in Figure I4, lithium-ion batteries (LIBs) manifest the highest energy density among all current major

battery technologies, much higher than lead-acid and nickel based batteries (J.-M. Tarascon & Armand, 2001). Li-metal batteries exhibit even higher values of energy density (Shen et al., 2018), but the direct application of metallic lithium represents a serious safety issue for the upscaling and diffusion of this technology in practical applications. In more recent times, research has explored alternative battery configurations trying to overcome the limits of lithium chemistry (Titirici, 2021; P. Xu et al., 2021) (substitution of lithium with other alkali elements, such as sodium (Nayak et al., 2018), potassium (Min et al., 2021), or magnesium (Shah et al., 2021); technologies implementing new electrode structures, like lithium-air (Chawla, 2019)) but the improvements,

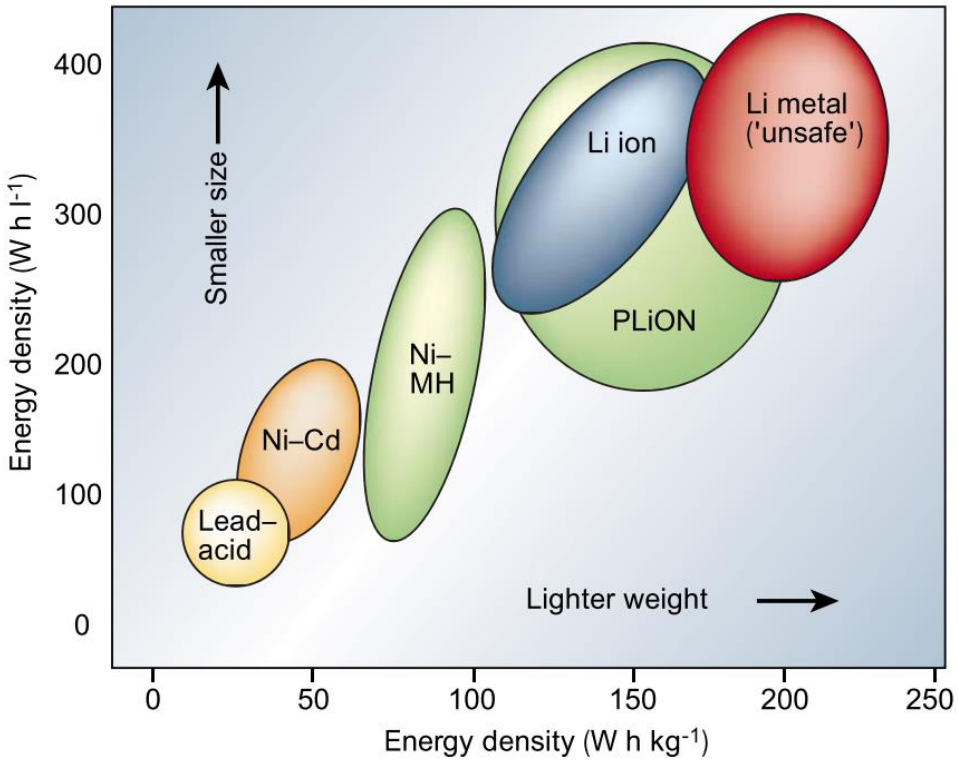

Figure I4. Compared values of the volumetric and gravimetric energy densities for different rechargeable battery technologies. Reproduced with permission from Ref.[18].

albeit promising, are still mostly limited to a laboratory scale, with scarce applications on a practical standpoint.

The present thesis is the result of a collaboration between university and industry, and it focused on the optimization of ceramic materials for applications as solid electrolytes in lithium batteries. More specifically, the research involved the modification and engineering of garnet-

structured electrolytes $Li_7La_3Zr_2O_{12}$ (LLZO) and $Li_5La_3Bi_2O_{12}$ (LLBO) and NASICON electrolyte $Li_{1+x}Al_xTi_{1-x}(PO_4)_3$ (LATP) The reasons behind the choice are to be found in the promising characteristics of these materials in terms of electrochemical stability towards lithium metal, relatively high ionic conductivity, high Li^+ ion transport properties and low water and air reactivity. All research activities were performed at the Centre d'Excellence en Électrification des Transports et Stockage d'Energie (CEETSE) of Hydro-Québec, renowned as a world-class innovation center in the field of energy storage and battery materials. The laboratory activities followed diverse approaches in the study and synthesis of the materials, which include the surface modification of the structure via incorporation of carbon additives, in order to see the results on the evolution of the material and the morphology of the particles. Other strategies include the insertion of doping agents to help stabilize the structure and improve electrochemical performance. All laboratory practices are bound together by a leitmotif, the application of solid-state synthesis and, in particular, the use of the hot-pressing technique, which involves the simultaneous usage of high pressure and temperature control during the sintering process, allowing for improved densification and enhanced performance.

The present thesis is structured by articles, and it is made of separate sections which can be considered independently from each other. Chapter I introduces the concept of lithium-ion battery from an historical perspective and the motivations behind the necessary safety improvements. A thorough review of the relevant literature about solid electrolytes, in terms of synthesis, performance and large-scale fabrication is presented here. The results of my activities are exposed in Chapters from II to V. Chapter II describes a study on the densification of $Li_{1.5}Al_{0.5}Ti_{1.5}(PO_4)_3$ (LATP) solid electrolyte at low temperatures. The formation mechanism of $AlPO_4$ secondary phases during the process has been explored and a small presence of impurities, combined with optimized densification conditions, has been proven beneficial on the electrochemical characteristics of the material. Particle nano-sizing enhanced the metastable behavior of LATP in the sintering process. In Chapter III an investigation on the properties of garnet-type $Li_5La_3Bi_2O_{12}$ (LLBO) undergoing hot-pressing is depicted. Densification of LLBO is achieved at much lower temperature than the standard needed for garnet materials and the electrolyte exhibits a fairly high conductivity after proper tuning of the synthesis. Segregation of Bi and presence of $LiLa_2O_{3.5}$ phase is detected at higher temperature and the formation mechanism has been described by density functional theory (DFT). Limited amounts of LLBO may be employed as a sintering aid

in the densification of $Li_7La_3Zr_2O_{12}$ (LLZO), enabling an increased conductivity after low-temperature annealing. Chapter IV reports a study about the synthesis mechanism of LLZO, which can be improved by the use of carbon additives. Supplementing the process with carbon reduces the formation temperature of LLZO while decreasing the particle size of the material. After hot-pressing, an improved densification is seen, which is affected by the nature of the additive itself, and an increment in ionic conductivity of about 40 % for the carbon-rich compound is reported after electrochemical testing. Chapter V illustrates the results of tellurium doping of LLZO and proves that the addition of tellurium can lower the formation temperature of the desired phase. Suited adjustments in the synthesis show a decrement in particle size for the material with high amount of Te, as well as a higher ionic conductivity after hot pressing. The study shows the advantages of proper elemental doping for the formation of LLZO solid electrolyte.

CHAPTER I
LITHIUM-ION BATTERIES AND SOLID ELECTROLYTES

1.1. Early Developments of Lithium-ion Batteries

The discovery of lithium dates back to the early 19th century, with the analysis of petalite minerals by Berzelius and Arfwedson (Berzelius, 1817), and the element was first isolated in 1821 by Brande and Davy via electrolysis of lithium oxide (Brande, 1821). The first investigation of the electrochemical properties of lithium was carried out by Lewis in 1913 (Lewis & Keyes, 1913), and it was understood quickly that the excellent physical properties of the element, which include its high specific capacity (3860 mAh g^{-1}) and low density (0.534 g cm^{-3}), as well as the lowest redox potential ever recorded (−3.04 V vs. SHE), could make it the perfect candidate for use as battery anode. However, lithium, like all alkali metals, is obviously incompatible with aqueous environments, thus its application required shifting from common aqueous electrolytes to more chemically stable alternatives. In the late 1950s, Harris analyzed the affinity of lithium towards a series of aprotic solvents (W. S. Harris, 1958), which included cyclic esters and molten salts, dissolved in propylene carbonate. In his studies, he saw an improved stability of lithium due to the formation of a passivation layer on the surface of the electrode which averted direct chemical reactions between the electrode itself and the electrolyte but, at the same time, enabled the movement of ions towards the solution during cell discharge. This discovery led to further studies concerning the stability of lithium batteries (W. S. Harris, 1958; Jasinki, 1969). The research interest on the possible commercialization of lithium-based storage systems (Reddy et al., 2020) increased significantly and the late 60s and early 70s saw the release on the market of several lithium-ion primary batteries, among which we can find lithium sulfur dioxide Li/SO_2 cells; lithium manganese oxide Li/MnO_2 batteries firstly commercialized by Sanyo in 1975; lithium copper oxide Li/CuO batteries, which are still in use today; long-term Li/LiI/I_2PVP batteries used since 1972 in cardiac pacemakers. The success of these families of primary batteries motivated the interest in creating secondary rechargeable batteries. The early 1970s saw rekindled research in the field of ion intercalation in crystalline structures which could serve as compatible cathodes in batteries. Typically, an intercalation reaction is favored when the host structure contains a number of empty sites in the form of vacancies or as correlated multidimensional channels in the 3D

framework (M. Armand & Touzain, 1977). The materials should fulfill a series of prerequisites to allow the proper development of the electrochemical process, which include: 1) the ability to accommodate and release guest ions in their open framework in a wide stoichiometric range with negligible structural change; 2) high diffusivity of the charge carrying ions within the frame; 3) the reversible evolution of both electronic (to balance the ion charge) and crystalline structure (to prevent structural collapse); 4) insolubility in the electrolyte used in the battery and absence of co-intercalation of electrolyte components; 5) chemical stability in operating conditions. In 1972, Armand et al. (M. B. Armand et al., 1972) demonstrated the intercalation phenomenon in Prussian-blue materials $M_{0.5}Fe(CN)_3$, and in the following years suggestions were made on employing transition metal chalcogenides MS_2 (M = Ta, Nb and Ti) as intercalation electrodes (Gamble et al., 1971), due to their ability to exchange lithium ions across their layered frame accompanied by a change in their valence state. Demonstration of the fast intercalation kinetics in metal disulphides was reported by the groups of Rouxel (Leblanc-Soreau et al., 1974) and Rao (G. V. S. Rao & Tsang, 1974) in 1974, and in 1976 the first Li/TiS_2 full battery (**Figure 1.1**) was patented by Whittingham (Ramström, 2019; Whittingham, 1977), who was working at Exxon. The battery contained $LiPF_6$ in propylene carbonate as liquid electrolyte and the cell reported an electromotive force (emf) of 2.5 V, with a diffusion coefficient of lithium ions in the TiS_2 lattice of 10^{-7} cm^2 s^{-1}

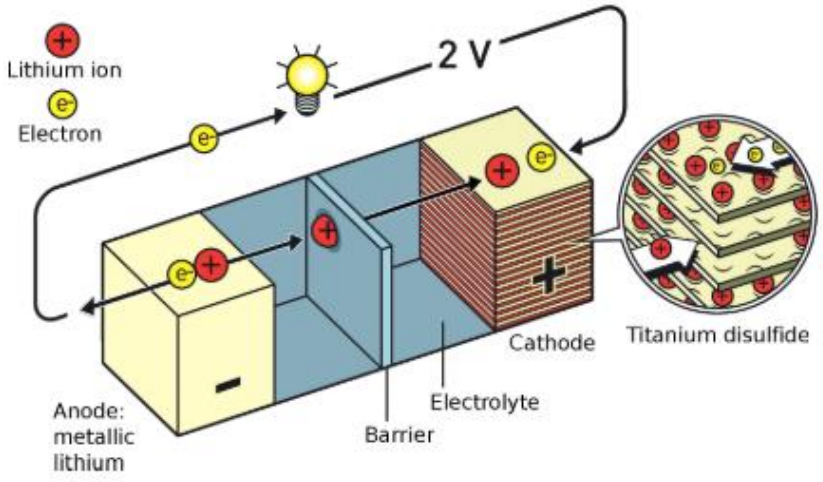

Figure 1.1. Whittingham's lithium-based battery using layered TiS_2 as the cathode. Reprinted from Ref. (Ramström, 2019).

(Whittingham, 1976).

The electrochemical intercalation process showed total reversibility, and the results paved the way for the development of commercial batteries. Li/TiS_2 battery were commercialized about a decade later (Akridge & Vourlis, 1986; Anderman et al., 1989) and other materials and configurations received some commercial interest, such as MoS_2 (Py & Haering, 1983) and $NbSe_3$ (Murphy & Trumbore, 1976). The first cells directly used lithium as the anode, but this configuration manifested some issues, due to the remarkably high reactivity of the alkali metal which easily reacts with the electrolyte, with the formation of a passivation layer known as solid electrolyte interface (SEI). However, irregular surface deposition of lithium appeared upon repeated charge-discharge cycles of the batteries, forming lithium dendrites large enough to pierce through the separator and extend to the opposite electrode, resulting in a short circuit and potential disastrous consequences. The problem was approached by looking for alternatives in which both electrodes can accommodate the charge carriers, in a configuration known as ion-transfer or "rocking-chair" (Lazzari & Scrosati, 1980; Scrosati, 1992). These cells avoid the use of metallic lithium, and serious efforts were made in researching new performant anode materials who could take the place of lithium. Carbon materials, such as graphite, were already known to exhibit ion intercalation (Fredenhagen & Cadenbach, 1926), and the phenomenon was confirmed in 1965 with the synthesis of LiC_6 (Guerard & Herold, 1975). These materials were seen as an attractive solution, considering their ability to host one lithium ion per six carbon atoms. Despite a diminished total cell emf compared to lithium, such a set up would be remarkably safer. However, their practical application was postponed due to the absence of proper electrolytes able to prevent co-intercalation. A solution to the problem came with the use of polymer-based electrolytes by the group of Armand in 1978 (M. Armand & Duclot, 1978) and the reversible intercalation process of lithium into graphite with a polymer electrolyte was definitively established by Yazami in 1980 (Yazami & Touzain, 1983). This breakthrough led to the modern lithium-graphite anode currently employed in lithium-ion batteries. In the same years, studies explored new advanced cathode compositions able to produce higher emf combined with high potential anodes, and research pointed towards transition metal oxides. A groundbreaking discovery came in the late 1970s with the discovery of the intercalation properties of rock-salt layered Li_xCoO_2 (LCO) by Goodenough et al. (Goodenough, Mizushima, et al., 1976) inspired by the investigations on Na_xCoO_2 by Hagenmuller et al. (Fouassier et al., 1973). The material presented a similar structure to TiS_2, being a MX_2-type chalcogenide compound, and showed separated CoO_2 layers which could host lithium

ions without significant lattice distortion. In the MX_2 configuration, using a strongly electronegative element X with a small dimension (and a higher charge density) was associated with a more negative free-energy change in the ion binding process and a higher cell emf. Oxygen was seen as an eligible choice in substituting sulfur, and the replacement of sodium with lithium in the framework gave a major advantage. The new cathode worked at very high voltage (4-5 V vs Li^+/Li) with a diffusion coefficient of about 5×10^{-9} cm^2 s^{-1} at room temperature (Mizushima et al., 1980). The material was also proven to be more stable in air than Na_xCoO_2, making it the perfect candidate for use in perfect applications and the most commercialized cathode for the next decades. In 1983 the group led by Yoshino reported a full cell prototype using LCO as cathode and polyacetylene polymer as anode. The polymer had low density, meaning a larger volume to get a high battery capacity, and it had chemical instability issues, thus the research moved to carbon materials derived from petroleum coke. These compounds contained a combination of graphitic and amorphous domains, the latter of which were supposed to protect the crystalline sites from exfoliation. Studies identified the more apt degree of crystallinity for lithium insertion with a low relative potential, and a new battery prototype with ion-transfer setup was engineered in 1985 (Hopkins, 1889), using LCO and the new carbon as electrodes (**Figure 1.2**). This is considered the birth of the modern lithium-ion battery, and this template is nowadays the most common configuration for commercial LIBs. For these fundamental contributions to modern technology Whittingham, Goodenough and Yoshino were awarded the Nobel Prize in Chemistry in 2019 (Ramström, 2019; The Royal Swedish Academy of Sciences, 2019).

Development of high-performance electrodes did not stop, and new families of materials were explored. In 1984, Thackeray et al. (Thackeray et al., 1984) reported early investigation on spinel material $LiMn_2O_4$. The material exhibits a better thermal stability compared to LCO and the cost of Mn is lower than that of Co, but the dissolution of the material into electrolytes at high temperature hampered its widespread application until more recent years. Another important type of cathodes is olivines, a class of polyanionic compounds which were spearheaded by Manthiram and Goodenough's group (Manthiram & Goodenough, 1989) and the most renowned of which is $LiFePO_4$ (LFP). This material has a noteworthy thermal stability and contains less costly elements such as Fe, making it a perfect alternative to LCO, but it was shown to work at a lower operating voltage (3.5 V) and reported poor values of reversible capacity (110 mAh g^{-1}) (Padhi et al., 1997). Other studies focused on the improvement of the thermal properties of LCO, based on the synthesis of solid solutions containing doping elements like Mn and Ni. In the early 1990s, efforts were done in the optimization of the mixed cathode $LiNi_xMn_yCo_zO_2$ (NMC) (Delmas, 1992), which would have later been commercialized by numerous companies. A more recent approach involves the functionalization of cathodes with active carbon to improve the electronic conduction (Dominko et al., 2007; Kwon et al., 2018). Incorporation of carbon supports the transfer of electrons through the material and carbon coating also protects the electrode particles from degradation and

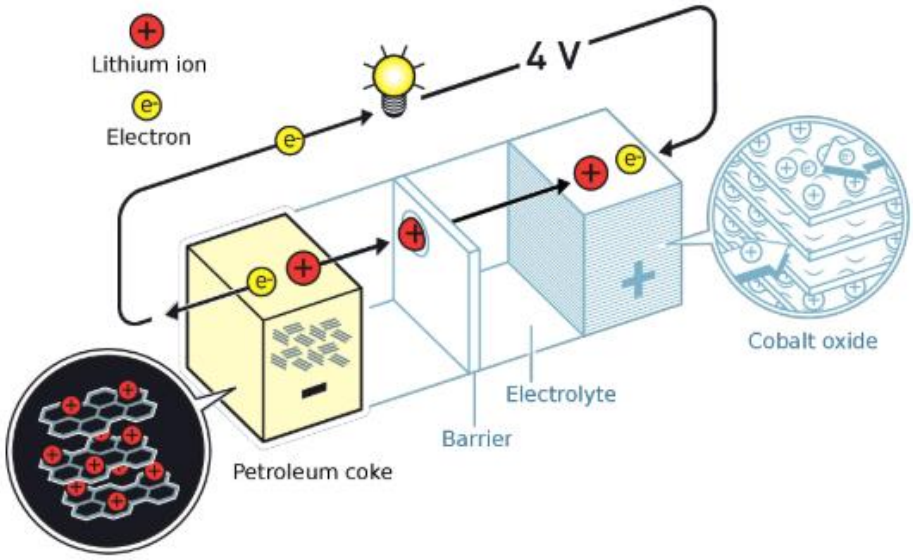

Figure 1.2. Yoshino's lithium-based battery prototype using LCO as the cathode. Reprinted from Ref. (Ramström, 2019).

dissolution in the electrolyte (Oh et al., 2010). Different carbonaceous materials have been explored, ranging from graphite to nanosized particles, to carbon nanotubes, showing distinct behavior in the electrode mix. The use of ball-milling showed a better mixing with graphitic carbons, while carbon nanoparticles underwent aggregation and formation of a surface layer. The thick interphase decreased lithium permeability and limited the specific capacity of the electrode (Kwon et al., 2018). On parallel with these studies, research was performed on alternatives to graphite as anode materials. The first batteries employed Li-alloys as negative electrodes but, due to the safety concerns related to metallic lithium, their commercial diffusion was limited. In the 1990s, lithium titanate $Li_4Ti_5O_{12}$ (LTO) spinel material was proposed as a substitute for graphite (Ferg et al., 1994), but the practical applications of the material remain very limited to high-power density requirements. This anode has found more specific usage in sodium-ion batteries, reporting a reversible capacity of 155 mA hg^{-1}, and it displays the best cycle performance among all reported oxide-based anodes (L. Zhao et al., 2012).

1.2. Safety Concerns in Batteries

1.2.1 Accidents and Faults

In 1991 the team lead by Nishi achieved the release of the first lithium-ion battery (Reddy et al., 2020). The technology was commercialized by Sony and Asahi Kasei. Since then, LIBs have rapidly risen to be one of the most widespread energy-storage systems, enabling an even wider diffusion of portable electronic appliances and electric vehicles (EVs). The advantages of this technology compared to the most common alternatives, such as lead-acid or nickel-metal hydride in terms of energy density and specific capacity have been demonstrated (Conte, 2006) and these systems also were proven to show a high efficiency, long cycle life and high operating voltage (Hannan et al., 2017). Demand for more functional and performant batteries is a central topic in modern research. This technology shows indeed a wide margin for improvement, and important efforts have been made and are still needed to address the major concerns for safe long-term operation of the battery.

Accidents involving LIBs are generally rare in probability, estimated between 1 per million to 1 per 10 million batteries. Nonetheless, due to the ever more widespread diffusion of LIBs,

battery-related accidents have become more and more common, which erodes the public trust in their reliability For example, from 2017 to 2019 more than 30 incidents related to LIBs were reported in South Korea (W. Cao et al., 2020). The majority of LIB-related accidents happen to small-sized gadgets, mainly portable electronics, and the consequences faced are generally minor. However, considering the opportunity of analogous hazards for larger systems or full battery packs, such as the ones operating on EVs, and the catastrophic outcome that can happen are reasons valid enough to anticipate the problem. A noteworthy example can be found in the Boeing 787 Dreamliner incident which happened at the beginning of 2013 (Hradecky, 2013). A number of aircraft underwent battery fires, and, in some cases, emergency landings happened. Further investigations revealed defects in the battery manufacturing and the absence of fire suppression systems, leading to serious safety issues. Statistical evaluations on battery-related accidents in regard to electric vehicles have pointed out some interesting correlations (**Figure 1.3**) (X. Yu et al., 2022). Most importantly, it can be seen that the increase in EV ownership does not reflect in a parallel increment of related accidents, which indicates an improvement in battery technology and manufacturing. The graphs also indicate that the largest number of incidents is observed from June to August, pointing out the impact of temperature and climate conditions on the cycle life of the battery. In fact, a main defect of LIBs is the very narrow working temperature range: the recommended operating temperature for lies between 20 and 40 °C (Greco et al., 2015) . The performance of LIBs at low temperatures are more modest on average (Jaguemont et al., 2016), possibly due to a limited ion mobility in the electrolyte and a higher charge transfer resistance at very low temperature (< −20 °C), and the life expectancy is sensibly reduced at high temperature (J. Wang et al., 2014).

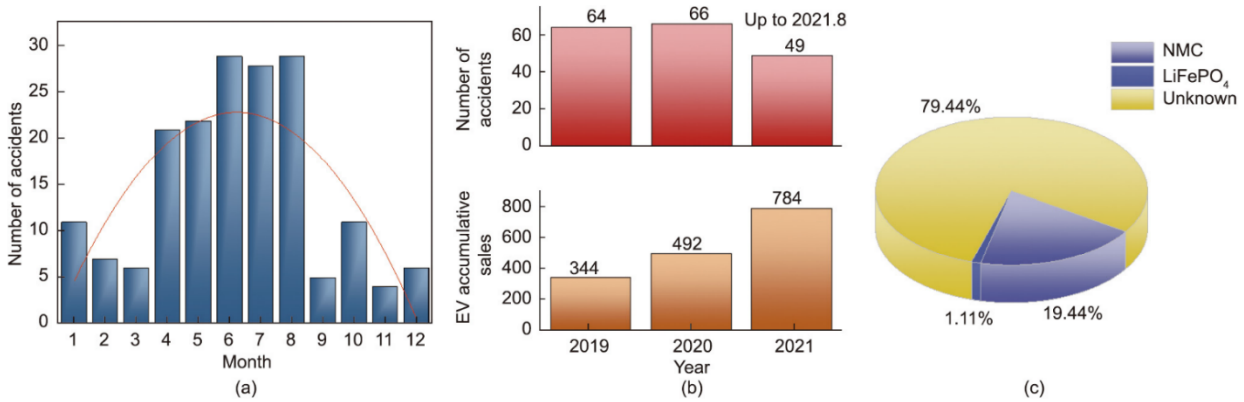

Figure 1.3. Analysis of fire accidents involving EVs from January 2019 to August 2021. a) Number of EV fire accidents monthly; b) number of EV fire accidents and number of EVs yearly; c) proportion of accidents caused by different types of LIBs. Reprinted with permission from Ref. (X. Yu et al., 2022)

Furthermore, the number of LIBs with NMC cathode involved in battery-related accidents is remarkably higher than that of batteries with LFP cathode, pointing out that a system with higher energy density is more prone to safety-related risks (Qiu & Jiang, 2022). This is due to the less stable chemical reactivity of the battery when more energy is stored in the electrode materials. Most of the accidents reported in electric vehicles are seldom related to car crashes or collisions and happen for no apparent reason, in a seemingly unpredictable fashion. The so-called spontaneous combustion is another factor undermining the trust in EV safety. The causes of the process may lie in an excessive deviation of the operating condition from the optimum, which can induce overheating of the battery or thermal runaway (Q. Wang et al., 2012), producing smoke and leading to fires and explosions. The comprehension of the dynamic behind battery hazard lies in the working principle itself of LIBs. A regular LIB consists in a series of tightly packed elements: a copper foil acting as the anodic current collector, on which the anode is deposited (typically carbonaceous anode); a permeable separator imbued with the liquid electrolyte; and the cathode, typically LCO, LFP or NCM on an aluminum foil collector (**Figure 1.4**).

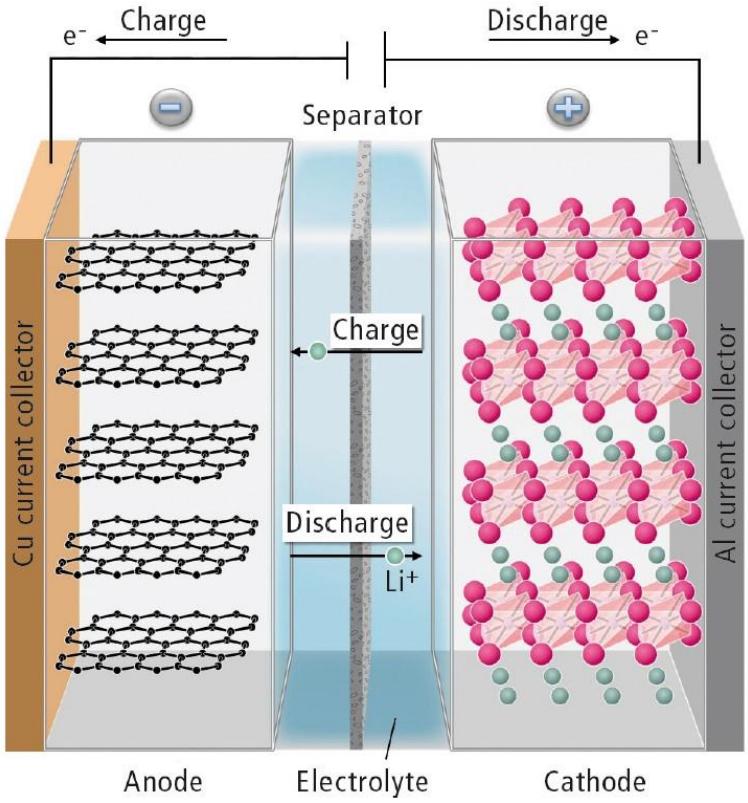

Figure 1.4. Schematic representation of the components and functional principles of a lithium ion battery. Reprinted from Ref. (Schultz et al., 2016)

During the first charge cycle, a thin layer (10-100 nm) known as solid electrolyte interphase (SEI) is formed on the surface of the anode. The SEI acts as a passivation layer preventing the anode from further reacting with the electrolyte but, at the same time, it increases the polarization during the process of ion intercalation/deintercalation. The very slow ion transfer across the SEI can lead to lithium deposition (H. Wang et al., 2020) on the electrode surface, and this phenomenon is more intense under low temperature charging and higher charge rates. Upon discharge, the oxidation at the anode extracts Li^+ ions from lithiated graphite Li_xC_6 and the intercalation is observed at the cathode through ion transfer across the electrolyte. Net charge balance is obtained by the simultaneous migration of electrons via the external circuit. During the charge phase, Li^+ ions and electrons are taken from the cathode and return to the anode. The alternate movement of the lithium ions between charge and discharge lead to the name ”rocking-chair” battery (Scrosati, 1992). The electrochemical process is expressed by the following reactions.

Cathode reaction: $Li_yMO_2 \underset{discharge}{\overset{charge}{\leftrightharpoons}} Li_{y-x}MO_2 + xLi^+ + xe^-$

With $0 \leq x \leq y \leq 1$

Anode reaction: $xLi^+ + xe^- + Li_zC_6 \underset{discharge}{\overset{charge}{\leftrightharpoons}} Li_{z+x}C_6$

With $z \geq 0$

Global reaction: $Li_yMO_2 + Li_zC_6 \underset{discharge}{\overset{charge}{\leftrightharpoons}} Li_{y-x}MO_2 + Li_{z+x}C_6$

Faults in energy storage systems can pertain to the battery itself or to the control systems (sensors) and can be diversified, depending on the source, in mechanical, electrical and thermal-related faults (**Figure 1.5**) (Doughty & Roth, 2012; Lisbona & Snee, 2011). Among mechanical causes of damage, we can list impact shocks, crushes, and penetrations (Qiu & Jiang, 2022; Sahraei et al., 2012). Mechanical deformation can lead to material disruption, structural disarray, and internal short-circuit, eventually causing the rise in internal temperature and fire ignition. Electrical abuse often involves external short-circuit or overcharge of the system. The latter is the most severe condition, forcing energy accumulation beyond the inherent voltage limits of the battery.

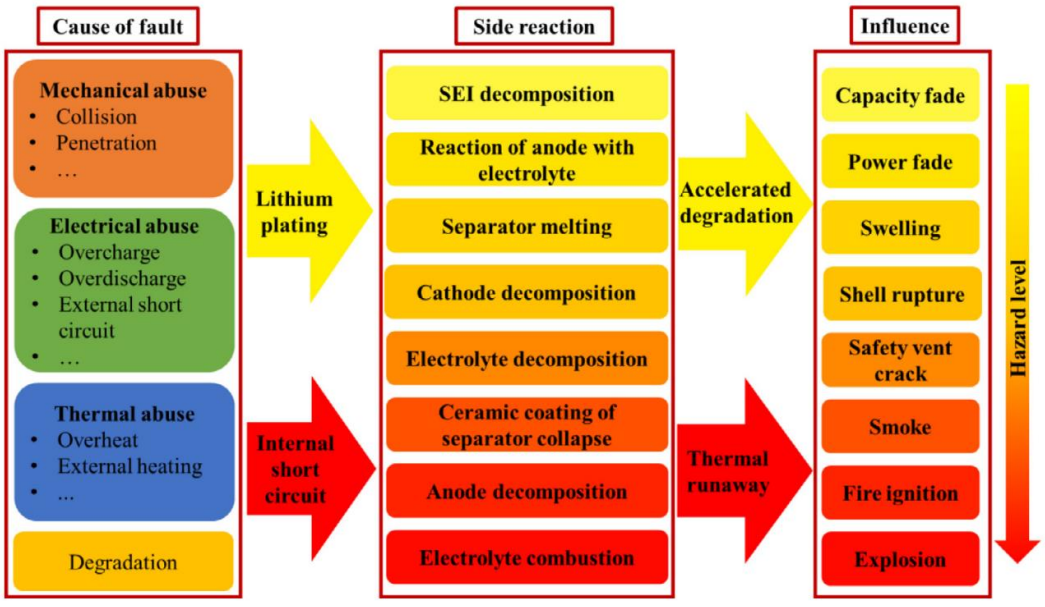

Figure 1.5. Schematic diagram of the causes, side reactions and influences of faults in LIBs. Reprinted with permission from from Ref. (Qiu & Jiang, 2022).

In a condition of overcharge, excess of lithium in the anode blocks additional insertion of ions, and lithium starts depositing on the surface starting the growth of dendrites (**Figure 1.6a**). The phenomenon is driven by the non-uniformity of the lithium surface, and subsequent discharge processes (lithium dissolution) generate lithium particles that are electrically isolated from the lithium anode (**Figure 1.6b**). The existence of dendrites has been confirmed by microscopic observations (**Figure 1.6c**) and their formation has been attributed to the presence of a passivation film (Aurbach et al., 1989; K. Xu, 2004). Plated lithium can also react with the electrolyte and produce lithium carbonate, further increasing the internal resistance (Schultz et al., 2016). Oxidative degeneration of the electrolyte can spur heat increase and thermal breakdown. On the contrary, excessive delithiation (overdischarge) can irreversibly deform and rupture the electrode, dissolving its components in the electrolyte and generate heat and oxygen evolution (Ouyang et al., 2018). The consequences of thermogenic faults on the condition of batteries can be hazardous as well (Q. Wang et al., 2012). External heating due to abnormal ambient temperature or mechanical overheating caused by loose contact may lead to thermal runaway if the excess of heat is not dissipated in a brief time. Irreversible heat generation depends on cell overpotential and

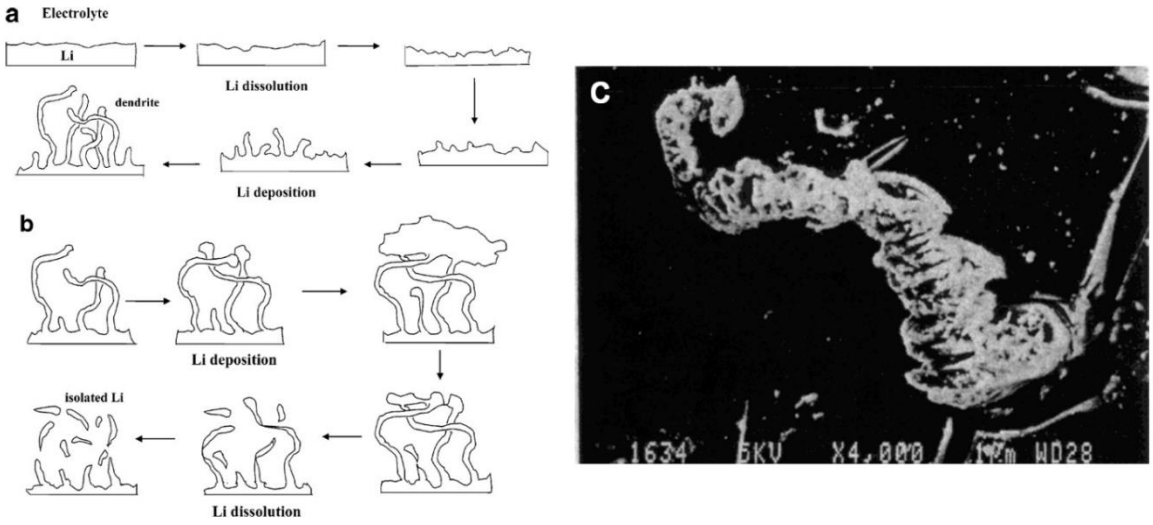

Figure 1.6. a) Representation of dendrite growth on Li surface. b) Scheme for the formation of isolated lithium particles from Li dendrites. The uneven dissolution of the dendrites leaves lithium crystals detached from the substrate. These particles are electrochemically inert but still reactive due to their high surface area. Reprinted with permission from Ref. (K. Xu, 2004). c) SEM micrograph of a single dendrite formed by lithium deposition in a PC/$LiClO_4$ solution. Reprinted with permission from Ref. (Aurbach et al., 1989)

internal cell resistance, whereas reversible heat more often depends on the reduction reaction at the positive electrode (Viswanathan et al., 2010).

1.2.2 Safety Strategies

Considering all the reliability flaws for LIBs, numerous methods have been undertaken to reduce the occurrence of accidents. The approaches for improving battery safety can be split into active strategies, dealing with condition diagnosis, damage detection and system management techniques, such as cooling/heating, and passive strategies. The latter family concerns the intrinsic design of the system and includes all modifications of materials and components to improve their resilience and chemical properties. Adaptation of electrodes can deal with element replacement and surface coating of both the anode and the cathode (Doughty & Roth, 2012), and can have a most visible effect on battery safety. Surface coating can shield the electrodes from immediate contact with the electrolyte, inhibit structural distortion and limit side reactions, ultimately decreasing heat generation. On the anode side, alteration of the SEI can hamper decomposition by modifying the reaction chemistry during battery operation. It can involve the removal of reaction sites within the graphite structure or the formation of a thicker passivation layer on the surface of the electrode, diminishing the reactivity.

Most battery-related accidents usually find their conclusion in the battery catching fire and exploding, and the factual responsibility for this outcome has to be found in the electrolyte used within the cell. The typical liquid electrolytes employed in LIBs are based on organic carbonates like DMC EC, DEC, and PC as the solvent and $LiPF_6$ as the lithium salt, owing to its high ionic conductivity (J. M. Tarascon & Guyomard, 1994), giving the best compromise in terms of performance and cost (**Figure 1.7a**). This combination, however, is not free of safety issues, mainly when used under serious thermal abuse conditions. The raise in temperature can induce reactions with the electrodes and promote the evolution of combustible gases, with disastrous results (Spotnitz & Franklin, 2003). In addition to this, the presence of $LiPF_6$ can negatively affect thermal stability; decomposing by following the reaction (Sloop et al., 2001)

$$LiPF_6 \leftrightarrows PF_5 + LiF \downarrow$$

generating insoluble LiF, that can contaminate and degrade the remaining solution, and the strong Lewis acid PF_5. The high susceptibility of P–F bonds to hydrolysis even at low temperature strongly favors reactivity with water and production of HF (Ping et al., 2010), which subsequently catalyzes parasitic reactions with the components of the SEI, leading to its depletion and rupture, as well as the organic solvent themselves (Kawamura et al., 2002). Modified compositions using different Li salts have been evaluated, but the final performances are often inferior to the ones shown by $LiPF_6$ (**Figure 1.7b**).

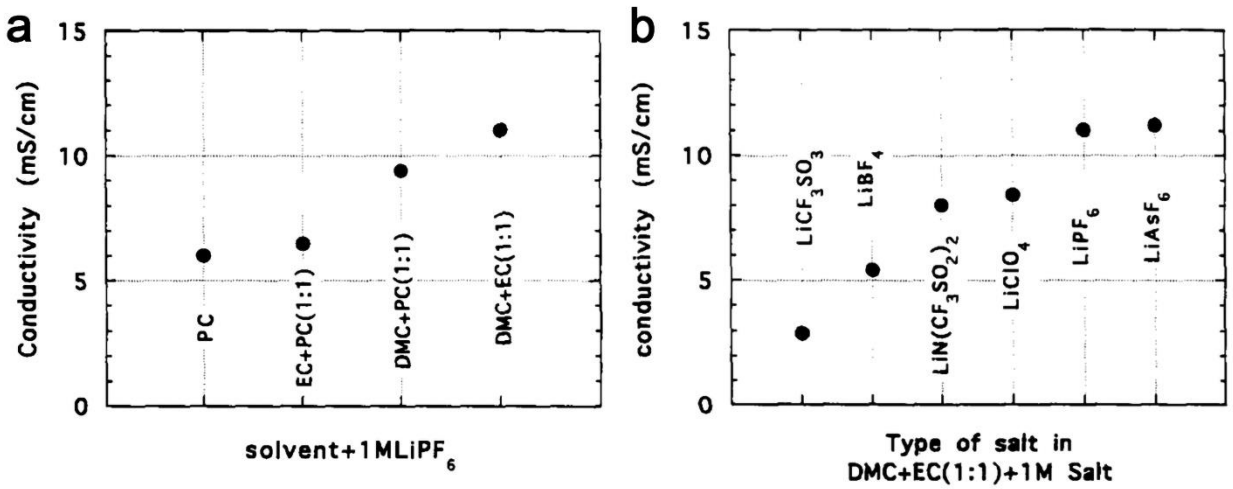

Figure 1.7. a) Room temperature ionic conductivities (at 20°C) of organic solvents mixtures with $LiPF_6$ 1M concentration. Reprinted with permission from Ref. (J. M. Tarascon & Guyomard, 1994); b) Room temperature ionic conductivity (at 20°C) of a DMC+ EC based electrolyte using different Li salts. Reprinted with permission from Ref. (J. M. Tarascon & Guyomard, 1994)

Several methods have been explored to adjust the electrolytes and improve their safety, and some procedures involve using different lithium salts, more stable in organic environments than $LiPF_6$ (Aravindan et al., 2011; Bushkova et al., 2017). Viable alternatives include $Li[(C_2F_5)_3PF_3]$ (LiFAP), which presents a higher stability towards the hydrolysis of P–F bonds, or imide-based salts such as $Li[N(CF_3SO_2)_2]$ (LiTFSI), which shows a higher thermal stability and a good dissociation degree in low-dielectric constant solvents. The lower ionic mobility of LiTFSI compared to $LiPF_6$ is balanced by the increased viscosity of the solution, allowing higher conductivity (Webber, 1991). Nonetheless, practical application of imide salts is hindered by their inability to produce a passivating layer. Other choices include borate-base salts like $Li[B(C_2O_4)_2]$ (LiBOB) which show some peculiar properties (Aravindan et al., 2011). This salt provides a good

chemical inertness (K. Xu, Zhang, et al., 2002) and thermal stability (Jiang et al., 2004), good ionic conductivity (Azeez & Fedkiw, 2010) in non-aqueous systems, ability to create a steady SEI, with the direct action of BOB anions, and lower toxicity compared to fluorine-based salts. The main drawback of LiBOB is its inferior solubility in carbonate solvents and the difficult production with a proper degree of purity at a higher scale (K. Xu et al., 2005). An efficient practice to enhance the stability of the electrolytes is the incorporation of additives which can support the formation of the SEI or act as flame-retardants to suppress the chance of combustion (Haregewoin et al., 2016). In the former group we can find organic compounds like vinyl ethylene carbonate (VEC) (Y. Yang et al., 2019) or fluoroethylene carbonate (FEC) (M. Han et al., 2021) that are proven to help creating a stable SEI. Flame-retardants act by removing reactive radical species formed by the electrolyte decomposition and globally reducing the flammable character of the solution (Hyung et al., 2003). The most employed materials used as flame-retardants are organophosphorus compounds, such as triphenyl phosphate (TPP) (Ciosek Högström et al., 2014), tributyl phosphate (TBP) (Nam et al., 2012) or dimethyl methyl phosphate (DMMP) (Z. Chen et al., 2020) (**Figure 1.8**), which have been proven to significantly increase the onset temperature even for small amounts of additive in the solution and decrease the exothermic heat from internal reactions. TPP and TBP manifested electrochemical stability up to 5 V with negligible effects on the cycling performance (Hyung et al., 2003). However, organophosphorus compounds present a high viscosity and are not able to form a stable SEI (K. Xu, Ding, et al., 2002). Alternatives to organic phosphates can be found in halogen-based flame retardants, most commonly fluorides (Q. Wang et al., 2019), which are capable of establishing a SEI and exhibit a lower viscosity (Chandrasekaran et al., 2009). However, high amount of fluoride in the electrolyte are poorly compatible with $LiPF_6$, hence the amount of additive in the mix is typically low (below 5% vol.).

The use of additives does not remove the combustible elements in the cell, and so attempts have been done to search for completely non-flammable materials, in order to substitute completely the organic electrolytes (Q. Wang et al., 2019). Organophosphorus solvents have been explored as liquid alternatives to carbonates when supported with supplements to form a stable SEI. Small amounts of FEC stabilized the cycling performance of LIBs using triethylphosphate (TEP) (Z. Zeng et al., 2018). Cells using DMMP as liquid electrolyte have reported performance comparable with cells using standard carbonate solvents (J. K. Feng et al., 2008). Another viable alternative is found in aqueous batteries, using water solutions as solvent, due to their

environmental compatibility and their high conductivity. Some important issues of these systems are the decomposition of water, which leads to a fast degradation of cycling performance, and a limited electrochemical stability window (J. Liu, Xu, et al., 2018). An interesting possibility is given by ionic liquids (IL), which are ionic compounds with low melting point (below 100 °C). This class of materials shows notable advantages in comparison with organic solvents. They are thermally stable and non-flammable, and they present a low vapor pressure, reflecting in a lower volatility (Francis et al., 2018). Their major limits are their high viscosity, which implies a meager ionic conductivity, and low compatibility with electrode materials.

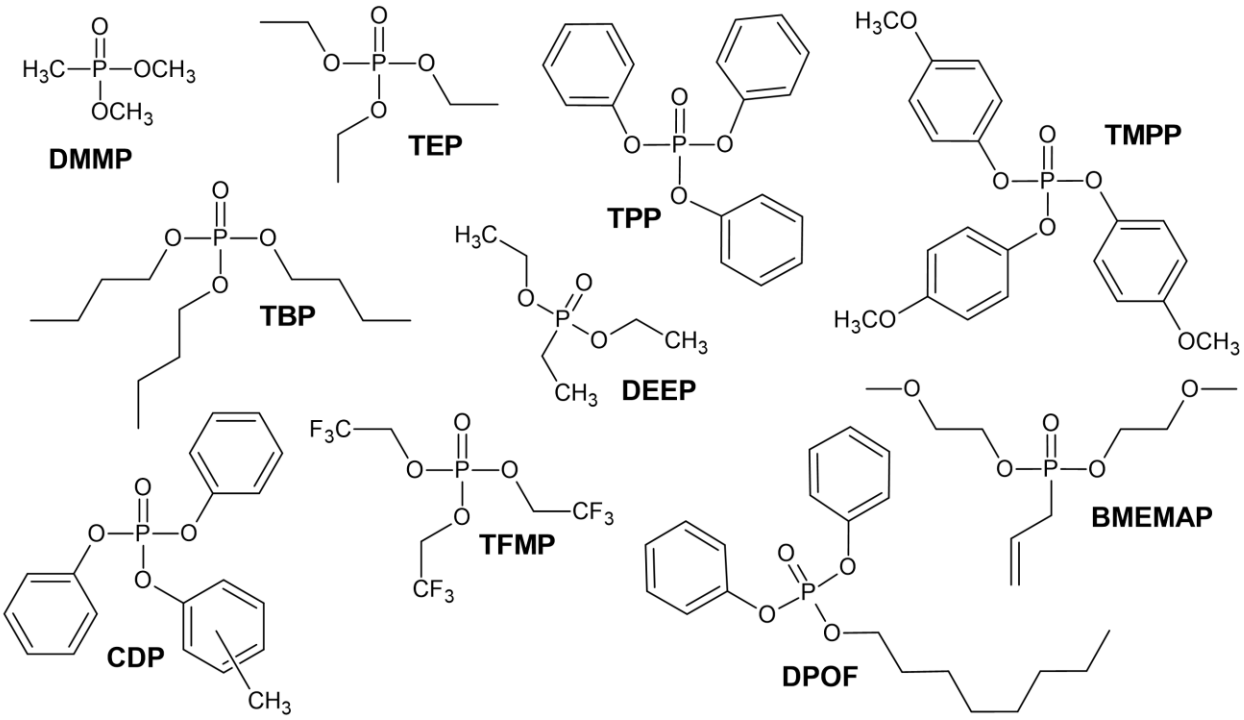

Figure 1.8. Structures of some organophosphorus flame retardant additives.

1.3. Ion Transport in Solids

One of the most fascinating alternatives is the modification of the battery by completely removing the liquid components within the cell and establishing an all-solid configuration, with the use of solid electrolytes (Fergus, 2010). Primeval investigations related to ionic transport in a solid environment date back to the beginning of 19th century, and observations of fast ionic conduction in solids is reported since the early 1900s (Tubandt & Lorenz, 1914), but the direct application of solid state ionics for electrolytes in batteries became relevant in the last decades of

the 1900s (Owens, 2000). LiI became the staple electrolyte in batteries for cardiac pacemakers in the early 1970s and its conduction features were first reported by Liang in 1973 (Liang, 1973). In 1978 Armand proposed a first concept of polymer solid electrolytes for lithium batteries (M. Armand, 1983), reporting the conduction of alkali metal ions in a polyethylene oxide (PEO) complex. A Cu-based ionic superconductor was reported by Takahashi et al. (Takahashi et al., 1979) in 1979, manifesting a conductivity of 0.34 S cm^{-1}, the highest value every showed by a solid electrolyte (**Figure 1.9**). Since the 1980s, the efforts in this field have increased constantly and ever more diverse compounds have been investigated in terms of electrochemical features for possible applications in a battery.

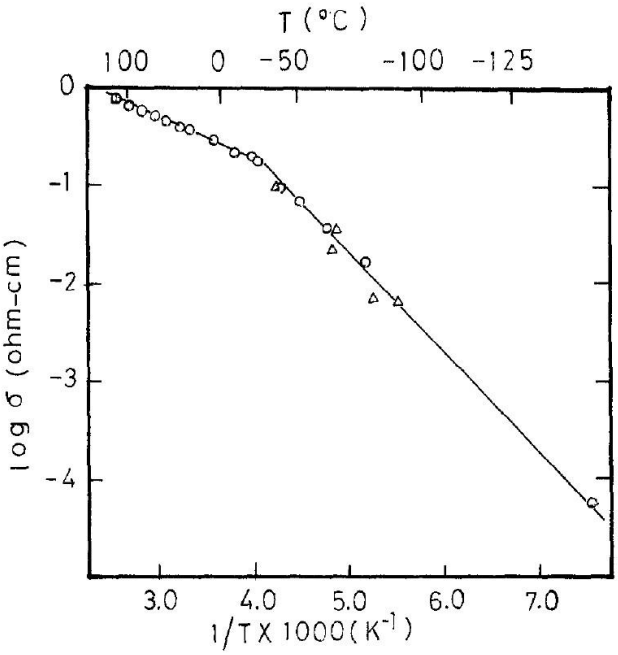

Figure 1.9. Arrhenius plot of the conductivity for CuCl - CuI - RbCl superconductor phase in the temperature range from −140 to 130 °C. ○: cooling, △: heating. Reprinted with permission from Ref. (Takahashi et al., 1979)

The typical configuration of an all-solid-state lithium battery (ASSLIB) consists of the two electrodes (anode and cathode) divided by the solid electrolyte which acts as the separator at the same time, simplifying the structure of the system. The electrochemical processes of charge and discharge follow the same principles as a traditional LIB: charge carriers (Li^+ ions) are extracted from the cathode and move to the anode during the charge, balanced by electron shift through the external circuit, and the opposite transfer happens during the discharge. The adoption of solid-state

batteries offers numerous advantages to the technology, beyond the simple (but still important) improvement in safety. Solid phases manifest an intrinsic slower reactivity compared to liquids, leading to remarkably longer expected lifecycles for solid-state cells. Results reported full-solid cells retaining more than 90% of the initial capacity for 10000 cycles (J. Li et al., 2015) with an extremely limited volume of electrolyte, hundreds of times smaller than liquid-electrolyte cells, and negligible decomposition of the electrolyte. A fundamental difference between conventional LIBs and solid-state batteries lies in the process of ion transport across the solid electrolyte. Ion migration in ASSLIBs is typically associated with a multiscale operation made of mechanisms expressed from the atomic scale to the macroscopic scale, which are globally reflected by the final impedance of the system (Famprikis et al., 2019).

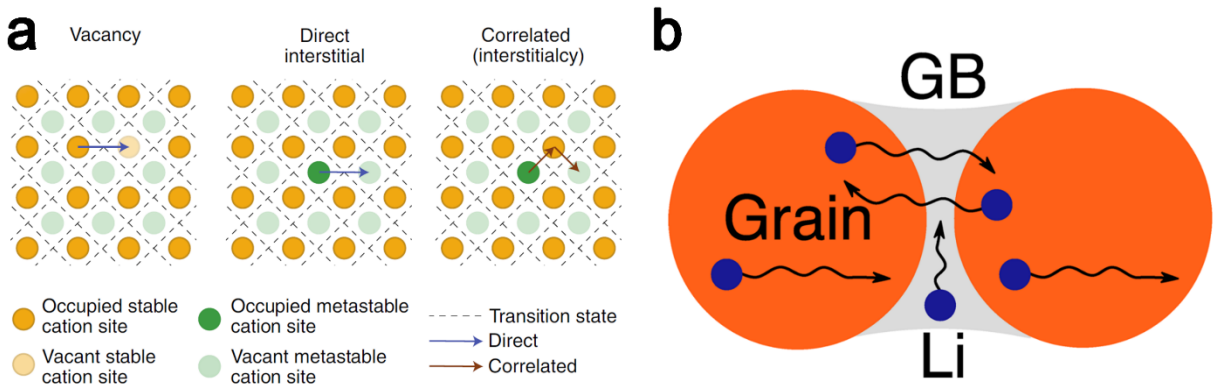

Figure 1.10. a) Schematic representation of the cation migration mechanisms in a solid: vacancy, direct interstitial and correlated. Reprinted with permission from Ref. (Famprikis et al., 2019). b) Representation of possible ion transport mechanisms at the grain boundaries of a solid electrolyte. Reprinted with permission from Ref. (Dawson, Canepa, et al., 2018).

On a lower scale, the diffusion of charge carriers (mobile ions) occurs via favorable transport pathways following ion hopping through low energy sites in the structure. The nature and energy of the sites are inherently correlated with their coordination environment and the anion interconnection and, consequently, with the crystal structure of the material. The most common mechanisms for ion mobility in crystals (**Figure 1.10a**) are vacancy diffusion, interstitial movement, and concerted ion displacement, or knock-on, in which the moving ion causes the dislocation of a lattice ion into an adjacent site. From a practical standpoint, vacancies and interstitials are identified as the mobile carriers. The mobility and concentration of the charge carriers are key factors in defining the ionic conductivity of the solid. The number of mobile

species depends on the temperature and is related to their formation energy, but it can be influenced by external substitution of lattice ions with aliovalent dopants, creating additional vacancies and interstitial sites, as well as disrupting charge conservation. Doping with large size elements can locally distort the crystal structure and induce an enlargement of transport channels, improving the ion conduction. Partial ion substitution can affect the conductivity also by altering the potential energy surface and decreasing the migration energy (Y. Deng et al., 2017). Concordant migration phenomena have been observed in amorphous solids as well, despite the absence of structural periodicity and regular long-range transport channels.

On a microscopic level, irregularities in structure and composition can have a major impact on the conductivity. Uneven contact surfaces between micro- and nano-scale crystals are defined as grain boundaries, and their nature can diverge significantly from the bulk of the crystal. Generally, the distortions at the boundaries caused by incongruent orientation of crystal domains hamper the seepage of charge carriers between different grains (**Figure 1.10b**), sensibly increasing the resistance for ion migration and affecting the conductivity (Dawson, Canepa, et al., 2018). Another factor which may contribute to the internal resistance of the solid phase is the imperfect contact between solid particles. The presence of pores makes the movement of ions more convoluted, leading to irregular current density and lower conductivity on a macroscopic level. Moreover, void spaces have been shown to make a favored location for uneven lithium deposition as the nucleation at the boundaries may give origin to tortuous structures resembling lithium dendrites, overturning the advantage of the solid electrolyte (C. Zheng et al., 2021). Nonetheless, the absence of flammable components in the cell would still soften the negative outcome of such an opportunity. Lithium plating at particles edges can be limited by the application of electrolyte with high Li^+ transference number (close to unity), which permits the employment of Li-metal anode for high energy density.

Considering the macroscopic scale, the ionic conduction and electrochemical performance is generally mirrored by the overall impedance of the system, which is defined by more contributions from distinct elements of the cell. On this level, the electrochemical stability of the solid electrolyte towards the electrodes plays a major role and the conductivity of the interphases still represent a main obstacle to ionic transport (C. Yu et al., 2017). A solid material with higher global ionic conductivity can manifest a higher impedance due to a poorer compatibility with the

electrode. Interfacial impedance is typically defined as area-specific resistance (ASR), and it is mainly influenced by the direct contact area between the electrode and the electrolyte. The effects of a meager contact can dominate the final resistance of the system. Moreover, at the solid interface electrochemical events between the different cell elements can happen, mostly direct electrolyte decomposition and reactions with the electrode. Decomposition is linked to the movement of charged cations and electrons from and to the electrolyte and it is most often observed when in contact with metallic lithium (Richards et al., 2016), while chemical reactivity can lead to the formation of additional chemical species at the interface (**Figure 1.11a**) (Richards et al., 2016). The occurrence of these phenomena is correlated to the external power and voltage applied. The voltage range tolerated by the electrolyte without experiencing decomposition delimits the electrochemical stability window of the material (**Figure 1.11b**), and it can be established considering the thermodynamics of the decomposition reactions as a function of the voltage. Solid electrolytes typically present a high stability towards oxidation, mainly due to their anion structure and their tendency to release electrons, whereas, on the other side, their proclivity to host electrons related to the distribution of non-mobile cations sets up their stability towards reduction (Famprikis et al., 2019; T. Yu et al., 2021). Interfacial transport character influences the reaction kinetics whereas impediments to ion transfer and electron mobility can limit the extension of the reaction, stabilizing the solid interface. However, since the cations must move across the interface to conduct the charge transfer, the interphase should exhibit good ionic conductivity while insulating from electron conduction.

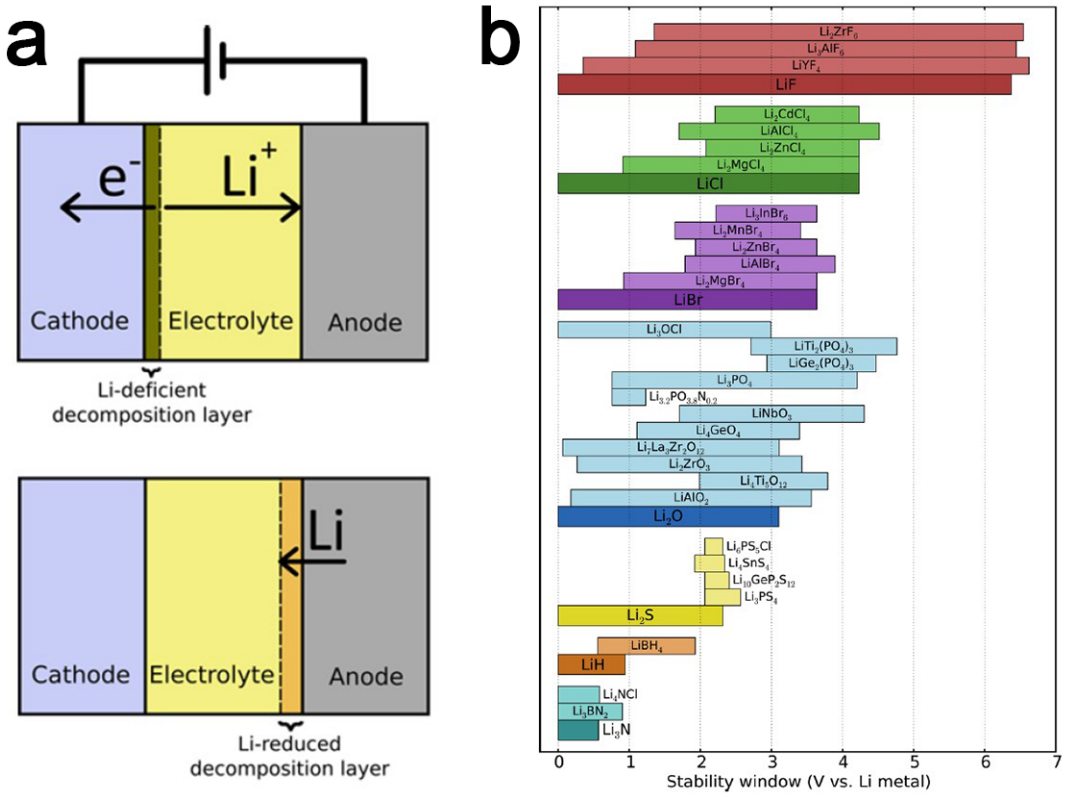

Figure 1.11. a) Schematic of a full cell showing decomposition of the electrolyte at the cathode/electrolyte interface during charging (top) and reduction of the electrolyte by the lithium metal anode (bottom). Reprinted with permission from Ref. (Richards et al., 2016). b) Electrochemical stability ranges of various electrolyte materials grouped by anion, with corresponding binary for comparison. Reprinted with permission from Ref. (Richards et al., 2016).

1.4. Classes of Solid Electrolytes

The ideal solid electrolyte should therefore present the transport properties, as well as chemical stability against external agents, such as water, and mechanical resilience and robustness. Other desirable properties include a facile synthesis process, limited environmental hazardousness, low toxicity, and relatively low production cost. To achieve these results, a vast range of materials has been investigated for practical applications as solid electrolytes, which are commonly divided into two general groups: inorganic ceramics and organic polymers (Fergus, 2010). These classes of materials differ primarily for their mechanical characteristics. Ceramic electrolytes present sensibly higher elastic moduli (Ni et al., 2012; Papakyriakou et al., 2021), reflecting in increased mechanical stiffness and making them a preferred choice for rigid battery configurations as in thin-

film systems. In contrast, polymeric materials are typically more malleable and therefore useful for flexible battery designs. The easier processing of polymers compared with ceramics reduces their fabrication cost, while ceramics are more apt for systems undergoing external stress, such as hot temperatures or other aggressive environments. A representation of the peculiar properties of different families of electrolytes is shown in **Figure 1.12** (N. Zhao et al., 2019).

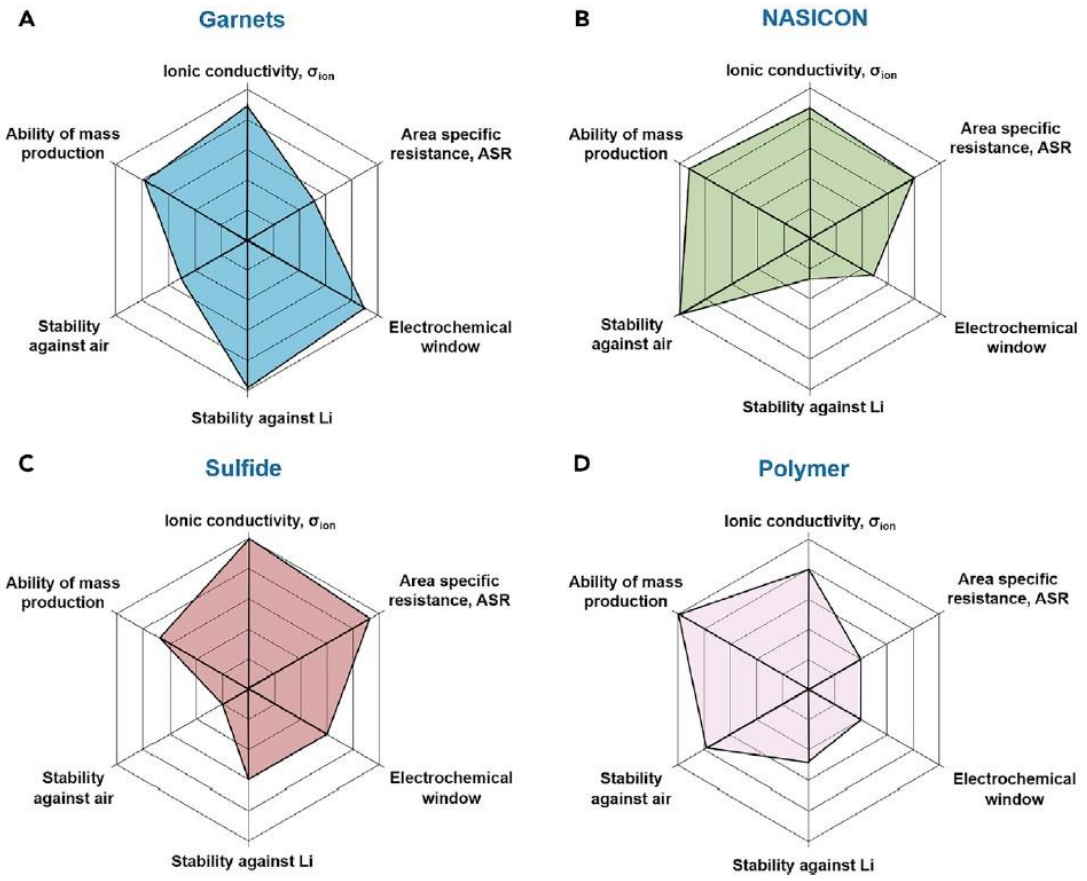

Figure 1.12. Representation in spider chart for the main properties of four different classes of solid electrolytes. Reprinted with permission from Ref. (N. Zhao et al., 2019)

1.4.1 Polymeric electrolytes

A polymer-based electrolyte should be capable of dissolving lithium salts within the matrix and couple with Li^+ ions, and for this purpose introducing polar functionalities in the polymer is a viable solution for helping the dispersion of lithium salts (Yao et al., 2019). Most solid-polymer electrolytes involve polyethylene oxide (PEO) or its derivatives as main components. The oxygen atoms in the chains possess a lone electron pair which coordinates to Li^+ ions by Coulombic interaction, enabling the dissociation of the lithium salt which is dispersed into the PEO matrix. Under the influence of an electric field, Li^+ ions have the tendency to shift between different coordination spots along the polymer section or hop from one segment to another (**Figure 1.13**) (K. Xu, 2004; Yao et al., 2019). Because of the dimensions of polymer chains, ion movement is hindered and the conductivity is correlated to the mobility of polymer segments and the number of lithium ions, which depends on the dissociation of the salt (Q. Zhang et al., 2017). A crucial parameter for the electrochemical behavior of polymer electrolytes is the glass transition temperature T_g, at which the material shifts from a hard glassy state to a more ductile and viscous one. Below T_g the molecules are scarcely mobile, and the material is fragile and stiff, while beyond T_g the material undergoes a downright change in physical properties, like hardness, density, dielectric constant, and many others. The degree of crystallinity in a polymer is another key factor to consider when evaluating the properties of an electrolyte. A higher crystallinity implies a more extended intrinsic order of the frame with a tighter packing of polymer chains, which decreases the free volume within the polymer and reduces the ion conduction.

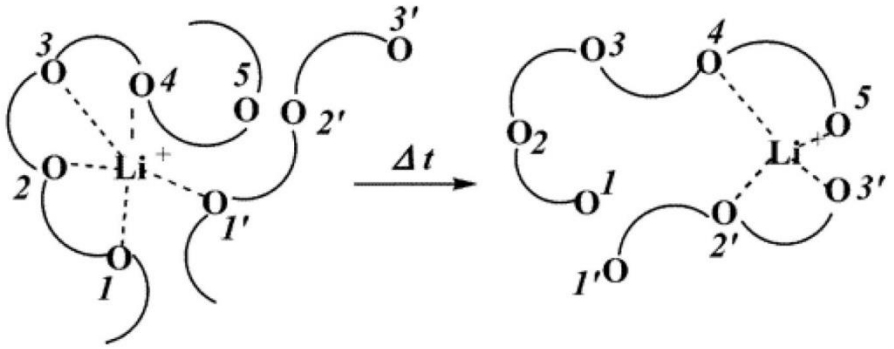

Figure 1.13. Schematic representation of lithium ion conduction mechanism of PEO-based polymer electrolyte. Reprinted with permission from Ref. (K. Xu, 2004)

Different research approaches that have been undertaken to ameliorate the mechanical properties of polymers include polymer/polymer coordination with copolymerization or crosslinking, but the results obtained by these techniques are limited. Other methods involve the implementation of additives, like plasticizers, or external composites, such as ionic liquids (Subianto et al., 2009). Another approach considers the incorporation of ceramic particles within the polymer matrix. Both inert and conductive inorganic fillers have been investigated and an improvement in the mechanical features of the polymer has been observed. Limited doping of PEO with $LiAlO_2$ (10% wt.) was shown to increase the conductivity of the composite (**Figure 1.14a**) (Capuano et al., 1991) and a smaller particle size (<10 μm) of the filler had a more beneficial effect on the conductivity. Incorporation of Al_2O_3 has been proven to decrease the degree of crystallinity and T_g of PEO (Tambelli et al., 2002). Another typical inert filler used in solid polymer electrolytes is SiO_2. A PEO-SiO_2 composite including EC/PC plasticizers was described with a value of ionic conductivity at room temperature of 2×10^{-4} S cm^{-1} with a very small loading of 2.5% wt. (**Figure 1.14b**) (Nan et al., 2003). Lin et al. reported a reinforced composite assembled with a rigid SiO_2 aerogel showing high ionic conductivity of 2×10^{-4} S cm^{-1} and high hardness modulus of 0.43 GPa (Lin et al., 2018). The composite presents distributed SiO_2 domains with extended acidic surfaces, which favor anion adsorption and create highly conductive pathways through the framework. This is beneficial to salt dissociation and enhancement of ionic conductivity. A PEO-$LiClO_4$ composite incorporating nanometric TiO_2 particles was presented by Croce et al. (Croce et al., 1998). The material displayed a conductivity of 10^{-5} S cm^{-1} at room temperature. Liu et al. engineered a solid electrolyte comprising Y_2O_3-stabilized ZrO_2 (YSZ) nanowires in polyacrylonitrile (W. Liu et al., 2016). The structure of the material presents numerous positive vacancies with acidic character, which act as anion sinks enabling the dissolution of lithium salts (**Figure 1.14c**). A continuous fast conduction pathway is observed for nanowires rather than nanoparticles. Introduction of YSZ nanowires improved ionic conductivity to 10^{-5} S cm^{-1} at room temperature, about two orders of magnitude higher than pristine polyacrylonitrile. The conductive fillers employed for polymer composites generally include inorganic electrolytes acting as fast ion conductors. The synergistic composition of conductive ceramic species with the polymer chains combines the positive features of the two parts, allowing an improved ionic conductivity due to

the inorganic component and incrementing the interface contact of the dispersed particles thanks to the polymer (Yao et al., 2019).

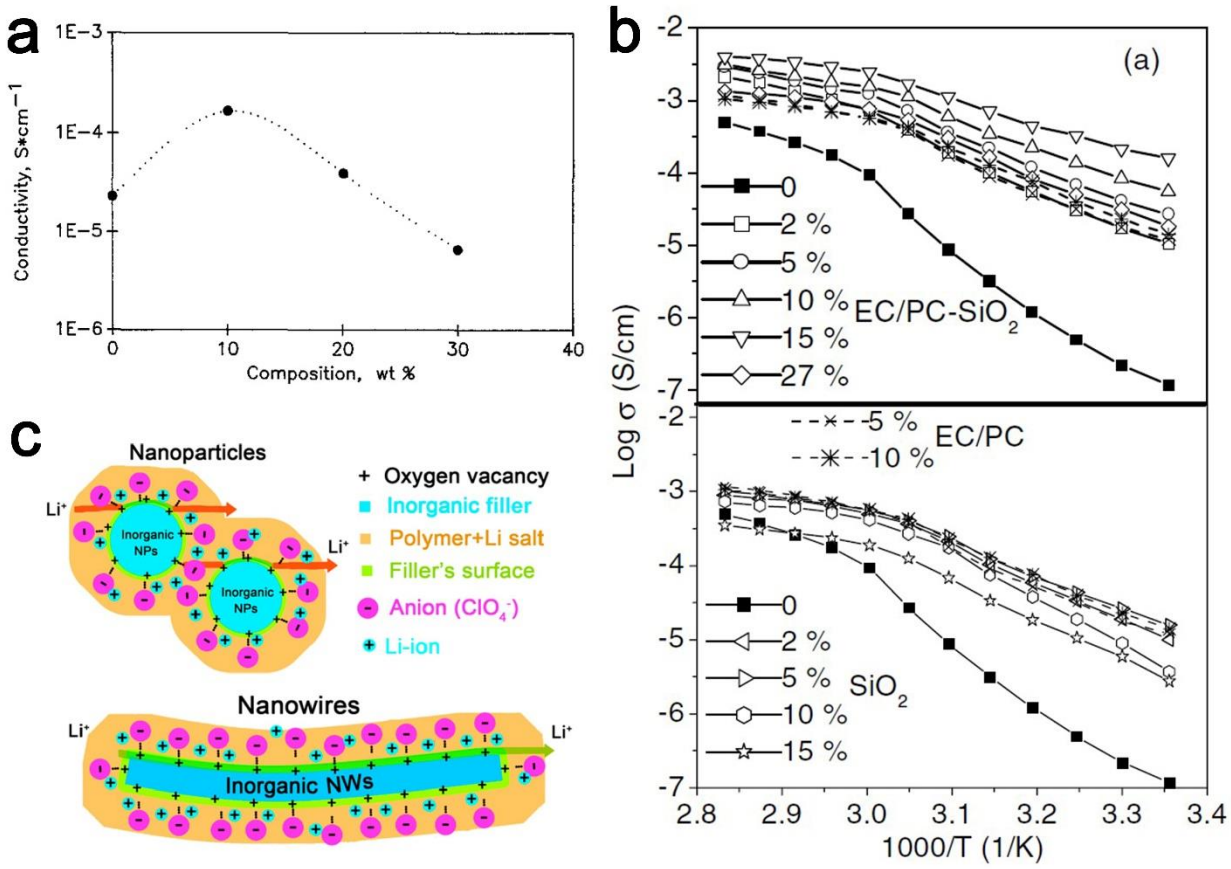

Figure 1.14. a) Ionic conductivity vs. composition of a $(PEO)_8LiClO_4–LiAlO_2$ composite polymer electrolyte at 60 °C. Reprinted with permission from Ref. (Capuano et al., 1991). b) Arrhenius plot of ionic conductivities for the PEO-Li/(EC/PC-SiO_2) films, compared with the values for PEO-Li/EC/PC and PEO-Li/SiO_2 films. Reprinted with permission from Ref. (Nan et al., 2003). c) Schematic illustration for Li-ion transport in composite electrolytes with nanoparticle and nanowire fillers. Reprinted with permission from Ref. (W. Liu et al., 2016).

1.4.2 Inorganic electrolytes

Inorganic materials have also been intensively studied for direct application as solid electrolytes, owing to their superior mechanical properties compared to polymers, including a higher thermal stability and stress resilience, as well as their better ionic transport features. Despite their advantages, few ceramics nowadays exhibit conductivities comparable in absolute values to conventional liquid electrolytes, but this drawback is partially mitigated by their ion transference number close to unity, which allows for relatively lower conductivities to achieve battery power densities commensurate with commercial LIBs. Within this class of electrolytes, a variety of subgroups have been examined, according to the crystalline framework of the materials. Among solid materials fascinating properties have been observed for several sulfides and oxides, and more recently, research has been delving into original structures to seek the best solution for practical purposes.

1.4.2.1. Sulfides

Sulfide Glasses and Thio-LISICONs

Various sulfide-based materials have been reported in literature, showing remarkably high conductivities (Z. Ma et al., 2018). Primary investigations on ionic conduction in sulfides were undertaken in glasses (Ribes et al., 1980) in the 1980s and systems such as Li_2S-P_2S_5 (Mercier et al., 1981) reported conductivities in the order of 10^{-3} S cm^{-1} glasses. The absence of transition metal elements in the composition of the materials avoids the narrowing of the stability window caused by side reactions. In 2000, the synthesis of the lithium germanium system Li_2S-GeS_2 was reported (Kanno et al., 2000) and a number of solid solutions with cation substitution manifested conductivities up to 6.5 $\times 10^{-5}$ S cm^{-1} for Ga-substituted Li_4GeS_4. These compounds are categorized as thio-LISICON, due to their structure analogous to $[Li_{14}Zn(GeO_4)_4]$ (**Figure 1.15a**) (H. Y. P. Hong, 1978) and Li_3PO_4 LISICON salts. Partial heterovalent substitution can help augmenting the ionic conduction via vacancy introduction by replacement of Ge^{4+} with P^{5+}, which led to an increase in conductivity up to 2.17×10^{-3} S cm^{-1}, with negligible electronic conductivity and electrochemical stability up to 5 V (Kanno & Murayama, 2001). Kamaya et al. (Kamaya et al., 2011) reported for the system $Li_{10}GeP_2S_{12}$ (LGPS) a value of room temperature ionic conductivity over 10^{-2} S cm^{-1}, comparable with organic electrolytes (**Figure 1.15b**). Due to the

excessive cost of Ge, practical application of these material may prove difficult, thus the substitution of this element with more affordable alternatives is crucial. Substitution with Al could be a feasible solution, as shown by Ooura et al. (Ooura et al., 2012) who reported an Al sulfide glass in the system $Li_2S–Al_2S_3–P_2S_5$. The materials were prepared with direct ball-milling at room temperature, with various degrees Al content, and the highest conductivity of 6×10^{-4} S cm^{-1} was observed for the sample with a 13.1% Al molar content, with stable cycling performances in a full battery. Amaresh et al. (Amaresh et al., 2014) presented the mixed system $Li_2S–Al_2S_3–GeS–P_2S_5$ with different Al/Ge ratios. The material with a molar ratio of 30:70 showed the best performance with a conductivity of 1.7×10^{-3} S cm^{-1} at 25 °C and a wide electrochemical window up to 5 V. Zhou et al. (P. Zhou et al., 2016) engineered the thio-LISICON $Li_{11}AlP_2S_{12}$ with full substitution of Ge in LGPS following a solid state synthesis at 500 °C. The material revealed a good conductivity of 8.02×10^{-4} S cm^{-1} and a low activation energy of 25.4 kJ mol^{-1}, with a stable chemical behavior towards lithium.

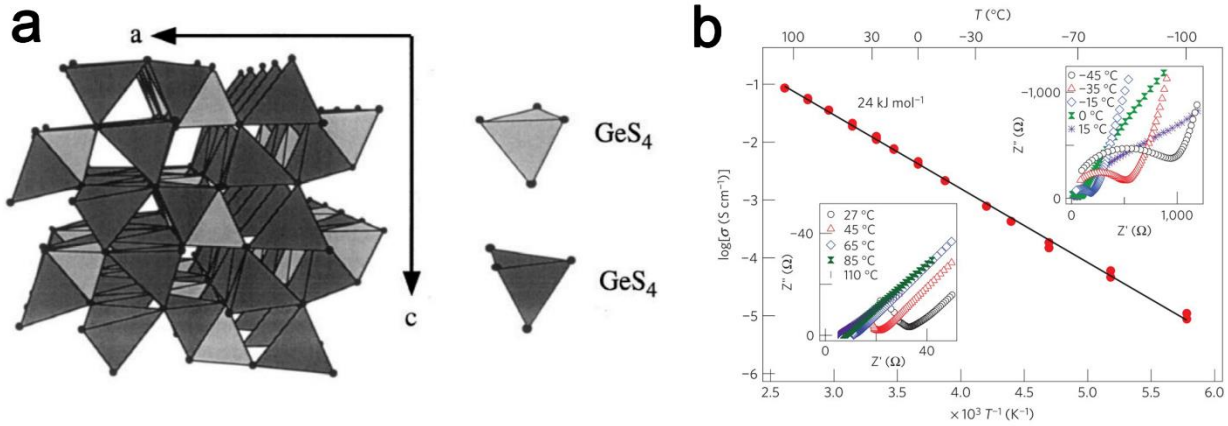

Figure 1.15. a) Structure of Li_4GeS_4 determined by X-ray Rietveld analysis. Reprinted with permission from Ref. (Kanno et al., 2000). b) Nyquist plots from low to high temperatures and Arrhenius conductivity plots of $Li_{10}GeP_2S_{12}$. Reprinted with permission from Ref. (Kamaya et al., 2011).

On the other hand, $Li_{10}GeP_2S_{12}$ promptly undergoes decomposition in contact with metallic lithium, forming a mixed interphase containing Li_3P, Li_2S and Li-Ge alloy and raising the resistance at the interface (Wenzel et al., 2016). Protection of the electrolyte has been attempted via diverse methods: the modification of the interface to form a LiH_2PO_4 protective layer allowed a long lifecycle of the cell with a capacity retention of 86.7% after 500 cycles and a limited polarization (Z. Zhang, Chen, et al., 2018). An alternative approach involves doping with high

valence ions: Xie et al. (Xie et al., 2018) attempted a partial introduction of Sb_2O_5 in glass-ceramic Li_3PS_4. The composition $Li_3P_{0.98}Sb_{0.02}S_{3.95}O_{0.05}$ presented the highest ionic conductivity of 1.08×10^{-3} $S \cdot cm^{-1}$ at room temperature, while excessive content of Sb_2O_5 led to a decrement in value because of the precipitation of Li_2S secondary phase during calcination. The increase in conductivity may be induced by a partial distortion of the Li transport channels caused by the larger Sb^{5+} ions inserted in the structure. The superionic conductor $Li_{9.54}Si_{1.74}P_{1.44}S_{11.7}Cl_{0.3}$ reported by Kato et al. (**Figure 1.16a**) (Kato et al., 2016) has been recently shown to exhibit an extremely high conductivity of 2.5×10^{-2} $S \cdot cm^{-1}$ and a good stability against lithium (**Figure 1.16b**). Cell performance showed a long-term cycling stability compared with a conventional LIB, with a Coulombic efficiency of about 100% after 1000 cycles and a higher retained capacity after cycling at high current density.

The introduction of oxygen atoms can show an improvement in conductivity for sulfide glasses, creating mixed oxysulfide systems. A modified Li_2S-P_2S_5 system with a small incorporation of P_2O_5 prepared with a solid state synthesis reported a room temperature conductivity of 8×10^{-4} $S \cdot cm^{-1}$, about 50% higher than the sample without oxygen (Tao et al., 2016). The lower activation energy for Li^+ diffusion of the resulting material may explain the improved conductivity. Simulation studies on oxygen-doped Ge-S glasses pointed out the presence of independent chains of GeS_4 and GeO_4 tetrahedra with Li^+ ions located in the empty spaces in between, creating coordinated chains (Messurier et al., 2009). Mixed silicon-oxysulfide glasses $Li_2S–SiS_2–Li_4SiO_4$ prepared by melt-quenching exhibited conductivities in the order of 10^{-3} $S \cdot cm^{-1}$ and long-term stable cycling, with a specific capacity of 60 mAh g^{-1} and a Coulombic efficiency close to 100% over 100 cycles (Hayashi et al., 2002). The insertion of oxygen atoms has also been proven useful in the stabilization of sulfide glasses towards reactivity with water, which can lead to the evolution of H_2S in ambient atmosphere: a mixed $Li_2S–P_2S_5–P_2O_5$ glass with the addition of ZnO showed a decrement in the generation of H_2S gas with negligible effect on the final conductivity (**Figure 1.16c**) (Hayashi et al., 2014). The water sensitivity of sulfide glasses is related to the intense water affinity of P–S bonds; oxygen atoms act as hard bases and show a tendency to react with P atoms to substitute soft base S. For this reason, variations on the structure to attain a phosphorus free material have been undertaken.

The material Li_4SnS_4 with partial As doping was described by Sahu et al. (Sahu et al., 2014) and the structure was centered on the soft acids Sn and As establishing less reactive bonds with sulfur and creating compounds more resistant to hydrolysis. The material displayed an improved stability against air atmosphere and the partial replacement with As allowed to achieve a conductivity of 1.39×10^{-3} S·cm^{-1}, about 20 times higher than pristine Li_4SnS_4 (Kaib et al., 2012). A modified sulfide superionic conductor with composition $Li_{3.85}Sn_{0.85}Sb_{0.15}S_4$ has been reported by Kwak et al. (Kwak et al., 2020). The material showed the orthorhombic crystal framework of the Li_4SnS_4 phase (Kaib et al., 2012), with a series of isolated MS_4 tetrahedra (M = Sn, Sb) containing four different Li^+ allocation sites (**Figure 1.16d**). The ionic replacement of Sn with Sb in the lattice diminished the global occupancy of octahedral Li^+ sites and induced the formation of Li vacancies, and the higher electronegativity of Sb^{5+} ions (1.971) with respect to that of Sn^{4+} (1.706) specifies a minor electron density of S atoms in Sb–S bonds compared to Sn–S. $Li_{3.84}Sn_{0.85}Sb_{0.15}S_4$ disclosed an astoundingly high value of conductivity of 8.5×10^{-2} S·cm^{-1} (**Figure 1.16e**) and a remarkable chemical endurance, with the formation of hydrated phases and negligible evolution of H_2S gas upon exposure to moisture. Cell testing in TiS_2/Li–In solid cells also displayed a noteworthy cycling performance, with a reversible capacity of 230 mAh g^{-1} upon the first cycle and a capacity retention close to 100% after 80 cycles. A series of mixed tin oxysulfides LiSnOS prepared through thermal precipitation was characterized by Kuo et al. (Kuo et al., 2019). The sample with a Li/Sn molar ratio of 2 revealed a NaCl-like structure consisting of a solid solution of Li_2SnS_3 and Li_2SnO_3 species and reported the highest conductivity among the compounds (1.92×10^{-4} S·cm^{-1}). The materials were employed to assemble solid/polymer composites with a poly(vinylidene fluoride-hexafluoropropylene) PVDF-HFP gel, and the resulting conductivities ranged between 10^{-3} and 10^{-4} S·cm^{-1}, with increasing values for a reduced amount of ceramic.

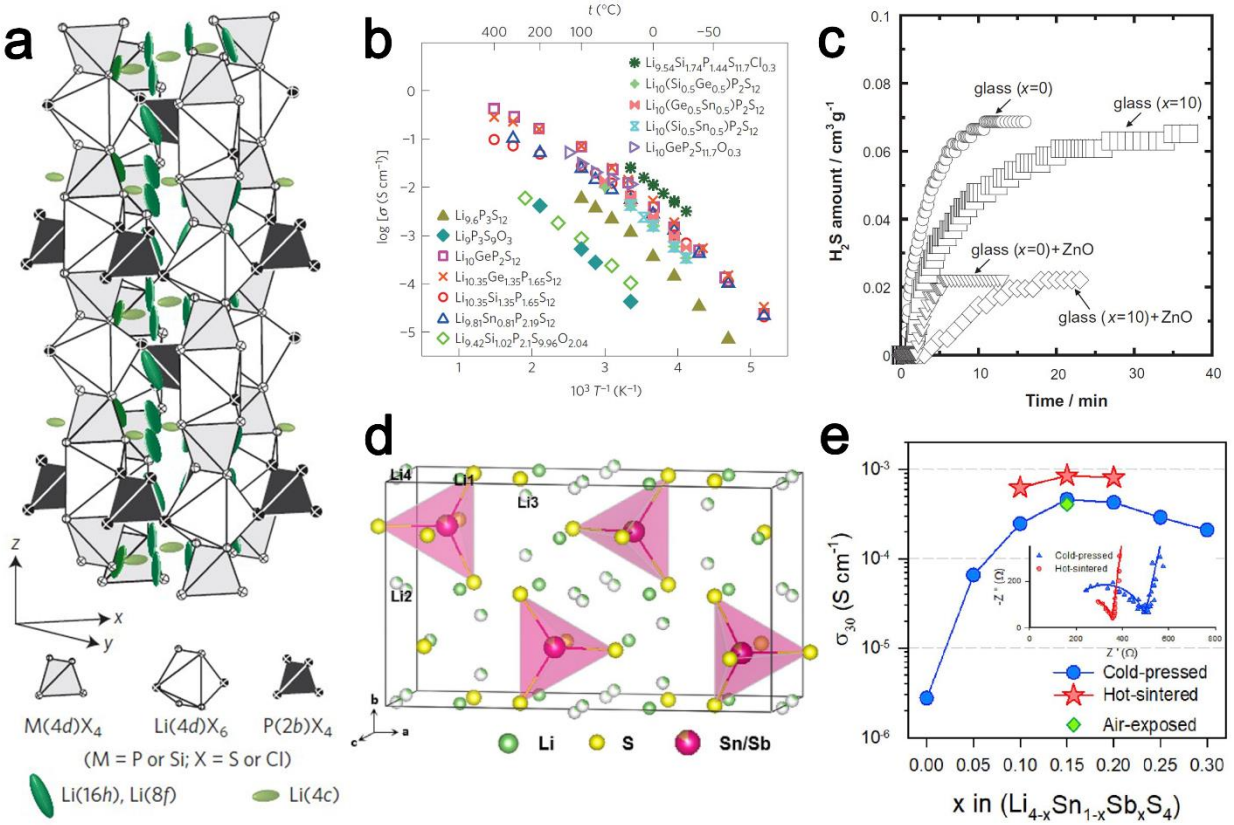

Figure 1.16. a) Crystal structure of $Li_{9.54}Si_{1.74}P_{1.44}S_{11.7}Cl_{0.3}$. The thermal ellipsoids are drawn with a 50% probability. Reprinted with permission from Ref. (Kato et al., 2016). b) Compared Arrhenius conductivity plots for the LGPS family and $Li_{9.54}Si_{1.74}P_{1.44}S_{11.7}Cl_{0.3}$. Reprinted with permission from Ref. (Kato et al., 2016). c) Evolution of H_2S gas generated from a series of Li_2S–P_2S_5–P_2O_5 glass composites (x = P_2O_5 ratio) after exposure to air. Reprinted with permission from Ref. (Hayashi et al., 2014). d) Crystal structure of Sb-substitutes Li_4SnS_4 with unit cell outlined. Reprinted with permission from Ref. (Kwak et al., 2020). e) Arrhenius plots at 30 °C and Nyquist plots (inset) for $Li_{4-x}Sn_{1-x}Sb_xS_4$. Reprinted with permission from Ref. (Kwak et al., 2020).

Li_6PS_5X Argyrodites

Another large family of sulfide solids is the halogen-substituted Li_6PS_5X (X = Cl, Br, I) lithium argyrodites (R. P. Rao & Adams, 2011) derived by partial replacement of sulfur with halogens in the parent phase Li_7PS_6 (Deiseroth et al., 2008). These materials show an inherently high ion conductivity in the order of $10^{-3}/10^{-2}$ S·cm^{-1} and can be synthesized via solid-state synthesis, with a relatively easy process. The crystal structure of argyrodites comprises PS_4^{3-} polyanions surrounded by other sulfur ions and the replacement with halogens involves the latter

ions in the frame (**Figure 1.17a**), originating Li vacancies which affects the local diffusion of Li throughout the ion channels (Kraft et al., 2017; Z. Zhang, Shao, et al., 2018) and overall influences the final conductivity. More specifically, the room temperature conductivities for crystalline Li_6PS_5Cl, Li_6PS_5Br, and Li_6PS_5I samples have exhibit ionic conductivity 1.9×10^{-3}, 6.8×10^{-3} and 4.6×10^{-7} $S \cdot cm^{-1}$, respectively (R. P. Rao & Adams, 2011). The discrepancy in values is due to the nature of the halogen atoms: Cl^- and Br^- have similar dimensions to S^{2-}, leading to partial ion interchange and a higher internal disorder, whereas the larger size of I^- hampered the interchange and resulted in a more ordered structure (Pecher et al., 2010). The ionic conductivity of Li_6PS_5I can possibly be enhanced via doping. An example was reported by Kraft et al. (Kraft et al., 2018) with the introduction of Ge ions in the system $Li_{6+x}P_{1-x}Ge_xS_5I$ as increasing Ge content produces local anion disorder, sharply decreasing the activation energy for ionic motion. The sample with x = 0.6 exhibited a very high ionic conductivity of 5.4×10^{-3} $S \cdot cm^{-1}$, which is furtherly increased by sintering to 1.8×10^{-2} $S \cdot cm^{-1}$. Isoelectronic substitution of S with Se in $Li_6PS_{5-x}Se_xI$ has been shown to modify the local polarizability of the lattice and expand the diffusion pathways for ion transport, contributing to the decrement of the activation barriers (Schlem et al., 2020). This allowed to increase the conductivity to 2.8×10^{-4} $S \cdot cm^{-1}$, two orders of magnitude higher than pristine Li_6PS_5I. Ohno et al. (Ohno et al., 2019) studied the substitution of P^{5+} ions with aliovalent cations Si^{4+} and Sn^{4+}, and a visible diminution in the activation energy for $Li_{6+x}P_{1-x}Si_xS_5I$ was detected, pointing out a more general mechanism for the amelioration of ionic conduction. The elemental substitution enhanced the room temperature conductivity to 2×10^{-3} $S \cdot cm^{-1}$ for Si and 1×10^{-4} $S \cdot cm^{-1}$ for Sn (**Figure 1.17b**).

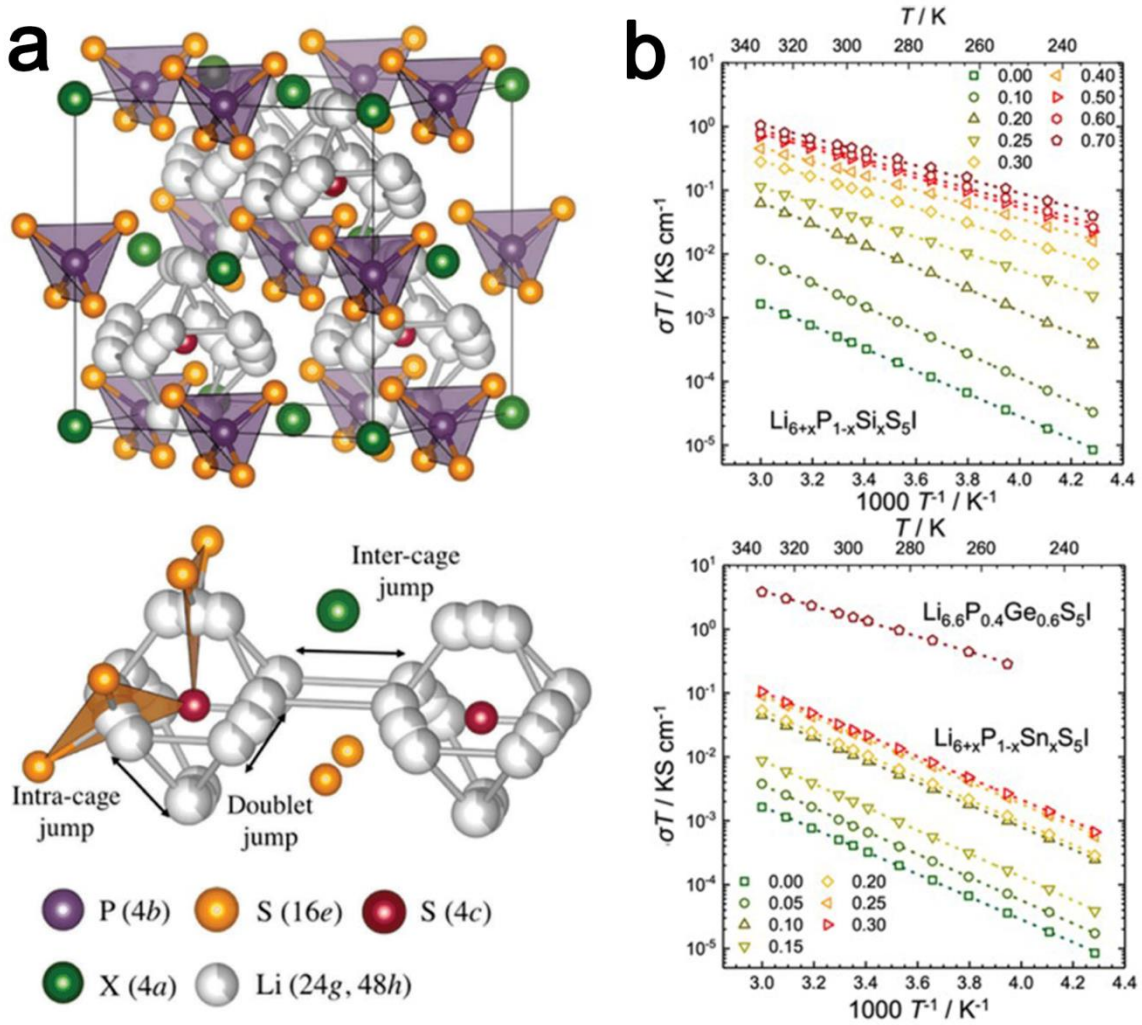

Figure 1.17. a) Crystal structures of Li_6PS_5X with X = Cl, Br, I. X^- anions form a cubic close-packed lattice with PS_4^{3-}tetrahedra in the octahedral sites and the free S^{2-} in half of the tetrahedral holes. The free S^{2-} anions and the corner of the PS_4^{3-} tetrahedra form Frank–Kasper polyhedra, which enclose two different Li positions. The Li positions form localized cages in which multiple jump processes are possible. Reprinted with permission from Ref. (Kraft et al., 2017). b) Arrhenius plots of the conductivity values for substituted $Li_{6+x}P_{1-x}M_xS_5I$ (M = Si, Sn, Ge) with different composition. Reprinted with permission from Ref. (Ohno et al., 2019).

The creation of halogen-rich phases with replacement of S with halides is a viable method to enhance the electrochemical performance of the materials. Adeli et al. (Adeli et al., 2019) showed a Cl-rich $Li_{5.5}PS_{4.5}Cl_{1.5}$ argyrodite with improved vacancy content caused by anion substitution. The material revealed a lower activation energy and an increased Cl^-/S^{2-} disorder, bringing to a boosted conductivity of 9.4×10^{-3} S·cm^{-1}. A modified $Li_{5.5}PS_{4.5}Br_{1.5}$ structure with substitution of S with Br has been presented by Yu et al. (C. Yu, Li, et al., 2020). The optimized

composition revealed a conductivity of 4.35×10^{-3} S·cm^{-1} (**Figure 1.18a**) and an increased compatibility with a lithium anode, with a stable cycling behavior over 2500 h and a limited variation in overpotential. Solvent-synthesized argyrodites presented comparable values of conductivity to the materials prepared by direct solid-state synthesis, due to a reduced presence of impurities and a limited amorphous character (L. Zhou et al., 2019). Mixed-anion compounds $Li_6PS_5Cl_xBr_{1-x}$ exhibited conductivities in the order of 3.5×10^{-3} S·cm^{-1}. Yubuchi et al. (Yubuchi et al., 2018) described the synthesis of Li_6PS_5X argyrodites following a liquid-phase path in an alcohol environment. Optimization of the process implied the use of ethanol, a short dissolution time and a high drying temperature; Li_6PS_5Br prepared via liquid-phase method reported a conductivity of 1.9×10^{-4} S·cm^{-1} at room temperature, lower than the typical value for Li_6PS_5Br prepared with a solid-state process, but this method enabled a more homogeneous solid-solid interface between the electrolyte and $LiCoO_2$ cathode. Performances in cell displayed a specific capacity of 70 mAh g^{-1}, much higher than the cell using the particles prepared via solid-state. Engineering of an interlayer between the electrode and the electrolyte can help protect and stabilize the material against decomposition. A polymeric composite of Li_6PS_5Cl and PEO_{10}:LiTFSI was investigated by Simon et al. (Simon et al., 2019) and the determination of the conductive properties permitted to observe values of conductivity of 1.01×10^{-3} S·cm^{-1} for PEO_{10}:LiTFSI and 1.57×10^{-2} S·cm^{-1} for Li_6PS_5Cl. In depth observations showed the formation of an interlayer at the solid-polymer separation surface due to degradation reactions at elevated temperatures This solid-polymer interface mainly consists of lithium fluoride and dissolved polysulfides (**Figure 1.18b**). These compounds diffuse to the lithium electrode and react with lithium, resulting in the formation of a modified interphase at the lithium/electrolyte interface and an increased conductivity.

Argyrodite structures can be modified to achieve a phosphorus-free composition, in order to increase the stability towards water and remove the hinderances related to the P_2S_5 species. Huang et al. (W. Huang et al., 2019) presented a novel superionic conductor obtained by mixed aliovalent substitution of P^{5+} with Si^{4+} and Al^{3+} with nominal composition $Li_{4+x}Al_xSi_{1-x}S_4$. The use of Al_2S_3 and SiS_2 precursors is preferred to the volatile P_2S_5 because of their lower cost and abundance and their higher malleability in practical applications. The material was prepared by melt-quenching synthesis and presented a typical argyrodite phase with a cubic *F-43m* structure comprised of $M(S/O)_4$ tetrahedra (**Figure 1.18c**). The ionic conductivity of the material was 2.54×10^{-4} S cm^{-1} at 28 °C, like other argyrodite electrolytes, possibly as a consequence of the local

distorted arrangement of lithium ions in the tetrahedral sites and the electrochemical stability vs. an In-Li anode in a cell was found in the 1.9-3.6 V range. Limited doping of the material with oxygen was subsequently attempted to prepare a $Li_{6.15}Al_{0.15}Si_{1.35}S_{6-x}O_x$ conductor (W. Huang et al., 2020), and anion substitution of S^{2-} with O^{2-} allowed to heighten the ionic conductivity of about five times reaching a value of 1.23×10^{-3} S·cm^{-1} for $x = 0.6$ (**Figure 1.18d**). Furthermore, the elemental modification extended the electrochemical stability window up to 5 V with the absence of relevant side reactions.

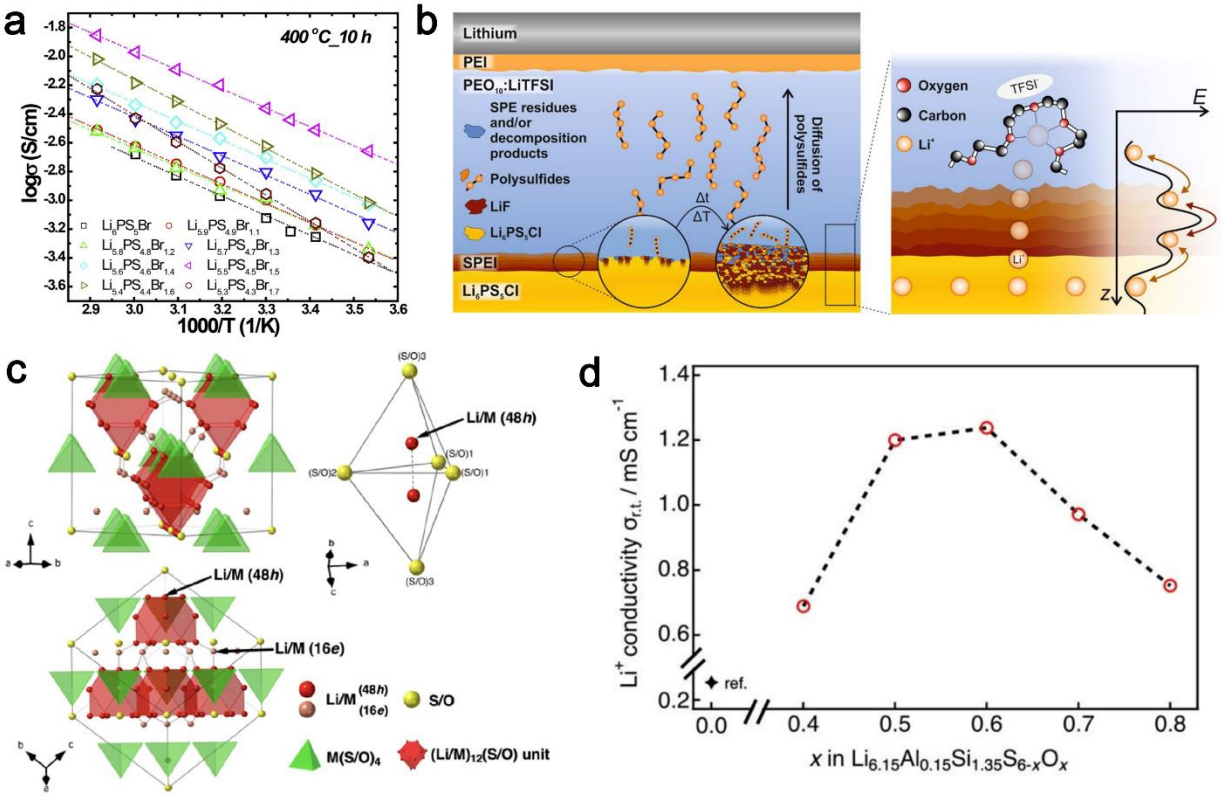

Figure 1.18. a) Arrhenius plots of $Li_{7-x}PS_{6-x}Br_x$ with different Br molar concentrations. Reprinted with permission from Ref. (C. Yu, Li, et al., 2020). b) Schematic of the interphase formation at the electrode/polymer interfaces. The close-ups show the onset of the interphase growth sample without heat treatment (left) and with temperature (right). On the right, the interfacial Li^+ transfer is visualized schematically. The energy diagram depicts the energy barriers for the lithium ion transfer. Reprinted with permission from Ref. (Simon et al., 2019). c) Crystal structure and local ion environment of the synthesized $Li_{4+x}Al_xSi_{1-x}S_4$. Reprinted with permission from Ref. (W. Huang et al., 2019). d) Lithium ion conductivity at 25 °C of $Li_{6.15}Al_{0.15}Si_{1.35}S_{6-x}O_x$ as a function of oxygen ratio. Reprinted with permission from Ref. (W. Huang et al., 2020).

1.4.2.2. Oxides and phosphates

LLTO and lithium perovskites

Among oxide-based compounds Li-rich perovskites have been deeply explored as possible solid electrolytes. Perovskite type materials display the crystal structure of $CaTiO_3$ and their features are correlated to the peculiar mechanical character of the ABO_3 frame, where the A-sites are partially occupied by Li or La atoms (Yashima et al., 2005a). The distribution of the cations typically follows an alternate stacking of La-rich and La-deficient layers along the *c* axis (**Figure 1.19a**) (Inaguma et al., 2002). The atomic arrangement allows the structure to sustain local distortion under variations of pressure and temperature, as well as ionic replacement, and enables a disorder of the frame which promotes charge transport (Catti et al., 2007; Sebastian & Gopalakrishnan, 2003). The archetypical lithium conductive perovskite is $Li_{3x}La_{2/3-x}TiO_3$ (LLTO), which exhibits a high bulk conductivity (up to 10^{-3} $S \cdot cm^{-1}$) and extremely low electronic conductivity (Inaguma et al., 1993). Variation in the stoichiometry and composition of LLTO has been shown to reflect on the structure of the material (Z. Zhang, Shao, et al., 2018). Li-poor compositions ($0.03 \leq x < 0.1$) reported an orthorhombic symmetry (space group *Cmmm*), showing an array of tilted of TiO_6 octahedra along the *b* axis (**Figure 1.19b**) (Abe & Uchino, 1974; Inaguma et al., 2002). The La atoms are alternatively arranged along the *c* axis, with high occupancy in the La-rich layers, and Li atoms are found in off-centered positions of the A site. In this configuration, the high La occupancy (~ 0.95) and poor vacancy concentration (~ 0.05) in the La-rich layers forms a barrier to Li^+ diffusion in the [001] direction (Yashima et al., 2005b). Li^+ ion diffusion at room temperature can be defined as a 2D model percolation, following *2c-4f-2c* or *2c-2d-2c* lines across the La-poor layer. On the other hand, the compositions with a higher ratio of Li ($0.1 \leq x < 0.167$) present a tetragonal structure (space group *P4/mmm*) with a decreasing ordering of La atoms for increasing values of Li content (Fourquet et al., 1996; Kawai & Kuwano, 1994). This structure manifests a lower La occupation (0.65), with a relatively higher concentration of Li vacancies in the La-rich layer (Inaguma et al., 2006). Such a display enables Li migration between alternating La1 and La2 layers, resulting in localized 3D conduction.

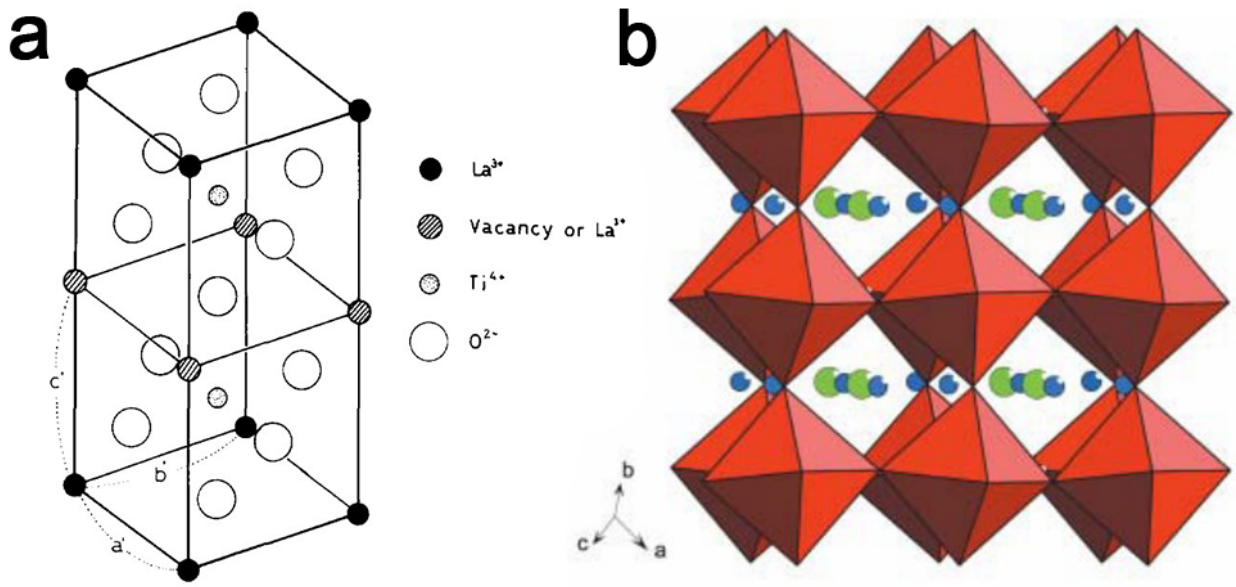

Figure 1.19. a) Proposed model for the unit cell of $La_{2/3}TiO_3$. Reprinted with permission from Ref. (Abe & Uchino, 1974). b) Structures of perovskite lithium ion conductor (Li,La)TiO_3. The green and blue circles denote La and Li, respectively. Reprinted with permission from Ref. (Sebastian & Gopalakrishnan, 2003).

A major restraint of this material lies in its low lithium intercalation potential (< 1.8 V vs Li/Li^+), which makes it not suitable for practical use in cells employing metallic lithium or lithiated carbon anodes (C. H. Chen & Amine, 2001). Furthermore, Ti^{4+} is easily reduced to Ti^{3+}, with the effect of increasing electronic conductivity, and the high mechanical stiffness of oxide particle brings to insufficient density and impedes the transport of Li^+ ions at the boundaries. Grain diffusion dominates the global conductivity, and the values are found in the range of 10^{-5} S cm^{-1}, about two orders of magnitude lower than the bulk. Investigations on the atomic scale reported an extensive structural anomaly at the boundaries, with a thickness of about 2 to 3 unit cells (C. Ma et al., 2014). In that location, the structure deviated from the ABO_3 framework and presented a Ti–O binary compound, associated with a partial reduction of Ti^{4+}, disruption of the Ti–O polyhedra, decrement in La content, and almost total depletion of Li carriers. Use of an amorphous phase may obviate the compatibility issues of LLTO. Zheng et al. (Z. Zheng et al., 2015) described the higher affinity of amorphous LLTO prepared by sol-gel method against metallic lithium, and the modified material featured a higher Li insertion potential compared with the crystalline form. Moreover, the amorphous phase displayed no relevant changes in conductivity when put in contact with Li metal, revealing a vast potential stability up to 12 V (**Figure 1.20a**). The major electrochemical features

of amorphous LLTO, further confirmed by the preparation of thin electrolyte films under different annealing conditions (Y. Zhang et al., 2019). An increase in conductivity of about two orders of magnitude, from 4×10^{-8} to 9×10^{-6} S cm^{-1} was found after solvent evaporation, but for longer annealing times the conductivity dropped sharply because of LLTO crystallization.

Several approaches have been attempted to ameliorate the conductive features of LLTO, the most common of which involve elemental doping. A complete substitution of La atoms with smaller lanthanide ions (Pr, Nd and Sr) leads to a decrement in conductivity (Inaguma et al., 1997), possibly because of the volume shrinking of A-sites induced by the replacement with smaller ions, reducing the bottleneck for Li^+ ion motion (Inaguma et al., 1994), whereas incorporation of larger ions such as Sr helps improving the conductivity, enlarging the ion channels and favoring ionic transport (**Figure 1.20b**) (G. X. Wang et al., 2000). B-site ion substitution seems to follow an opposite behavior (Chung et al., 1998). A modest increment in conductivity is observed upon insertion of small ions like Mn and Ge in Ti locations, whilst a decrement is caused by larger Sn and Zr ions (Chung et al., 1998). Moreover, hypervalent cations such as Ta and Nb negatively affect the conductivity when replacing Ti atoms, indicating a dominating effect of local lattice distortion on the activation energy of ion transport (Katsumata et al., 1996). $Li_{3x}La_{1/3-x}NbO_3$ was found to show a conductivity of about two orders of magnitude lower than $Li_{3x}La_{2/3-x}TiO_3$ (Katsumata et al., 1998). On the other hand, substitution of Ti with lower-valence atoms resulted in an increase in ion conduction for LLTO. $La_{0.55}Li_{0.361}Ti_{0.995}Al_{0.005}O_3$ was reported with a value of conductivity of 1.1×10^{-3} S cm^{-1}, slightly higher than the undoped perovskite (Thangadurai & Weppner, 2000). Adjustment in the stoichiometry of the doping element can improve the conductivity even further (L. X. He & Yoo, 2003), with a room temperature value of 1.58×10^{-3} S cm^{-1} for the composition $(Li_{0.39}La_{0.54})_{0.99}Al_{0.02}Ti_{0.98}O_3$. Yttrium doping on crystalline LLTO was reported by Lee et al. (S. J. Lee et al., 2019) and their study showed a monotonic accretion of the total conductivities for increased Y content. $Li_{0.33}La_{0.46}Y_{0.1}TiO_3$ revealed a bulk conductivity of 9.51×10^{-4} S cm^{-1}. Double substituted $Li_{0.355}La_{0.35}Sr_{0.3}Ti_{0.995}M_{0.005}O_3$ (M = Al, Co and In) materials disclosed similar conductivities in the order of 10^{-5} S cm^{-1}, with minimal variation depending on the dimension of the dopant which affects the interatomic Ti-O distance and the bond strength (K. Yu et al., 2019).

Despite all the efforts, elemental doping shows a marginal effect on ionic conduction, thus alternative methods have been explored. Creation of hybrid composites with polymers have proven relatively effective as the incorporation of LLTO in a PEO-$LiClO_4$ matrix showed enhanced conduction (Milian Pila et al., 2019), with the highest value of 2.8×10^{-3} S cm^{-1} reported for the composite with 10 % wt. of LLTO. The reason lies in the decrement in the glass transition of the polymer and in the increased amount of free charge carriers upon ceramic insertion in the matrix. Another modification of perovskites concerns the insertion of intergranular phases, in order to increase contact between particles and reduce grain boundary resistance. Addition of limited amounts of inert SiO_2 increases the conductivity to 10^{-4} S cm^{-1}, as shown in **Figure 1.20c** (Mei et al., 2008). In this case, inert silica accumulates at the grain boundaries, avoiding Li volatilization during the sintering and forming an amorphous lithium silicate phase, which benefits Li ion conduction by enlarging the bottleneck between separate grains. A $Li_{0.5}La_{0.5}TiO_3$ composite prepared by solid-state reaction with the addition of SiO_2 presented an improved interphase between grains and a raise in conductivity to 5.02×10^{-3} S cm^{-1} (Y. Deng et al., 2009). Low-temperature calcination with Al_2O_3 filler boosted the grain boundary conductivity of about 2.5 times, leading to a total value of 9.33×10^{-4} S cm^{-1}, with a decrease in activation energy from 0.48 to 0.37 eV for a 10 % wt. Al_2O_3 content (H. Zhang, Liu, et al., 2013). The composite electrolyte showed an improved junction between the LLTO particles and the presence of a lithiated $LiAl_5O_8$ spinel phase dispersed along the boundaries, which enabled interstitial diffusion of lithium ions. The inclusion of a LLZO sol in an LLTO ceramic mold was reported by Chen et al. (K. Chen et al., 2013), and led to a grain boundary conductivity of 1.5×10^{-4} S cm^{-1}, with a slight improvement compared with pristine LLTO. Analysis of elemental distribution, depicted in **Figure 1.20d-e**, displayed a main Zr presence at the boundaries, with no significant presence in the bulk of the material. The modified material, however, did not report a relevant amelioration of the stability towards lithium in a cell.

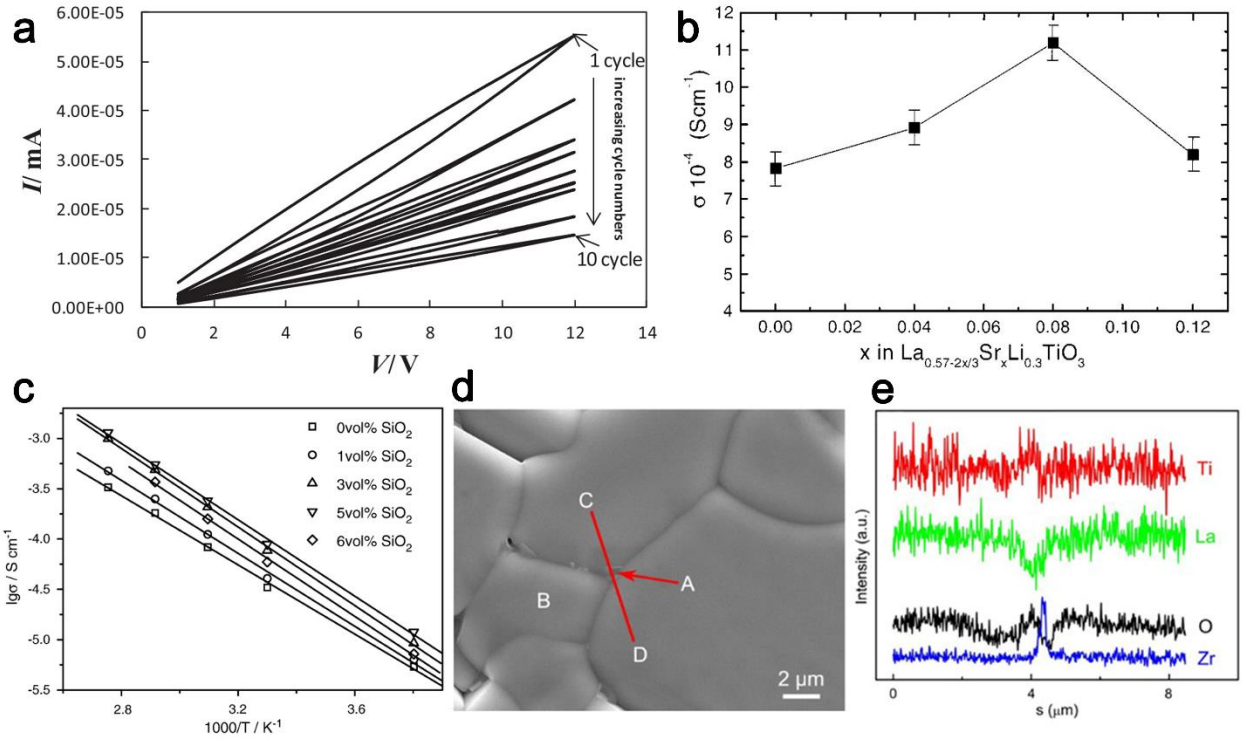

Figure 1.20. a) Cyclic voltammogram of amorphous LLTO samples at a scan rate of 1 mV s^{-1}. Reprinted with permission from Ref. (Z. Zheng et al., 2015). b) Lithium ion conductivity of Sr-substituted LLTO at 25 °C. Reprinted with permission from Ref. (G. X. Wang et al., 2000). c) Arrhenius plots for the total conductivity of LLTO/SiO_2 composites. Reprinted with permission from Ref. (Mei et al., 2008). d) SEM image of LLTO-LLZO ceramic and e) elemental distribution along the CD line. Reprinted with permission from Ref. (K. Chen et al., 2013).

Halide Anti-perovskites

A relatively novel group of solid conductors is the lithium-rich anti-perovskite (LiRAP) family with formula $A^{-}B^{2-}X_3^{+}$ (Y. Zhao & Daemen, 2012), inspired by highly conductive perovskites like $Na_{1-x}K_xMgF_3$ and $KZnF_3$ (Yoshiasa et al., 2005). These materials have a similar structure to conventional $A^{+}B^{2+}X_3^{-}$ perovskites (space group $Pm\bar{3}m$), reported in **Figure 1.21a**, but they show a reversed disposition of anion and cation sublattices and replacement of the electronegative element X^{-} with Li^{+}, hence the name of anti-perovskites. In the typical cubic pattern of Li_3OX anti-perovskites, X^{-} ions are located at the corners of the cubic cell, O^{2-} ions occupy the body-centered site, and Li^{+} ions are disposed in an octahedral coordination around O^{2-} (M. H. Braga et al., 2014). Ion disposition in a bcc arrangement has been proven optimal for fast ionic conduction (Y. Wang et al., 2015), due to the direct hopping of Li atoms between adjacent

tetrahedral sites, and composition such as Li_3OCl and Li_3OBr reported values of room temperature ionic conductivity around 10^{-3} S cm^{-1} at room temperature, reaching 8.5×10^{-4} S cm^{-1} for pure Li_3OCl and 1.94×10^{-3} S cm^{-1} for a mixed-halogen phase $Li_3OCl_{0.5}Br_{0.5}$ after a thermal treatment at 250 °C **(Figure 1.21b**) (Y. Zhao & Daemen, 2012). Thermal activation may prove necessary to achieve high ionic conduction (**Figure 1.21c**), since in the pre-treated material the Li^+ cations are strictly bound in their octahedral sites and directly coordinated with two oxygen anions, restricting ion jumps and resulting in low conductivity. Lack of vacancies may also be responsible for the stagnant ion transfer, limiting the movements to neighboring Schottky defects in the lattice. The increased structural disarray is coupled with higher thermal vibration, most intensely at the lithium sites. The different halide anions affect the intrinsic conduction as well. Small Cl^- ions in Li_3OCl allow larger spaces for the movement of Li^+ ions, but their tinier radius induces a collapse of the perovskite framework by octahedral tilting, decreasing the space for ionic transport. On the other hand, larger Br^- anions in Li_3OBr partially clog Li^+ ions channels, reducing their diffusion. A concurrent presence of both Cl^- and Br^- ions expands the volume of the unit cell and reduces the octahedral tilting at the same time, producing a more uniform framework. In this setting, larger polyhedra allow a wider space for the Li^+ cations to shift through via a Frenkel mechanism. The primary influence on Li^+ transport lies in the structural disorder and the presence of Li vacancies which decrease the energy barrier across the migration pathways, while halogen vacancies provided irrelevant advantages to ion conduction (Y. Zhang et al., 2013). Pristine Li_3OCl crystals inquired via atomistic calculations displayed a significant discrepancy between the concentration of LiCl Schottky defects and Frenkel interstitials of about 6 orders of magnitude lower for the latter, due to the much higher formation energy of interstitials. However, samples originated by LiCl deficiency exhibited a comparable concentration of both crystal defects, with increased presence of interstitial due to charge compensating mechanisms, pointing out a possible reversed transport process for the material (**Figure 1.21d**) (Mouta et al., 2014). Li_3OCl and Li_3OBr presented a thermodynamically metastable behavior towards decomposition into Li_2O and LiCl/LiBr, showing nonetheless an increased susceptibility to decomposition for applied voltage higher than 2.5 V (Emly et al., 2013). First-principle calculations were undertaken to define a model for optimizing the performance of the materials and the results pointed out a significant role of the halide ions on the energy barrier of the diffusion path. Practical applications estimated the relative concentration of halide species to allow the highest conductivities in the $Li_3OCl_{1-x}Br_x$

system for $0.235 \leq x \leq 0.395$ (Z. Deng et al., 2015a). A study by Dondelinger et al. (Dondelinger et al., 2019) highlighted a linear Arrhenius trend for Li_3OCl in the temperature range from 20 to 100 °C, with no significant phase transformations. The material was tested in cells with C/Cu electrode observing a decreased activation energy of the lithium intercalation in the graphite scaffold associated with increased operating temperature, along with a stabilized cyclic voltammetry cyclability at higher temperature. Half cells expressed a strong capacity retention over long-term cycling with improved capacity retention around 80 % after 7 months.

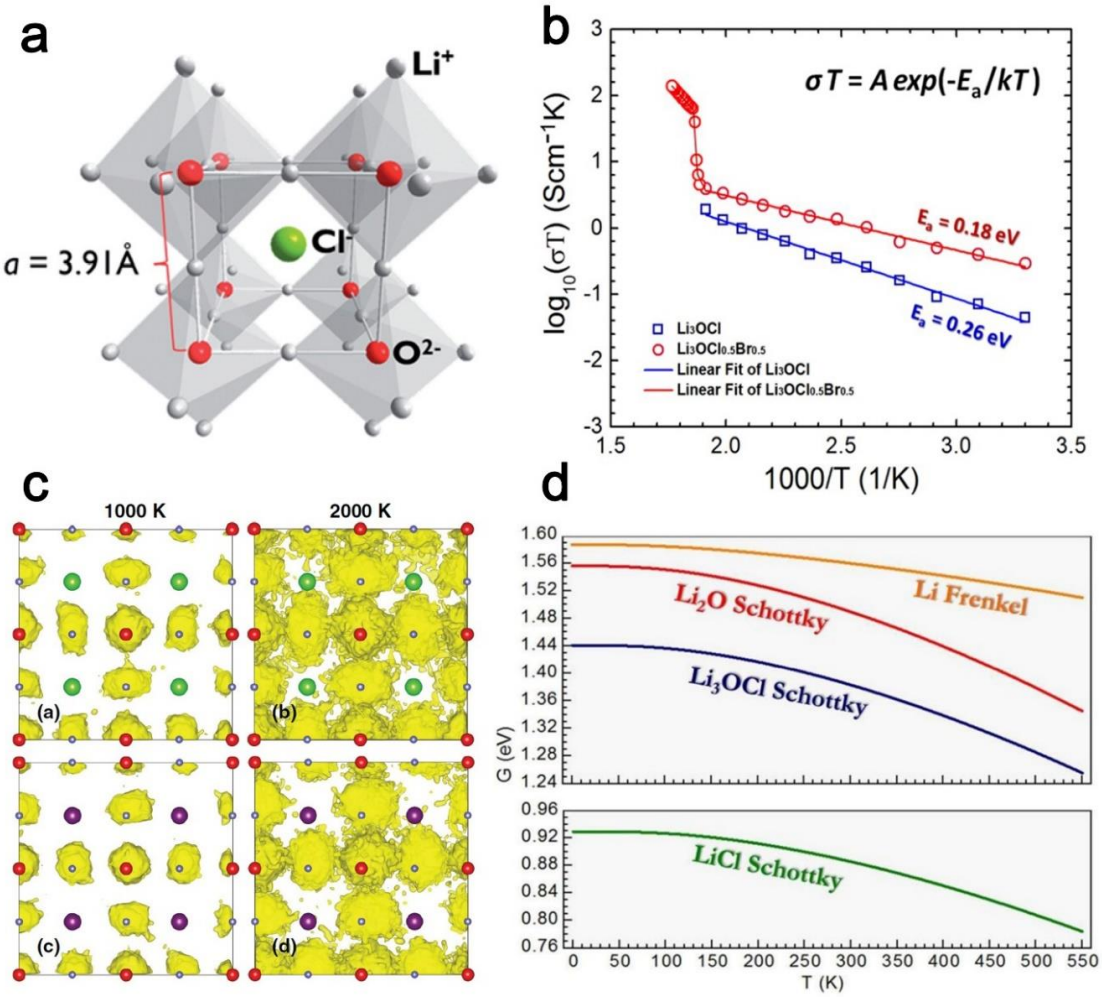

Figure 1.21. a) The crystal structure of a Li_3ClO cubic $Pm\bar{3}m$ antiperovskite. Reprinted with permission from Ref. (M. H. Braga et al., 2014). b) Arrhenius plots for Li_3OCl and $Li_3OCl_{0.5}Br_{0.5}$. Reprinted with permission from Ref. (Y. Zhao & Daemen, 2012). c) Projection (yellow) of Li trajectories in a supercell at 1000 and 2000 K for Li_3OCl (top) and Li_3OBr (bottom). O: red, Cl: green, Br: purple, Li: blue. Reprinted with permission from Ref. (Y. Zhang et al., 2013). d) Temperature behavior of Gibbs energy (per point defect) of the basic lithium-containing neutral defects. Reprinted with permission from Ref. (Mouta et al., 2014).

Low-dimensional network LiRAPs are a modified concept of this class of conductors, with a decreased dimensionality of the octahedral structural units (Z. Lu et al., 2020). In this configuration BX_6 units are connected along (001) planes and form a 2D network within the main lattice, as shown in **Figure 1.22**. A notable example has been reported by Zhu et al. (Zhu et al., 2016) with the engineering of layered $Li_7O_2Br_3$ via solid-state reaction. Structural investigation revealed a tetragonal structure (space group *I4/mmm*) and a metastable character with respect to Li_3OBr, owing to the high stability of LiBr. This reflects on a more challenging synthesis process from a thermodynamic viewpoint, making the achievement of a pure phase more difficult. Mixed $Li_7O_2Br_3$-Li_3OBr compound reported an improved ionic conductivity of 2.4×10^{-5} $S \cdot cm^{-1}$ compared to pure Li_3OBr, possibly because of the arrangement of $Li_7O_2Br_3$ structure. Intrinsic depletion in the layers generates a higher concentration of vacancies and creates new migration channels along the edges of the octahedral units, favoring the movement of Li^+ ions and improving the conductivity. This spots a light on the influence of network dimensionality on ionic circulation (Z. Lu et al., 2020). Li motion pathways in the anti-perovskite structure can be distinguished in two types such as interchain motion along the edges of one single OLi_6 octahedron and intrachain jumping between separate units. Low-DN anti-perovskites generally display lower energy barriers than 3D networks for both types, with interchain transport dominating the process in lower-dimension networks 1DN and 0DN frameworks supposedly manifest values of room temperature conductivity of 5.4×10^{-3} and 2.12×10^{-2} S cm^{-1} respectively, sensibly higher than 3DN-Li_3OCl. DFT computations expressed a thermodynamically metastable character for these materials and low values of decomposition energy.

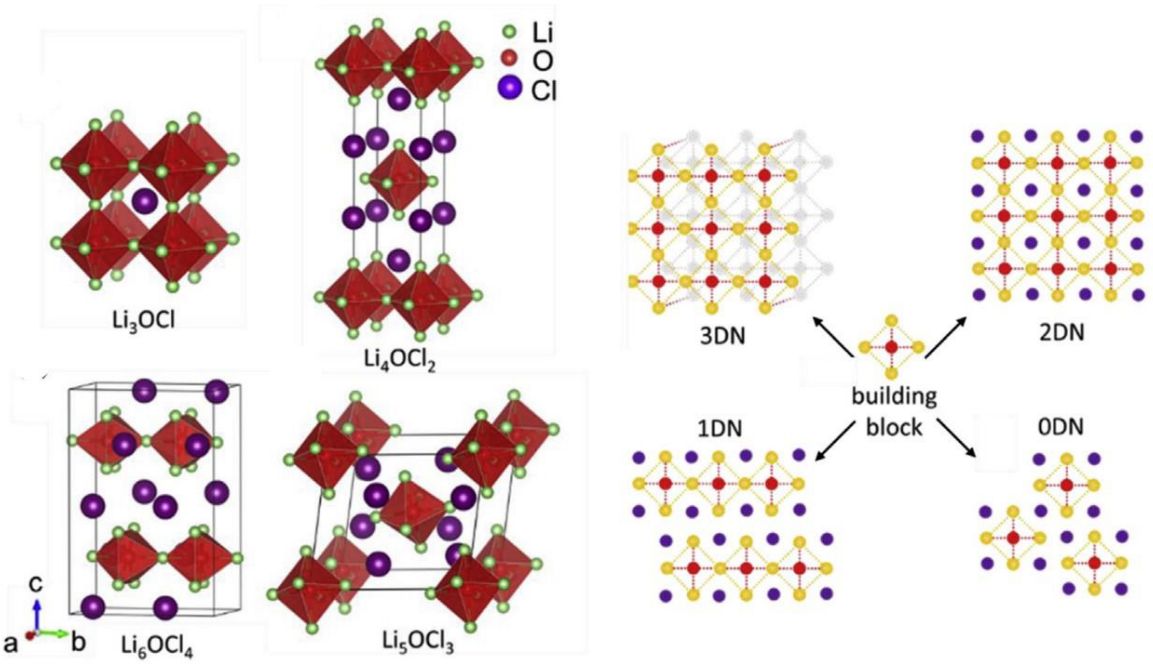

Figure 1.22. Unit cells of 3DN-Li_3OCl, 2DN-Li_4OCl_2, 1DN-Li_6OCl_4, and 0DN-Li_5OCl_3 anti-perovskites and ilustration of the connectivity of low-DN anti-perovskites. A-site ions are signaled in the schematic as purple dots. Reprinted with permission from Ref. (Z. Lu et al., 2020).

Albeit presenting these advantages, their extreme hygroscopicity makes these materials unstable to the puniest traces of materials. A major endeavor is therefore required for their stabilization in ambient atmosphere, which may comprise of a different synthesis approach or the incorporation of stabilizing species. Synthesis via a solid-state route may prove effective in increase the purity of the product, and the incorporation of agents like LiH in the sintering mass reduces the presence of OH traces in the resulting material (S. Li et al., 2016). Modified structures with hypervalent ion doping were described by Braga et al. (M. H. Braga et al., 2014) who reported the vitreous electrolytes with composition $Li_{3-2x}M_xXO$ (M = alkali earth metals Ca^{2+}, Mg^{2+} or Ba^{2+}). The higher-valence cations introduce Li vacancies within the sublattice, lessening the relative activation energy for Li^+ conduction. A liquid-to-solid reversible transition was identified, which notably increased the viscosity of the material with no relevant structural alterations. The effect of the different doping atoms in the glass transition was evaluated via DFT calculations and a decrement in the phase transition temperature coincided with larger radii for the inserted species. $Li_{2.99}Ba_{0.005}ClO$ reported an outstanding room temperature conductivity of 2.5×10^{-2} $S \cdot cm^{-1}$,

further augmented to 2.4×10^{-1} S·cm^{-1} at 100 °C, while the mixed-halide compound $Li_{2.99}Ba_{0.005}Cl_{0.5}I_{0.5}O$ exhibited a value of 1.21×10^{-1} S·cm^{-1} at 50 °C (**Figure 1.23a**), as well as low electronic conductivities in the order of $10^{-9} – 10^{-7}$ S·cm^{-1}. The modified electrolytes revealed an improved affinity towards metallic lithium, with a potential stability window extending up to 8 V, and long-term cycling displayed a limited increase in interfacial resistance after 460 h (M. H. Braga et al., 2014). A glass-amorphous conductor was derived from water solvation of an A_3OCl (A = Li, Na) anti-perovskite parent material, via hydro-thermal reaction with a small inclusion of hydroxide agents, such as $Ba(OH)_2$ or $Ca(OH)_2$, to reduce the glass transition temperature. The Li-based compound revealed a very low activation energy of about 0.06 eV and room temperature conductivity higher than 10^{-2} S·cm^{-1}, and chronopotentiometry tests reported a stable impedance against Li metal over 19 days of cycling. Application of the glass electrolyte in a solid state cell is characterized by a reversible Li and Na plating/stripping, and a tailored cathode was engineered by blending the electrolyte, carbon, and MnO_2 as a redox agent (M. H. H. Braga et al., 2017). The electrode yielded a working voltage of 3 V with no significant reduction of the cell capacity. In this cell arrangement the electrolyte has higher wettability towards the metal anode and no reduction is observed, with no visible evolution of lithium dendrites and a solid interphase.

A study by Li et al. (Y. Li et al., 2016) on the structure of anti-perovskites indicated for Li_3OX materials a more plausible composition of Li_2OHX, implying a non negligible presence of hydroxide in the composite (**Figure 1.23b**). A direct preparation of Li_2OHBr by melting of LiOH and LiBr precursors was not achieved, and the removal of H atoms was found difficult due to the relative strength of O–H bonds in the hydroxide. Addition of water (< 10% wt.) in the starting mixture led to the formation of a mixed product with cubic Li_2OHBr and layered $Li_7O_2Br_3$. Substitution of OH^- with F^- converts the crystal structure from an orthorhombic phase Li_2OHCl to a cubic phase with composition $Li_2(OH)_{0.9}F_{0.1}Cl$, with a wide electrochemical stability window up to 9 V and a room temperature conductivity of 3.5×10^{-5} S·cm^{-1} in accordance with molecular dynamics predictions (Z. Deng et al., 2015b). Synthesis of H-free Li_3OCl was attempted by Hanghofer et al. (Hanghofer et al., 2018) through a number of methods such as hydrothermal and solid-state, but a proper discrimination of Li_2OHCl and H-free Li_3OCl polymorphs could not be achieved by X-ray diffraction and neutron powder diffraction. The utmost reactivity of LiRAPs with moisture makes them unstable even under inert Ar atmosphere and causes decomposition after brief exposure to air (**Figure 1.23c**), casting a shadow on the actual existence of ultra-high

conductive LiRAPs. Decomposition products included hydrated LiCl, whose presence can justify the high conductivity of glassy anti-perovskites. The superior hygroscopicity of Li_3OCl is explained by the relevant exothermic hydration enthalpy of the species, pointed out by molecular calculations (Dawson, Attari, et al., 2018) and long-distance Li transport is strictly correlated with the spatial disposition of OH groups.

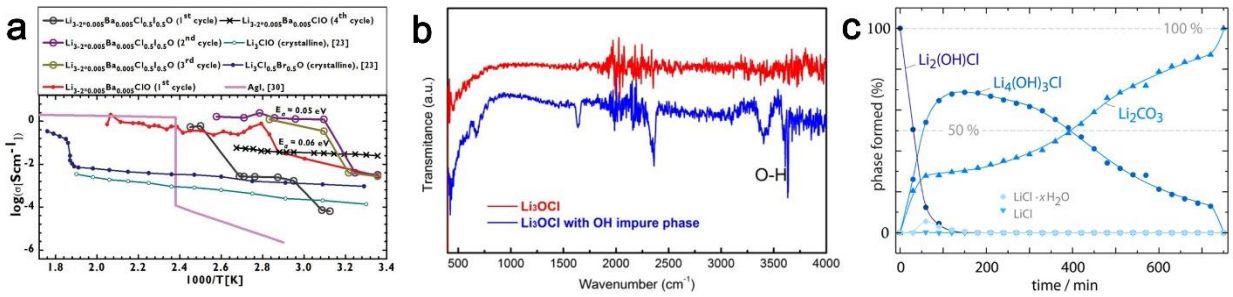

Figure 1.23. a) Ionic conductivities of Li_3ClO and Ba-doped derivates, including $Li_{2.99}Ba_{0.005}ClO$ and $Li_{2.99}Ba_{0.005}Cl_{0.5}I_{0.5}O$, compared with AgI. Reprinted with permission from Ref. (M. H. Braga et al., 2014). b) IR spectra of Li_3ClO synthesized from Li metal without or with OH phase Reprinted with permission from Ref. (S. Li et al., 2016). c) Phase composition of Li_3ClO antiperovskite upon prolonged exposure to air. Reprinted with permission from Ref. (Hanghofer et al., 2018)

NASICON conductors

Among the solid electrolytes, phosphate NASICON structures exhibit an improved stability to moisture, with reduced formation of Li_2CO_3, a wide potential stability window and lower manufacturing temperatures in both synthesis (700–800 °C) and sintering (< 900 °C) compared with other oxide electrolytes (DeWees & Wang, 2019), allowing a less expensive fabrication. The first NASICON electrolytes with formula $Na_{1+x}Zr_2Si_{2-x}P_xO_{12}$ were reported in the 1970s (Goodenough, Hong, et al., 1976; H. .-P. Hong, 1976) via modification of $NaZr_2(PO_4)_3$ with substitution of P^{5+} with Si^{4+}. The typical NASICON frame consists in a $M_2(PO_4)_3^-$ scaffold of MO_6 octahedra and PO_4 tetrahedra with shared O atoms (Giarola et al., 2017), which presents for the lithiated phase $LiM_2(PO_4)_3$ a rhombohedral symmetry (space group $R\bar{3}c$) for M = Ti and Ge (**Figure 1.24a**) (Alami et al., 1991; París et al., 1996), whereas for larger cations M = Zr, Hf, Sn show a low-symmetry triclinic arrangement (space group $C\bar{1}$) (Losilla et al., 1997). The rhombohedral disposition presents two distinct sites for lithium ions such as octahedral M1 *6b*

locations situated enclosed by six O atoms and transition M2 *18e* locations between the *6b* sites with a 10 oxygen coordination, while the distorted triclinic phase shows a four oxygen coordination for Li sites (Catti, 1999). Out of all $LiM_2(PO_4)_3$ compositions, $LiTi_2(PO_4)_3$ represents the best candidate for Li conduction due to its lattice dimensions, but the conventional pellet preparation via sintering reported excessively high porosity and relatively low density, reflecting on a final conductivity around 10^{-7} $S \cdot cm^{-1}$ at room temperature (Chowdari et al., 1989; Shannon et al., 1977). The structure can be modified with a partial aliovalent substitution of Ti^{4+} with M^{3+} ions like Y, In, Sc, Ga and Al (Ado et al., 1992; Arbi et al., 2004; Best, 2000; Qui et al., 1988), which positively affects ionic conduction. In particular, a Al-doped material with formula $Li_{1.3}Al_{0.3}Ti_{1.7}(PO_4)_3$ (LATP) (Aono et al., 1990) displayed a room temperature conductivity of 7×10^{-4} $S \cdot cm^{-1}$ (**Figure 1.24b**). An analogous behavior was found for trivalent replacement of Ge in the $LiGe_2(PO_4)_3$ system, and Al substitution brought to an improved conductivity of 2.4×10^{-4} $S \cdot cm^{-1}$ for $Li_{1+x}Al_xGe_{2-x}(PO_4)_3$ (LAGP) phase (Aono et al., 1992). The variation in ion conduction enlarges the bottleneck increasing the concentration of charge carriers in the structure, accompanied by a decrease in activation energy for interstitial motion (Lang et al., 2015).

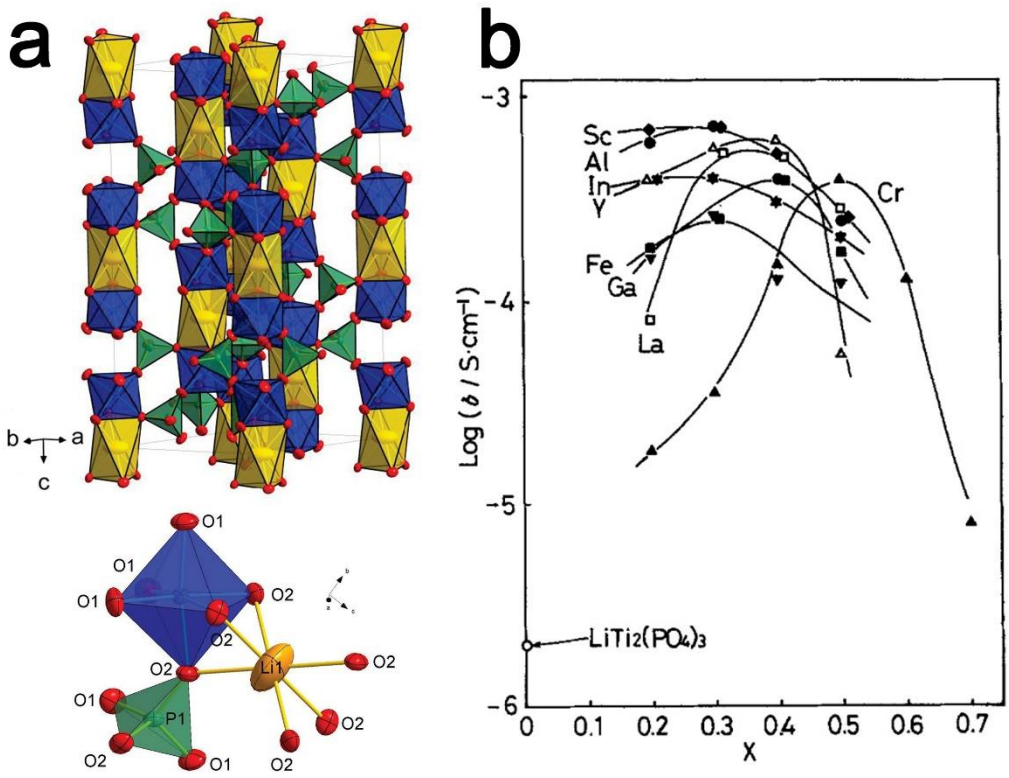

Figure 1.24. a) Unit cell (space group $R\bar{3}c$) and local environment of $LiTi_2(PO_4)_3$. Yellow elongated octahedra are occupied by Li^+, blue octahedra are occupied by Ti^{4+}, green tetrahedra are occupied by P^{5+}. O^{2-} is located at the corners of the polyhedra (small red circles). Adapted with permission from Ref. (Giarola et al., 2017). b) Variation of the conductivity for a series of $Li_{1+x}M_xTi_{2-x}(PO_4)_3$ systems at 298 K, as a function of elemental substitution. Reprinted with permission from Ref. (Aono et al., 1990).

Moreover, elemental substitution helped improving pellet densification and diminished grain boundary resistance, allowing for the increment of this contribution to the total conductivity (Kahlaoui et al., 2017). A boron substituted $Li_{1+x}B_xTi_{2-x}(PO_4)_3$ (x = 0.2) revealed a conductivity of 2×10^{-4} $S \cdot cm^{-1}$ at room temperature, and B_2O_3 precursor acts as a sintering aid for ceramic densification (Peng et al., 2012). Excess of B_2O_3 leads to the formation of a B-rich intergranular phase thwarting Li^+-ion movement between the grains. Silicon-doped LATP synthesized via a solution-method reported an improved conductivity of about 10^{-3} $S \cdot cm^{-1}$ (Zhu et al., 2022). The introduction of silicon has a slightly negative effect on bulk conduction, but silicon can affect the microstructure of the material. Structural analysis revealed a segregation of $LiTiOPO_4$ at the grain boundaries, which can deter the irregular growth of LATP grains and increase grain boundary conduction. Higher amounts of Si promoted an inordinate formation of $LiTiOPO_4$, reducing the

total conductivity, as shown in **Figure 1.25a**. Preparation of LATP via sol-gel method requires a lower calcination temperature (650 °C) to achieve a high-purity product (M. Liu, Li, et al., 2018): Si-doped $Li_{1.7}Al_{0.3}Ti_{1.7}Si_{0.4}P_{2.6}O_{12}$ presented a rhombohedral structure and characterized by a conductivity of 1.3×10^{-3} S·cm^{-1} after sintering at 1000 °C, with a low activation energy of 0.25 eV. Mixed Ti-Ge NASICON compositions were reported in literature with varying values of conductivity ranging from 10^{-4} S·cm^{-1} for $Li_{1.6}Al_{0.6}Ge_{0.8}Ti_{0.6}(PO_4)_3$ (Maldonado-Manso et al., 2003) to 10^{-3} S·cm^{-1} for the Ti-richer $Li_{1.45}Al_{0.45}Ge_{0.2}Ti_{1.35}(PO_4)_3$ (**Figure 1.25b**) (Xuefu et al., 2016). A high-purity LATP synthesized through a molten flux process (Tolganbek et al., 2020) presented an ionic conductivity in the range of 10^{-4} S·cm^{-1}. Production of a pure material can be achieved via a solution method in aqueous environment with H_3PO_4 as phosphorus precursor followed by thermal annealing at 700 °C (F. Ma et al., 2016). This process allows to obtain a product with a conductivity of 1.2×10^{-4} S·cm^{-1}, about 10 times higher than the material employing $NH_4H_2PO_4$ as precursor, and the reason can be found in the evolution of gas during the synthesis process (X. Lu et al., 2020). Hydrothermal reaction using H_3PO_4 was observed at low temperature (180 °C), but the rhombohedral structure was observed only after thermal calcination at 600 °C, along with a high amount (40 % wt.) of $(TiO)_2P_2O_7$ secondary phase. The precursor mixture with $NH_4H_2PO_4$ showed reduced hydrothermal reactivity, but a lower ratio of impurity after calcination, with better crystallization of the rhombohedral phase. The lower conductivity of the latter sample was attributed to the higher porosity and lower relative density after sintering (**Figure 1.25c**), caused by the early crystallization of $LiTi_2(PO_4)_3$. Modification of the synthesis condition can affect the conductive properties of NASICON as shown by a recent study by Paolella et al. (Paolella, Zhu, Bertoni, Perea, et al., 2020b) who evaluated the effect of pressure on the densification of LAGP. It was reported that hot-pressing at 112 MPa for 1h allowed to decrease the sintering temperature of LAGP ceramic pellets to 600-650 °C, a much lower value compared to the ones required for long-term sintering, as observed in **Figure 1.25d**. The sample hot-pressed at 650 °C displayed a conductivity of 3.3×10^{-4} S·cm^{-1} more than twice the value of a pellet prepared with standard sintering at 850 °C. An increase of the hot-pressing temperature to 750 °C produced more brittle pellets which, however, presented higher conductivities of 4.24×10^{-4} S·cm^{-1}. The hot-pressed material unveiled a capacity of 125 mAh g^{-1} with a retention above 90% after 10 cycles at a rate of C/30.

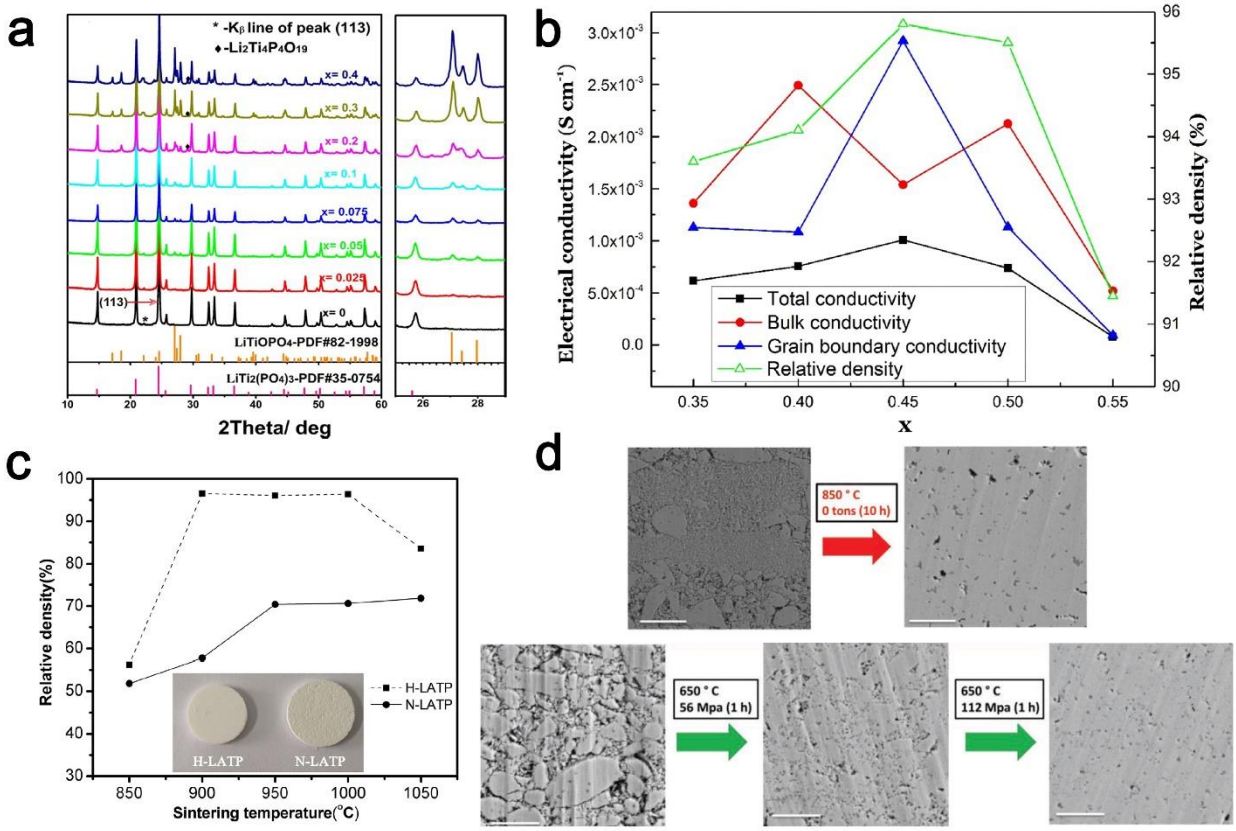

Figure 1.25. a) XRD patterns of Si-doped LATP (x = 0 – 0.4) samples, compared with references. Reprinted with permission from Ref. (Zhu et al., 2022). b) Variation of the conductivities and relative density for $Li_{1+x}Al_xGe_{0.2}Ti_{1.8-x}(PO_4)_3$ as a function of x. Reprinted with permission from Ref. (Xuefu et al., 2016). c) Relative densities of LATP pellets prepared using H_3PO_4 (H-LATP) and $NH_4H_2PO_4$ (N-LATP), as a function of the sintering temperature. Inset: photos of H-LATP and N-LATP sintered pellets. Reprinted with permission from Ref. (X. Lu et al., 2020). d) SEM images of LAGP pelelts after conventional cold-pressing (top) and hot-pressing at 650 °C in Ar (bottom). Scale bar = 10 µm. Adapted with permission from Ref. (Paolella, Zhu, Bertoni, Perea, et al., 2020b).

Despite their good performance, however, NASICON materials suffer from instability towards Li metal, causing the reduction of Ti^{4+} and Ge^{4+} ions and increasing interface resistance (Hartmann et al., 2013; C. Yang et al., 2017). Lithium intercalation in LATP is accompanied by a phase transition which generates a Li-rich interphase at the electrode surface (**Figure 1.26a**) (Zhu et al., 2020), thus increasing the electronic conductivity of about three orders of magnitude from 3×10^{-9} to 2.9×10^{-6} S·cm^{-1}. Electrochemical reduction of Ti^{4+} to Ti^{3+} restricts the band gap and enhances electronic conduction at the interface. A potential gradient favors a lithium deposition

on a local scale, with possible evolution of lithium dendrites and conductive secondary phases, resulting in performance degradation. This issue can be partially mitigated by introducing a separating layer between the electrolyte and metallic lithium. An attempt with a Li_3PO_4 interlayer revealed an incremented stability towards Li reactivity, with a higher capacity retention beyond 95 % upon repeated cycling with respect to cells without the protective layer (J. Liu et al., 2017). The main drawback lied in the inert nature of the phosphate filler, which significantly raised the impedance at the electrode interface, reducing Li conduction. Hybrid systems incorporating lithium electrolyte around the solid particles could obviate the problem. Indeed, it was shown that even very small amounts of liquid phase (2 µL) can ameliorate ion transport at the interface and produce a high specific capacity (C. Wang et al., 2018), while preventing reduction of Ti by Li metal. Ceramic interlayers may also prove a feasible alternative for improving electrochemical performance. A LiRAP coating between LATP and a LCO cathode, described by Feng et al. (W. Feng et al., 2022), allowed to sensibly decrease the sintering temperature of the battery to 290 °C, thanks to the low melting point of the LiRAP phase. *In situ* lacquering was conducted via dissolution of the precursors in deionized water, and the basic character of the solution suppressed Li^+/H^+ exchange and limited the formation of additional phases. The good conductivity of LiRAP decreased the interface resistance from 15288 to 817 Ω cm^{-2}, as shown in **Figure 1.26b**, and the high deformability permitted to obtain a ductile interphase more resilient to strain deformation, improving cycling stability. Liu et al. (C. Liu et al., 2022) detailed the insertion of a secondary borosilicate glass phase during the sintering of LATP. The high-temperature stability of borosilicate reduces the reactivity with the ceramic and allows inter-grain diffusion and uniform coalescence to form a solid mixture with reduced presence of pores and grain boundaries. The solid blend exhibited a fracture strength of about 74 MPa, almost 2.5 times larger than pure LATP, and a relative density higher than 97 % for a 6 % filler content, while a surplus of boron glass (10%) resulted in bulky grains with poorer contact and decreased density. Li plating/stripping showed a stable behavior for more than 200 h and a high capacity of 154.5 $mAh \cdot g^{-1}$.

A study by Chen et al. (R. Chen et al., 2021b) investigated the thermal stability of LATP pellets against metallic lithium. Despite their smaller contact area with the electrode, ceramic pellets showed a poorer thermal stability compared with the powders, leading to the formation of lithium structures within the pellets through the structure defects. The reactive lithium triggered interfacial reactions which eventually lead to thermal runaway of the battery. Lithium penetration

is further enhanced by higher current densities (Kazyak et al., 2020) and increment in stack pressure (Doux et al., 2020). A modified electrolyte using $LiPO_2F_2$ as a sintering aid reported a higher thermal stability compared with pristine LATP (**Figure 1.26c**) (R. Chen et al., 2021a). Use of Al_2O_3 as coating agent can protect the electrode interface and increase the stability towards lithium. An ultra-thin (15 nm) Al_2O_3 interlayer introduced by atomic layer deposition on LATP electrolyte developed a stable interface with a cycle life of 600 h and a low overpotential of 0.9 V after 300 cycles (Y. Liu, Sun, et al., 2018). The modified electrolyte displayed a conductivity of about 1.5×10^{-4} S·cm^{-1} at room temperature, and the Al_2O_3 limited Li penetration and Ti reduction at the interface, as well as decreasing resistance upon the formation a Li–Al–O conductive layer. Metallic protection layers can shield NASICON electrolytes from Li-driven reactions. An amorphous Ge coating on LAGP electrolyte upgraded the contact between Li metal and the ceramic and inhibited the reduction of Ge^{4+} in contact with lithium (Y. Liu, Li, et al., 2018). The performance of the modified electrolyte in a symmetric cell unveiled a superior stability compared with the untreated material, with an interfacial resistance of 1150 **Ω** after 300 cycles and a low polarization around 0.1 V after 200 h at 0.1 mA cm^{-2}. On the other hand, pristine LAGP showed a huge resistance over 10^5 **Ω** after only 30 cycles and an unstable plating/stripping performance, with increased polarization above 1.5 V after 60 h. Application in a Li-air battery confirmed the stability of Ge-LAGP producing a stable capacity after 30 cycles. Cortes et al. (Cortes et al., 2020) presented a Cr thin interlayer (30 nm) produced by metal sputtering which extended the lifecycle of LAGP against Li to more than 1000 h. Cr deposition promoted a regular interphase growth and a reversible LAGP conversion rather than Li plating at the surface, allowing the transit of Li^+ ions. An Al modified layer has been shown to prevent Li deposition and mutual reactivity at the interphase (Zhong et al., 2018) allowing a full-solid cell with a $LiMn_{0.8}Fe_{0.2}PO_4$ cathode to deliver a high capacity of 153 mAh g^{-1} with a capacity retention above 96% after 100 cycles. Al deposition produces a Li-Al alloy with decreasing reaction potential for higher presence of Li. The Li^+ motion across the alloy layer is hindered at lower voltages and the full lithiation of outer surface cannot be achieved. During the charge process, voltage difference drives the local deposition of Li, allowing a more uniform plating and reducing the formation of dendrites.

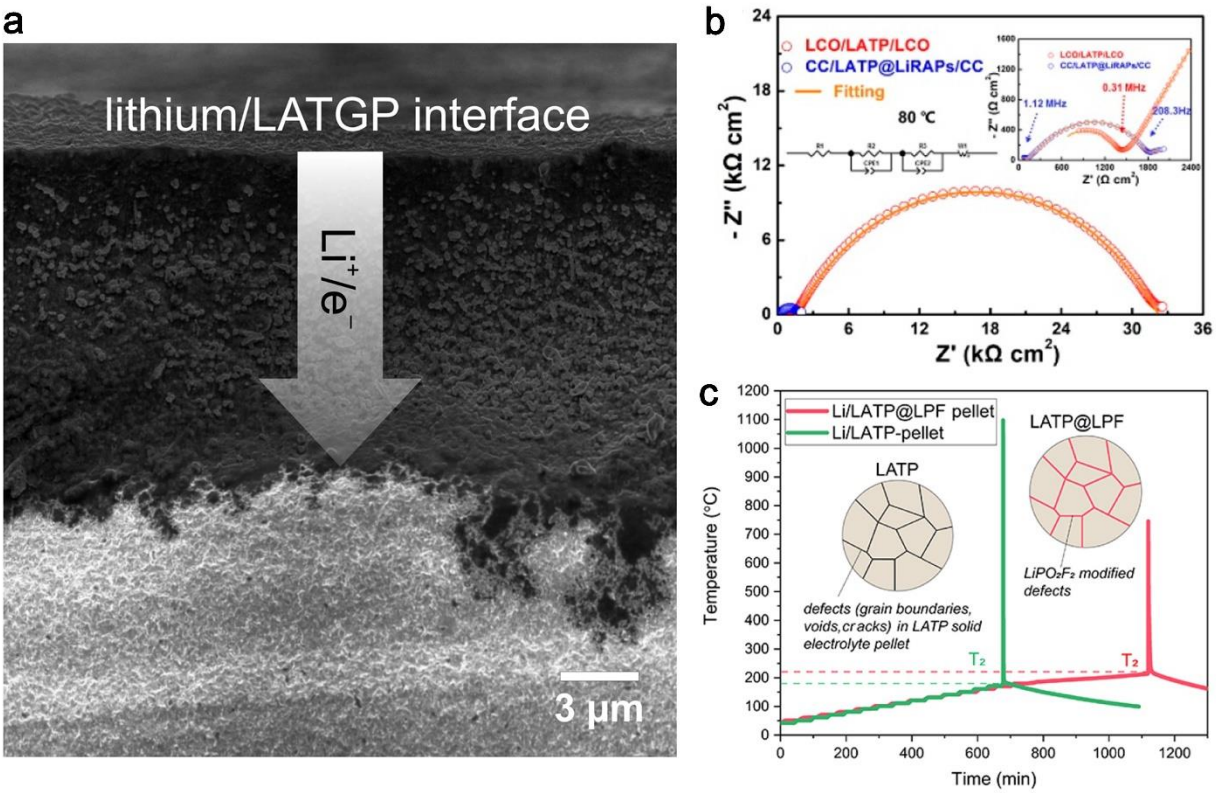

Figure 1.26. a) SEM cross-section image of a LATGP sample after approximately 12 h contact with lithium metal. The white arrow indicates the diffusion of lithium. Reprinted with permission from Ref. (Hartmann et al., 2013). b) EIS profiles of composited LATP/cathode symmetric cells without and with LiRAPs. Reprinted with permission from Ref. (W. Feng et al., 2022). c) Compared accelerating rate calorimetry (ARC) results of a Li/LATP pellet and a Li/LATP@$LiPO_2F_2$-pellet. Reprinted with permission from Ref. (R. Chen et al., 2021a).

A flexible PEO polymer interlayer was shown to decrease the interface resistance of LATP of about one order of magnitude compared with unprotected LATP, simultaneously acting as a separator and increasing surface wettability of the ceramic material, and hence promoting Li ion transport between electrode and electrolyte (Z. Yang et al., 2020). Differences in the systems with and without polymer spacer were observed in the polarization voltage (0.2 V with PEO vs 1.5 V without PEO) and long-term stability upon cycling. A full Li/PEO-LATP/$LiFePO_4$ cell displayed a discharge capacity of 155 mAh g^{-1} at 0.1 C with a high reversibility over 100 cycles (Coulombic efficiency > 99 %) whereas the cell without polymer reported a meager value of 24 mAh g^{-1} at 0.1 C. He et al. (L. He et al., 2019) explored the failure mechanism of LAGP towards metallic Li, observing a gradual disruption of LAGP particles evolving from the grain boundaries to the bulk

of the particles, with the reduction of Ge^{4+} to metallic Ge and formation a Li-Ge alloy. Stabilization of the ceramic can be achieved with the application of a polymeric interlayer of poly(acrylic acid-*co*-maleic acid) (P(AA-*co*-MA)), which permitted the application of a Li-Sn alloy anode with no significant decomposition reactions. The use of ZnF_2 to modify the surface of LAGP was explored by Yu et al. (J. Yu et al., 2022), with the engineering of an *in situ* LiF@Li-Zn nanometric interlayer upon direct reaction with Li metal. This configuration reported an improved stabilization of the interface with absence of side reactions and dendrite evolution. A symmetric cell using the modified interface showed an increment in critical current density up to 2 mA cm^{-2} and a long-term cycling stability over 1000 h with low overpotential. A full cell Li/LAGP/LFP revealed a high reversible capacity of 150 mAh g^{-1} at 0.1 C at room temperature. A thin polypropylene (PP) layer was introduced by Bosubabu et al. (Bosubabu et al., 2019) on the surface of LAGP and the modified material showed a significant decrement in interface resistance and improved cyclability compared with the material without surface modification. The absence of the separator resulted in a more unstable electrolyte with rapid deterioration of the performance in cell. Comparison with liquid electrolyte cells showed for the latter a higher initial capacity but a faster capacity degradation, due to parasitic reactions at the surface of the cathode to form a thick SEI. Solid LAGP-PP displayed a higher capacity retention of 98.5 % with a Coulombic efficiency of 100 % after 200 cycles at 0.5 C. Application in a Li-S cell revealed a reduced capacity degradation thanks to a partial suppression of the polysulfide shuttle effect.

Combination of LATP nanofibers dispersed in a PEO mold showed a perfect hybrid between the properties of the ceramic and polymer electrolytes (Zhai et al., 2017), reporting an enhanced conductivity of 5.2×10^{-5} $S \cdot cm^{-1}$ and an improved affinity against lithium. Dendrite growth in the composite was inhibited by the increased Young's modulus of the ceramic-polymer mix, indicating a higher stress resistance. A polymer interlayer for LATP employing succinonitrile (SN) and polyacrylonitrile (PAN) was presented by Cao et al. (W. Cao et al., 2021), following an investigation on the deterioration of LATP combined with SN. The reactivity with metallic lithium catalyzes the formation of SN polymer with delocalized π electrons, which can shift throughout the conjugated π system via the p_z orbitals. The free distribution increases the electronic conduction of the polymer and allows a constant flow of electrons which contribute to the deterioration of LATP. Incorporation of PAN at the interphase inhibits the polymerization of SN and suppresses the electron transfer, improving the chemical stability. Cell performance reported a long-term

stable cycling of 300 h for symmetric cells and a capacity retention of almost 90% after 170 cycles at 0.1 C.

An alternative method for decreasing interfacial resistance is the application of a thin electrolyte film in a solid-state battery. Thin LAGP layers with an average thickness of 200 μm were produced by diamond wire slicing of crystalline and glass-amorphous LAGP and revealed conductivities of 3.3×10^{-4} S·cm^{-1} and 1.2×10^{-4} S·cm^{-1}, respectively (Kotobuki et al., 2019). The lower value for the glassy material is caused by the lower uniformity of the particles and the increased presence of pores. Chen et al. (Z. Chen et al., 2021) presented the interfacial coating of a thin hybrid LATP composite with PVDF polymer and a $Pyr_{14}FSI$ (N-butyl-N-methylpyrrolidinium bis- (fluoromethanesulfonyl) imide) ionic liquid. The protective layer consisted of a thin polynorbornene (PTNB) polymer applied in direct contact with Li metal. The application of the interlayer enabled a six times longer plating-stripping lifetime, without formation of dendrites, and a significant decrement in interfacial resistance. An ultra-thin (< 100 μm) self-standing LAGP layer reported a ionic conductivity of 2×10^{-5} S·cm^{-1} and a very low electronic conductivity of 1.1×10^{-9} S·cm^{-1}, with an increment in interfacial resistance for cell performance at high temperature (80 °C) that resulted in cell short circuit (Paolella, Zhu, Xu, et al., 2020). The presence of fractures and an uneven elemental distribution was detected, with $AlPO_3$ particles and Ge-rich species within the ceramic pellet, pointed out an improved reactivity with lithium at higher temperature. Composite LAGP/PEO films were described by Jung et al. (Y.-C. Jung et al., 2015) and displayed a conductivity of 1×10^{-5} S·cm^{-1}, about two orders of magnitude higher than pristine PEO: the dispersion of the ceramic species in the polymer matrix lowered the crystallinity of the composite and enhanced the ionic conduction. A solid-state Li/LAGP-PEO/LFP battery showed a good capacity retention (> 80%) after 100 cycles at 55 °C, with final capacity values in the range of 113.4∼121.5 mAh g^{-1}.

LLZO and Garnet-type Materials

The typical structure of a garnet follows the formula $A_3B_2M_3O_{12}$ (A = Ca^{2+}, Mg^{2+}, Fe^{2+}; B = Al^{3+}, Cr^{3+}, Fe^{3+}, or Ga^{3+}; M=Si^{4+}, Ge^{4+}) in the cubic $Ia\bar{3}d$ space group with the A, B and M sites showing an 8-, 6- and 4-fold coordination, respectively (**Figure 1.27**) (Z. Zhang, Shao, et al., 2018). Li-containing structures present the formula $Li_3Ln_3M_2O_{12}$ with a lanthanide element (Ln = Y^{3+}, Pr^{3+}, Nd^{3+}, or Sm^{3+}–Lu^{3+}, M = Te^{6+}, W^{6+}) in the B spot, with the lithium ions located in tetrahedral *24d* sites (Kasper, 1969; Kotobuki, 2017). One of the first garnet-type material to be explored in terms of conductive properties was $Li_5La_3M_2O_{12}$ (M = Ta, Nb) (Thangadurai et al., 2003a), which showed a Li^+ ionic conductivity of about 10^{-6} S cm^{-1}. Nb-garnets reported a slightly lower activation energy than Ta-garnets, but the latter expressed a surprising stability towards molten Li and moist air, due to the inferior reduction tendency of Ta with respect to Nb.

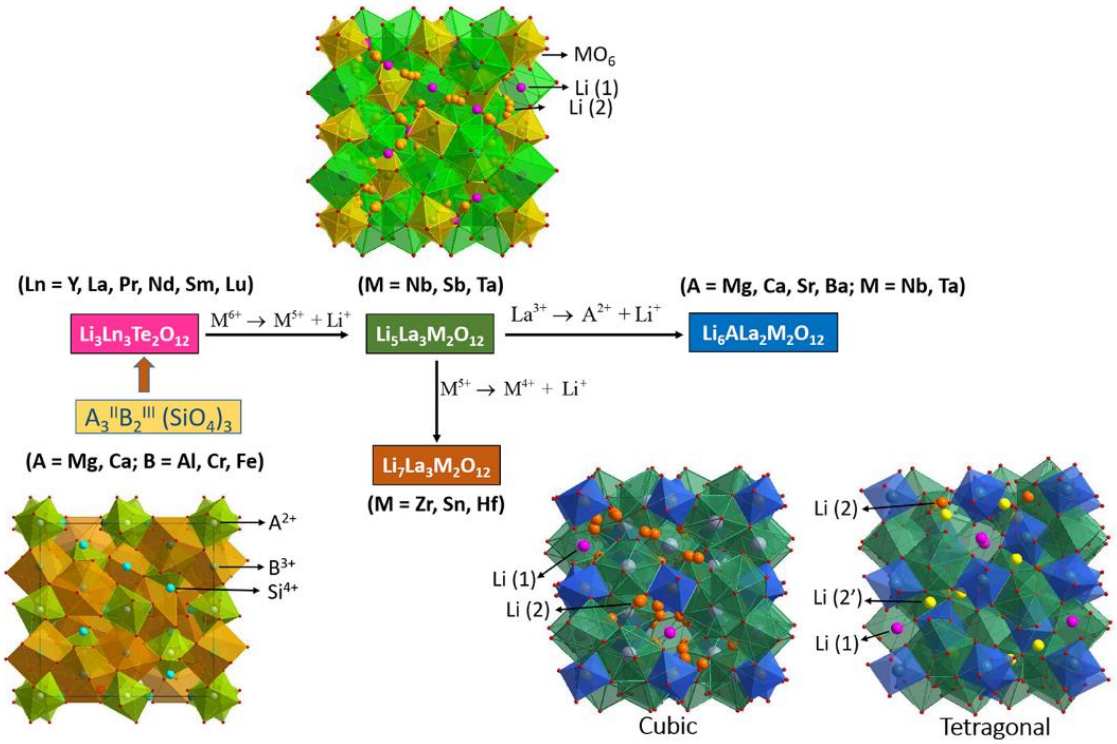

Figure 1.27. Different possible compositions for garnet-type solid electrolytes. Reprinted with permission from Ref. (C. Wang et al., 2020)

Conductivity of the Nb-garnet was improved with an elemental substitution (Thangadurai & Weppner, 2006); partially replacing Nb^{5+} with In^{3+} and La^{3+} with K^{+} allowed to obtain a conductivity in the order of 10^{-4} S cm^{-1} at 50 °C and an activation energy of 0.51 eV. The substitution of smaller Nb cations with larger In ions caused an increase in the lattice parameters for the structure. The surplus of Li atoms for charge balance cannot be accommodated in the tetrahedral sites and excess Li^{+} ions reside in the 6-fold site and garnet structures with extra occupation of Li are defined as Li-rich garnets. Elemental swapping in the La site with bivalent alkali-metal cations (Ca, Sr, Ba) gives origin to a modified class of garnets (Thangadurai & Weppner, 2005a, 2005b). Among these materials, $Li_6BaLa_2Ta_2O_{12}$ reported a high room temperature conductivity of 4×10^{-4} S·cm^{-1} and was found to be stable up to 6 V vs. Li/Li^{+} (Thangadurai & Weppner, 2005a). Antimony-based garnet structures $Li_5Ln_3Sb_2O_{12}$ were also studied, and exhibited ionic conductivities around 10^{-4} S·cm^{-1} at room temperature, with higher values reported for structures including larger rare-earth elements (La, Pr, Nd) (Percival et al., 2008). Structural analysis indicated for $Li_5La_3Sb_2O_{12}$ a cubic cell (space group $Ia\bar{3}d$). Substitution of M-site ions with tetravalent cations can produce Li-rich garnets with formula $Li_7La_3M_2O_{12}$ (Awaka et al., 2010; Murugan et al., 2007; Percival et al., 2009). Tin-based $Li_7La_3Sn_2O_{12}$ garnet reported a tetragonal distortion in the crystal structure in the space group $I4_1/acd$, allocating Li ions in three fully occupied distinct sites, with an minimum Li-Li distance of 2.5 Å (Percival et al., 2009). This distorted coordination diminishes the Li transit between separate sites, reflecting in a low total conductivity around 10^{-5} S·cm^{-1} at room temperature. Hafnium garnet $Li_7La_3Sn_2O_{12}$ exhibited an analogous tetragonal framework and an even lower conductivity of 9.85×10^{-7} S·cm^{-1} (Awaka et al., 2010).

On the other hand, $Li_7La_3Zr_2O_{12}$ (LLZO) reported a number of fascinating properties which make it a widely studied material for use as a solid electrolyte (C. Wang et al., 2020). First reports by Murugan et al. (Murugan et al., 2007) unveiled a cubic crystal structure similar to the Nb/Ta garnets and fast conduction properties, with a conductivity well above 10^{-4} S·cm^{-1}. Thermal analysis revealed a high thermal stability, with no relevant phase transition for temperature up to 900 °C, and the material showed a notable chemical stability against lithium, with a broad potential window up to 6 V (Murugan et al., 2007). The remarkable mechanical hardness and rigidity helps reducing the evolution of lithium dendrites. However, LLZO presents a tetragonal polymorph (Awaka et al., 2009) like the other Li-rich garnets and this phase is thermodynamically more stable

at room temperature and exhibits a conductivity of about two orders of magnitude lower than the cubic phase (**Figure 1.28**). The main difference between the two conformations is found in the spatial distribution of Li ions. The tetragonal LLZO (t-LLZO) (**Figure 1.28a**) shows the three-site allocation of the other tetragonal garnets (Li(1) at tetrahedral voids *8a*, Li(2) at octahedral gap *16f*, Li(3) in eccentric octahedral *32g*) (**Figure 1.28b**) with highly ordered Li vacancies, which makes ion transfer between adjacent positions more difficult (Aktaş et al., 2019; Awaka et al., 2009; L. Xu et al., 2021). On the other hand, cubic LLZO (c-LLZO) (**Figure 1.28c**) only has two distinct slots for Li (Li(1) at tetrahedral voids *24d*, Li(2) in eccentric octahedral *96h*) (**Figure 1.28d**) with alternate disposition and increased inherent disorder. The shifting of Li ions within the lattice can be defined with a concerted mechanism controlled by the unsettled positioning of Li at the *24d* sites and the spatial restrictions which force only specific Li atoms pathways (Jalem et al., 2013). The inner asymmetry can spur Li ion motion and local rearrangement.

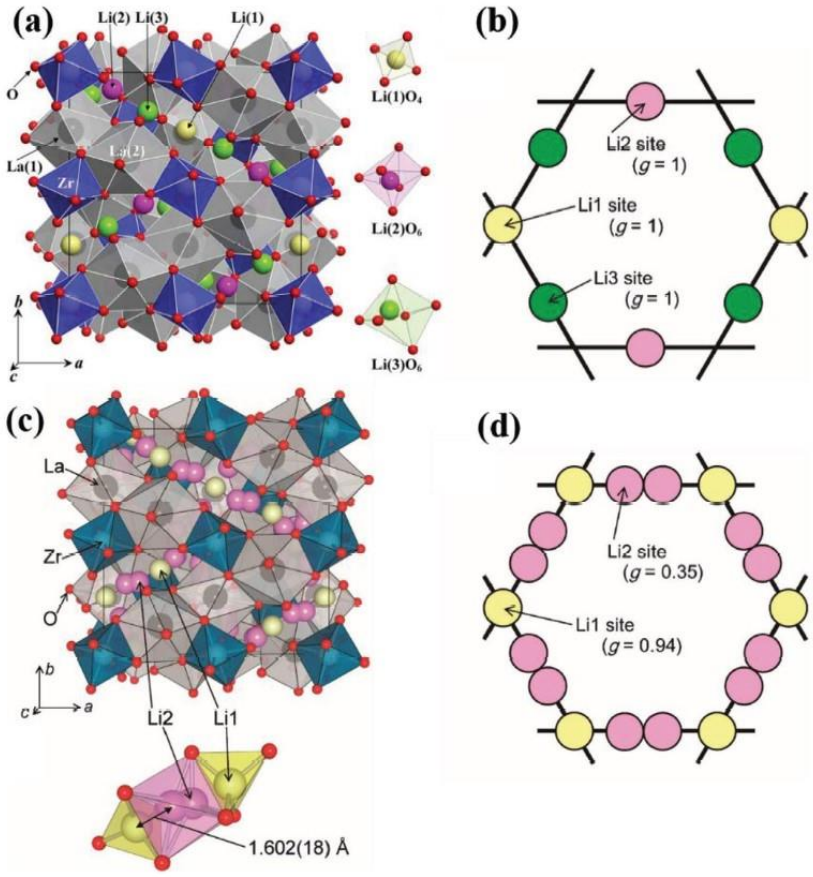

Figure 1.28. a) Crystal structure of tetragonal LLZO with b) corresponding lithium ions site disposition. c) Crystal structure of cubic LLZO with d) corresponding lithium ions site disposition. Reprinted with permission from Ref. (L. Xu et al., 2021).

Considering the instability of c-LLZO at low temperature, the structure requires stabilization which can be realized by means of elemental doping. Aliovalent substitution affects the concentration of Li vacancies and improves the conductivity of the material (Salimkhani et al., 2021). Density functional theory (DFT) computations permitted to describe all feasible elemental replacement in LLZO (**Figure 1.29**) (Miara et al., 2015). A first example of the stabilization of c-LLZO was described by Geiger et al. (Geiger et al., 2011b) who investigated LLZO synthesized via solid-state method and pointed out a peculiar fact. LLZO prepared using Pt crucibles showed fine crystals with tetragonal phase and structural analysis at different temperature revealed a tetragonal-to-cubic transition at around 150 °C, while the same material treated in alumina crucibles reported larger crystals with cubic phase at room temperature. A thorough elemental analysis showed a small presence of Al in the material, possibly deriving from the crucibles themselves, and the incorporation of Al preserved the cubic phase at low temperature (Buschmann et al., 2011; Geiger et al., 2011b). A more precise analysis by Rangasamy et al. (Rangasamy et al., 2012) defined a minimum amount of 0.204 moles of Al to be introduced in order to ensure the stability of the cubic polymorph. A surplus of Al exceeded the solubility in the cubic phase and gave life to $LaAlO_3$ by-products. At the same time, overabundance of Li induced a shift to the tetragonal phase, due to the distortion of the unit cell by the filling of Li vacancy sites. This points out the role of Li concentration in the formation of c-LLZO. Optimized Al-LLZO hot-pressed at 1000 °C showed an ionic conductivity of 4×10^{-4} $S \cdot cm^{-1}$.

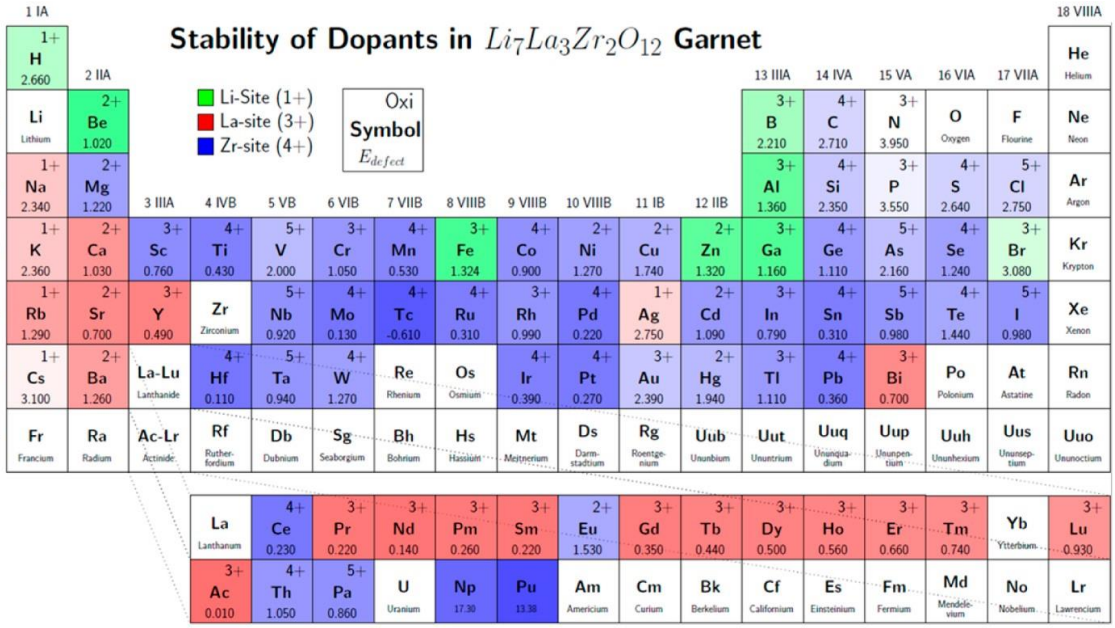

Figure 1.29. Summary of all possible doping elements for LLZO garnet. The color represents the preferred cation site. Darker colors signify lower defect energy. The box also displays the preferred oxidation state and the defect energy (in eV). Reprinted with permission from Ref. (Miara et al., 2015).

Use of Ga as a dopant has been shown to enhance the ionic conductivity up to 10^{-3} S·cm^{-1} (Rettenwander et al., 2016; J. F. Wu et al., 2017). A concentration of Ga above 0.2 per formula unit generates a pure cubic phase, with a primary distribution of Li atoms in the *96h* octahedral sites (**Figure 1.30a**). The migration between two *96h* sites reflects on a high Li-ion mobility and is the most determinant on the final conductivity (**Figure 1.30b**) (J. F. Wu et al., 2017). The larger radius of Ga^{3+} in the coordination environments of LLZO can enlarge the tetrahedral and octahedral gaps, improving ion motion. Variation in Ga content displays a shifting tendency in the conductivity (Jalem et al., 2015). A reduced amount (< 0.1 per f.u.) is accompanied by a decrease in the value and a higher ratio (0.1 ÷ 0.3 per f.u.) shows a flat trend. A cubic phase modification from $Ia\bar{3}d$ to acentric $I\bar{4}3d$ was observed in Ga-stabilized LLZO (**Figure 1.30c**) (Wagner, Redhammer, Rettenwander, Senyshyn, et al., 2016), due to a preferential disposition of Ga cations in *96h* sites, with a three-fold allocation of Li^+ ions (tetrahedral *12a* and *12b*, and *48e*) that differs from the typical garnet structure, possibly being the origin of the high conduction (**Figure 1.30d**). An analogous behavior was reported for Fe^{3+} doping in Li positions (Wagner, Redhammer, Rettenwander, Tippelt, et al., 2016), with the cubic $I\bar{4}3d$ modification of the structure, and the

material exhibited a high conductivity of 1.38×10^{-3} S·cm^{-1}. A balanced co-doping of Al and Ga in $Li_{6.4}Al_{0.2-x}Ga_xLa_3Zr_2O_{12}$ shows a regularly shifting tendency in the conductivity of LLZO, with the cubic transition observed for a 0.05:0.15 Al:Ga ratio (Rettenwander et al., 2016), on parallel with a sharp decrease in the activation energy to 0.26 eV. The conductivities ranged from 2.6×10^{-4} to 1.2×10^{-3} S·cm^{-1} with increasing Ga content, which also reflected in decreased grain size, improved densification of the ceramic and inferior surface resistance (from 78 to 24 Ω cm^{-2}).

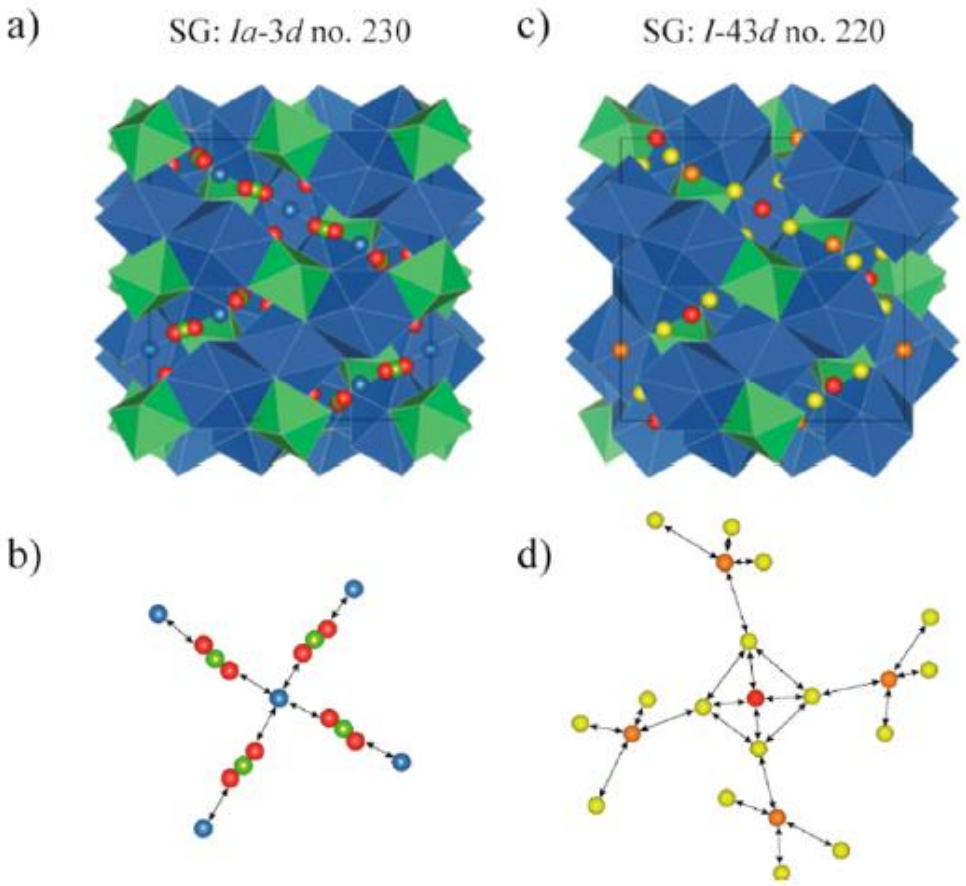

Figure 1.30. a) Structure and b) Li-ion diffusion pathway of $Ia\bar{3}d$ LLZO, showing LaO_8 dodecahedra (blue), ZrO_6 octahedra (green) and three-site Li distribution: *24d* tetrahedral coordination (red spheres), *48g* octahedral coordination (green spheres), and distorted *96h* octahedral coordination (blue spheres); c) Structure and d) Li-ion diffusion pathway of $I\bar{4}3d$ LLZO, showing Li distribution over three sites: two tetrahedrally-coordinated *12a* (red spheres) and *12b* (orange spheres), and 4*8e* octahedral coordination (yellow spheres). Adapted with permission from Ref. (Brugge, 2018; Wagner, Redhammer, Rettenwander, Senyshyn, et al., 2016)

Substitution in the La-site influences the conductivity by varying the bottleneck size for Li transfer and among the possible dopants, alkali-earth metals can allow for a more stable structure. Sr-substituted LLZO presented an improved room temperature conductivity of 5×10^{-4} S·cm^{-1} for a 1.7% wt. of Sr, about twice as high than the undoped material (Dumon et al., 2013). The incorporation of $SrCO_3$ improved the densification of the ceramic and increased the grain size, but excess of doping produced secondary $SrZrO_3$ phases, and lowered the performance. A compared evaluation between different alkali-earth metals demonstrated the substitution in the La site and reported conductivities in the order of 10^{-4} S·cm^{-1}, with the highest value for Sr-doping (Kammampata et al., 2019), while a subsequent study by Song et al. (S. Song et al., 2017) observed much higher values for the insertion of Ba (up to 1.13×10^{-3} S·cm^{-1}) and an extended stability window towards lithium up to 9 V (S. Song et al., 2017). In this study however, the substitution with the alkali-earth elements was observed at the Zr site, which is the most explored doping environment for LLZO, due to the more intense effect on conductivity compared with Li and La doping(L. Xu et al., 2021). Substitution of Zr^{4+} with trivalent Y^{3+} was attempted by using yttria-stabilized ZrO_2 as precursor (Murugan et al., 2011) and a small insertion of dopant delivered a conductivity of 8.1×10^{-4} S·cm^{-1}, 2.5 times higher than a material with Y-doping at the La site (3.2×10^{-4} S·cm^{-1}) (Deviannapoorani et al., 2016a). Elemental substitution typically involves pentavalent cations such as Sb^{5+}, Ta^{5+} or Nb^{5+} (Z. Zhang, Shao, et al., 2018), giving compositions with formula $Li_{7-x}La_3Zr_{2-x}M_xO_{12}$. In these systems, substitution is observed at the octahedral *16a* zirconium sites(Cussen, 2006) and a reduced amount of dopant is required (< 0.2 per f.u.) to produce the cubic phase. Co-doping formulations including Sb can enhance the conductivity of LLZO up to three times compared with the pristine material (T. Yang et al., 2018), with an improved densification of the ceramic (Z. Cao et al., 2015). Nb-doped $Li_{6.75}La_3Zr_{1.75}Nb_{0.25}O_{12}$ presented a wide electrochemical stability window with no reactions detected up to 9 V vs. Li/Li$^+$ (**Figure 1.31a**). Battery tests unveiled a discharge capacity of 129 mAh g^{-1} with a remarkable stability over 100 cycles (Ohta et al., 2011). An observation by Thompson et al. confirmed that Ta-doped LLZO exhibits a high conductivity without the presence of Al impurities and the stabilization of the cubic structure is detected when 0.4 – 0.5 Li vacancies per formula unit are present (Thompson et al., 2014). The creation of vacancies by hypervalent replacement decreases the inner repulsion between positive Li^+ ions improving ion conduction and the effect is further amplified by multiple doping in different positions, showing a conductivity of 1.24×10^{-3} S·cm^{-1}

for a ternary Ga-Ba-Ta doped LLZO (Meesala et al., 2019). A more prominent effect is observed for hexavalent substitution with W^{6+}, Mo^{6+} or Te^{6+}, which allow to generate even more Li vacancies in the structure (Deviannapoorani et al., 2013; Y. Li et al., 2015, 2018). W-doped LLZO presented a higher densification because the formation of low-melting point aggregates during sintering decreases the size of intergranular pores and reduces the grain boundary resistance. The material was found stable against Li metal anode, with an electrochemical window extending up to 5 V, and displayed an improved reversibility in batteries (Y. Li et al., 2015). Te-doped LLZO enabled a lower temperature annealing of the ceramic and reported a remarkably high conductivity of 1.02×10^{-3} S·cm^{-1} at room temperature (**Figure 1.31b**)(Deviannapoorani et al., 2013).

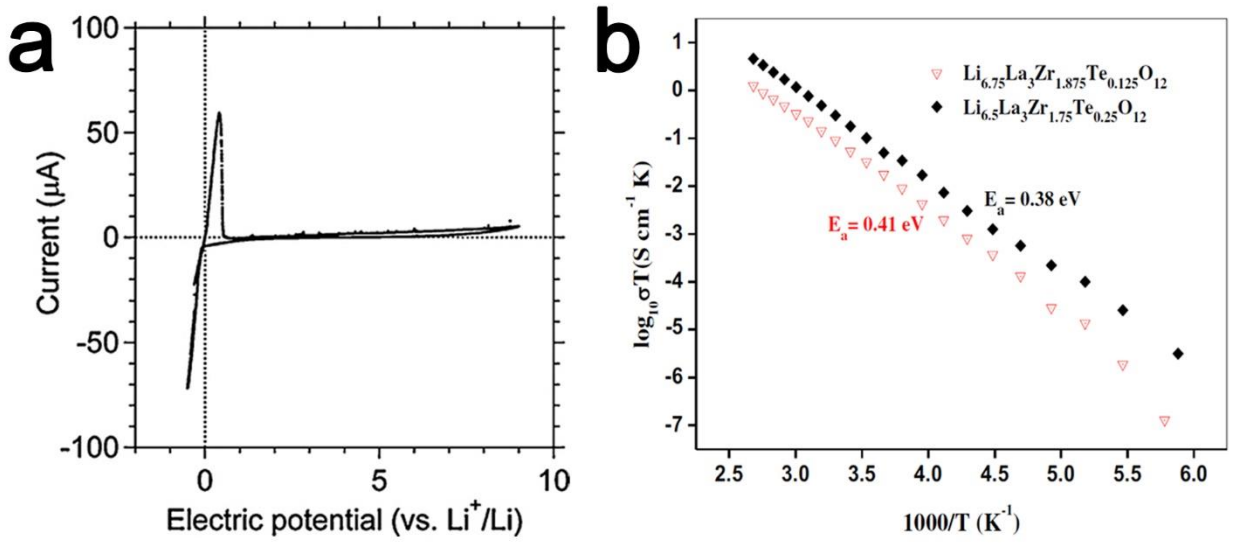

Figure 1.31. a) Cyclic voltammogram of $Li_{6.75}La_3Zr_{1.75}Nb_{0.25}O_{12}$, performed at a scanning rate of 1 mV s^{-1} at 25 °C. Reprinted with permission from Ref. (Ohta et al., 2011). b) Arrhenius plot of total conductivities for different compositions of Te-doped LLZO. Reprinted with permission from Ref. (Deviannapoorani et al., 2013).

An alternative method to augment the conductivity of garnets comprises the use of additives to attain a material with improved density and decrease the synthesis temperature at the same time (Janani et al., 2014). Moreover, sintering aids can increment the interface contact of the particles, as demonstrated by Ohta et al. (Ohta et al., 2011) with the incorporation of Li_3BO_3 in Nb-LLZO and LCO cathode. Melted borate would distribute between the cathode particles and at the interphase, resulting in an absence of pores and an improved contact. Moreover, the low melting point of Li_3BO_3 (700 °C) allows to achieve a more intimate contact between the particles at lower

sintering temperatures, as low as 790 °C (Ohta et al., 2014). Other inert additives included Li_3PO_4 and Li_4SiO_4 and the latter showed a better enhancement of the densification of LLZO prepared by sol-gel method, with a final relative density of 96% and a conductivity of 6.1×10^{-4} S·cm^{-1} after sintering at 1200 °C (**Figure 1.32a**), as well as a stabilized cubic phase (Janani et al., 2014). The addition of Li_3PO_4 to Ta-doped LLZO showed an augmented concentration of P at the grain boundaries, with the formation of an amorphous phases at the grain boundaries upon a self-limiting reaction with Li. The conductivity of the doped sample was lower than the phosphate-free material, due to the inert nature Li_3PO_4 which affects ion conduction at the boundaries, but the former reported an area-specific resistance (ASR) about half as large than the latter (1008 vs 2080 Ω·cm^2) (B. Xu et al., 2017). A direct synthesis between $La_2Zr_2O_7$ and lithium-lanthanum oxides to prepare LLZO was attempted by Deviannapoorani et al. and the results revealed the stabilization of the cubic phase only for high sintering temperature (1200 °C), whereas for LLZO samples prepared from conventional elemental oxides and LiOH the cubic phase was observed at 950 °C(Deviannapoorani et al., 2015). Glass/ceramic composites have shown enhanced mechanical and thermal features and improved conduction. The introduction of a $LiPO_3$ glass increased the conductivity of t-LLZO of about one order of magnitude, while the effect on c-LLZO was of smaller entity, with the highest value of 1.1×10^{-4} S·cm^{-1} achieved for a 1.1 % wt. insertion of glass (**Figure 1.32b**) (Pershina et al., 2017). Higher amounts of $LiPO_3$ led to the formation of Li_3PO_4 and $La_2Zr_2O_7$ impurities at the grain boundaries, which reduced the Li mobility and the total conductivity. Boron-silicate (Il'ina et al., 2018) and aluminum-silicate (Tang et al., 2017) glasses displayed a similar behavior, inducing an increment in conductivity up to a critical content, with distribution of conductive phases at the grain boundaries, and showing a decrement for an excess of glass due to the formation of poorly conductive inert phases. Despite their higher activation energies, boron-composites manifested conductivities in the order of 10^{-4} S·cm^{-1} above 100 °C, higher than Al-doped cubic LLZO. The introduction of a LiF additive to Ta-doped $Li_{6.5}La_3Zr_{1.5}Ta_{0.5}O_{12}$ was proposed to stabilize the solid electrolyte towards moisture (Y. Li et al., 2017). The inherent strength of the ionic Li–F bond makes it insoluble in water and when inserted in the ceramic it is distributed along the grain boundaries, suppressing the diffusion of water and CO_2 in the ceramic pellet, and avoiding surface reactions. As a result, chemical degradation was reduced and the electrolyte showed an ionic conductivity of 5.2×10^{-4} S·cm^{-1}, like the LiF-free sample (5.5×10^{-4} S·cm^{-1}), but with a significantly lower interfacial resistance of 345 Ω·cm^2.

Addition of a polymer interlayer granted a discharge capacity of 142 mAh g^{-1} at a current density of 80 µA cm^{-2} in a full-solid cell, with a Coulombic efficiency close to 100% after 100 cycles (**Figure 1.32c**).

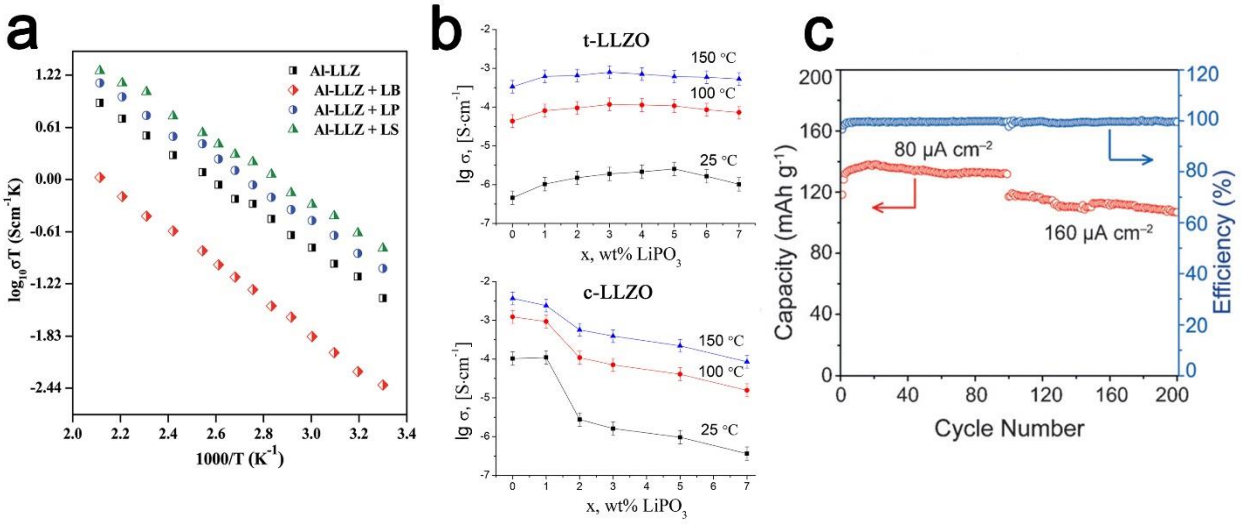

Figure 1.32. a) Arrhenius plots for the total conductivity of pristine Al–LLZO and Al–LLZO added with 1% wt. of Li_3BO_3, Li_3PO_4 and Li_4SiO_4. Reprinted with permission from Ref. (Janani et al., 2014). b) Total conductivity of t-LLZO and c-LLZO as a function of wt% of $LiPO_3$ additive. Reprinted with permission from Ref. (Pershina et al., 2017). c) Capacity retention and cycling efficiency of LFP/polymer-LLZTO-LiF/Li cells at 80 and 160 mA cm^{-2}. Reprinted with permission from Ref. (Y. Li et al., 2017).

Such modifications can indeed help mitigating the major shortcoming of garnet-type conductors. Their electrochemical performance against Li metal are generally more stable compared with other solid electrolytes (L. Xu et al., 2021; N. Zhao et al., 2019). However, their notably high interfacial resistance (Tsai et al., 2016) can render their practical application more impractical. The troublesome conduction at the interface is caused by their poor lithium wettability and further inflated by the surface deposition of inert impurities like Li_2CO_3 (Huo et al., 2020; Sharafi et al., 2017), which is formed upon reaction with moist air. Surface chemistry is a preeminent factor in the interface properties of LLZO as reported by Sharafi et al. (Sharafi et al., 2017) who pinpointed the contact qualities of the LLZO/Li interface in terms of adhesion and contact angle. The measured angle for the Li_2CO_3/Li interface was 142°, in agreement with calculations and more than double the value for LLZO/Li (62°), with an adhesion energy of 0.1 J m^{-2} vs 0.62 J m^{-2} for LLZO, pointing out the less favorable character of carbonate to surface

contact. A more considerate engineering of the surface microstructure is therefore pivotal to obtain a limited interface resistance, and a study by Cheng et al. (L. Cheng et al., 2015) dealt with the manufacturing of garnet heterostructures with controlled grain size and orientations. The procedure involved a precise tweaking of the sintering conditions by mixing of precursor powders with different grain distribution, which can be affected by the nature of the covering powder during the thermal treatment (L. Cheng et al., 2014). Samples with smaller grains on the outer surface displayed an ostensibly lower ASR, as low as 37 $\Omega \cdot cm^2$, allowing a more stable cycling performance (L. Cheng et al., 2015).

Application of an interlayer may be a valid choice for a more elaborate solid interface. Addition of a thin Al coating enabled the formation of a Li-Al alloy interlayer at the electrode surface (Fu et al., 2017) leading to an improved wettability towards Li metal and a reduction of the surface pores, which is reflected in a decrease in the ASR of more than ten times for the Al-coated ceramic (75 vs 950 $\Omega \cdot cm^2$). The elemental distribution of the Al alloy at the grain boundaries was clearly visible at low magnification SEM with partial diffusion of Al towards the bulk of the electrolyte. This demonstrates the more lithiophilic character of the garnet surface, allowing a better adherence of the Li anode. Symmetric cells revealed a regular long-term behavior, indicating the stability of the charge transfer at the interface. Surface covering of LLZO with Al_2O_3 was performed via atomic-layer deposition (ALD) (X. Han et al., 2017) and the experimental results showed an exceptional decrease in the ASR for the coated garnet, from 1710 to 1 $\Omega \cdot cm^2$, practically nullifying the resistance. The reason lies in the conducting properties of lithiated alumina, which has a strong binding energy with metallic Li and acts as a Li-ion conductor with efficient paths for Li ion motion while insulating the solid electrolyte from a direct reaction with the anode. The modified material displayed satisfactory performance in a solid-cell with a high-voltage $Li_2FeMn_3O_8$ cathode, with a stable capacity of 110 mAh g^{-1} after 50 cycles. A distinctive approach has been described by Shao et al. (Shao et al., 2018) who applied a soft graphitic layer on the surface of doped $Li_{5.9}Al_{0.2}La_3Zr_{1.75}W_{0.25}O_{12}$ by the use of a pencil (Shao et al., 2018). The modified interface demonstrated a more intimate contact and wettability between the garnet and Li, with a uniform distribution of lithium in the graphite layer forming LiC_6 lithiated carbon which can spontaneously accept and release lithium at room temperature. Furthermore, the graphite coating shows a higher flexibility and ductility compared with other interfacial phases. Stable plating-stripping behavior with a puny overpotential of 6 mV was reported for the stabilized

material, while bare LLZO showed a high polarization of 150 mV caused by Li infiltration. A full cell using an NMC cathode produced a reversible capacity of 141 mAh g^{-1} at a 3 C current, comparable with liquid-electrolyte cells, and a stable performance at higher temperature and currents. As well as solid fillers, ion conductive liquids can be performant wetting agents, imbuing the surface pores of the electrodes and incrementing the contact area. Interface modification by using the ionic liquid $Pyr_{14}FSI$-LiTFSI at the interface of doped $Li_{6.5}La_{2.5}Ba_{0.5}ZrNbO_{12}$ unveiled a good chemical compatibility of the liquid with the garnet (Pervez et al., 2020), showing no relevant structural variation of the pellets after prolonged exposure to the ionic liquid. Minor degradation was however detected upon repeated cycling, forming only a thin interlayer at the surface. Introduction of the liquid agent brought the ASR against lithium down of over one order of magnitude compared with the untreated electrolyte (145 vs 2440 $\Omega \cdot cm^2$) and evaluation in a cell with LFP revealed an ASR of 265 $\Omega \cdot cm^2$, pointing out an improvement in interface properties at both the cathode and anode sides.

Polymeric interlayers can be another functional solution for getting a high-performance solid electrolyte configuration, bringing together the elasticity and good wettability of the polymers with the Li^+ mobility and electrochemical stability of the ceramic garnets. A sandwiched multilayered arrangement using a poly(ethylene glycol) methyl ether acrylate (PEGMEA) cross-linked network demonstrated a remarkable stability towards lithium, with no observed reactivity up to 4.75 V (W. Zhou et al., 2016). The modified architecture of the polymer chains, with the inert polyacrylate acting as a support for the free-swinging PEO chains, enables a stable framework with enhanced mobility for the Li^+ ions and thermal analyses observed no significant decomposition processes up to 270 °C, confirming the apt stability of the polymer for use in a solid battery. Use of the interlayer reflected in more homogeneous interfaces with a uniform ion flow and improved adhesion of Li metal to the polymer, and the thin LLZO ceramic membrane blocked electron transit through the polymer which could be detrimental to the long-term stability of the polymer layer itself. A modified asymmetric disposition of the previous configuration, employing a LLZO nanoparticle layer at the Li metal side combined with a PEGMEA coating at the cathode side, attempts to solve both lithium dendrite evolution and surface contact issues at the same time (Duan et al., 2018). A strong adhesion was observed between the electrodes and the electrolyte in post-mortem battery analysis and the combination of the ductile PEGMEA and the rigid LLZO membrane hindered Li nucleation and dendrite formation, showing an outstandingly stable Li

deposition profile over 3200 h. Dispersion of garnets directly in a polymer matrix can affect the ionic transport properties of the electrolyte, as shown by Zheng et al. (J. Zheng & Hu, 2018) who investigated the conduction mechanism in LLZO-PEO-LiTFSI composites by varying the concentration of LLZO in the mix. The analysis reported a steep decrement in the ionic conduction for solid electrolyte contents higher than 50% wt. Delving deeper in the nature of the ionic motion revealed the shift of the Li transport pathways to intra-ceramic percolation routes made of disjoined LLZO particles for amounts of ceramic above a critical threshold. The addition of liquid plasticizers such as TEGDME increased the particle mobility in the polymer and resulted in a disruption of the ceramic network, shifting the main ion conduction back to the polymer.

CHAPTER II
THESIS SCOPE AND OBJECTIVES

The previous chapter presents a brief historical perspective on the development of lithium-ion batteries. The current limitations of the technology in terms of safety and reliability are illustrated, along with a series of implementations for the solution of such problems. The mechanism of ion transport in solid electrolytes is detailed as well.

The question of energy storage requires to be addressed promptly; for this matter, batteries and new conversion systems can provide a valid choice for exploiting sustainable resources and decrease the use of fossil sources. The development of more efficient technologies, such as solid-state batteries, is therefore a necessity for the replacement of current combustion engines and the expansion of grid energy storage. In the present work, NASICON and garnet-type ceramic materials are synthesized following a solid-state pathway and fully explored as a platform for the improvement of solid electrolytes, in order to resolve some of the major limitations which are still affecting solid-state batteries.

The aim of this thesis is briefly described as a list of objectives, all part of a structured project based on the optimization of NASICON and garnet materials:

1. **Improvement of the densification of LATP**. NASICON-type $Li_{1.5}Al_{0.5}Ti_{1.5}(PO_4)_3$ (LATP) is a valid material to develop fully-inorganic solid electrolyte. Nonetheless, the preparation of this material may prove to be complicated, requiring sensibly high temperatures for synthesis and densification which favor side reactions and decomposition in poorly conductive phases. Thus, the preparation of the material can be improved by reducing calcination times and increasing the density of the pellets. This work evolved through the following points:
   - *Characterization of the powders*: *In-situ* high-temperature X-ray diffraction was used to understand the formation mechanism of LATP and the evolution of additional phases.

- *Optimization of the synthesis temperature:* different calcination temperatures were tested and the differences in structure and morphology between the samples were investigated with different techniques.
- *Preparation of dense ceramic electrolytes:* thin electrolyte pellets were prepared by hot-pressing.
- *Evaluation of the ionic conductivity*: the ionic conductivity was measured by electrochemical impedance spectroscopy (EIS) to evaluate the final performance of the materials.

2. **Low temperature densification of LLBO**. $Li_5La_3Bi_2O_{12}$ (LLBO) garnet is reported to have easy synthesis conditions and appropriate ionic performances for practical applications, but the effects of hot-pressing on the densification have not been fully explored before. This activity was carried out through the following points:
   - *Low temperature densification of the material*: solid electrolyte pellets were prepared by hot-pressing of the powders at a remarkably low temperature.
   - *Influence of temperature on the stability:* densified powders were characterized to understand the effect of temperature on the chemical stability and explore the evolution of unwanted impurities. Computational studies were performed to unveil the dynamics of electrolyte decomposition at high temperatures.
   - *Preparation and testing of electrolyte composites:* mixed LLBO-LLZO powders were prepared, and the effects of LLBO on the sintering of LLZO at low temperatures and on the ionic diffusion in the mixed system were investigated by means of different characterization techniques.
3. **Use of carbon additives in the synthesis process of LLZO**. The synthesis of garnet $Li_5La_3Zr_2O_{12}$ (LLZO) is typically achieved with very high temperature processing which is known to negatively affect the final material. The formation process can be promoted at lower temperatures by using surfactants or capping additives during the temperature treatment, which can help stabilizing the desired phases. Among these agents, carbon materials have rarely been employed in ceramic processing. The following steps were carried out:
   - *Observation of the formation mechanism of the garnet*: *In-situ* high-temperature XRD was employed to comprehend the evolution of the cubic-LLZO structure and the

formation of intermediate phases. Thermal analysis allowed to unveil the decomposition process of the precursors and how it contributed to the reaction in the solid melt.

- *Influence of carbon additives on the nature of the product*: Several powder samples prepared with different carbon content were thoroughly characterized in terms of structure and morphology and observations on the particle size of the products were conducted. The effects of diverse carbon additives on the formation of particles were studied.
- *Evaluation of the ionic conductivity*: the ionic conductivity was measured by electrochemical impedance spectroscopy (EIS) to evaluate the final performance of the materials.

4. **Effect of Te doping on the stabilization of LLZO**. Elemental doping is a very common method for improving the electrochemical behavior of solid electrolytes. Introduction of dopants has also proven effective in the preservation of the cubic LLZO phase at room temperature, benefitting the ionic conductivity. Furthermore, doping agents can possibly affect the formation mechanism of the material during the calcination steps. This study evolved through the following steps:
   - *Observation of the formation mechanism of the garnet*: The stability of cubic-LLZO polymorph synthesized at low temperatures with Te incorporation was analyzed via *in-situ* XRD to understand the evolution of intermediate phases and their influence on the formation process.
   - *Effect of different amount of Te doping*: A series of material samples with distinct final stoichiometries were synthesized and their structure and morphology were investigated.
   - *Evaluation of the ionic conductivity*: the powders were hot-pressed at relatively low temperatures and the ionic conductivity of all the resulting samples was evaluated by EIS and compared to commercial samples treated in the same working conditions.
   - *Effect of hot-pressing on density*: morphological analyses were performed on the hot-pressed pellets to verify the effect of the procedure on the densification and on the elemental distribution in the final materials.

2.1. Thesis organization

The present thesis is subdivided into chapters, which are organized as follows:

Chapter 1 The history of lithium-ion batteries is briefly described, including a presentation of their limitations and safety concerns. The concept of ion conduction in solid materials is introduced. Information on the state-of-the-art of solid-state batteries are provided, focusing in particular on inorganic ceramic materials.

Chapter 2 The organization and the objectives of the thesis are presented.

Chapter 3 The synthesis process of LATP solid electrolyte is depicted. The influence of $AlPO_4$ impurities and the effects of hot-pressing on the electrochemical properties of LATP are investigated.

Chapter 4 The consequences of hot-press densification on the physical properties of LLBO are described. The optimization of the synthesis conditions is presented, and the structural characterization of the material is reported. Use of LLBO as sintering aid for LLZO is also described.

Chapter 5 The effect of carbon incorporation as sintering agent for the solid-state synthesis of LLZO is described. The synthesis mechanism and the low-temperature densification are thoroughly investigated.

Chapter 6 The effect of partial substitution of Zr with Te on the chemical features of LLZO is presented. The effects on the synthesis mechanism and on the electrochemistry of the material are reported.

Chapter 7 The conclusions of the study and some future perspectives on the topic are presented. Furthermore, a brief outlook on future investigations related to the thesis is proposed.

CHAPTER III

INFLUENCE OF $AlPO_4$ IMPURITY ON THE ELECTROCHEMICAL PROPERTIES OF NASICON-TYPE $Li_{1.5}Al_{0.5}Ti_{1.5}(PO_4)_3$ SOLID ELECTROLYTE

Chapter published in ChemElectroChem, **2022**, 9 (24), e202200984

3.1. Introduction

In Chapter I the properties of NASICON electrolytes were exposed in detail, as well as the most common approaches for the engineering of these materials. In this chapter, the focus is on the solid NASICON electrolyte LATP and its behavior upon densification via hot-pressing technique. The goal of this chapter is to better understand how the mechanical and electrochemical properties of LATP evolve following sintering and how the variations in the synthesis process led to different microstructures in the densified samples. An investigation on the presence of impurities in the final material was also conducted, demonstrating the unavoidable evolution of secondary $AlPO_4$ phases which influence the conductivity of the solid electrolyte. A proper choice of the synthesis parameters can allow to achieve a powder with the desired properties (in terms of particle size and impurities) which afterwards reflect on the final nature of the ceramic pellet after densification. The motives behind this research mainly come from the absence of detailed literature cases reporting the application of hot-pressing to LATP electrolyte compared to other oxide conductors such as garnets. For this reason, solid state synthesis and hot-pressing cover an important part of the study, with the preparation of the ceramic samples subsequently investigated in terms of structure and surface morphology. XRD analysis allowed us to determine the difference in phase content before and after calcination, pointing out the conditions which led to the evolution of by-products. A limited quantity of impurities acting as a filler can help achieve a higher densification of the ceramic, reducing the influence of grain boundaries and positively affecting the conductivity. SEM observations of the LATP powders after the synthesis revealed a varied morphology with different grain size which eventually have a different effect on the densification.

Evaluations of the chemical process via density functional theory (DFT) were performed to define the metastability range of LATP towards decomposition. The results indicate that an apt choice of the temperature and pressure can decrease the formation energy for LATP, resulting in a limited decomposition and a reduced ratio of impurities. The solid electrolyte manifested an improved room temperature conductivity after calcination at relatively low temperatures.

Author contributions: Daniele Campanella participated in the design of the study, the synthesis of the materials and the final assembly of the cells. He performed the XRD analysis, SEM analysis and electrochemical testing, as well as obtaining and analyzing the experimental data. He was responsible for the writing and the correction of the manuscript and the bibliographic research. Sergey Krachkovskiy performed and provided the results for the NMR analysis and assisted in the article redaction. Cyril Faure and Wen Zhu assisted in the *in situ* XRD analysis. Zimin Feng performed the computational analysis and provided the results and interpretation of the data. Sylvio Savoie and Gabriel Girard were involved in the synthesis of the materials and contributed to the electrochemical testing. Hendrix Demers participated in the SEM analysis of the samples. Ashok Vijh, Chandramohan George and Michel Armand provided contributions to the design of the study and participated to the critical revision of the manuscript. Prof. Daniel Belanger supervised the research project and participated in designing the study. He was also involved in writing, critically reviewing, and revising the manuscript. Dr. Andrea Paolella supervised the study and was directly involved in the interpretation of the experimental data. He participated to the drafting, revising and submission of the manuscript.

3.2. Article 1: Influence of $AlPO_4$ Impurity on the Electrochemical Properties of NASICON-Type $Li_{1.5}Al_{0.5}Ti_{1.5}(PO_4)_3$ Solid Electrolyte

Daniele Campanella[1,2], Dr. Sergey Krachkovskiy[1], Dr. Cyril Faure[1], Dr. Wen Zhu[1], Dr. Zimin Feng[1], Sylvio Savoie[1], Gabriel Girard[1], Dr. Hendrix Demers[1], Dr. Ashok Vijh[1], Dr. Chandramohan George[3], Dr. Michel Armand[4], Prof. Daniel Belanger[2] and Dr. Andrea Paolella[1,2,5*],

[1]Hydro-Québec, Center of Excellence in Transportation Electrification and Energy Storage, Varennes, Québec J0L 1N0, Canada

[2]Université du Québec à Montréal, Département de Chimie 2101, rue Jeanne-Mance, Montréal, Québec, H3C 3P8

[3]Dyson School of Design Engineering, Imperial College London, SW7 2AZ, London, UK

[4]CIC Energigune, Parque Tecnológico de Álava, Albert Einstein, 48, 01510 Vitoria-Gasteiz, Álava, España

[5]Austrian Institute of Technology (AIT), Giefinggasse 4, 1210 Vienna, Austria

* Corresponding authors: andrea.paolella@ait.ac.at

3.2.1 Abstract

Densification of ceramic electrolytes is a key enabler in producing electrolyte pellets for solid-state batteries. This requires understanding the correlation between the starting grain size of electrolytes, chemical phase evolution and degree of compaction which determine ion conductivity and chemical stability of solid electrolytes. We observed an improved densification of LATP at 700 °C, with a total ionic conductivity of 3.45×10^{-4} S cm^{-1} after hot pressing, owing to an optimized crystallite size and presence of $AlPO_4$ impurities. The formation of $AlPO_4$ secondary phases has been proven to be inevitable during the densification process. By combining *in situ* heating X-ray diffraction (XRD), scanning electron microscopy (SEM) and nuclear magnetic

resonance (NMR), we explored the formation mechanism of $AlPO_4$ during the synthesis process of NASICON-type $Li_{1.5}Al_{0.5}Ti_{1.5}(PO_4)_3$ (LATP) electrolyte and we showed the effects of the annealing temperature on the crystal size of the material. Density functional theory (DFT) calculations on the chemical stability of the electrolyte imply a metastable behavior of LATP further enhanced by particle nano-structuring at high temperature. Our results point to facile manufacturing of ceramic electrolytes towards energy dense and safe solid-state battery technology.

3.2.2 Introduction

Lithium batteries represent a promising technology for enabling global electrical mobility via electric vehicles (EVs) (M. Armand & Tarascon, 2008), which can help reduce CO_2 emission from the combustion of gasoline by internal combustion engines (ICEs). To this end requires a widespread deployment of battery technologies without compromising battery safety, reliability, and electrochemical performance. Lithium metal is considered as one of the top alternative anodes for the next-generation of rechargeable batteries owing to its high energy (~4000 mAh g^{-1}) compared to the traditional graphite (~370 mAh g^{-1}). Indeed, when graphite is replaced by metallic lithium at the negative electrode, it allows to deliver specific energies more than double the values of current lithium-ion batteries, when coupled with high performance cathodes. However, in actual practice, the use of lithium metal as an anode with a flammable liquid electrolyte (J. Wang et al., 2018; Q. Zhao et al., 2019) is limited by the formation of lithium dendrites, which may cause battery short circuits and safety issues.

The use of a solid electrolyte represents an alternative because it acts as a physical barrier to prevent short circuits and increase the battery's energy density (in lithium metal batteries). In recent years, a wide range of new solid electrolytes based on polymer (D. Zhou et al., 2019), ceramic (Murugan et al., 2007), or hybrid polymer–ceramic (W. Lee et al., 2019) materials have been proposed in the literature. Among ceramic electrolytes, NASICON structured phosphate (Harada et al., 2020; Z. Yang et al., 2021) based electrolytes $Li_{1.5}Al_{0.5}Ge_{1.5}(PO_4)_3$ (LAGP) (Paolella, Zhu, Xu, et al., 2020; Safanama et al., 2014) and $Li_{1.5}Al_{0.5}Ti_{1.5}(PO_4)_3$ (LATP) (Soman et al., 2012) have garnered much attention. Their high ionic conductivity (around 10^{-4} S cm^{-1}) (Thokchom et al., 2008), high voltage stability (up to 5 V) and water stability (M. Zhang et al.,

2013) make them versatile enough for innovative battery chemistries such as Li-O_2 (H. Song et al., 2020), Li-S (N. Li et al., 2014) and all solid-state batteries (ASSBs). Nonetheless, the development of full NASICON electrolyte-based battery is still limited to 1 mm-thick pellets and low C-rates (charge/discharge currents, C/30) (Paolella, Zhu, Bertoni, Perea, et al., 2020a). The use of ceramic in hybrid ceramic-polymer configuration allows to reduce the thickness, thus increasing the energy density, although the contribution of the ceramic to lithium ions diffusion is uncertain(Commarieu et al., 2018).

A high temperature is required for synthesizing LATP as shown by Pogosova et al. (Pogosova et al., 2020), who obtained solid-state LATP by the annealing of a ball milled mixture of Li_2CO_3, $Al(NO_3)_3{\cdot}nH_2O$, TiO_2, $(NH_4)H_2PO_4$ for 6 h at 850 °C. Arbi et al. (Arbi et al., 2015) reported a LATP synthesis by heating Li_2CO_3, $(NH_4)_2HPO_4$,Al_2O_3 and TiO_2 at 950 °C. Solution-based syntheses, such as sol-gel and co-precipitation methods, which are usually characterized by milder conditions, still require temperatures above 800 °C to obtain pure LATP(C. Yu, Choi, et al., 2020). Additionally, further densification and annealing steps are required to improve the inter-particle contacts and increase the density. These additional steps are often carried out at even higher temperatures than those employed for the synthesis: as for example Oda et al. densified $Li_{1.5}Al_{0.5}Ti_{1.5}(PO_4)_3$ pellet at 1000 °C to achieve a 90% density and an ionic conductivity of 7.0×10^{-4} S cm^{-1} at 30 °C. The strict synthesis conditions open the way to possible side reactions occurring at high temperatures, which may produce some impurities poor in oxygen, such as $LiTiP_2O_7$. Formation of $AlPO_4$ impurities has been observed after sol-gel synthesis followed by high temperature sintering at 900 °C, possibly due to partial loss of lithium via evaporation (Tolganbek et al., 2020). Acetic acid was used by Liu et al. (Y. Liu et al., 2019) as sintering aid to reduce densification temperature to 650 °C, and finally achieve a final conductivity of 8.04×10^{-5} S cm^{-1} at room temperature (RT). To sum up, the densification of electrolytes at low temperatures has been limited to date owing to low conductivity, high amount of impurity and presence of off-stoichiometry phases, which present major roadblocks to the manufacture of solid electrolytes.

In this work, we investigated the formation mechanism of $AlPO_4$ impurity during hot press densification of LATP in a sintering temperature range between 550 and 950 °C. By using *ex situ* and *in situ* heating X-rays diffraction (XRD), scanning electron microscopy (SEM) and nuclear magnetic resonance spectroscopy (^{7}Li and ^{27}Al), we shed new light on the mechanism of

densification of LATP ceramics under pressure and optimization of the conditions to obtain LATP that has high ion conductivity and density.

3.2.3 Results and Discussions

3.2.3.1. Phase and Crystal Size Influence on LATP Densification

High-temperature *in situ* X-ray diffraction (XRD) was used to monitor the stepwise formation of the LATP phase in order to understand the reactivity of TiO_2 (rutile) precursor and its effect on the kinetics of the phase formation (see **Figure 3.1a**). The process was carried out by heating a mixture of Li_2CO_3, Al_2O_3, TiO_2 (rutile) and $(NH_4)_2HPO_4$ to 700 ^oC at a temperature rate of 3 °C per minute. For temperatures above 100 ^oC, an initial decomposition of $(NH_4)_2HPO_4$ to $(NH_4)H_2PO_4$ can be observed, with the release of NH_3 and a new phosphate phase. The reaction of Li_2CO_3 with hydrogen ammonium phosphate brought to the formation of Li_3PO_4 according to ($2(NH_4)_2HPO_4 + Li_2CO_3 \rightarrow Li_3PO_4 + 4NH_3 + 3H_2O + 3CO_2$). First detection of LATP phase was observed at a temperature as low as 400 ^oC, with a gradual increase in the relative peak intensities with the increase of temperature, reaching its maximum at 700 °C. This points out that the kinetics of LATP phase evolution is remarkably fast as the phase formation is almost at full completion upon reaching the temperature ~700 ^oC (**Figure 3.1a**, red curves). After cooling, the final sample contains LATP as a main phase, but traces of Li_3PO_4 and $Li_4P_2O_7$ were detected as minor phases (**Figure 3.1a**, black curves). The rapid formation kinetics of LATP and its phase stabilization (upon cooling) observed during the heating step of the *in situ* XRD revealed the possibility to synthesize the LATP at lower temperatures with an adequate phase purity despite the presence of impurities as minor phases. Subsequently, three distinct LATP intermediates were densified via hot-pressing under inert Ar atmosphere at 750 °C. The different samples consisted of LATP powder synthesized at 550° C, 700 °C and 950 °C (named LATP550, LATP700 and LATP950, respectively, and the hot-pressed pellets are named HP-LATP550, HP-LATP700 and HP-LATP950). The different powders also served to draw a comparison between samples. The ionic conductivities of the three different pellets were evaluated by electrochemical impedance spectroscopy (EIS) performed in a temperature range between 10 and 80 °C (**Figures 3.1b-c**). The associated Nyquist impedance plots (**Figure 3.1b**) show two semicircles, the first one of which appears at high frequencies, whereas the second one is observed at lower frequencies. Previous

results reported in literature for ceramic electrolytes were not able to associate the second semicircle to a specific electrochemical phenomenon (La Monaca et al., 2022; Tenhaeff et al., 2014), thus the equivalent circuit chosen to represent the electrochemical system is reported in **Figure 3.1b**. The depressed semicircles are represented with a combination of resistors (R) and constant phase elements (CPE) instead of pure capacitors. R_0 is the intrinsic resistance of the circuit; R_{gb} and CPE_{gb} represent the grain boundaries contribution to ionic transport, R_{low} and CPE_{low} indicate the low-frequency semicircle and eventually CPE_{el} is related to the electrode double layer. Hot-pressed samples at 550 and 750 °C display relatively low values of resistance (about 650 Ω) which is significantly lower than the one expressed for the sample densified at 900 °C, showing a semicircle amplitude of about 6000 Ω, about 10 times wider than the other samples. Data fitting of the Nyquist plots in accordance with the equivalent circuit previously described allowed to derive the total ionic conductivity, the values of which are represented by the Arrhenius plots in **Figure 3.1c**. In the working temperature range, the ionic conductivities of the three pellets are in the order of $\sigma_{700} > \sigma_{550} > \sigma_{950}$, where the conductivity of HP-LATP700 is slightly higher than that of HP-LATP550. At room temperature, we obtained the following total conductivities: $\sigma_{700} = 3.45 \times 10^{-4}$ S cm^{-1}, $\sigma_{550} = 2.44 \times 10^{-4}$ S cm^{-1} and $\sigma_{950} = 3.7 \times 10^{-5}$ S cm^{-1}.

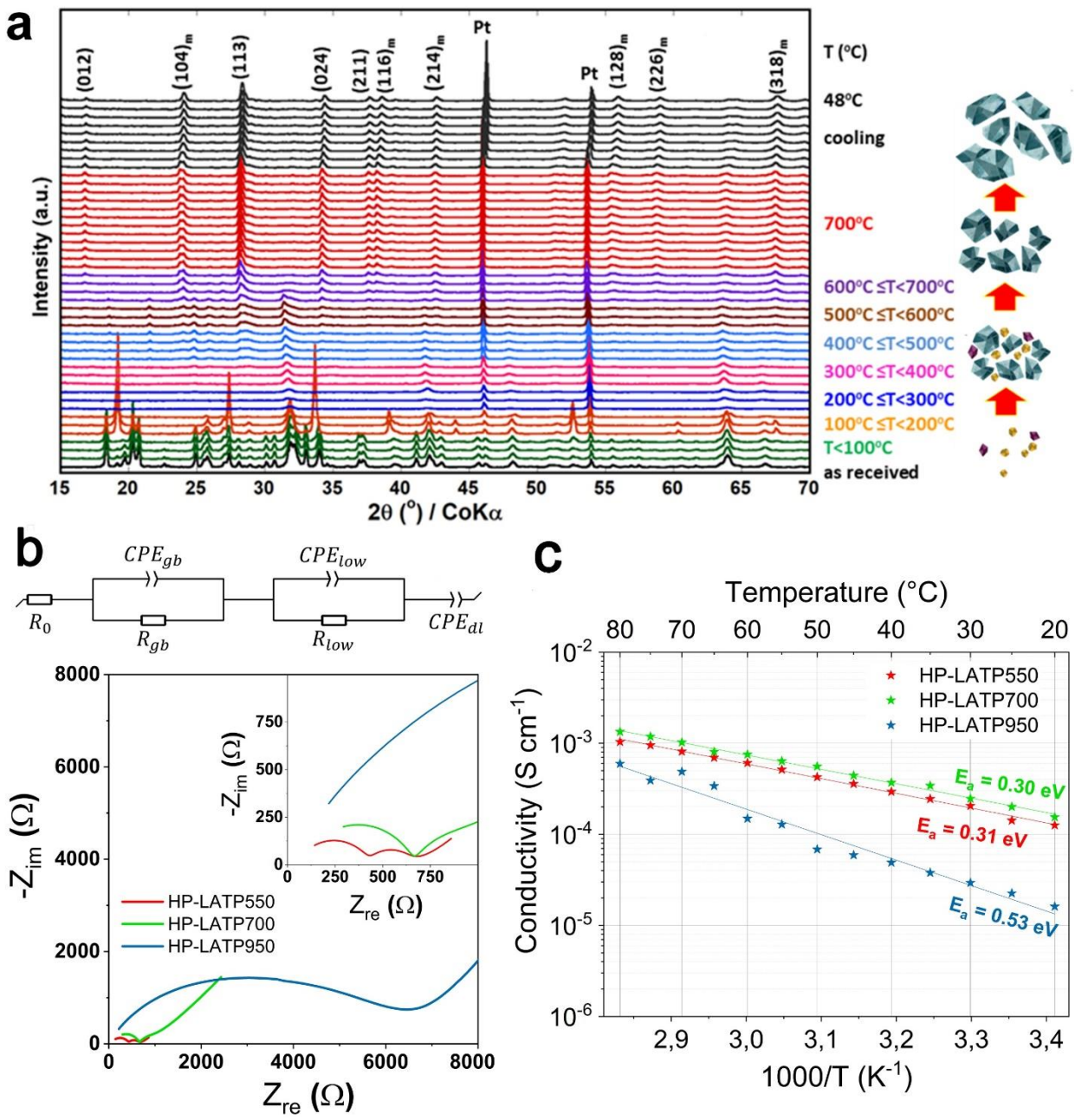

Figure 3.1: (a) Evolution of X-ray diffraction (XRD) spectra during heating of precursors of $Li_{1.5}Al_{0.5}Ti_{1.5}(PO_4)_3$ (LATP). The (hkl) of LATP are labelled on the peaks, the subscript "m" of the (hkl) indicates it contains multiple lines. Platinum (Pt) is from crucible; (b) Equivalent circuit and Nyquist plots at room temperature for the three LATP samples synthesized at 550, 700 and 950 °C. All the samples were densified via hot-pressing at 750 °C; (c) Arrhenius plots of total ionic conductivity of the three LATP samples.

The values of total conductivity for HP-LATP950 were significantly lower than those of HP-LATP550/HP-LATP700, so a structural characterization was performed in order to understand the reasons behind such a discrepancy. **Figure 3.2** reports the XRD patterns of the samples before and after hot pressing, as well as the average crystallite sizes estimated via the Halder-Wagner method implemented in the PDXL2 (Rigaku). Before performing the hot pressing, LATP550 shows the presence of a series of peaks corresponding to several phases, including the desired NASICON phase $Li_{1.5}Al_{0.5}Ti_{1.5}(PO_4)_3$, as well as $LiPO_3$, Li_3PO_4, $AlPO_4$ and unreacted precursors (mainly TiO_2 rutile and Li_2CO_3). After hot pressing, NASICON $Li_{1.5}Al_{0.5}Ti_{1.5}(PO_4)_3$ is shown to be the main phase in the sample; with the presence of $AlPO_4$ as main impurity and other minor phases (**Figure 3.2a**). LATP700 sample after hot pressing displays an increased amount of $AlPO_4$ and other impurities (**Figure 3.2b**) compared to LATP550. The reference LATP950 sample is an almost pure phase of $Li_{1.5}Al_{0.5}Ti_{1.5}(PO_4)_3$ before and after hot pressing, although negligible amounts of unidentified impurities formed during the hot-pressing process. The sharp diffraction peaks in the spectra, reported in **Figure 3.2c**, point out the presence of large well crystalized grains in both LATP950 and HP-LATP950, which are also indicated by the high average crystallite size and are further confirmed by SEM observations (see **Figure 3.3)**. The narrower peaks for LATP950 are highlighted in **Figure 3.2d**, which also displays the variation in intensity of the relative peaks corresponding to the secondary $AlPO_3$ phase. **Figure 3.2e** shows the ^7Li and ^{27}Al NMR spectra of the three LATP samples after hot pressing. ^7Li spectra display a quadrupolar resonance with isotropic shift δ_{iso} = 0 ppm and quadrupolar constant C_Q = 45 kHz, which perfectly corresponds to LATP spectra previously reported in literature (Arbi et al., 2015; Epp et al., 2015). It is notable, however, that line broadening of the signals increases from 400 Hz in HP-LATP950 sample, to 750 Hz (HP-LATP700) and to 900 Hz (HP-LATP550). We did not observe any differences in longitudinal (T_1) and transverse (T_2) relaxation times measured at static conditions (T1 = 60 ms and T2 = 4 ms for each sample at 50 °C). Therefore, the difference in line broadening could be explained by the increased magnetic field inhomogeneity associated with the smaller particle size in the samples synthesized at lower temperature (**Figure 3.3**) and, therefore, with the higher surface/bulk ratio in them. In the ^{27}Al MAS NMR spectra the main peaks observed at δ = -15 ppm correspond to aluminum atoms in octahedral coordination (Al_O) which are related to the NASICON phase, however, the presence of a secondary peak at δ = 40 ppm is visible in the spectra

of HP-LATP700 and HP-LATP550 samples and it is assigned to tetrahedral Al (Al_T) associated with the secondary $AlPO_4$ phase (Wong et al., 1998).

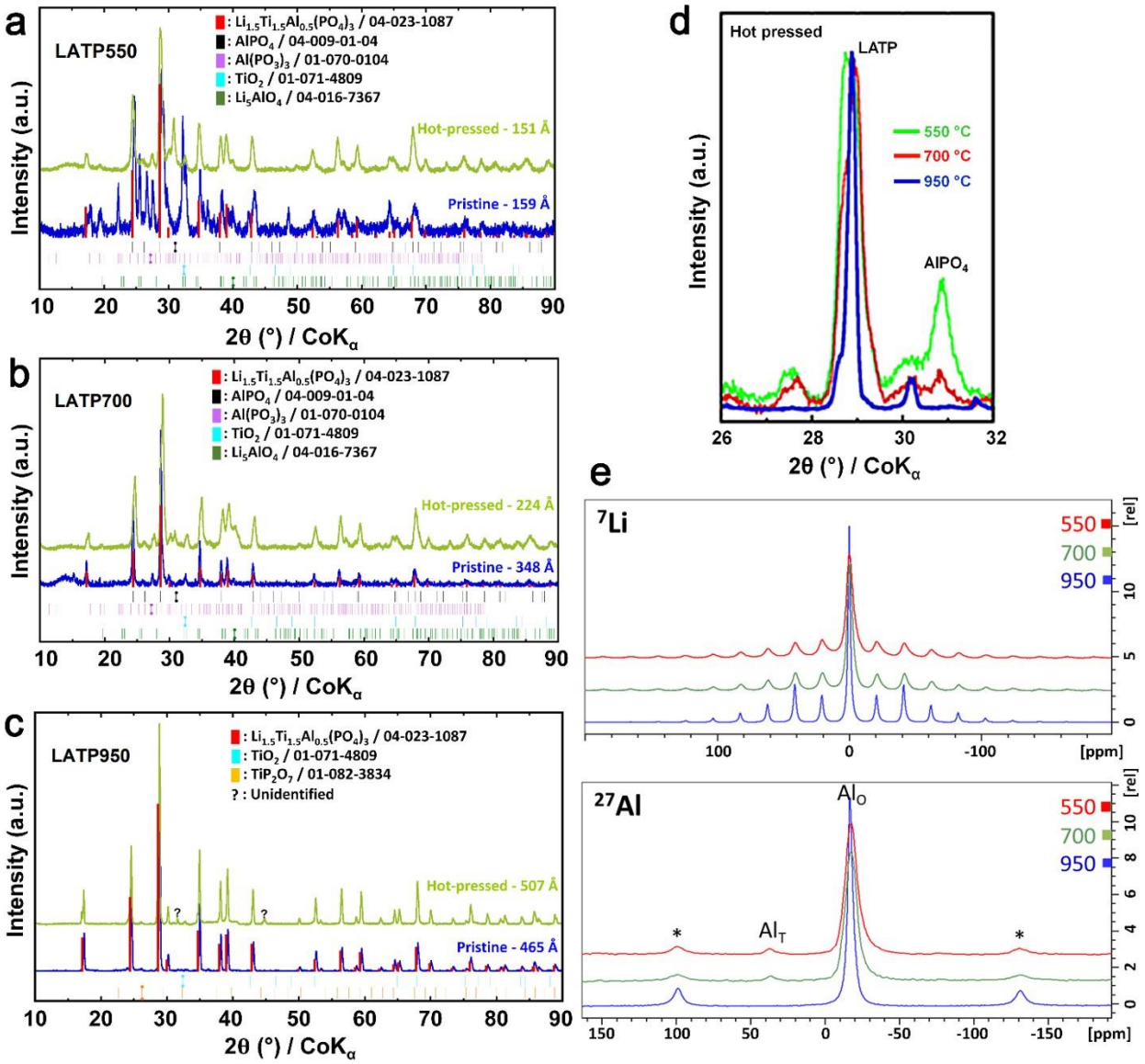

Figure 3.2: (a-c) X-ray diffraction (XRD) patterns of LATP precursors synthesized at (a) 550 °C (LATP550); (b) 700 °C (LATP700); (c) 950 °C (LATP950) and corresponding 750 °C hot pressed ceramics. The average crystallite sizes are labelled corresponding to their patterns; ↕ Indicates the strongest relative peak of the phase; (d) zoomed XRD spectra showing the $AlPO_4$ phase in different pellets. (e) ^{7}Li and ^{27}Al NMR spectra for LATP550, LATP700 and LATP950 after hot press.

In order to better understand the distribution of impurities in the materials and obtain more insight about the difference in the conductivities of the three intermediates, SEM measurements were performed to analyze the microstructure of the annealed powders and hot-pressed pellets. Micrographs of the three powders are shown in **Figure 3.3a**, which clearly shows that secondary particles of LATP550 consist of a large amount of nanometric sized particles. On the other hand, LATP950 particles contain larger well-crystallized grains, in the order of 2-10 μm and LATP700 powder aggregates lie in between the two. The nanoparticles of LATP550 powder facilitated the sintering process due to their large sintering stress and large surface area. In addition, the small LATP crystals, which are formed during the hot pressing, also help facilitating the densification, therefore resulting in a higher final density for the pellet. Conversely, the sintering of large-grained LATP950 powder is a slower process because of the reduced sintering stress and reduced particle surface, thus the obtained pellet shows a series of large pores and manifests a low density. The density of the HP-LATP700 pellet is intermediate between HP-LATP550 and HP-LATP950. **Figure 3.3b** reports the back-scattered electron (BSE) images and the corresponding phase distribution maps, with red and blue representing impurity phases and pores. Analysis of the exposed areas allowed to obtain values of apparent density of about ~ 100, 81 and 75% for HP-LATP550, HP-LATP700 and HP-LATP950, respectively.

The lithium diffusion in the analyzed samples was investigated using pulsed-field gradient nuclear magnetic resonance (PFG NMR) technique (K. S. Han et al., 2021; Price, 1998). Short-duration magnetic field gradient pulses are introduced into spin-echo sequence to detect particles displacement in PFG NMR experiments. The resulted signal intensity (I) depends on parameters of the applied gradients and the self-diffusion coefficient (D) of the observed species by the following equation: $I = I_0 e^{-BD}$, where I_0 is the NMR signal intensity without gradients application and B represents experimental conditions as: $B = \gamma^2 g^2 \delta^2 \left(\Delta - {}^{\delta}/_{3}\right)$, with γ – gyromagnetic ratio of observed nuclei, g and δ – strength and duration of the gradient pulses, Δ – delay between the encoding and the decoding gradients. An example of a logarithmic plot of signal attenuation vs. B-factor obtained for HP-LATP950 at 50 °C is shown on **Figure 3.4a**. Double exponential fit is required to accurately fit the data, meaning that lithium transport in LATP

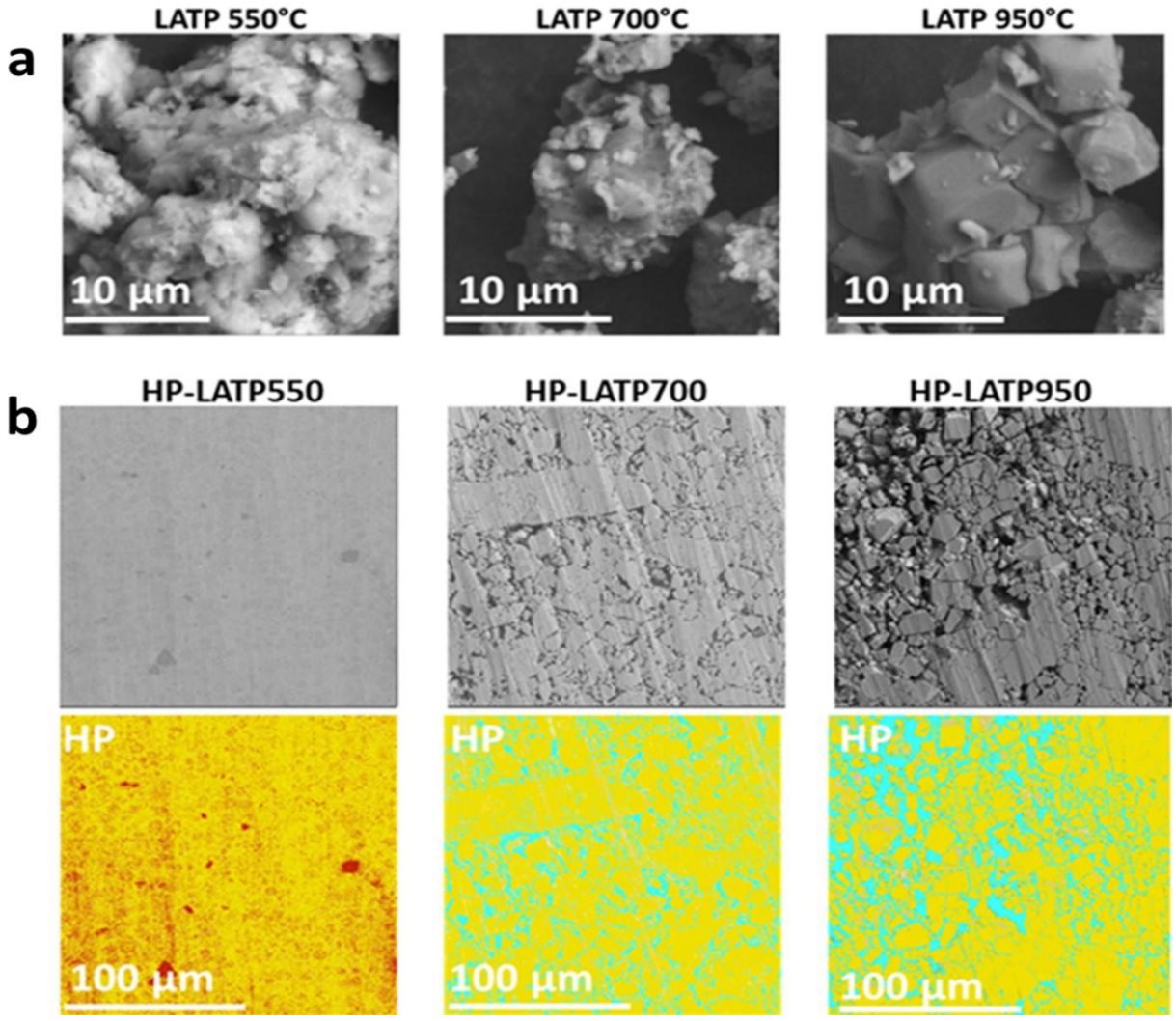

Figure 3.3. (a) Scanning electron microscopy (SEM) micrographs of Li1.5 Al0.5 Ti1.5(PO4)3 (LATP) powders heated at 550°C, 700°C and 950°C; (b) Back-scattered electron (BSE) images of LATPs hot pressed at 750°C with precursor powders treated at different temperatures and the corresponding phase distribution maps. Yellow: LATP; red: impurities; blue: pores.

consists of two processes. The relative ratio of fast diffusing to slower diffusing component is 1:4. However, the intensity of the slower component can be suppressed because of the fast signal relaxation. It would be better to combine PFG NMR experiment with spin-spin relaxation measurements to accurately estimate population of each component (Javed et al., 2017). The existence of two distinct Li^+ elementary hopping processes with similar activation energy of 0.16-0.17 eV and estimated diffusion coefficients of 3×10^{-13} and 5×10^{-12} m^2 s^{-1} at 30 °C has been demonstrated previously for LATP by utilization of NMR spin-lattice relaxometry (SLR) (Epp et

al., 2015). While SLR is sensitive to ion dynamics on the angstrom length scale and provides information regarding ion hopping between neighboring Li sites, PFG NMR operates in a micrometer range (the mean squared displacement (MSD) of Li^+ during the experiment ranges in between 0.5 – 1 μm), which is comparable to the average size of the crystallites and allows to estimate grain boundary effect on Li^+ transport.

Diffusion coefficients of Li^+ for all three samples in the temperature range from 20 to 50 °C are listed in **Table 3.1**, while the Arrhenius plots of ln(*D*) vs. $(k_BT)^{-1}$ are shown in **Figure 3.4b**. The crystallite size of HP-LATP950 is about 10 times larger than MSD of Li^+ during the PFG NMR experiment. For this reason, the measured data mostly reflect Li^+ movement inside the bulk NASICON structure while an influence of boundary effect between particles in the sample is not detected. This limitation becomes evident in comparison of lithium diffusion coefficients obtained by PFG NMR with the ones estimated from the ionic conductivity σ via the Nernst–Einstein equation: $D_\sigma = \sigma \frac{k_B T}{c q^2}$. Here, k_B is the Boltzmann constant, T is the temperature, c is the concentration of charge-carriers in units of particle number per unit volume, and q is the charge of the carriers. For example, D_σ at 50 °C is expected to be 1.0×10^{-12} m^2 s^{-1}, which is lower than the PFG NMR measured values of HP-LATP950, indicating a poor contact between crystals in the densified pellet (**Figure 3.3**). In samples with a smaller crystallite size (HP-LATP700 and HP-LATP550), the influence of grain boundaries on PFG NMR measured diffusion coefficients becomes significant, decreasing the measured values of Li diffusivity inside secondary particles. Higher ionic conductivity of these samples in comparison with HP-LATP950 could be explained by a better contact between the particles, which apparently overcomes the evident advantage given by faster Li transport within larger grains.

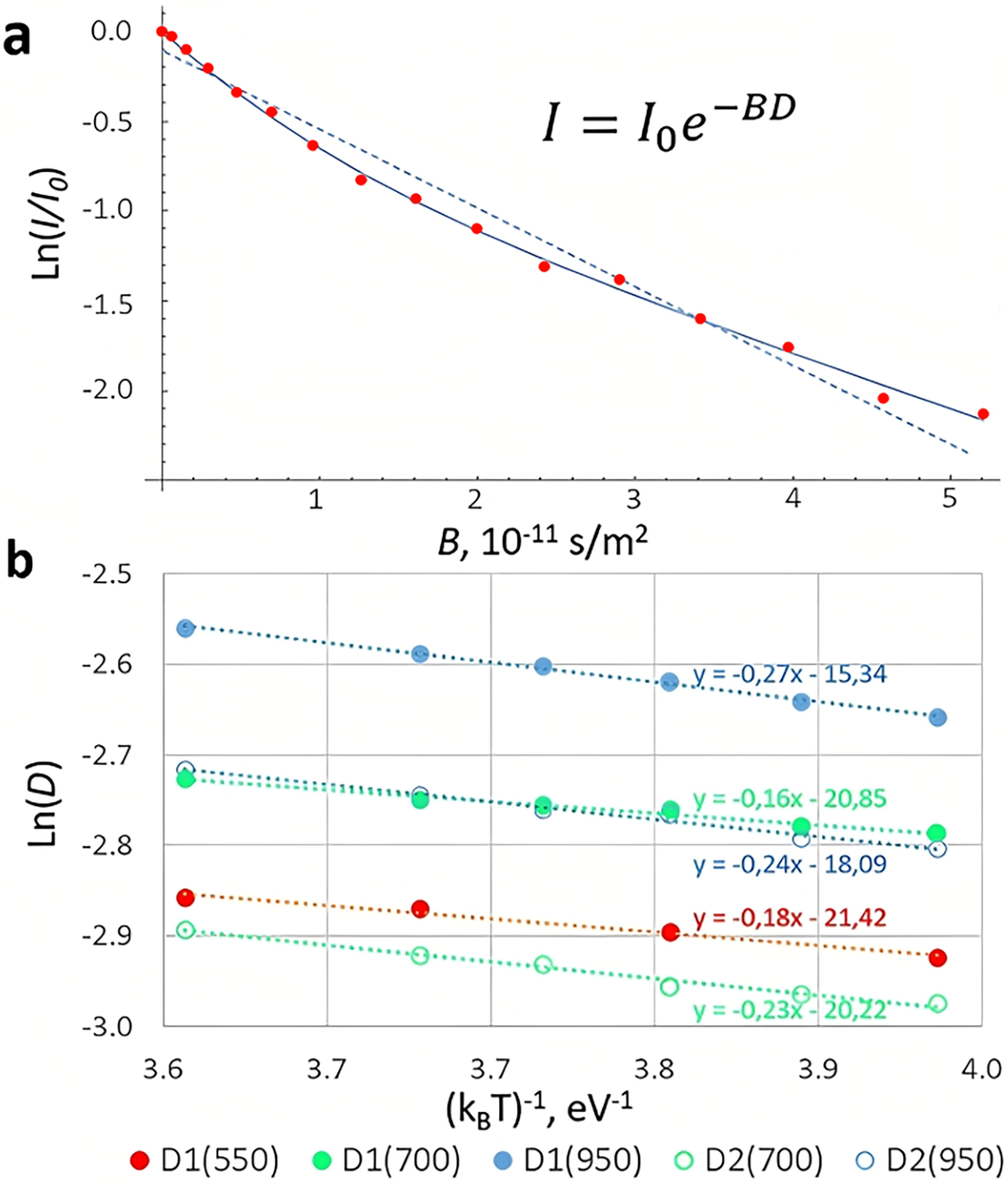

Figure 3.4 (a) An example fit of a pulsed-field gradient nuclear magnetic resonance (PFG NMR) signal attenuation curve for HP-LATP950 sample at 50 °C. Experimental points are shown with red dots. Single- and double-exponential fits are shown with dashed and solid blue lines respectively. (b) Arrhenius plots of measured diffusivities. Lines slopes correspond to activation energy expressed in eVs.

Sample		Temperature, °C						E_a, eV
		20	25	30	35	40	50	
950	D_1, 10^{-12} m^2 s^{-1}	4.7±0.2	5.6±0.3	6.9±0.3	8.3±0.4	9.5±0.5	12.6±0.6	0.27±0.03
	D_2, 10^{-12} m^2 s^{-1}	1.1±0.1	1.2±0.1	1.6±0.1	1.7±0.1	2.0±0.1	2.7±0.1	0.24±0.02
700	D_1, 10^{-12} m^2 s^{-1}	1.3±0.1	1.4±0.1	1.7±0.1	1.8±0.1	1.9±0.1	2.4±0.1	0.16±0.02
	D_2, 10^{-12} m^2 s^{-1}	0.20±0.01	0.22±0.01	0.24±0.01	0.31±0.02	0.34±0.02	0.45±0.02	0.23±0.02
550	D_1, 10^{-12} m^2 s^{-1}	0.33±0.02	-	0.44±0.03	-	0.57±0.04	0.64±0.04	0.18±0.03
	D_2, 10^{-12} m^2 s^{-1}	N/A*	-	N/A*	-	N/A*	N/A*	N/A*

Table 3.1 Lithium diffusion coefficients measured by pulsed-field gradient nuclear magnetic resonance (PFG NMR) and calculated activation energy. *Only one component was unambiguously identified for HP-LATP550 sample, because of fast signal relaxation and the limitations for the maximum gradient strength.

As for the PFG NMR measured activation energy, it is interesting that the values match very well with the evaluated activation energy of ion hopping between neighboring lithium sites extracted by SLR (Epp et al., 2015). That points out that E_a in densified secondary particles is mostly determined by ion transport through grains and not along the grain boundaries, even though the latter slows down the average Li diffusion. A decrease of the grain boundary effect on activation energy of Li transport in solid electrolytes after mechanical compression has been also reported by Adeli et al. (Adeli et al., 2021). The structure of Li^+ ion pathways have a close relationship with the diffusive diffraction behavior in which lithium cations experience multiple-time collision–diffraction processes with other ions in the crystal (Hayamizu & Seki, 2017). PFG NMR data suggests that this process is more temperature dependent than the Li^+ transfer between adjacent crystallites. However, when comparing the activation energy derived from the conductivity of pellets to PFG NMR measured activation energy of Li transfer inside LATP

crystals, one can see that much larger gaps between the secondary particles essentially double the value. As shown above, HP-LAPT950 pellet manifests the lowest value of conductivity and the highest activation energy among the analyzed samples. We assume that the large pores in the densified pellet reduce the contact area available for ion transfer between the crystals. The high porosity of the sample lengthens the diffusion path and slows down the ion transport through the pellet. In contrast, higher density of the samples with smaller grains provides larger contact area between the secondary particles and enhances the ionic conductivity. In this scenario $AlPO_4$ assumes a more important role as an inert filler: the larger presence of phosphate impurities can disrupt the contact between active material particles in a similar way as the large pores do, and this is reflected in a negative way on the ionic conductivity. The microstructure of HP-LATP700 seems to have a balance between density and impurity, therefore it demonstrates the best performance of all the three hot pressed samples.

3.2.3.2. The Influence of LATP from Temperature and Pressure from Density Functional Theory

To support the observation above, we performed a density functional theory analysis to quantify the values of pressure associated with high temperature influencing the densification. The hot-pressing process is an indispensable step in ensuring the optimal densification of the pellets, and our calculations show that the working pressure should be accompanied by elevated temperature in order to well-manage and control the impurity level in the material. We consider the reaction of LATP decomposition:

$$Li_{1.5}Al_{0.5}Ti_{1.5}(PO_4)_3 \rightarrow 0.25\ Li_3PO_4 + 0.75\ LiTi_2(PO_4)_3 + 0.5\ AlPO_4$$

and calculate the free energy cost of this decomposition with or without pressure at elevated temperatures. Evidently, a higher cost of free energy during decomposition shifts the equilibrium towards the l.h.s of this reaction and is favorable.

According to the calculated results (see **Table 3.2**), increasing pressure alone can allow for the formation of LATP from its precursors to be less favorable, in the sense that the formation enthalpies at higher pressure becomes less than that at zero pressure (at 750 °C, 0.35 meV per atom less at 1 kbar than at 0 kbar). Nevertheless, increasing temperature can well compensate for this

decrease in enthalpy. As we can see from **Table 3.2**, the increase of formation free energy is roughly 10 times as that of the decrease due to pressure at 1 kbar. For the typical pressure and temperature used for hot pressing, the issue of decomposition due to excessive pressure is negligible. Although the formation of $AlPO_4$ is inevitable, the ionic conductivity of LATP can be maximized by tuning the temperature of sintering and particle size of pristine particles. In our experiments we effectively observed that maximum amount of $AlPO_4$ was detected in LATP550 sample, which had the smallest pristine particles, while the highest ionic conductivity was observed for the LATP700 sample. The densification of three intermediate LATP samples having different crystallite sizes (~2-10 µm, ~1 µm and < 100 nm) revealed the mechanistic pathways taking place in LATP, which led to various degrees of crystal densification and amounts of inert $AlPO_4$ impurity.

T	$G_{p=0}$	$G_{p=1}$	$G_{p=1} - G_{p=0}$
0	8.80	8.58	-0.21
750	11.47	11.12	-0.35
1000	12.30	11.91	-0.39

Table 3.2 Free energy of decomposition (T=temperature in K, P=pressure in kbar, free energy in meV per atom.

3.2.4 Conclusions

We investigated the formation mechanism of $AlPO_4$ impurity during hot pressing densification of NASICON type $Li_{1.5}Al_{0.5}Ti_{1.5}(PO_4)_3$ (LATP) electrolyte following the chemical phase evolution of LATP via *in situ* heating X-ray diffraction, scanning electron microscopy and nuclear magnetic resonance. $AlPO_4$ was detected as main secondary phase and its formation is inevitable during sintering. Interestingly LATP electrolytes synthesized at low temperatures (550 and 700 °C) still exhibit high ionic conductivity; in particular, the samples synthesized at 700 °C shows values up to 3.45×10^{-4} S cm^{-1} at room temperature despite the presence of $AlPO_4$ impurity. The material appears to have benefitted from an optimal combination of the densification degree, $AlPO_4$ impurity amount and porosity. We have also exposed the chemical stability of NASICON during hot-pressing via density functional theory (DFT) calculation which presents a metastable

behavior of LATP at high temperature that is enhanced by particle nanosizing. Our results represent an important step in further development of solid electrolytes with tailored ionic conductivity and chemical stability for solid-state battery technology.

3.2.5 Experimental Section

M.1 Materials and Solid-state synthesis: Synthesis precursors Li_2CO_3, Al_2O_3, $(NH_4)_2HPO_4$ and TiO_2 (rutile) were purchased from Sigma Aldrich. Following a standard solid-state synthesis, stoichiometric amounts of the precursors were ball milled for 15 minutes in a SPEX mixer and subsequently annealed at 550 °C for 2 h. The material resulting from this first thermal treatment is identified as LATP550. An additional annealing of LATP550 for 2h at 700 °C and 950 °C led to the preparation of two modified samples, respectively named LATP700 and LATP950. After the first thermal step, about 0.75 g of powder of all distinct samples was hot pressed at 750 °C for 1 h. The process was carried on in a 16 mm diameter titanium–zirconium–molybdenum (TZM) die by applying a pressure of 56 MPa. The hot-pressed samples were named respectively HP-LATP550, HP-LATP750 and HP-LATP900, depending on the temperature of the first annealing step.

M.2 Imaging and chemical mapping: Scanning electron microscopy (SEM) images were acquired using annular dark field mode (ADF-STEM) on a JEM-2200FS transmission electron microscope operating at 200 kV (JEOL, Japan). Chemical mapping was performed using an energy dispersive X-ray spectrometer (EDXS) in the scanning mode. Cross-sections of the hot-pressed samples were obtained using an Ar Ion Milling IM4000 Plus (Hitachi, Japan) system with an ion beam energy of 6 kV using a fast 30º rotation for 4 h. The cross-section surfaces were analyzed using a (SEM) Lyra 3 (TESCAN) scanning electron microscope and the elemental composition was obtained using windowless energy dispersive spectrometer (EDS) Extreme (Oxford instruments). The micrograph and X-ray map were acquired at an accelerating voltage of 5 and 10 kV, a probe current of 500 pA, and a working distance of 10 mm. The phase distribution in **Figure 3.4b** was obtained from a compositional (BSE) image. A range of pixel intensity is manually selected for each phase and the Tescan software tool Object Area is used to calculate the image pixel fraction of each phase and a phase image.

M.3 X-Ray diffraction: A mixture of Li_2CO_3, Al_2O_3, TiO_2 (rutile) and $(NH_4)_2HPO_4$ was heated at a rate of 3 ˚C per minute to 700 ˚C and held at temperature for 2 h, then cooled to room temperature in air atmosphere. High temperature X-ray diffractometer (CoK_α radiation, Smartlab, Rigaku) was employed to monitor the phase formation process of $Li_{1.5}Al_{0.5}Ti_{1.5}(PO_4)_3$ (LATP) from above precursors. The scanning step is 0.04°, and the speed is 6.14°/min.

M.4 Ionic conductivity: In order to perform the electrical conductivity measurements, LATP powders were hot-pressed between two thin carbon paper discs. After densification at 750 °C, the electrolyte pellets were sandwiched between stainless steel discs inside a coin cell. Electrochemical impedance spectroscopy (EIS) measurements were performed in a temperature range between 20 and 80 °C (5 ºC step) with a BioLogic VMP-300 potentiostat working with an AC amplitude of 5 mV and a frequency range of 250 kHz to 10 mHz at 0.0 V versus open circuit voltage (OCV).

M.5 Density functional theory computation: The density functional theory (DFT) calculations of LATP and its precursors were carried out using VASP with the projection augmented wave scheme. Perdew-Burke-Ernzerhof exchange-correlation functional was used. The energy cut-off was set to 520 eV. The *k*-points in Brillouin zone were set so that the average *k*-point density is 1.7×10^{-5} per $Å^{-3}$. The free energy was calculated assuming quasi-harmonic approximation. Force constants were obtained via frozen-phonon method as implemented in VASP and free energy calculation was performed using the Phonopy calculation package.

M.6 Nuclear Magnetic Resonance (NMR): All NMR experiments were performed on a 500 MHz WB Bruker AVANCE NEO NMR spectrometer. ^7Li and ^{27}Al magic angle spinning (MAS) NMR spectra were acquired using a 4 mm triple resonance probe. 16 scans with a π/2 pulse of 3 μs and a relaxation delay of 30 s were collected at the MAS of 4 kHz for ^7Li NMR. 64 scans with a π/2 pulse of 3 μs and a relaxation delay of 10 s were collected at MAS of 15 kHz for ^{27}Al NMR. ^7Li NMR diffusion measurements were done using a Diff50 probe and 8 mm double resonance ^7Li-^1H/^{19}F RF insert in a temperature range from 20 °C to 50 °C. To determine the measuring conditions, ^7Li T_1 and T_2 were observed by standard inversion recovery and Carr-Purcell-Meiboom-Gill (CPMG) pulse sequences, respectively. A stimulated echo with longitudinal eddy current delay pulse sequence was used for the measurement. The gradient pulse

was in the range of 2.1 - 2.7 ms and the diffusion time was in the range of 30 - 50 ms depending on the temperature. The gradient strength was varied in 16 equidistant steps from 100 G cm^{-1} to 2500 G cm^{-1}.

3.2.6 Acknowledgments

This research was financially supported by Hydro-Quebec, Ministry of Economy and Innovation, Quebec Government and Mitacs, for a fellowship to D.C. The authors want to thank Alina Gheorghe Nita, Daniel Clément and Dr. Chisu Kim of CEETSE for their help. C.G. acknowledges the Royal Society, London for an URF (UF160573)

Keywords

$AlPO_4$, Densification, LATP, Impurities, Solid electrolytes

CHAPTER IV
METASTABLE PROPERTIES OF GARNET TYPE $Li_5La_3Bi_2O_{12}$ SOLID ELECTROLYTE TOWARDS LOW TEMPERATURE PRESSURE-DRIVEN DENSIFICATION

4.1. Introduction

In the following chapters the scope of the work is shifted from NASICONs to garnet-type electrolytes. The features of this family of electrolytes are described more in detail in Chapter I and the methods employed for enhancing their physical properties are presented as well. Chapter IV focuses specifically on the garnet $Li_5La_3Bi_2O_{12}$ (LLBO), which has been chosen because of the lower temperatures required for its synthesis compared with other garnets. The aim of the investigation is to determine the consequences of hot-press sintering on the solid electrolyte and if it is possible to tune the densification to achieve better electrochemical features. Reports on the application of hot-pressing to garnets are limited in literature, more specifically on LLBO, therefore this study offers an original perspective on the subject. Hot-pressing permits a low temperature densification of the ceramic, enabling electrochemical properties comparable to those of the material fabricated with conventional high-temperature methods, but without the need for such strict conditions. The study delved deeper in the synthesis optimization, aiming to improve the process and produce a high-performance material. A relevant result of the investigation involves the metastable behavior of LLBO with respect to decomposition: increasing the calcination temperature generates a higher concentration of impurities which is observed by SEM imaging and EDS analysis. The elemental distribution points out a phase segregation in agreement with the assumed decomposition. Amore precise evaluation on the decomposition phenomenon is undertaken using DFT calculations and the results point out a correlation between the applied pressure to the sample and the decomposition. For a more intense external pressure, the energy of decomposition increases as well and the reaction becomes less spontaneous, stabilizing the material. Another important section of the study concerned the use of LLBO as additive for garnet LLZO during the sintering process. With this artifice, the densification of LLZO can be obtained at significantly lower temperatures than the usual ones for ceramic powders, and the final material

manifests a conductivity comparable with the conventional high-temperature garnets with a minimum addition of LLBO. The densification conditions affect Li ion diffusion in the materials, with a more prominent effect for LLBO, which shows higher Li diffusion coefficients for higher densification temperatures. This indicates a more intimate contact between the particles promoted by the sintering temperature, which is also reflected by the higher density of the pellets.

Chapter published in Journal of Materials Chemistry A, **2023**, 11 (1), 364-373

Author contributions: Daniele Campanella participated in the design of the study, the synthesis of the materials and the final assembly of the cells. He performed the XRD analysis, SEM analysis of the powders and electrochemical testing. He also gathered, analyzed, and interpreted the experimental data. He was responsible for the writing and the correction of the manuscript and the bibliographic research. Sergey Krachkovskiy performed and provided the results for the NMR analysis and assisted in the article redaction. Giovanni Bertoni performed the TEM analysis and helped with the interpretation of experimental results. Gian Carlo Gazzadi performed the FIB procedure to obtain the cross-sections of the samples. Maryam Golozar and Shirin Kaboli helped performing the cross-section SEM analysis of the samples and provided the experimental results of the tests. Sylvio Savoie, Gabriel Girard, and Alina Gheorghe Nita aided in laboratory procedures for the synthesis of the materials. Kirill Okhotnikov and Zimin Feng performed the computational analysis and DFT calculations and provided the results and the interpretation of the experimental data. Raynald Gauvin participated to the SEM analysis of the samples and the final redaction and review of the manuscript. Abdelbast Guerfi and Ashok Vijh provided contributions to the design of the study and participated to the critical revision of the manuscript. Prof. Daniel Belanger supervised the research project and participated in designing the study. He was also involved in writing, critically reviewing, and revising the manuscript. Dr. Andrea Paolella supervised the study and was directly involved in the interpretation of the experimental data. He participated to the drafting, revising and submission of the manuscript.

4.2. Article 2: Metastable Properties of Garnet type $Li_5La_3Bi_2O_{12}$ Solid Electrolyte towards Low Temperature Pressure Driven Densification

Daniele Campanella[1,5], Sergey Krachkovskiy[1], Giovanni Bertoni[2], Gian Carlo Gazzadi[2], Maryam Golozar[3], Shirin Kaboli[1], Sylvio Savoie[1], Gabriel Girard[1], Alina Cristina Gheorghe Nita[1], Kirill Okhotnikov[4], Zimin Feng[1], Abdelbast Guerfi[1], Ashok Vijh[1], Raynald Gauvin[3], Daniel Bélanger[5], Andrea Paolella[1,6*]

[1]Centre d'Excellence en Électrification des Transports et Stockage d'Énergie, Hydro-Québec, 1806 Boulevard Lionel-Boulet, Varennes, Québec, J3X 1S1, Canada

[2]Istituto Nanoscienze, Consiglio Nazionale delle Ricerche, Via Campi 213/A, 41125 Modena, Italy

[3]Mc Gill University, Mining & Materials Engineering Department 3610 University Street Montréal, Québec, Canada, H3A 0C5

[4]Independent researcher, 31-421 Reduta 38/9, Kraków, Poland

[5]Université du Québec à Montréal (UQAM), Département de Chimie, 2101 rue Jeanne-Mance, Montréal, Québec, H3C 3P8, Canada

[6]Austrian Institute of Technology, Battery Technologies, Giefinggasse 2, 1210, Wien, Austria

* corresponding author: andrea.paolella@ait.ac.at;

4.2.1 Abstract

Solid state electrolytes represent an attractive alternative to liquid electrolyte in rechargeable batteries. However, the fabrication of batteries with ceramic materials requires high temperature that could be detrimental to their electrochemical performance. In this work we show that it`s possible to densify garnet-type $Li_5La_3Bi_2O_{12}$ solid electrolyte at low temperature (600 ºC) with respect to standard high sintering temperature (T > 1000 ºC) used for zirconium-based $Li_7La_3Zr_2O_{12}$ doped garnet. $Li_5La_3Bi_2O_{12}$ showed a high conductivity (1.2×10^{-4} S cm^{-1}) after hot pressing at 600 ºC. Synthesis conditions have been optimized: at 700 ºC we observed the presence

of $LiLa_2O_{3.5}$ phase as a consequence of LLBO metastability, and the formation mechanism has been described by density functional theory (DFT) and density functional perturbation theory (DFPT) calculations. Moreover, we have reported the application of small amounts of LLBO as a sintering aid (5-10%) in the densification of LLZTO. Our investigation successfully demonstrated that LLBO introduction positively affects the densification process and global performances of LLZTO garnet, allowing to obtain an ionic conductivity higher than 10^{-4} S cm^{-1} after annealing at 600 ºC.

4.2.2 Introduction

In the modern days, one of the most crucial elements in taking full advantage of new renewable energy sources, is the evolution and production of reliable and efficient energy storage systems. Among the explored technologies, lithium-ion batteries (M. Armand & Tarascon, 2008; Di Lecce et al., 2017) are still considered the most impactful high-performance electrochemical storage system (Scrosati et al., 2011). Despite their worldwide diffusion and their noteworthy properties, a series of major challenges still require to be addressed. The use of organic flammable liquid electrolytes, in particular, represents an important safety concern that hinders the widespread deployment of this technology (S. J. Harris et al., 2009; Lisbona & Snee, 2011). Furthermore, flammable electrolytes (Weiss et al., 2021) limit the practical application of metallic lithium as anode because of the possible formation of lithium dendrites (L. Fan et al., 2018) that can lead to short circuits with disastrous consequences. Solid electrolytes can offer a viable alternative (Hu, 2016; Janek & Zeier, 2016; J. Li et al., 2015; F. Zheng et al., 2018) to the conventional organic liquids, acting as a physical barrier against short circuits and, at the same time, increasing the energy density of the battery. In the recent years, numerous solid electrolytes based on polymeric materials (Agrawal & Pandey, 2008; Khurana et al., 2014; Z. Li et al., 2020), oxide or sulfide-based ceramics (Z. Gao et al., 2018; Kato et al., 2016; Z. Ma et al., 2018; Thangadurai et al., 2014) and polymer-ceramic hybrid composites (L. Chen et al., 2018; Commarieu et al., 2018; N. Wu et al., 2020; J. Zheng et al., 2017) were investigated and reported in literature. Li-rich garnets (Murugan et al., 2007; Thangadurai et al., 2014) such as $Li_7La_3Zr_2O_{12}$ (LLZO) are promising candidates for practical battery applications, because of their interesting mechanical properties and high ionic conductivity, up to 10^{-4} S cm^{-1} (Z. Huang et al., 2020). However, full-ceramic solid electrolytes typically require strict synthesis conditions, such as high densification temperatures

(well above 800 °C) over a long annealing time: LLZO with gallium (Rawlence et al., 2018) or aluminium (Murugan et al., 2007) doping can require a synthesis temperature of 1000 °C for 10-12 h. Moreover, high synthesis temperatures are not desirable due to the evolution of side reactions with high-voltage working cathodes: for example, $LiNi_{0.6}Mn_{0.2}Co_{0.2}O_2$ (NMC622) and LLZO may lead to the formation of Li_2CO_3, $La_2Zr_2O_7$ and $La(Ni,Co)O_3$ at 700 ºC (Y. Kim et al., 2020). Despite these shortcomings, garnet materials exhibit the widest electrochemical stability window when compared with other classes of solid electrolytes, like NASICONs or sulfides (F. Han et al., 2016). Within this wide family of materials, bismuth-based garnets, such as $Li_5La_3Bi_2O_{12}$ (LLBO), have been investigated due to their lower synthesis temperature (~ 800º C), as reported by Murugan et al. (Murugan et al., 2007) who observed for this material a total conductivity of 1.9×10^{-5} S cm^{-1} at room temperature. A comparable value of conductivity was observed by Gao et al. (Y. X. Gao et al., 2010): a ceramic pellet compacted at 300 MPa and subsequently annealed at 750 ºC for 6 h presented a final conductivity of 2.4×10^{-5} S cm^{-1} at room temperature. Tin-replaced $Li_6La_3BiSnO_{12}$ synthesized at 785 °C displays similar values of conductivity, about 0.85×10^{-4} S cm^{-1} at room temperature (Peng et al., 2015). Production of LLBO by quenching method (Minami et al., 2007), which involves a rapid cooling of the material to room temperature, has been shown to increase the ionic conductivity up to 2×10^{-4} S cm^{-1} (Peng et al., 2017b), about ten times the value observed for the conventional synthesis. In the present work, we explored the densification mechanism of LLBO and thoroughly investigated its metastability properties, which allow a lower temperature densification, by using density functional theory (DFT) and density functional perturbation theory (DFPT) calculations. We found that hot pressing LLBO at 600º C led to a remarkable ionic conductivity (> 10^{-4} S cm^{-1}). In the present study, limited amounts of LLBO were also explored as a sintering aid for $Li_{6.4}La_3Zr_{1.4}Ta_{0.6}O_{12}$ (LLZTO) and we were able to perform the densification of Ta-doped LLZO at 600º C, achieving an ionic conductivity of 1.5×10^{-4} S cm^{-1}.

4.2.3 Materials and Methods

M.1 Materials and preparation. $Li_5La_3Bi_2O_{12}$ (LLBO) was synthesized via a conventional solid-state route. Anhydrous LiOH, La_2O_3 and Bi_2O_3 synthesis precursors were purchased by Sigma-Aldrich. Commercial Ta-doped LLZO (LLZTO) was purchased from Ampcera. LiOH, La_2O_3 and Bi_2O_3 were mixed in a 5.5:1.5:1 molar ratio and subsequently milled for 12 h in a Retsch PM-100 planetary ball mill. The final mixture was annealed at 775 °C in a

muffle furnace for 6 h and subsequently quenched to room temperature. The LLZTO-LLBO composites were prepared by mixing LLZTO and LLBO in a SPEX mixer in the appropriate mass ratios.

M.2 Hot pressing. The resulting powders were densified by hot pressing under flowing Ar atmosphere. The pellets were prepared using about 1 g of powder. The annealing has been performed in a 16 mm Si_3N_4 die with WC mobile parts, to allow the correct densification and avoid pellet gluing, and thin carbon paper films were set up on both sides of the powder to act as a conductive coating for the material. The final densification of LLBO was carried out at 550 °C, 600 °C, 650 °C and 700 °C for 1 h with the application of a pressure of 56 MPa, and a temperature ramp of 20 °C/min during the heating step. LLZTO/LLBO mixtures were densified at 600 °C in the same working conditions.

M.3 Scanning Electron Microscopy. Chemical mapping of the materials was performed via an energy dispersive X-ray spectrometer (EDS) in scanning mode. Pellet cross sections were obtained using an IM4000 Plus (Hitachi, Japan) Ar ion mill with a beam sputtering energy of 6 kV, applying a fast 30° rotation for 4 h. The cross-section surfaces were investigated using a Lyra 3 (TESCAN) scanning electron microscope (SEM) and the elemental composition was obtained with an Extreme (Oxford instruments) windowless energy dispersive spectrometer (EDS). EDS maps were also acquired at higher spatial resolution from thin cross-sectional samples in a scanning transmission microscope (Thermo-Fischer Scientific Talos 200S) at an incident energy of 200 kV, along with annular dark field images (ADF) which are sensitive to the elemental composition (Z-contrast). Thin cross-sections (ca. 100 nm in thickness and with an area of few microns) were successfully obtained via focused-ion beam milling (FIB) after the deposition of a thin layer of metallorganic Pt at the surface to avoid damage and Ga implantation during milling. To enhance the signal from the EDS quantification, a compression/denoising using principal component analysis (PCA) was performed, by keeping the first 10 components in the spectral images.

M.4 Electrochemical analysis. After the densification, the resulting ceramic pellets were sandwiched between two stainless steel disks in coin cell. Electrochemical impedance spectroscopy measurements were performed with a BioLogic VMP-300 potentiostat in a

temperature range from 20 to 80 °C (with a 5 °C step). The electrical conductivity of the samples was calculated considering the sample dimensions, the distance between the electrodes and the values of resistance (Ω) obtained. Cyclic voltammetry was performed in a Li//LLBO//Graphite cell at a 0.5 mV s^{-1} scan rate.

M.5 Nuclear Magnetic Resonance (NMR). ^{7}Li NMR diffusion measurement experiments were performed on 500 MHz WB Bruker AVANCE NEO NMR spectrometer using Diff50 probe and 8 mm double resonance ^{7}Li/^{19}F RF insert at 50 °C. A stimulated echo with longitudinal eddy current delay pulse sequence was used for the measurement. The gradient pulse was in the range of 1.0 – 1.5 ms and the diffusion time was in the range of 400 - 800 ms depending on the sample. The gradient strength was varied in 16 equidistant steps from 100 G cm^{-1} to 2500 G cm^{-1}.

M.6 Modelling. The DFT and DFPT calculations were conducted using VASP (Kresse & Furthmüller, 1996) in a project-augmented wave scheme. Perdew-Burke-Enzerhof exchange-correlation functional (Perdew et al., 1996) was adopted. The energy cutoff was set to 500 eV and structures were relaxed until the maximum force on every atom was below 0.01 eV $Å^{-1}$. The vibrational free energies were obtained using Phonopy (Togo & Tanaka, 2015). The representing configurations of LLBO were chosen using the program *supercell* (Okhotnikov et al., 2016) for the partial occupancy of Li in LLBO.

4.2.4 Results and Discussions

LLBO was synthesized by solid state route (see Materials and Method section for more details) by quenching the powder at 775 ºC after 6 h of annealing, obtaining micron size particles having a pure phase as shown in **Figure 4.1a** while the scanning electron image (SEM) and the electron dispersion spectroscopy (EDS) mapping showing La and Bi distribution of the final product are depicted in **Figure 4.1b.**

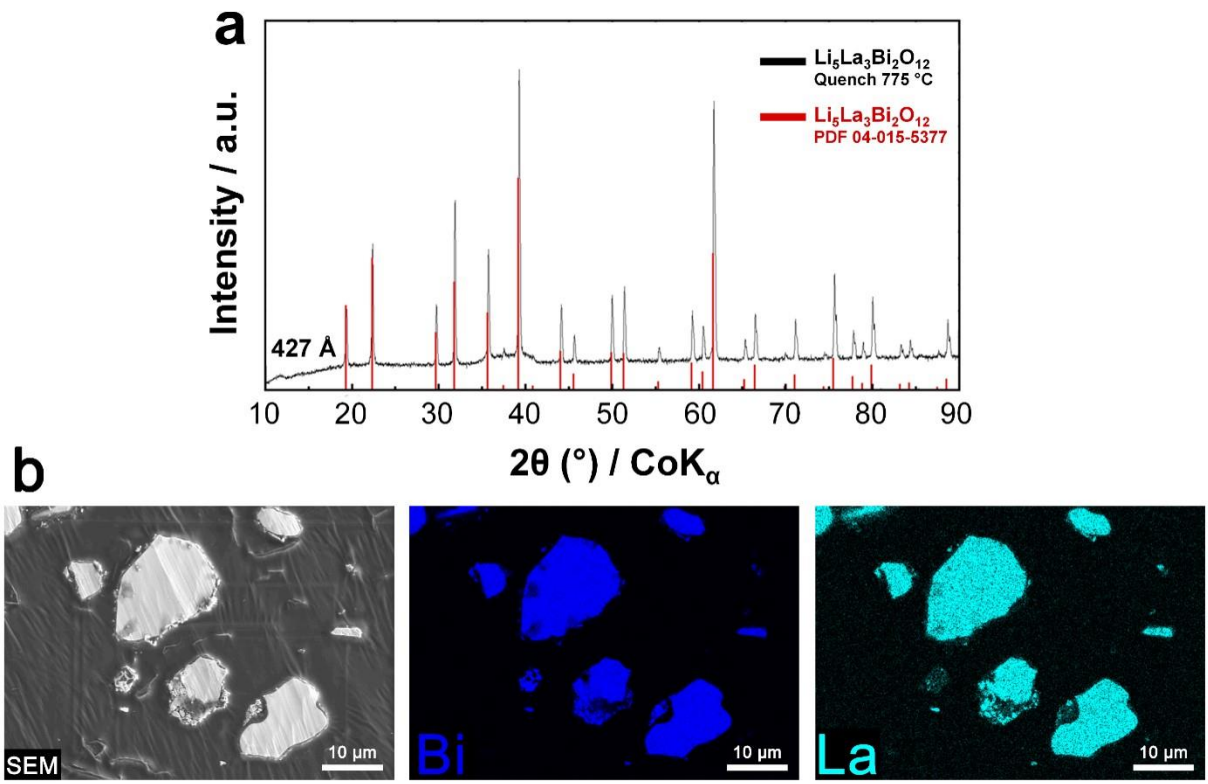

Figure 4.1: a) X-rays diffraction pattern and b) EDS mapping of pristine LLBO.

To unveil the effects of different densification temperatures on the ionic conductivity of LLBO, electrochemical impedance spectroscopy measurements were performed on hot-pressed pellets in a densification temperature range from 550 to 650 °C. **Figure 4.2a** shows the Nyquist plots collected at room temperature for the samples annealed at 550, 600 and 650 °C and the Arrhenius plot for LLBO densified at different temperatures is reported in **Figure 4.2b**. **Figure 4.2a** also presents the equivalent circuit used for the fitting of the impedance data, in which the two separate RC elements are related to the bulk and grain boundaries contributions, respectively. The conductivity curves show a non-dissimilar impedance behavior for the materials. In particular, the samples hot-pressed at 600 ºC and 650 °C exhibit values of total ionic conductivity of about 1.2×10^{-4} S cm^{-1} at room temperature. Both values are sensibly higher than the one for the LLBO sample densified at 550 ºC, (8×10^{-5} S cm^{-1}). At higher densification temperature (700°C) the pellet is easily broken. **Figure 4.S1** reports the values of apparent density of the LLBO samples densified at different temperatures and it shows that the density has an increasing trend with the densification temperature, reaching a value of 5.92 g cm^{-3} for the sample densified at 700 ºC, about 94% of the theoretical density value of pure LLBO (6.234 g cm^{-3}) (Peng et al., 2017a).

In **Figure 4.2c** the ADF cross-section image and the EDS elemental mappings of the LLBO sample hot-pressed at 600 °C are reported. In the image, the metallorganic Pt protecting layer deposited on the sample before FIB milling is indicated (Pt), together with the ca. 2 µm carbonate layer (*) formed at the surface. In the EDS mapping the uniform elemental distribution of La, Bi and O throughout the densified pellet can be visibly observed. The strong relative signals for O and C denote the formation of a thin carbonate layer near the surface of the sample. Moreover, the C map displays a clear presence of signals along the cracks (indicated by the arrows in the map), which point out the evolution of carbonate also at the boundaries between distinct LLBO crystals. The polycrystalline nature of lithium carbonate is confirmed by TEM observations, by which it can be observed that the respective electron diffraction pattern (reported in **Figure 4.2d**) shows no preferential orientation in contrast with the pattern for LLBO (**Figure 4.2e**). **Figure 4.S2** shows the CV response of hot-pressed LLBO in a C//LLBO//Li cell in a potential interval between 0 and 6 V at a scan rate of 0.5 mV s^{-1}. The presence of an irreversible peak at high potential (>5 V vs Li^+/Li) can be clearly seen during the first cycle, which indicates the irreversible redox Bi^{3+}/Bi^{5+} reaction. The cycling stability of hot-pressed LLBO towards Li is furtherly confirmed in **Figure 4.S3**, which reports the performance of a Li//LLBO//Li symmetric cell. The measurement was carried out at a current of 0.3 mA cm^{-2} (5 h charge and 5 h discharge) and a temperature of 50 °C and, as observed from the stability curve, the cell exhibits a low polarization of about 0.4 V over a period of 300 h, indicating a high affinity of the material towards lithium.

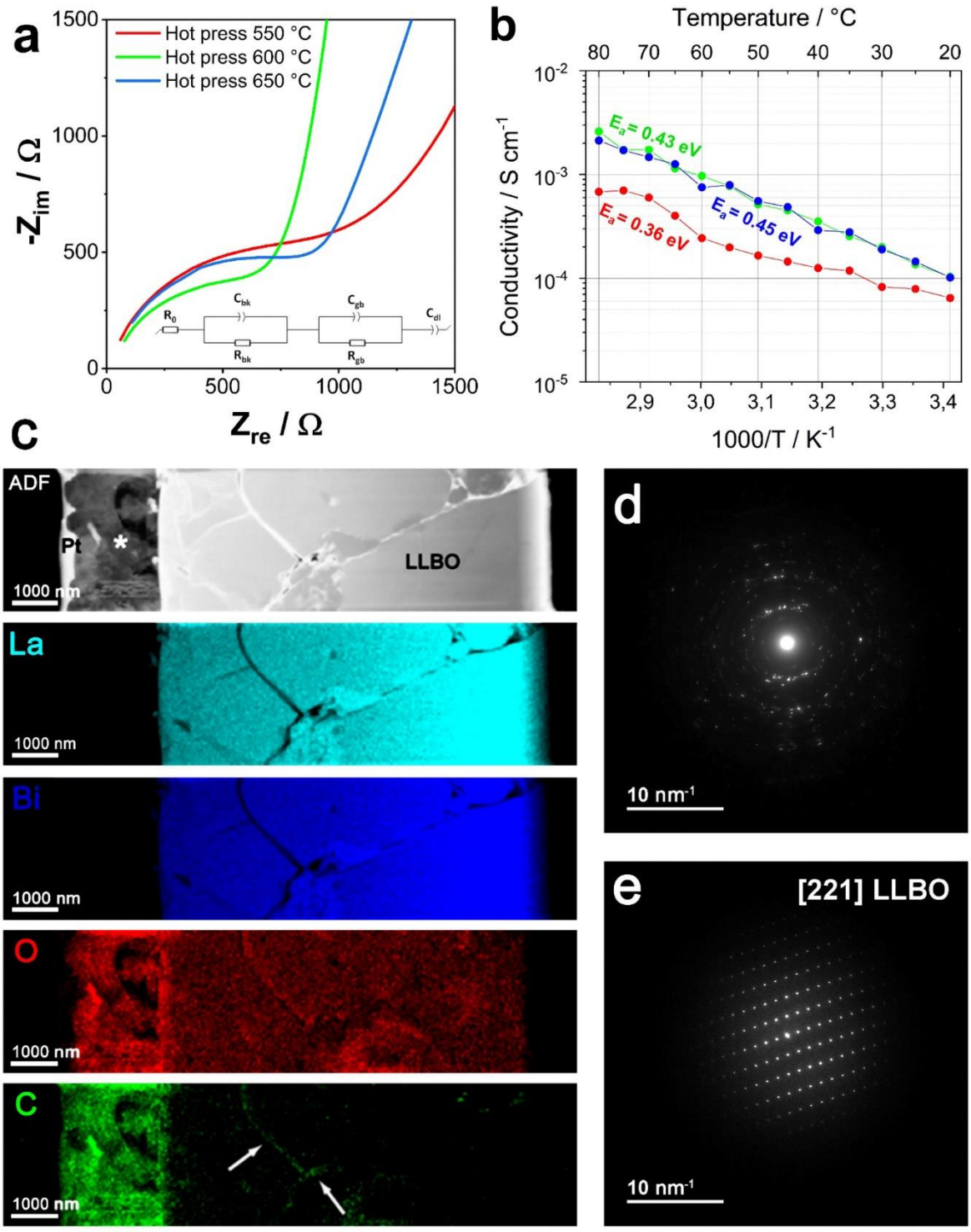

Figure 4.2: a) Nyquist plot at room temperature with equivalent circuit and b) Arrhenius plot of the hot-pressed samples at 550, 600 and 650 °C; c) STEM-obtained cross-section ADF image and EDS maps for the LLBO sample hot-pressed at 600 °C. The ADF image (top left) shows the thin cross section of the sample with the top surface of the sample on the left; d-e) Electron diffraction pattern of d) polycrystalline lithium carbonate and e) LLBO.

Hot pressed LLBO shows a metastability range: after the hot pressing of LLBO, a sensitive increment in $LiLaO_2$ impurities can be observed while the hot pressing temperature increases, as shown in the XRD pattern in **Figure 4.3a**. LLBO structure undergoes an important shrinkage in the cell parameter (**Figure 4.3b**, red line) when passing from 650 to 700 °C, indicating the presence of a side reaction for operating temperatures higher than 650 °C. Interestingly, the crystallite size decreases when LLBO sample is annealed at 650 ºC (430 Å to 270 Å) to subsequently increase again after annealing at 700 °C (430 Å) as shown in **Figure 4.3b** (blue line). The cross-section SEM images and EDS mapping in **Figure 4.3c** shows a homogeneous distribution of La and Bi for the sample densified at 600 °C. On the other hand, the elemental distribution for the sample hot-pressed at 700 °C exhibits specific areas with a larger presence of Bi and a relatively lower occurrence of La, which denote a partial elemental segregation in form of Bi_2O_3 that is formed according to:

$$4Li_5La_3Bi_2O_{12} \rightarrow 4Bi_2O_3 + 6LiLa_2O_{3.5} + 7Li_2O + 4O_2 \uparrow$$

Figure 4.S4 reports a higher magnification image of LLBO hot-pressed at 600 °C, which clearly shows the uniform presence of La on the surface of the sample.

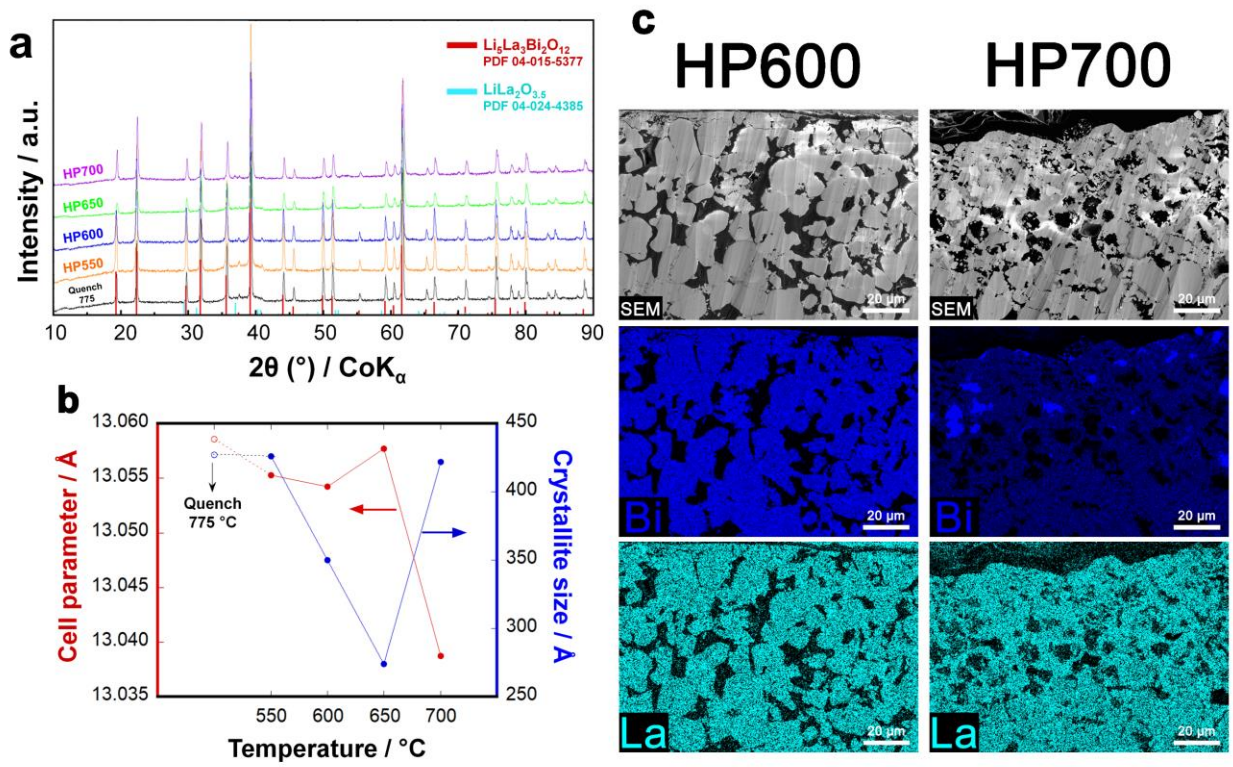

Figure 4.3: a) X-rays diffraction patterns and b) evolution of cell parameter and crystallite size of the samples hot-pressed at different temperatures (550, 600, 650 and 700 °C), c) cross section SEM image and EDS elemental mapping for Bi and La of LLBO hot pressed at 600 and 700 °C.

In addition, the working equipment was not sealed, which makes the evolution of oxygen even easier. Fortunately, according to first principles calculations with harmonic approximation, the decomposition temperature of $Li_5La_3Bi_2O_{12}$ could be raised by applying external pressure. Density functional theory (DFT) and density functional perturbation theory (DFPT) calculations allowed to derive the free energies of the solid phases using harmonic approximation. Basically, the values of free energy are approximated with the sum of zero-temperature binding energy from DFT, the kinetic energies are obtained from their harmonic vibration and the temperature dependent term involving the entropy is derived from the harmonic vibration, as stated in the formula:

$$G \cong F = E_{bind} + E_{vib} - TS_{vib}$$

where the Gibbs free energy for solid phases is approximated with the Helmholtz free energy because the effect from pressure is either negligible or included in the binding energies in our case. Without anharmonicity, the partition function then becomes a well converged geometric progression, then the free energy and entropy are directly obtained from partial derivatives of it. This procedure is implemented in Phonopy (Togo & Tanaka, 2015) as a post-processing tool of the DFT calculation package VASP (Kresse & Furthmüller, 1996). In addition to this, the partial occupancy of lithium ions in $Li_5La_3Bi_2O_{12}$ crystal creates further complication. In order to obtain a configuration representative enough of the actual crystal, we enumerated all possible configurations in a primitive cell of $Li_5La_3Bi_2O_{12}$ as implemented in *supercell* (Okhotnikov et al., 2016); the configurations were sorted according to their electrostatic energies from low to high using Ewald summation, assuming point charges for the constituent ions. DFT calculations were then used to single out the configuration with minimum total energy for the subsequent free energy calculations. For the oxygen gas, the total internal energy can be split into the O_2 molecular binding energy contribution plus the kinetic energy. An offset of -1.36 eV per O_2 molecule is added to the calculated free energy at 298.15 K under 1 atm to compensate for the artificial over-binding from our computational method. Therefore, the total Gibbs energy of oxygen gas can be written as:

$$G = E + c + \frac{5}{2}RT + pV - TS = H + c - TS$$

where E is the value of binding energy from DFT, c is the constant over-binding correction, R is the gas constant, T is the temperature in Kelvin, p is the pressure (1 atm in this case, as the chamber is not sealed), V is the volume of the gas, S is the entropy and H is the enthalpy. The enthalpy and entropy of O_2 gas are adopted from JANAF tables. This way, we can estimate the Gibbs energy change for this reaction. If the change is negative, decomposition of $Li_5La_3Bi_2O_{12}$ is favored in the equilibrium state. The results of Gibbs energy change are shown in **Figure 4.4**. We can see that the decomposition is more and more favored as the temperature raises, in general. Without external pressure applied, the equilibrium decomposition starts above 626 K (353 °C); nevertheless, under a pressure of 0.5 kbar, the equilibrium decomposition temperature increases to 723 K (450 °C). For an ulterior increase of pressure up to 2 kbar, the decomposition temperature keeps rising up to 775 K (502 °C). Although DFT and DFPT can generate significant error in predicting temperatures, a visible tendency in the increase of decomposition temperature under

applied pressure is observed. The decomposed LLBO sample after hot pressing at 700 °C is shown in **Figure 4.4c**.

Considering the present results, we investigated the effects of LLBO as a sintering aid for the densification of LLZTO at 600 ºC. The Nyquist plots of pristine LLZTO and LLZTO/LLBO samples are shown in **Figure 4.5a**. The Arrhenius plot (**Figure 4.5b**) shows the conductivity trend in the range of temperature from 20 to 80 °C. The highest value of conductivity is reported for LLZTO with the addition of 10% LLBO, showing a value of 1.5×10^{-4} S cm^{-1} at room temperature, while the sample with 5% LLBO displays a slightly lower value (9×10^{-5} S cm^{-1}). Above 50 °C a trend reversal is observed and LLZTO/5%LLBO exhibits a higher conductivity than LLZTO/10%LLBO. Both samples have a superior ionic conductivity than pristine LLZTO sample (1×10^{-6} S cm^{-1}). Interestingly, the introduction of larger amounts of LLBO leads to a significant decrement in the conductivity, as observed for the sample with 30% LLBO which shows the lowest ionic conductivity at room temperature (4.9×10^{-5} S cm^{-1}). The graph reported in **Figure 4.S5** shows the values of apparent density of a series of LLZTO/LLBO samples according to the relative LLBO content. The highest values of density are observed for the samples prepared with 30% of LLBO, around 5.4 g cm^{-3}, whilst increasing LLBO content further leads to a decrement in density (LLZTO/50%LLBO shows a value of 4.94 g cm^{-3}. The reasons behind such a discrepancy may possibly depend on the hot-pressing process itself; high temperature treatment can lead to partial material loss which can impact the production of the pellets and the density of the material, therefore measuring effective values of density is often complicated. Additional electrochemical investigation on the material involved a cyclic voltammetry test (**Figure 4.S6**), performed on LLZTO/10%LLBO. The pattern exhibits a broad irreversible peak at high voltages (> 4 V vs Li^+/Li) in the oxidation step during the first cycle, which may indicate the bismuth oxidation reaction from Bi^{3+} to Bi^{5+}. The cycling stability of the hot-pressed material was also investigated and **Figure 4.S7** reports the performance of a Li//LLZO-LLBO//Li symmetric cell. Measurement was performed at a current of 0.3 mA cm^{-2} and a temperature of 50 °C. The graph reports that the symmetric cell exhibits a higher polarization compared with the cell with pristine LLBO (**Figure 4.S3**), with an initial value of 1 V during both charge and discharge which slightly peters down to 0.5 V after 300 h of cycling. The presence of more resistive LLZO as a main component can

explain the difference in performance between the cells, being LLZO a more resistive material than LLBO.

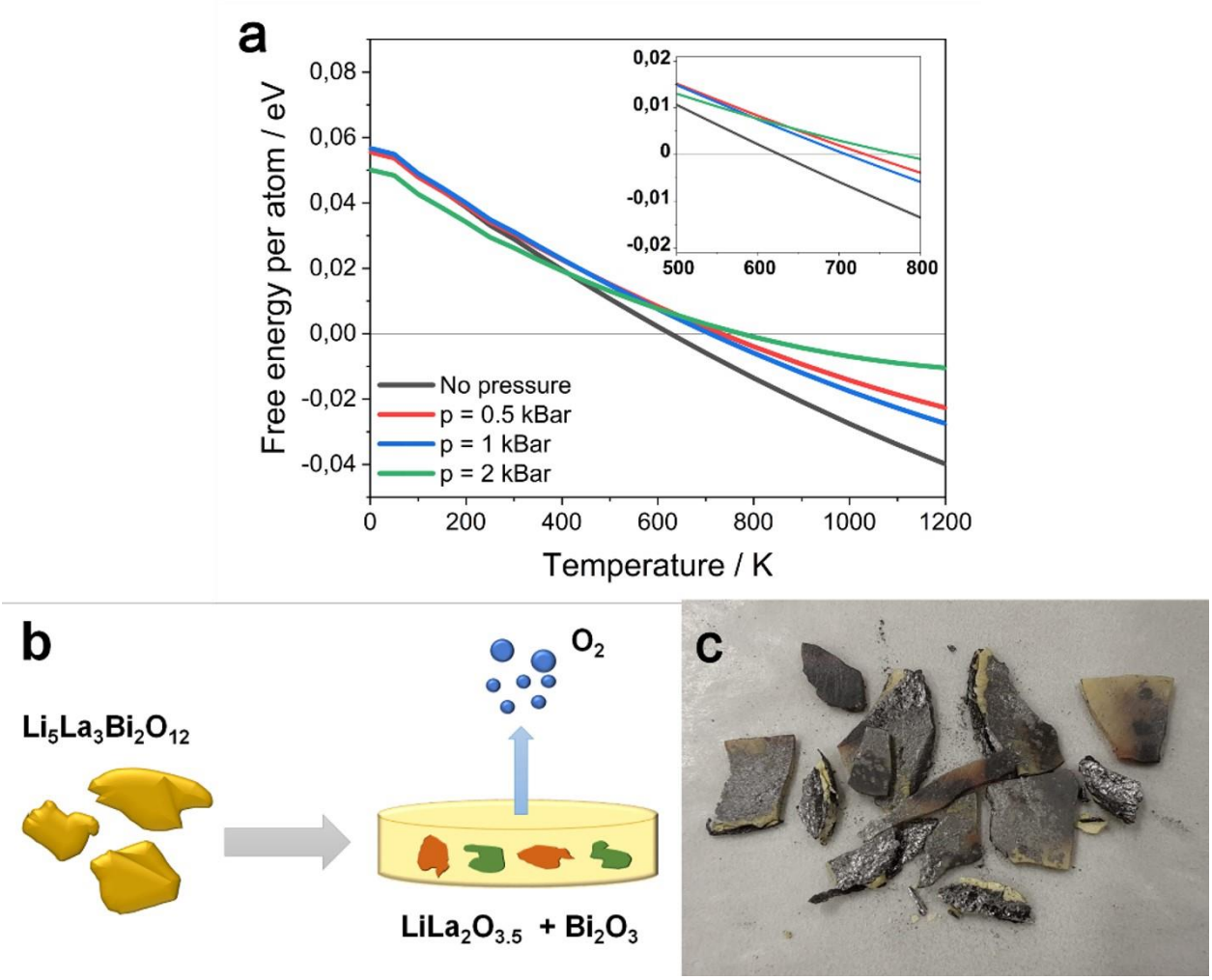

Figure 4.4: a) Graph showing Free Energy vs temperature of LLBO decomposition under variation of pressure and b) Schematic of the reaction process. c) Picture of decomposed LLBO sample after thermal annealing at 700 °C.

The LLZTO sample containing 10% LLBO was subsequently analyzed via SEM and EDS and the presence of local LLBO-rich islands dispersed throughout the LLZTO matrix was observed, as reported in **Figure 4.5c.** These observations suggest the absence of a bulk reaction between the two phases of LLZTO and LLBO, while at the same time the structure of the LLBO phase is preserved. **Figure 4.S8** shows a higher magnification SEM image of LLZTO/10%LLBO in which the uniform distribution of La on the whole surface of the pellet is clearly visible. The

XRD diffraction pattern of hot-pressed LLZTO/10%LLBO is reported in **Figure 4.S9** and it can be observed that after the hot-pressing treatment the LLZO cubic phase is preserved, and no significant presence of impurities is observed in the structure.

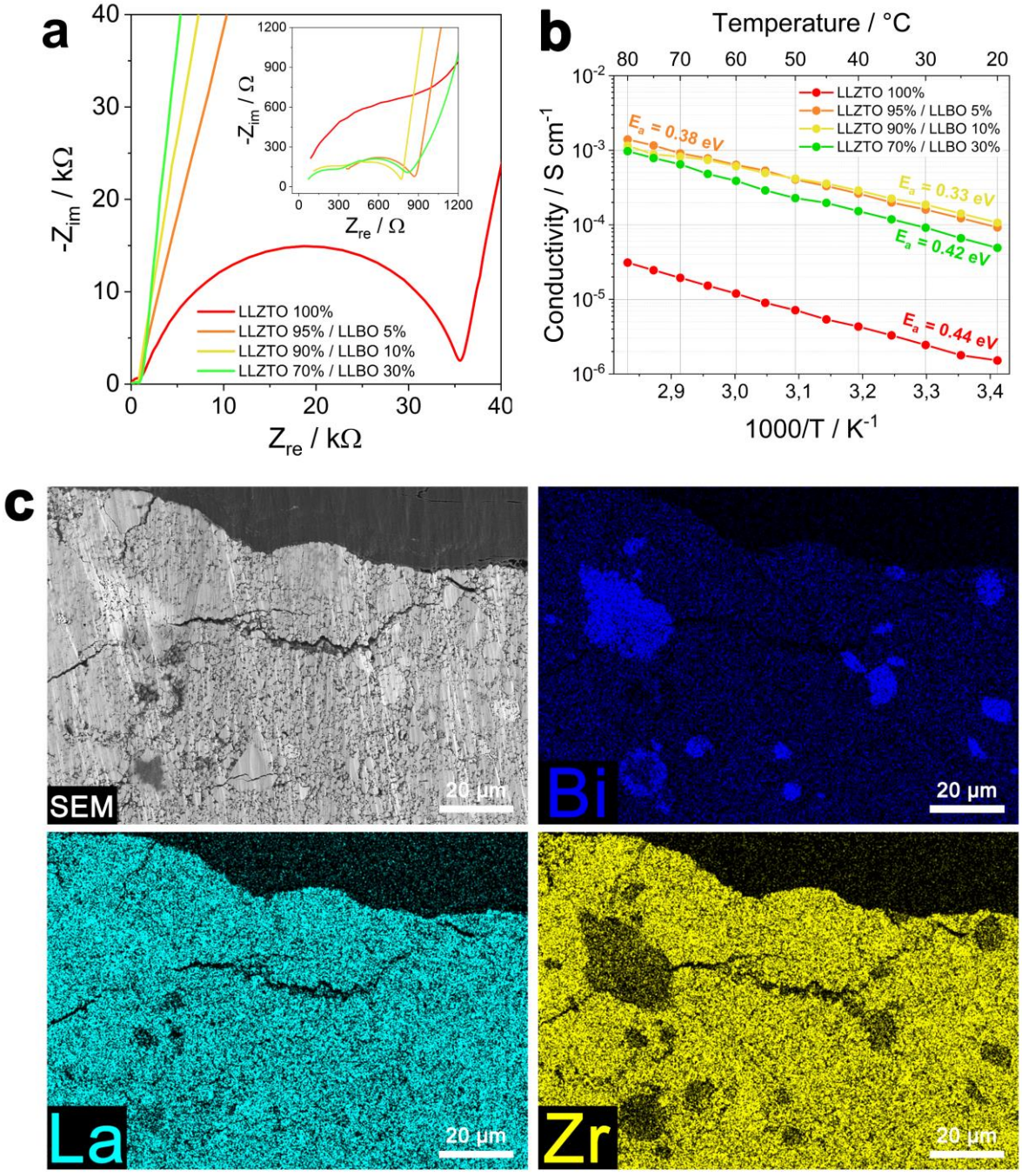

Figure 4.5: a) Nyquist plots measured at room temperature and b) Arrhenius plot of the LLZTO/LLBO samples having different LLBO %; c) SEM image and EDS elemental maps for Bi, La and Zr of LLZTO/10%LLBO sample.

To better understand Li transport properties of the material, Li diffusion coefficients were measured by ^{7}Li pulsed-field gradient nuclear magnetic resonance (PFG NMR) technique in LLBO samples densified at different temperatures, as well as in LLZTO with 10% of LLBO composite hot pressed at 600 °C. Short-duration magnetic field gradient pulses are introduced into spin-echo sequence to detect particles displacement in PFG NMR experiments (K. S. Han et al., 2021). The resulted signal intensity (I) depends on parameters of the applied gradients and the self-diffusion coefficient (D) of the observed species by the following equation: $I = I_0 e^{-BD}$, where I_0 is the NMR signal intensity without gradients application and B represents experimental conditions as: $B = \gamma^2 g^2 \delta^2 \left(\Delta - {}^{\delta}/_{3}\right)$, with γ – gyromagnetic ratio of observed nuclei, g and δ – strength and duration of the gradient pulses, Δ – delay between the encoding and the decoding gradients. An example of stacked ^{7}Li PFG NMR spectra of LLBO sample collected at different gradient strengths (g varied from 100 G cm^{-1} to 2500 G cm^{-1} in 16 equidistant steps) is shown in **Figure 4.6a**. The obtained values of lithium diffusion coefficients for all samples measured that way are listed in **Figure 4.6b**. The mean squared displacement of Li during NMR experiment could be estimated as $d = \sqrt{2Dt}$. With $D \sim 10^{-13}$ m^2 s^{-1} and with diffusion time during PFG NMR experiment $\Delta = 0.5$ s the displacement d is about 0.3 μm. This is an order of magnitude larger than the crystallite size (**Figure 4.3b**), but smaller than the crystal size of the analyzed compounds. It means that the obtained values of Li diffusion coefficients reflect mostly Li mobility inside secondary particles (through crystallites and grain boundaries between them), while Li transition between the particles has a negligible effect on the collected data. One can see that Li diffusion in LLBO depends on densification conditions. It means that densification at higher temperature promotes a better contact quality between crystallites decreasing the grain boundary effect. In contrast, there is no difference in Li diffusion between LLZTO and LLZTO/10% LLBO samples. Possibly, hot pressing temperature of 600 °C is not high enough to affect LLZO crystals. At the same time, a partial incorporation of LLBO, with higher Li diffusivity, increases bulk conductivity of the electrolyte (**Figure 4.5b**). LLBO is shown to help the densification of LLZTO by keeping secondary particles closer as reported in the scheme in **Figure 4.6c**.

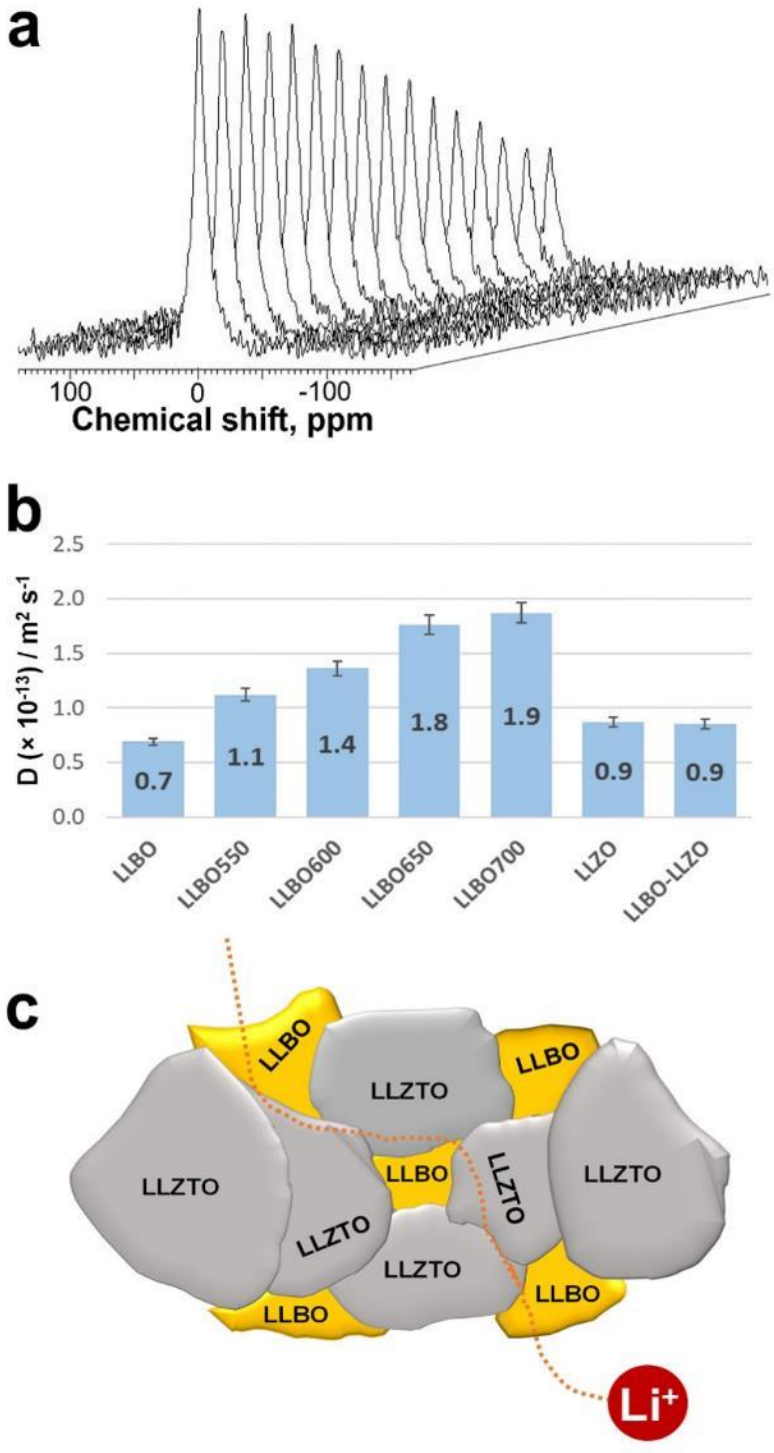

Figure 4.6: a) Stacked ^{7}Li PFG NMR spectra of LLBO sample collected at different gradient strengths. b) Li diffusion coefficients measured by PFG NMR in pristine LLBO, in LLBO densified at 550, 600, 650 and 700 °C, in pristine LLZTO and in LLZTO/10% LLBO composite. c) Schematic representation of Li^{+} ion diffusion in the LLZTO/LLBO composite.

4.2.5 Conclusions

In the present work we successively reported the pressure driven densification of garnet-type $Li_5La_3Bi_2O_{12}$ solid electrolyte at 600 ºC, a value of temperature significantly lower than the standard temperature (T > 1000 ºC) typically required for zirconium-based $Li_7La_3Zr_2O_{12}$. By the application of hot pressing, the densification conditions for $Li_5La_3Bi_2O_{12}$ have been optimized, leading to a high ionic conductivity of 1.2×10^{-4} S cm^{-1} after hot pressing at 600 ºC. Treatment performed at 700 ºC brought to a partial segregation of bismuth and to the formation of $LiLa_2O_{3.5}$ secondary phase as a consequence of LLBO metastability. The impurity formation mechanism has been subsequently described by density functional theory (DFT) and density functional perturbation theory (DFPT) calculations. Moreover, we demonstrated that LLBO may be usefully employed as sintering aid (5-10%) for LLZTO solid electrolyte, allowing to obtain an ionic conductivity higher than 10^{-4} S cm^{-1} after densification at low temperature (600 ºC).

4.2.6 Acknowledgements

This research was funded by Hydro-Québec's Center of Excellence in Transportation Electrification and Energy Storage, Varennes, Québec. A.P. want to thank dr. Chisu Kim, dr. Hendrix Demers, Daniel Clement of CEETSE (Canada) and Sergio Marras of Italian Institute of Technology (Italy) for their useful suggestions. D.C. acknowledges the financial support of Mitacs.

4.2.7 Supplementary Information

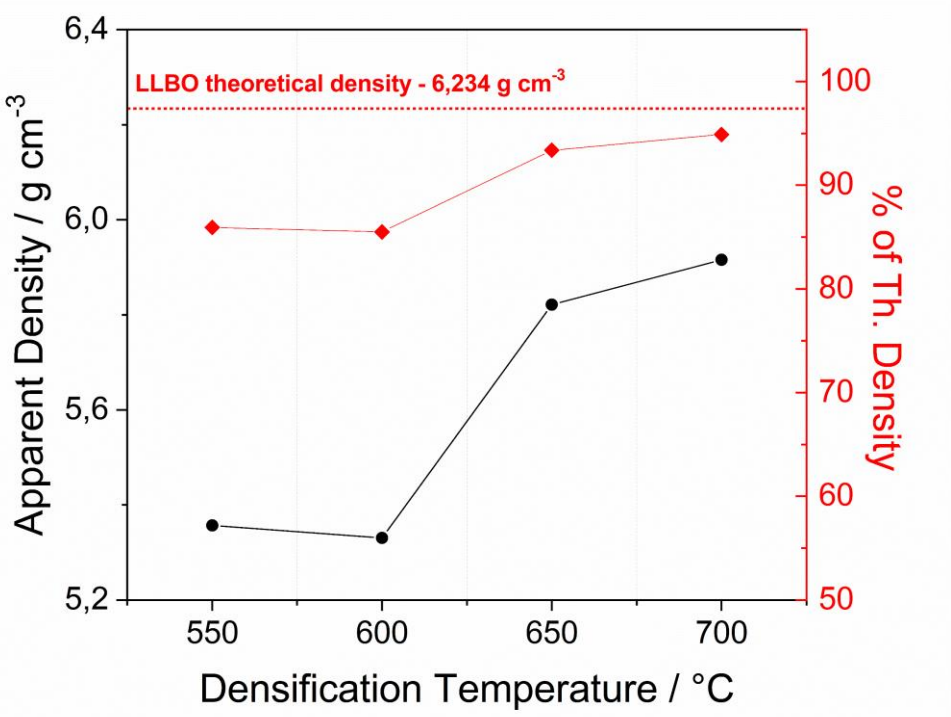

Figure 4.S1. Graph of apparent density of LLBO samples densified at different temperatures

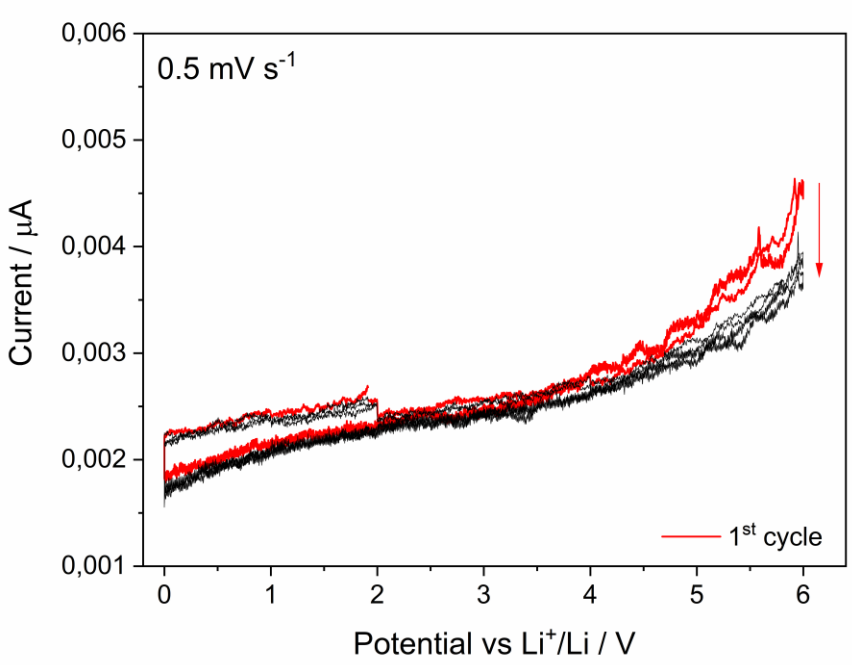

Figure 4.S2. Cyclic voltammetry of LLBO hot pressed at 650 °C, performed in a C//LLBO//Li cell at a potential scan rate of 0.5 mV s^{-1}.

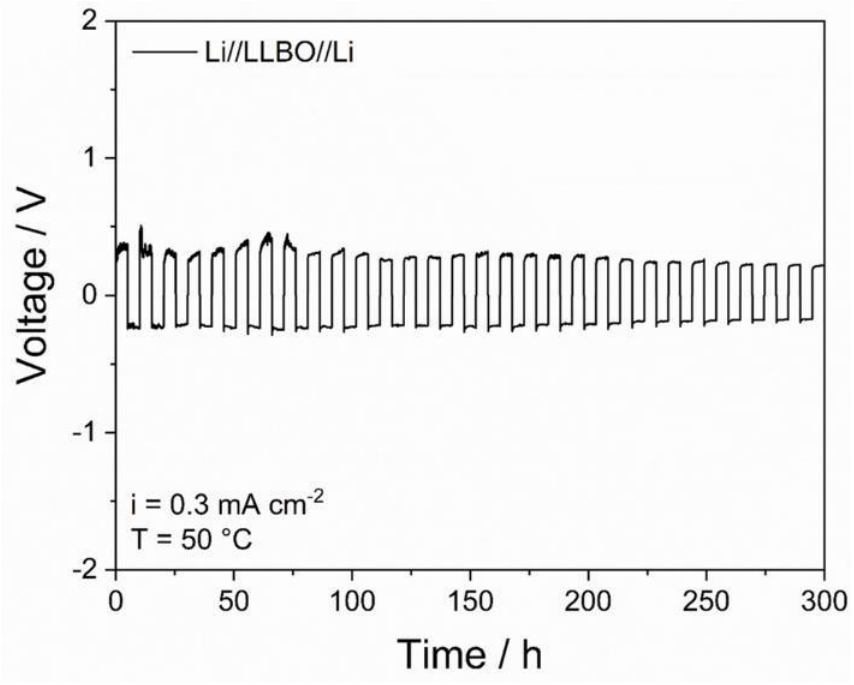

Figure 4.S3. Li stability curve of hot-pressed LLBO performed in a symmetric Li// LLBO//Li cell at 50 °C with a current density of 0.3 mA cm^{-2}

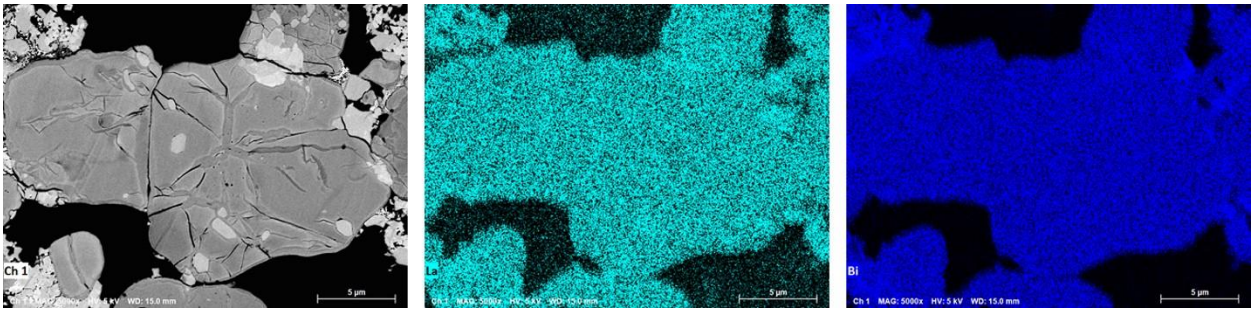

Figure 4.S4. High magnification SEM image and EDS elemental mapping for La (cyan) and Bi (blue) of LLBO hot pressed at 600 °C

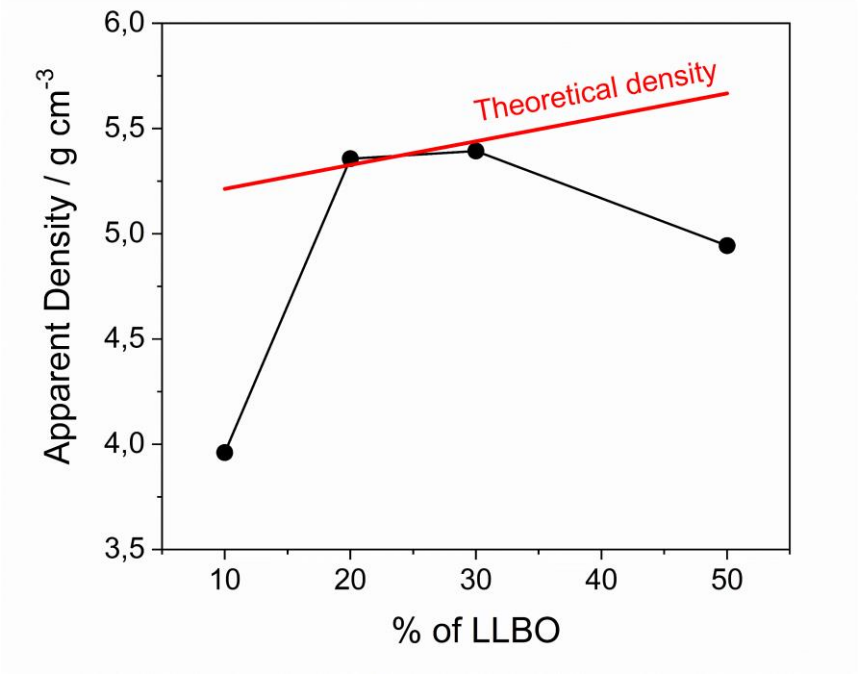

Figure 4.S5. Values of apparent density of LLZTO-LLBO samples with different LLBO content, compared with the theoretical value for the same electrolyte composition.

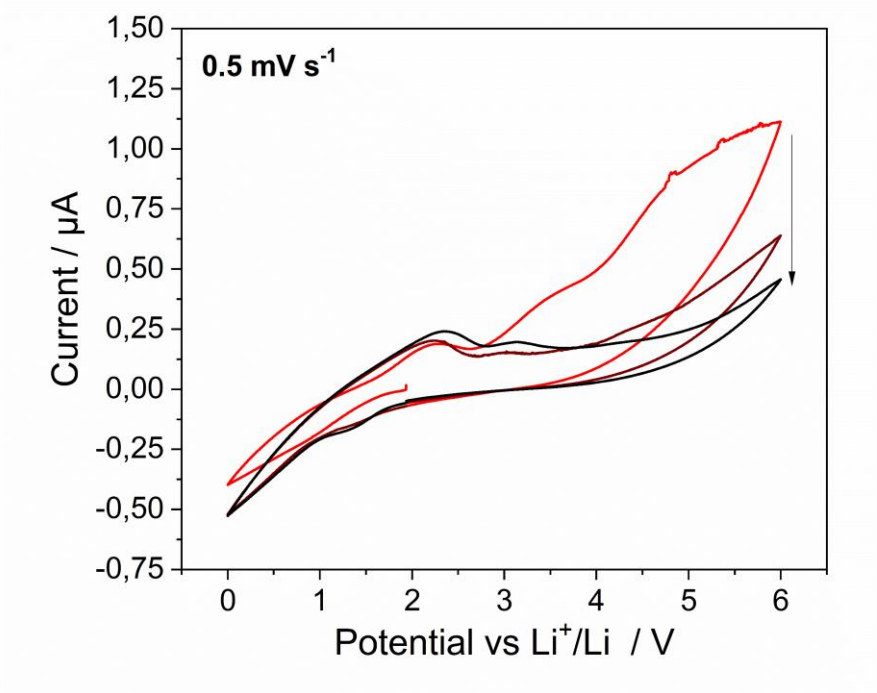

Figure 4.S6. Cyclic voltammetry of LLZO/10%LLBO hot pressed at 650 °C, performed in a C//LLZO/10%LLBO//Li cell at a potential scan rate of 0.5 mV s^{-1}.

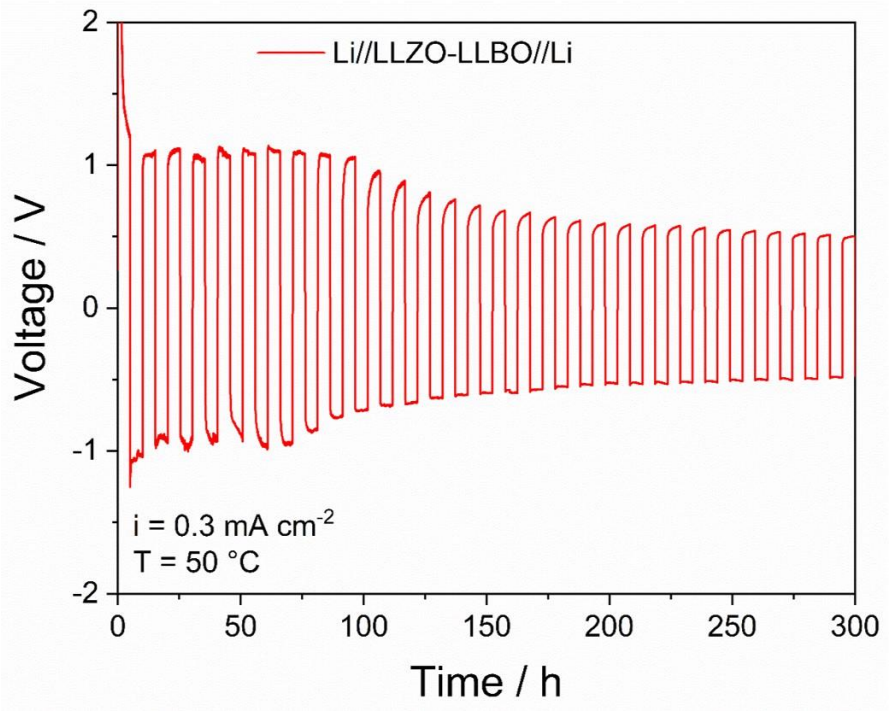

Figure 4.S7. Li stability curve of hot-pressed LLZO-LLBO performed in a symmetric Li//LLZO-LLBO//Li cell at 50 °C with a current density of 0.3 mA cm^{-2}

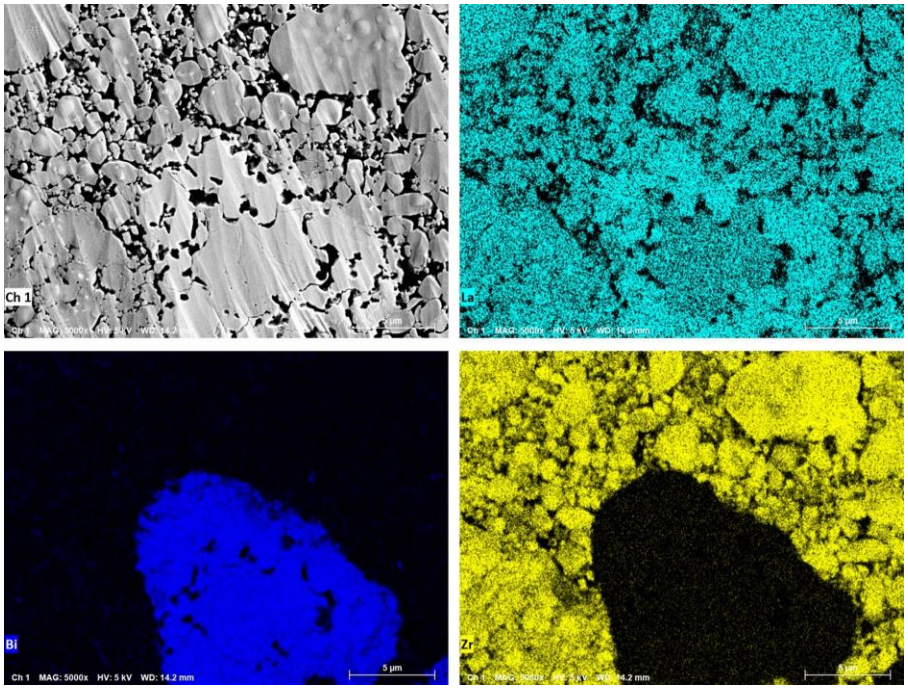

Figure 4.S8. High magnification SEM image and EDS elemental mapping for La (cyan), Bi (blue) and Zr (yellow) of LLZTO/10%LLBO hot pressed at 600 °C

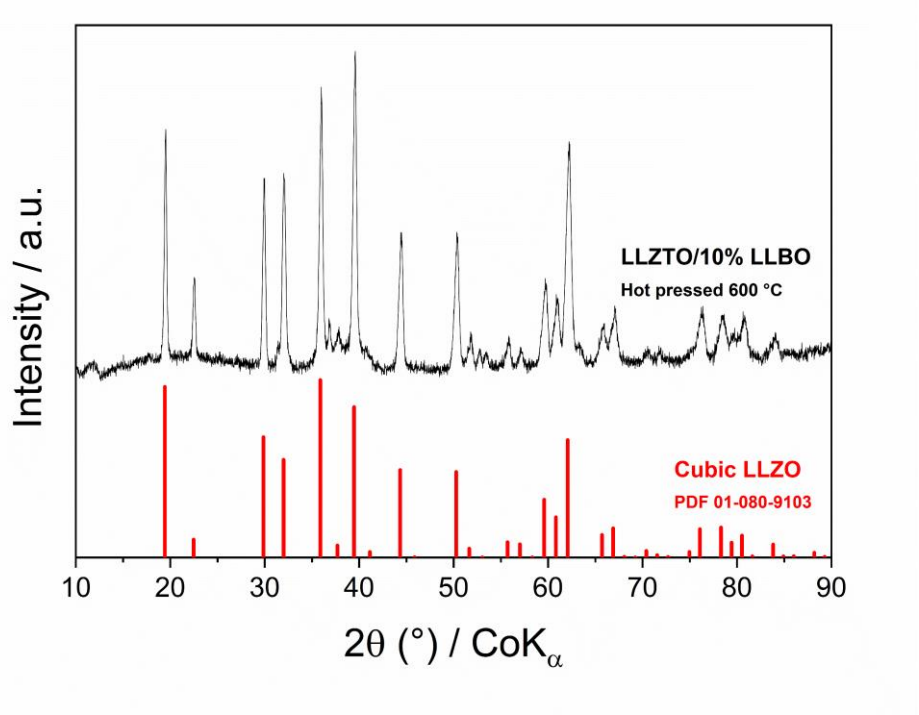

Figure 4.S9. XRD pattern of LLZTO/10%LLBO hot-pressed at 600 °C, compared with the reference pattern for cubic LLZO

CHAPTER V
GRAM-SCALE CARBOTHERMIC CONTROL OF LLZO GARNET SOLID ELECTROLYTE PARTICLE SIZE

5.1. Introduction

In the previous chapter the protagonist of the research was LLBO, and garnet LLZO was a secondary character, whose densification properties were modified by using a sintering aid. Chapters V and VI explore the densification of LLZO more extensively, aiming to obtain a simpler synthesis with less demanding starting conditions in terms of temperature and pressure. Among the sintering agents for ceramic, in this investigation carbonaceous materials were the preferred choice, due to their notable electrochemical and thermal properties which can allow to stabilize the crystalline phases of the product. Carbon additives are typically employed in the fabrication of electrodes, but their effects on the production of ceramics via solid-state synthesis have not been extensively explored. Mediation of the carbon additives on the synthesis mechanism of LLZO is explored, unveiling a low decomposition temperature (around 670 °C) of the Li_2CO_3 synthesis precursor in presence of carbon and evolution of CO; the formation of LLZO is accelerated and achieved at lower temperature (720 °C) compared with the mixtures without carbon (780-800 °C), with the presence of a well-defined cubic structure stabilized at low temperatures. The mechanism for the carbon free samples involves, on the other hand, the slower reaction between intermediates, which postpones the formation of the final product. The nature of the additives themselves is shown to have a certain degree of influence on the structural features of the resulting material: incorporation of carbon helps decreasing the average particle size in the powder compared with pristine LLZO, and the effect is even more visible when using nanometric sized carbons, such as acetylene black DENKA, instead of larger graphitic MAG carbons. TEM imaging reveals the distribution of the carbon agent around the ceramic particles, showing the exfoliation of layers for graphitic carbons and the spread of finer particles for nanometric carbons. The reduced particle size is shown to help improving the densification of the ceramic pellets after low-temperature sintering, manifesting a more limited presence of pores and an increment in the apparent density. The as-modified LLZO materials reported better electrochemical performance in cells than the

pristine one, with higher values of conductivity and a more stable cell behaviour against metallic lithium. In particular, the observations revealed a higher value of conductivity for the samples using nanometric carbon as sintering additive compared with the graphitic carbon: a reduced amount of DENKA carbon allowed to improve the conductivity of LLZO of about 40% with respect to the pristine sample, while using graphitic MAG carbon required a much higher amount of additive to observe similar effects on conductivity.

Chapter published in Chemical Engineering Journal, **2023**, 457, 141349

Author contributions: Daniele Campanella participated in the design of the study, the synthesis of the materials and the final assembly of the cells. He performed the XRD analysis, SEM analysis of the powders and electrochemical testing. He also gathered, analyzed, and interpreted the experimental data. He was responsible for the writing and the correction of the manuscript and the bibliographic research. Giovanni Bertoni performed the TEM analysis and helped with the interpretation of experimental results. Wen Zhu performed the *in situ* XRD testing and helped in the interpretation of the experimental data. Michel Trudeau performed the thermal analysis (TGA) and provided the experimental results. Daniel Clément helped performing the cross-section SEM analysis of the samples and provided the experimental results of the tests. Sylvio Savoie and Gabriel Girard aided in laboratory procedures for the synthesis of the materials and the electrochemical testing. Abdelbast Guerfi, Ashok Vijh and Chandramohan George provided contributions to the design of the study and participated to the critical revision of the manuscript. Prof. Daniel Belanger supervised the research project and participated in designing the study. He was also involved in writing, critically reviewing, and revising the manuscript. Dr. Andrea Paolella supervised the study and was directly involved in the interpretation of the experimental data. He participated to the drafting, revising and submission of the manuscript.

5.2. Article 3: Gram-scale Carbothermic Control of LLZO Garnet Solid Electrolyte Particle Size

Daniele Campanella[1,2], Giovanni Bertoni[3], Wen Zhu[1], Michel Trudeau[1], Gabriel Girard[1], Sylvio Savoie[1], Daniel Clément[1], Abdelbast Guerfi[1], Ashok Vijh[1], Chandramohan George[4], Daniel Bélanger[2] and Andrea Paolella[1,2,5,*]

[1]Centre d'Excellence en Électrification des Transports et Stockage d'Energie (CEETSE), Hydro-Québec, Varennes, Québec J3X 1S1, Canada

[2]Université du Québec à Montréal (UQAM), Département de Chimie, 2101 Rue Jeanne-Mance, Montréal, Québec, H3C 3P8, Canada

[3]Istituto Nanoscienze, Consiglio Nazionale delle Ricerche, Via Campi 213/A, 41125 Modena, Italy

[4]Dyson School of Design Engineering, Imperial College London, SW7 2AZ London, U.K.

[5]Austrian Institute of Technology (AIT), Giefinggasse 4, 1210 Wien, Austria

* Corresponding author: andrea.paolella@mail.mcgill.ca

5.2.1 Abstract

In recent years, solid electrolytes have become an enticing alternative to liquid electrolytes in lithium batteries. However, the high synthesis temperatures and difficult optimization of solid-state electrolytes are an important drawback in a high-scale application. In this work, we demonstrate that the synthesis process of garnet-based $Li_7La_3Zr_2O_{12}$ (LLZO) electrolyte can be accelerated while reducing the formation temperature of cubic LLZO to about 720 °C from a standard temperature of 780 °C by supplementing the process with a carbon additive. These carbon-rich LLZO samples have a homogeneous particle distribution with a decreased average size, which is influenced by the type of the carbon additive itself. The materials with high carbon content show an improved densification after hot-pressing at a low temperature of 800 °C, which

is reflected in their electrochemical performance, since LLZO sample with 10% of DENKA carbon additive shows a total ionic conductivity of 5.95×10^{-5} S cm^{-1}, about 40% higher than the one of carbon-free LLZO (3.53×10^{-5} S cm^{-1}).

5.2.2 Introduction

Current developments in the field of energy storage are fundamental to fully exploit the advantages of renewable energy sources, such as wind and solar energy, and to meet the increasing energy demand. Lithium-ion batteries are considered one of the most promising energy storage systems, owing to their long cycle stability and high energy density, and enable a broad range of applications in portable electronics and electric vehicles (M. Armand & Tarascon, 2008; Scrosati et al., 2011; Terada, 2001) and beyond. Despite their obvious advantages, crucial issues related to battery safety have to be tackled; in particular, organic electrolytes are a significant limitation to future upscale applications due to the formation of flammable gases (S. J. Harris et al., 2009). Furthermore, the use of high-energy metallic lithium anode is hampered by liquid electrolyte due to the growth of dendrites which could lead to short-circuits with potentially disastrous consequences (W. Li et al., 1994; Lisbona & Snee, 2011). Solid electrolytes may represent a promising alternative and have garnered a renewed interest in the last decades (L. Fan et al., 2018). Being the key component of all-solid-state batteries, solid electrolytes should meet a series of requirements, including a) a high Li^+-ion conductivity, b) a wide potential stability window (0-5 V), c) a Li^+ transference number close to 1 and d) a low formation and densification temperature (Bintang et al., 2021; Campanella et al., 2021; C. Cao et al., 2014; F. Zheng et al., 2018). Recent advances have led to the discovery of fully inorganic materials suitable for this application, including perovskites (Inaguma et al., 1994), NASICONs (Anantharamulu et al., 2011), sulfide-based electrolytes (Kato et al., 2016; Z. Ma et al., 2018) and Li-stuffed garnets (Abouali et al., 2021; Thangadurai et al., 2014). $Li_7La_3Zr_2O_{12}$ (LLZO) is the most important representative of this last class of electrolytes (Sun et al., 2023), which was introduced in 2007 by Murugan et al. (Murugan et al., 2007) as a potential candidate for practical applications, owing to its good mechanical properties, increased interfacial stability and high ionic conductivity of 10^{-4} S cm^{-1} (Deviannapoorani et al., 2013; W. Lu et al., 2021).

Following investigations on the framework and crystal structure reported for LLZO, there are two main crystal polymorphs (F. Chen et al., 2018; Geiger et al., 2011a): a tetragonal and a cubic phase (Thompson et al., 2014). The latter was revealed to be the high-conductivity phase and subsequent studies demonstrated that its room temperature stability can be suitably tuned with partial elemental substitution (S. Cao et al., 2019b). Aliovalent doping with small amounts of Al, Ga, Ta, Nb, etc. (Deviannapoorani et al., 2013; M. Huang et al., 2012; Meesala et al., 2019; Salimkhani et al., 2021; Schwanz et al., 2020; Thompson et al., 2014) was proven to improve the ionic conductivity of the electrolyte up to 10^{-3} S cm^{-1} (Deviannapoorani et al., 2013) and to ensure a higher phase stability of the cubic polymorph at room temperature (Gai et al., 2018). A critical challenge regarding ceramic electrolytes involves the synthesis-and densification of the material at low temperature in order to avoid possible side reactions with cathode materials (Vardar et al., 2018). In order to achieve a pure cubic phase with conventional methods, the sintering process is generally carried out at very high temperatures, well above 1000 °C. Extreme conditions may have a negative effect on the structure, with an increased loss of lithium and partial decomposition that can produce impurities and hamper a proper densification (Paolella, Zhu, Bertoni, Savoie, et al., 2020; Yan et al., 2019; S. Zhang et al., 2020). Recent strategies for promoting the densification of ceramic materials include the control of reaction atmosphere (Z. Huang et al., 2017; Y. Li et al., 2014), application of more performant sintering techniques, such as hot-pressing (David et al., 2015; Raju et al., 2021), and the introduction of sintering agents, such as Li_3BO_3 (Janani et al., 2014) or Al_2O_3 (Y. Wang et al., 2016). Another well explored method for particle size reduction of nanocrystals involves the use of surface-capping agents (Losch et al., 2019), including metal oxide and ionic salts (H. Zhang, Jin, et al., 2013), which act as surfactants and directly influence the distribution of active crystal surfaces, leading to different crystal shapes and sizes. However, the application of surfactants reduces the scalability of the whole process, hence there is the need for more tailorable methods for size modification. For this, we propose the use of carbon-based additives to tune both the synthesis rate and temperature, as carbon can stabilise the electrolyte phases at high temperatures due to their excellent electrical and thermal conductivity and stability. Therefore, carbon additives should not only mediate the high temperature sintering process but act as dopant or phase stabilising agent to offer better synthesis flexibility in terms of phase and particle size distribution, which is important step towards the optimisation of electrolyte densification, thus enabling solid electrolyte technologies. Although carbon is commonly used as

additives to process Li ion electrodes (e.g., slurry casting (X. Fan et al., 2021)), their beneficial roles in ceramic synthesis have not been characterized to date.

In the present work, we investigated how the incorporation of carbon affects the synthesis process and chemical properties of $Li_7La_3Zr_2O_{12}$ (LLZO) solid electrolyte. The material was synthesized by a modified standard solid-state route using two types of carbons. These include a low surface area graphitic carbon and a high surface area activated nanometric carbon black. *In situ* and *ex situ* X-ray diffraction allowed to study the crystallization and phase formation while the particle morphology was explored by scanning and transmission electron microscopy. Our analysis focused, in particular, on the evolution of solid phases throughout the annealing process, densification of the material and resulting particle size. Electrochemical analyses were eventually performed, and the total ionic conductivity of the material was evaluated. (The results of this work are protected by the patent No. US 2021/0147299 A1) (Paolella et al., 2021).

5.2.3 Experimental

Ga-doped LLZO samples with nominal composition $Li_{6.25}La_3Zr_2Ga_{0.25}O_{12}$ were synthesized via a conventional solid-state reaction. Stoichiometric amounts of Li_2CO_3 (99.99%, Sigma-Aldrich), La_2O_3 (≥99.9%, Sigma-Aldrich), ZrO_2 (99%, Sigma-Aldrich) and Ga_2O_3 (≥99.99%, Sigma-Aldrich) were used as precursors. MAG graphitic carbon (Hitachi) and DENKA acetylene carbon black were added in fixed amounts to the precursors mix (from 10 to 100 wt.% of the mass of Li_2CO_3). A 10 wt.% excess of Li_2CO_3 was added to the mixture to compensate for the loss of lithium during synthesis. The precursors were mixed and finely ground for 8 h at 400 rpm using a Retsch PM-100 planetary ball mill with 16 mm zirconia balls. The powders were first calcined at 1000 °C for 3 h in Ar atmosphere to ensure the formation of cubic LLZO and subsequently reground and treated again at 1000 °C under air atmosphere to remove any trace of carbon. The hot-press treatment was carried out on ~1 g of powder by applying a pressure of 56 MPa for 1 h at 800 °C under Ar atmosphere, with a temperature ramp of 20 °C per minute. The annealing process was carried out in a 16 mm Si_3N_4 die, and carbon films were applied on both sides of the pellet.

In-situ high temperature X-ray diffractometer (Smartlab, Rigaku) was employed to monitor the LLZO phase formation from the sample mixtures with and without carbon. The mixtures of

LLZO precursors were heated to 900 °C at a rate of 5 °C/min and held at the temperature for 2 hours under nitrogen flow. The XRD data were collected at a step size of 0.04° and a scan rate of 13.7°/min with Co-K_α radiation. *Ex-situ* X-ray diffraction was performed using a Rigaku Miniflex600 diffractometer with Co-K_α radiation at room temperature in a 2θ range of 10°-100° at a step of 0.02°. Thermal analyses (TGA and DTA) were performed with the help of a Netzsch STA 449 C thermobalance in the temperature range from 35 to 1000 °C at a temperature ramp of 10 °C/min. The surface morphology and microstructure of the powders were investigated by scanning electron microscopy (SEM, Hitachi FlexSEM1000) at a 5 kV accelerating voltage. Annular dark field scanning transmission electron microscopy (ADF-STEM) and bright field high resolution transmission electron microscopy (HRTEM) (Thermo Fischer Scientific Talos 200S) were used to examine the local microstructure of carbon doped LLZO under operating voltage of 200 kV. Cross-section surfaces were prepared by using an Ar Ion Milling IM4000 Plus (Hitachi, Japan) with an ion beam energy of 6 kV at a fast and 30° rotation for 4 h and subsequently analyzed using a Lyra 3 (TESCAN) SEM. Impedance spectra were collected to measure ionic conductivity, using a BioLogic VMP-300 potentiostat by applying an AC perturbation of 5 mV in a frequency range from 7 MHz to 1 Hz, in a temperature interval between 25 °C and 80 °C. Stability towards Li metal was explored in Li/Li symmetric cells assembled by placing thin Li foil on both sides of the ceramic pellet. The cells were cycled at 25 °C and 80 °C, applying a current density of 100 µA cm^{-2} during both charge and discharge.

5.2.4 Results and Discussion

The evolution of LLZO phase with carbon addition was explored using *in situ* XRD to better understand the reactivity of the precursors and their roles in the phase formation process (**Figure 5.1a**). For the carbon-free sample, the decomposition of Li_2CO_3 into Li_2O, possibly to nano-size or amorphous form, is observed at temperature above 700 °C, according to the equation $Li_2CO_3 \rightarrow Li_2O + CO_2$. On the other hand, the incorporation of carbon additive in the mixture is shown to shift the starting decomposition temperature of Li_2CO_3 to a lower value, about 670 °C, **Figure 5.1c**. Previous results reported in literature showed a consistent behavior, presenting a lower decomposition temperature of carbonates in the presence of carbon with direct evolution of CO and faster formation of oxide according to the reaction $Li_2CO_3 + C \rightarrow Li_2O + 2\ CO$ (J.-W. Kim & Lee, 2001). XRD patterns do not reveal a presence of the oxide phase and detection of the

first traces of LLZO started at temperature as low as 730 °C for the carbon-added sample. Therefore, it is reasonable to assume the reaction followed the route of 3.5 Li_2O + 2 ZrO_2 + 1.5 $La_2O_3 \rightarrow$ c-$Li_7La_3Zr_2O_{12}$. The characteristic peaks displayed in **Figure 5.1b** (black pattern) show that cubic LLZO becomes the major phase in the sample upon reaching about ≥ 820 °C. In the carbon-free sample, a noticeable amount of $La_2Zr_2O_7$ is first observed at 745°C, (**Figure 5.1b**, red pattern) and the presence of LLZO starts at ~800°C in the final mixture. LLZO becomes one of the major phases only above 820 °C. The formation of the cubic LLZO phase is mainly related to the reaction between the mixed phases and other Li containing phases (possibly according to $La_2Zr_2O_7$ + Li_2ZrO_3 + Li_2O + $La_2O_3 \rightarrow$ c-$Li_7La_3Zr_2O_{12}$). For temperatures above 865 °C, the patterns for both LLZO samples (with and without carbon addition) show the main presence of cubic LLZO phase. This investigation reveals that the introduction of carbon in the mixture tends to decrease the synthesis temperature of the material. The main differences between carbon-rich and carbon-free LLZO formation are: (1) carbon incorporation decreases the onset temperature of LLZO formation; (2) it eliminates the formation of intermediate phases, mainly $La_2Zr_2O_7$, and LLZO formed from simple oxides; (3) more unreacted La_2O_3 was observed in the carbon-added LLZO than the carbon-free material.

To better understand the evolution of the materials during the synthesis, a thermal analysis of the mixture of precursors was carried out and the results are reported in **Figure 5.1c**. The TGA curves (black lines) were collected between 35 and 1000 °C and the curve for the carbon-free powder shows an onset temperature of the mass loss of about 745 °C, whereas the curve related to the sample prepared with carbon displays a notable decrease in the temperature to 687 °C, with an average mass loss of about 20%, which is in agreement with the results of the *in situ* XRD analysis and confirms the lower decomposition temperature of the carbonate. The continuous increment in the DTA curve (red lines) for the carbon-doped sample, which begins at the onset temperature of the mass loss, indicates that the carbothermic decomposition of the carbonate is a process having a strongly endothermic behavior. The scheme reported in **Figure 5.1d** shows a representation of the effects of carbon addition on the synthesis of LLZO as revealed by the *in situ* investigation. The introduction of carbon additive in the mixture leads to a partial evolution of CO gas upon heating and allows to generate Li_2O at lower temperature which is below the formation temperature of intermediate phase, such as $La_2Zr_2O_7$; thus, the formation of this Li free phase is limited. The

presence of liquid in the reactants promotes a direct reaction between those isolated reaction precursors and Li_2O allows for a formation of cubic LLZO at lower reaction temperature. In **Figure 5.S1** we reported the TGA curves of Li_2CO_3 with and without addition of DENKA carbon and a similarity in the thermal behavior can be observed, with the sample incorporating carbon showing a more rapid onset for mass loss than the pristine Li_2CO_3 and a steeper curve at higher temperatures (above 800 °C), indicating the influence of carbon in the decomposition process.

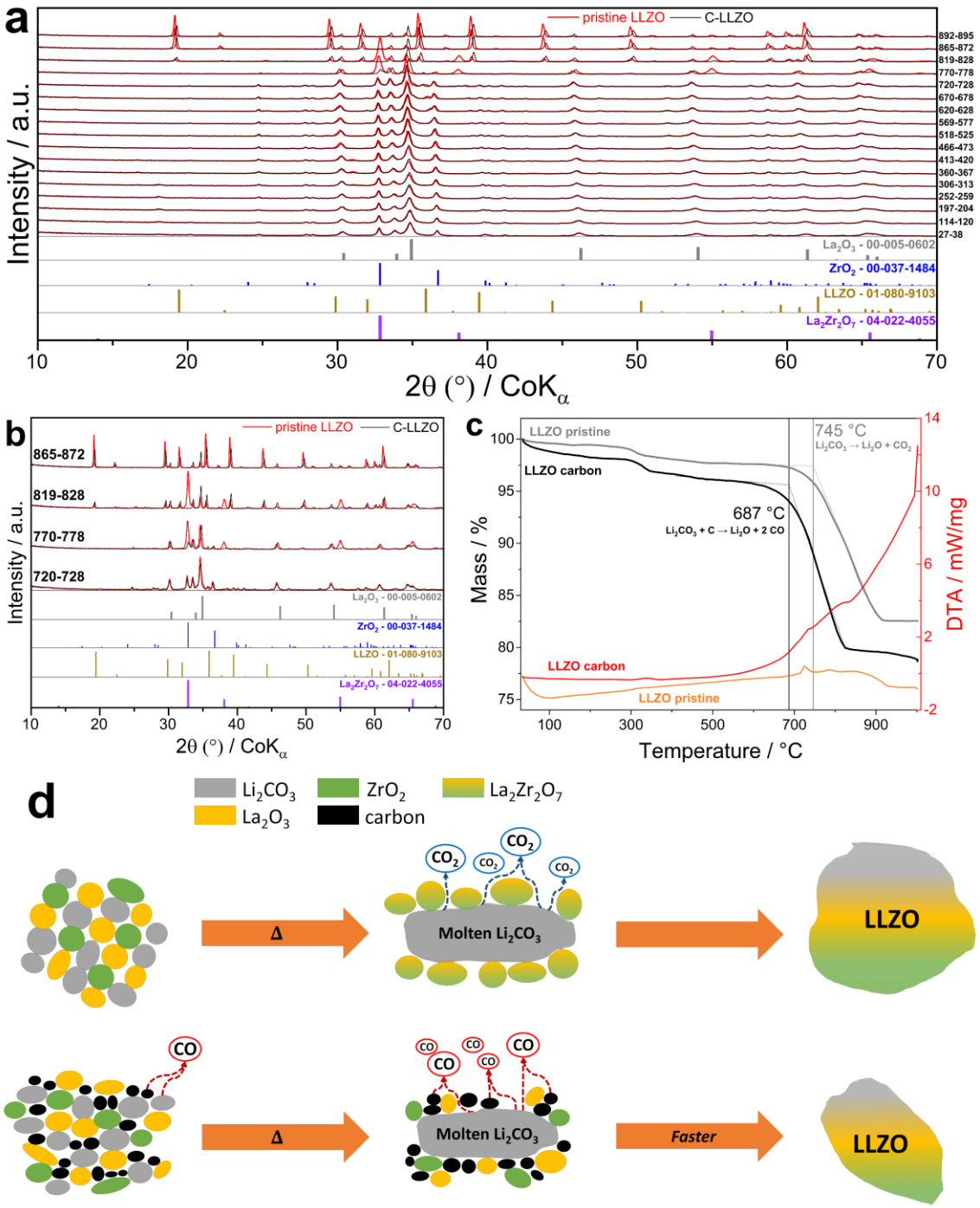

Figure 5.1. a) Evolution of XRD patterns during the heating process of LLZO precursors from room temperature up to 900 °C; b) Highlighted XRD patterns in a narrower range of temperatures (from 720 to 872 °C); c) Thermal curves (TGA and DTA) for the LLZO powder precursors with and without carbon addition, in the temperature range from RT to 1000 °C; d) Schematic representation of the effects of carbon addition on the LLZO formation process.

To better expose the effects of the introduction of carbon even in presence of doping agent, a more defined structural characterization was performed on Ga-doped LLZO samples. **Figure 5.2a** presents XRD patterns for a series of LLZO samples prepared with different carbon contents and the tests were performed after a first annealing step in inert Ar atmosphere and after a subsequent step under air flow. For pristine LLZO a single pattern is reported, after the sintering step in Ar atmosphere. After the preliminary treatment at 1000 °C in Ar for 3 h, the presence of a major cubic-LLZO phase can already be observed for the samples with a lower carbon content (MAG10 and DENKA10, both with 10 wt.% carbon with respect to Li_2CO_3). Interestingly, the diffraction patterns for the MAG50 and MAG100 samples, with a higher carbon-to-lithium ratio, after the first treatment in the same working conditions, display additional diffraction peaks which refer to unreacted precursors such as La_2O_3 and ZrO_2. The presence of carbon can explain this phenomenon: the excess of carbon in the starting mixture can envelop the particles of precursors in the mixture, with a possible detrimental effect on their interaction during the annealing, leading to an incomplete formation of the final phase. This can also be visibly observed by a direct comparison of the resulting powders after the calcination. Photos of the powders resulting after the first thermal treatment in Ar are reported in **Figure 5.S2** and from the images it is clearly visible that the samples with low carbon content have an aspect similar to the pristine carbon-free powder in terms of color and grain, whereas the MAG50 and MAG100 samples, with high carbon content, after the first treatment still display a very dark grey color due to carbon still present in the mix.

After the first calcination step under Ar flow, all the samples were re-treated at 1000 °C in air atmosphere to remove the unreacted carbon. The XRD patterns after the second thermal treatment under air display the typical peak pattern of a pure cubic LLZO phase for all the different samples, with the disappearance of the extra peaks in the high-carbon content samples (e.g., La_2O_3). **Figure 5.2b** shows the average values of the crystallite size for the different materials (see the red curve). The graph shows the highest value of the crystallite dimensions for the sample without carbon addition (533 Å), whilst even a reduced incorporation of carbon leads to the decrease of the crystallite size, as observed for the MAG10 sample (467 Å) showing a decrement in size of about 13%. The lowest values are reached for the MAG50 (404 Å) and MAG100 (427 Å) samples with the highest carbon content, with a decrement in size of 20% with respect to the pristine material. The cell parameter for the different compounds is also reported in the graph (blue

curve) and it can be observed that the resulting values lie around 12.98 Å with negligible variation. The values of the cell parameter are consistent with the ones already reported in literature (Xiang et al., 2019), indicating that the incorporated carbon does not affect the crystal structure of LLZO but remains confined at the grain boundaries, hindering the grain growth during the synthesis.

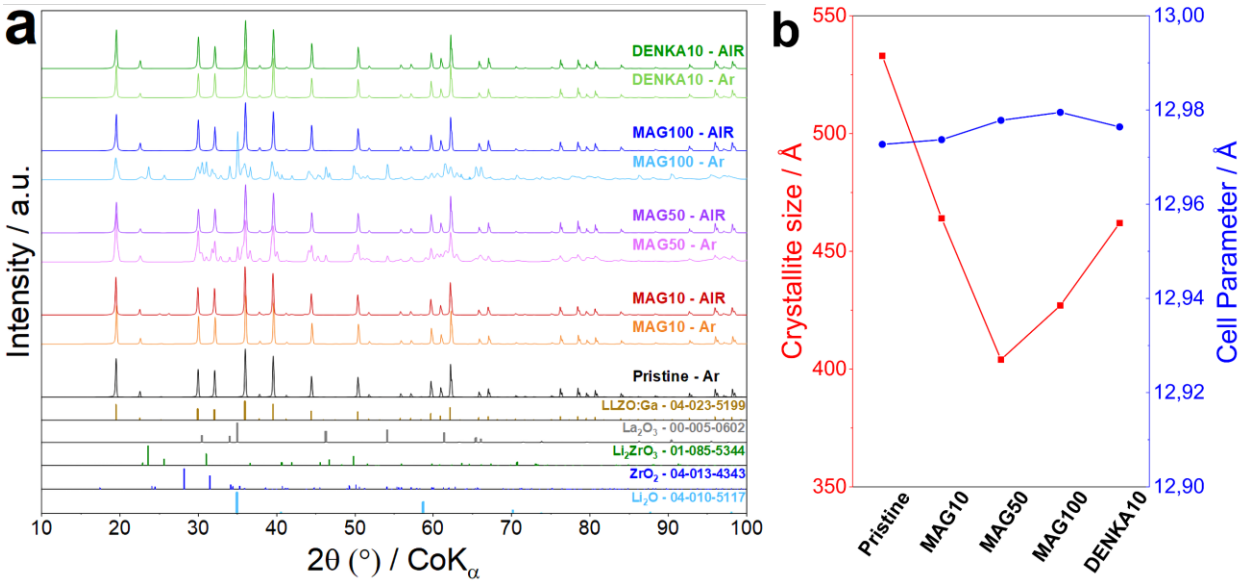

Figure 5.2. a) Comparison between the diffraction patterns of different Ga-doped LLZO samples prepared with increasing carbon content, after a first annealing step in Ar atmosphere and a second thermal treatment in air; b) Reported values of the average crystallite size and cell parameter for the different LLZO samples after the thermal treatment in air.

To evaluate the consequences of carbon addition on the morphology of the materials we performed SEM observations on the powders of the different materials. The resulting images are reported in **Figure 5.3.** The SEM images reveal for all the compounds the typical potato morphology of garnet LLZO with well-distinguishable micrometric particles of heterogeneous size. At the same time, however, the images display an evident reduction in the average particle size for the samples with increased content of carbon. The MAG50 (**Figure 5.3c**) and MAG100 (**Figure 5.3d**) samples manifest the presence of very small particles on the surface, in the dimension range of 1-2 μm and with a smooth and rounded shape. The introduction of high amounts of carbon in LLZO is therefore shown to have remarkable impact on the dimension of the final particles. A similar situation can be observed for the DENKA10 sample (**Figure 5.3e**) prepared with nanometric-sized carbon, for which the presence of particles with reduced average size can be observed, along with larger grains with an irregular elongated shape. A statistical

analysis has been performed on the SEM images to estimate the average particle size and the rough values obtained are reported in **Table 5.S1**. The results indicate a clear decreasing trend in the particle average dimension going from 7.87 μm for pristine LLZO to about 3.4 μm for MAG50 and MAG100, confirming the effects of the carbon additives on particle formation. The diminution of the standard deviation values also points out a more homogeneous particle size for carbon-rich materials. The value reported for DENKA10 sample is also interesting, 3.98 μm, definitely smaller than the value for MAG10 (5.88 μm) despite the incorporation of carbon in the same mass ratio. This indicates that the nature of the carbon additive itself influences the formation of LLZO particles in different ways and the utilization of smaller-sized nanometric carbon may lead to more equable distribution of the carbon particles in the grain boundaries, hindering the grain growth. Furthermore, the more intimate mixing of the precursors with the additive allows carbon combustion to occur more homogeneously in the bulk of the material. Consequently, the uniform temperature increment in the powder results in the formation of ceramic particles with smaller dimensions.

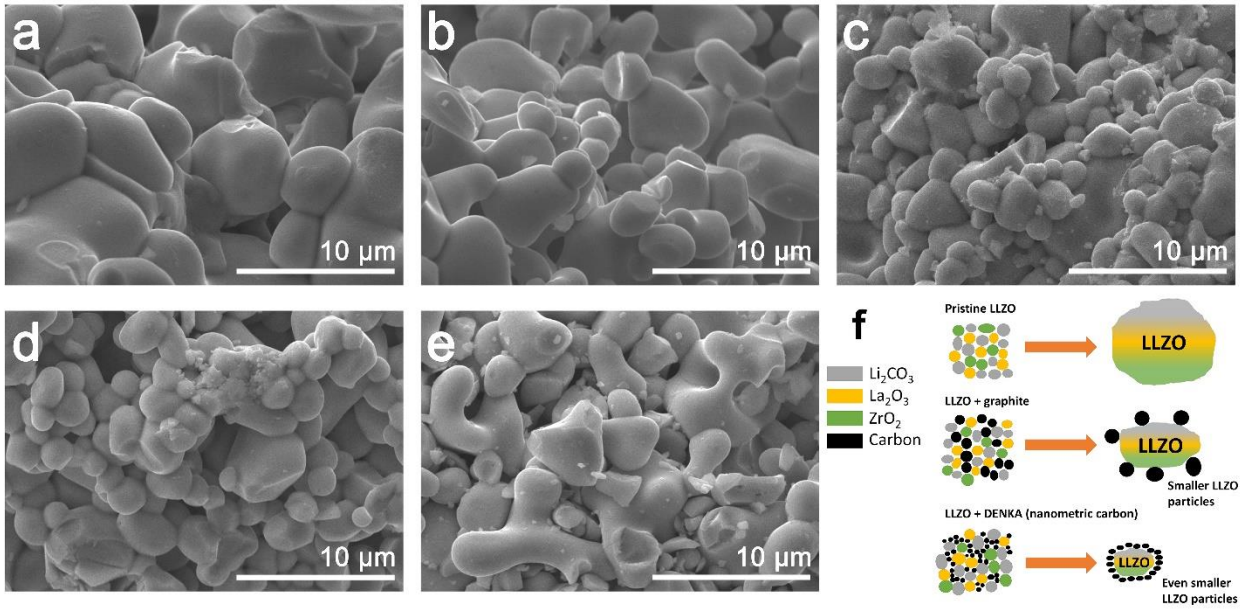

Figure 5.3. SEM images of Ga-doped LLZO powder samples after final treatment in air atmosphere: a) Pristine; b) MAG10; c) MAG50; d) MAG100 and e) DENKA10; f) Schematic representation of the influence of different carbon on the particle size of LLZO.

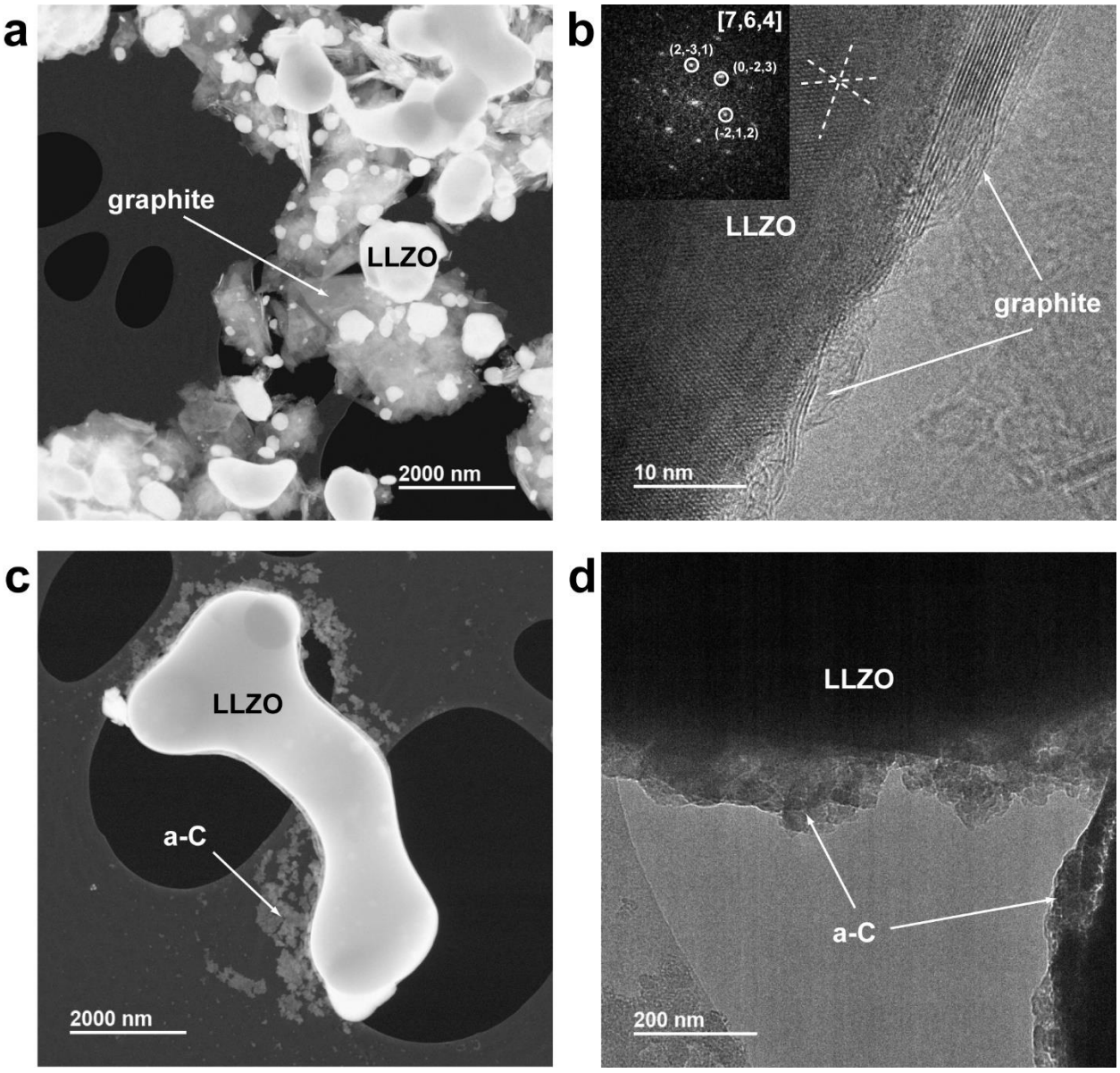

Figure 5.4. Comparison of MAG100 (a, b) and DENKA10 (c, d) LLZO samples from transmission electron microscopy. a) ADF STEM image from MAG100. LLZO appears white due to La and Zr heavy atoms, while carbon looks darker due to its low atomic number. Large flakes of graphite are indeed present between the LLZO crystals. (The darker film with holes is the amorphous carbon film support of the TEM grid). b) HRTEM image from MAG100. In inset, FFT-derived diffractogram of the LLZO crystal, showing the orientation in the [7,6,4] direction and the corresponding families of planes (indicated with dashed lines in the HRTEM image). c) ADF STEM image from DENKA10 sample showing LLZO and carbon. d) HRTEM image from DENKA10

A more precise investigation on the effects of using different carbon was performed via transmission electron microscopy (TEM) of the powders. **Figure 5.4** shows TEM images of MAG100 and DENKA10 samples. It can be observed that, for the MAG100 sample, large flakes of graphitic carbon are present in between the small LLZO particles, and the formation of a graphite layer indicates a partial exfoliation reaction of the graphite flakes during the milling process (**Figure 5.4a**). The HRTEM image and diffractogram in **Figure 5.4b** demonstrate the presence of a pure LLZO phase at the interphase with graphite flakes, without any intermediate phase. In the image, a ≤10 nm graphitic carbon layer (with the characteristic (002) planes of graphite at 0.34 nm) is clearly visible at the edge of the LLZO crystals, as indicated by the white arrows. For the DENKA10 sample, **Figure 5.4c** shows the presence of a ~50 nm layer rich of carbon nanoparticles (a-C) on the surface of the LLZO crystals as shown by a closer inspection with HRTEM (**Figure 5.4d**).

To evaluate the total conductivity of the different LLZO materials, ceramic pellets were prepared by hot-pressing the annealed powders at 800 °C under a pressure of 56 MPa. The resulting pellets were subsequently inserted in coin cells between stainless steel blocking electrodes (**Figure 5.5a**). The EIS analyses were performed in a temperature range from 20 to 80 °C. The corresponding Nyquist plots display the presence of two partially convoluted semicircles, the first one of which is collected at high frequencies and the second one appears at lower frequencies. A similar behavior for hot-pressed LLZO has been reported by Tenhaeff et al. (Tenhaeff et al., 2014), but the exact nature of the phenomenon associated with the low-frequency semicircle was not explained. The equivalent circuit employed to describe the separate contributions is represented in **Figure 5.5b.** The circuit comprises resistors (R) and constant-phase elements (CPE), the latter of which were used instead of pure capacitors due to non-ideal behavior of capacitive contributions. More specifically, R_0represents the external circuit resistance, not associated with the material; the parallel R_{gb} and CPE_{gb} elements are related to the grain-boundaries ion transport. R_{low} and CPE_{low} give rise to the unidentified low-frequency semicircle and CPE_{dl} indicates the double-layer capacitance of the blocking electrodes. The Nyquist plots collected at 25, 50 and 80 °C, respectively, are reported in **Figure 5.5c-e**. Fitting of the EIS data with the equivalent circuit of Figure 5b allowed to derive the total ionic conductivity of the pellets of different LLZO samples. **Figure 5.5f** reports the Arrhenius plot with the resulting values of conductivity and it can be

observed that the materials prepared with higher amounts of carbon are in general more conductive than the pristine material. Linear fitting of the Arrhenius plot expressed in the form $\ln(\sigma) = \ln(A) - E_a/RT$ was used to determine the values of activation energy, which lie in the range of 0.41-0.43 eV. These results agree with typical values for LLZO previously reported in literature (El Shinawi & Janek, 2013b; C. Li et al., 2017; Tenhaeff et al., 2014). The ionic conductivity shows an increasing trend starting from pristine carbon-free LLZO, moving to samples with increasing carbon content (**Table 5.1**). In particular, MAG100 exhibits a room temperature ionic conductivity of 5.02×10^{-5} S cm^{-1}, with an increment of about 30% with respect to pristine LLZO (3.53×10^{-5} S cm^{-1}). Furthermore, the material reporting the highest values of conductivity is DENKA 10, which exhibits a room temperature ionic conductivity of 5.95×10^{-5} S cm^{-1}, a value about 40% higher than LLZO made by a carbon-free route. This difference in conductivity increases to about 65% at high temperature (7.40×10^{-4} S cm^{-1} for DENKA10 versus 4.47×10^{-4} S cm^{-1} for pristine LLZO at 80 °C). This phenomenon can be explained by the variation in the particle size produced by the carbon incorporation in the sintering process. As previously stated in **Figure 5.3**, the carbon additive is shown to have an impact on the grain dimension and the smaller size of the particles has a positive effect on the compactness of the final pressed pellet. The effect of particle size on densification can be observed in the cross-section SEM images reported in **Figure 5.S3**, in which a general reduction of the grain dimension along with a visible decrement in the extension of void spaces and pores is achieved. The images therefore give additional indication that the incorporation of carbon helps improve the densification process of the ceramic pellets. To have a better view of the possible application of carbon-LLZO as a solid electrolyte in batteries tested LLZO-DENKA10 in a Li/Li symmetric cell to observe its behavior towards metallic Li. The results are reported in **Figure 5.S4**. The Li//LLZO//Li symmetric cell cycled at 25 °C shows a ragged cycling profile with a high polarization in the first hours. After 60 hours of cycling, the polarization peters down to 0.1 V, whereas the cycling profile remains uneven. This mainly depends on the very resistive interface between LLZO and Li metal, and the effect is further amplified by the possibly poor contact between the pellet and the Li foil during the assembly of the cell. To overcome this issue, another cell was assembled using a polymeric interface (PEO:LiTFSI) between the electrode and the electrolyte. This cell, cycled at 80 °C, exhibits a significantly more regular cycling profile and a low polarization of 0.05 V from the beginning, which remains constant for over 60 h. A comparison was attempted with commercial Al-doped LLZO, but the densification in the same

working conditions (800 °C/1 h) resulted in an extremely brittle pellet, which crumbled into pieces just after the process, as shown in **Figure 5.S5**.

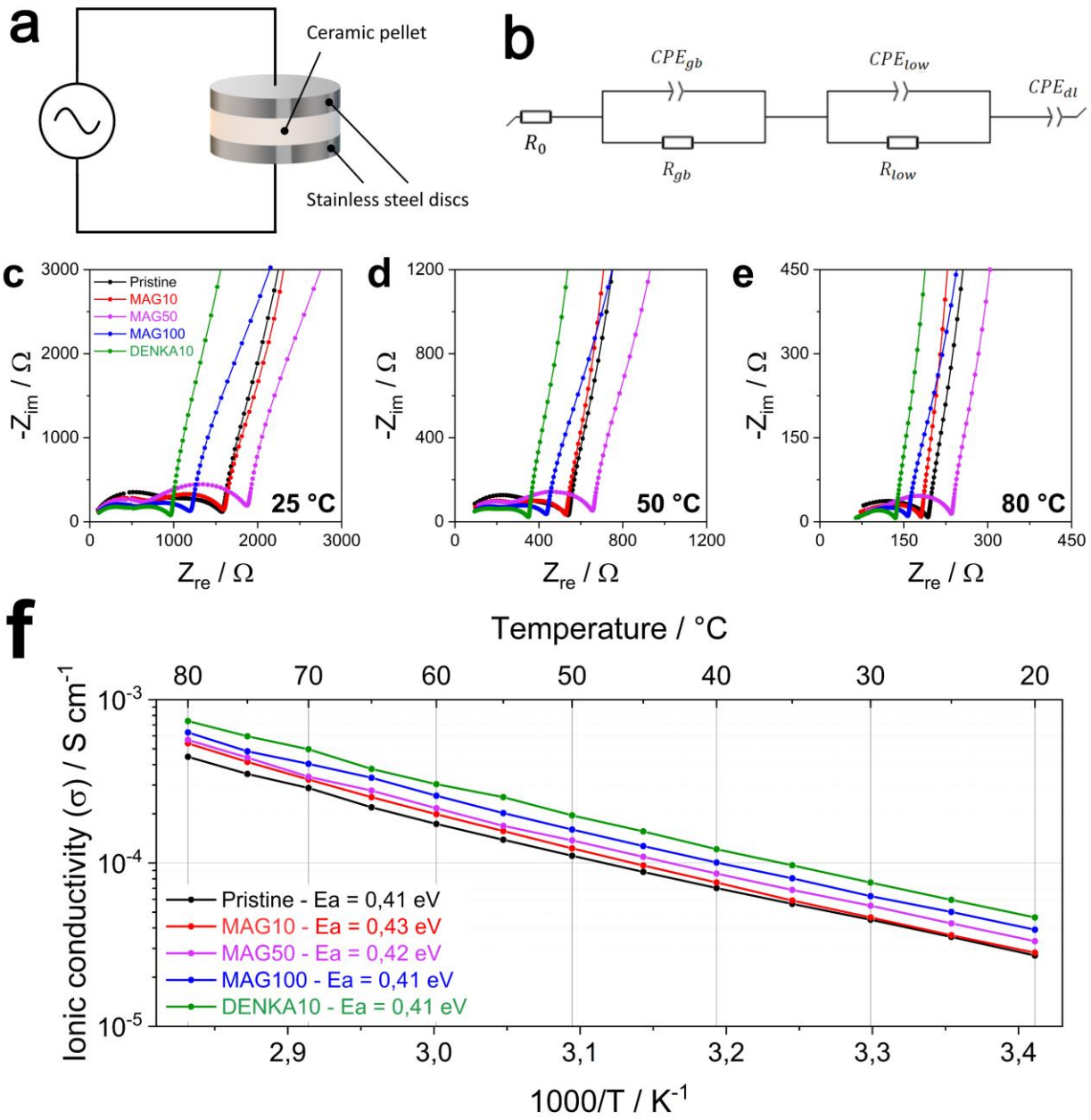

Figure 5.5. a) Schematic representation of the cell setup employed for EIS tests of the materials; b) Representation of the equivalent circuit used for data fitting; c-e) Nyquist plots of the impedance for different LLZO samples measured at c) 25 °C, d) 50 °C and e) 80°C, respectively; f) Arrhenius plot for total ionic conductivity of the different LLZO samples in the temperature range from 20 to 80 °C.

Table 5.1. Values of conductivity at different temperatures of the different LLZO samples

Sample	σ (25 °C) / S cm^{-1}	σ (50 °C) / S cm^{-1}	σ (80 °C) / S cm^{-1}
Pristine	3.53×10^{-5}	1.11×10^{-4}	4.47×10^{-4}
MAG10	3.61×10^{-5}	1.23×10^{-4}	5.40×10^{-4}
MAG50	4.27×10^{-5}	1.23×10^{-4}	5.68×10^{-4}
MAG100	5.02×10^{-5}	1.60×10^{-4}	6.30×10^{-4}
DENKA10	5.95×10^{-5}	1.96×10^{-4}	7.40×10^{-4}

5.2.5 Conclusions

In our work we reported the effects of carbon incorporation in the synthesis and calcination of LLZO solid electrolyte prepared via conventional solid-state route. The addition of carbon in the precursor mix is shown to have an impact on the nature of the reaction mechanism and the decomposition temperature of lithium carbonate, allowing the formation of cubic-phase LLZO at temperatures as low as 720 °C. Moreover, the presence of the carbon additive has a remarkable effect that reduces the crystallite size, where the use of smaller-sized nanometric carbons such as DENKA has even more prominent effect on the average particle dimensions compared to the pristine carbon-free material, resulting in smaller particles with a lower carbon ratio in the precursor mix. The insertion of carbon has also shown to ameliorate the ceramic densification in hot-press even at lower temperatures, leading to a higher density. Electrochemical impedance spectroscopy measurements confirmed the results, showing an increment in total ionic conductivity for carbon-rich LLZO of more than 30 % compared with pristine LLZO, with the best value of 5.95×10^{-5} S cm^{-1} reported for DENKA10. The present work shows a new and original method to improve the physical and electrochemical properties of garnet based solid electrolytes.

5.2.6 Acknowledgements

This research was funded by Hydro-Québec's Center of Excellence in Transportation Electrification and Energy Storage, Varennes, Québec. A. P. thanks Prof. Karim Zaghib of Concordia University (Canada) and dr. Hendrix Demers of CEETSE (Canada) for their useful suggestions. D.C. acknowledges the financial support of Mitacs. C.G. acknowledges the Royal Society, London for an URF (UF160573)

5.2.7 Supplementary Information

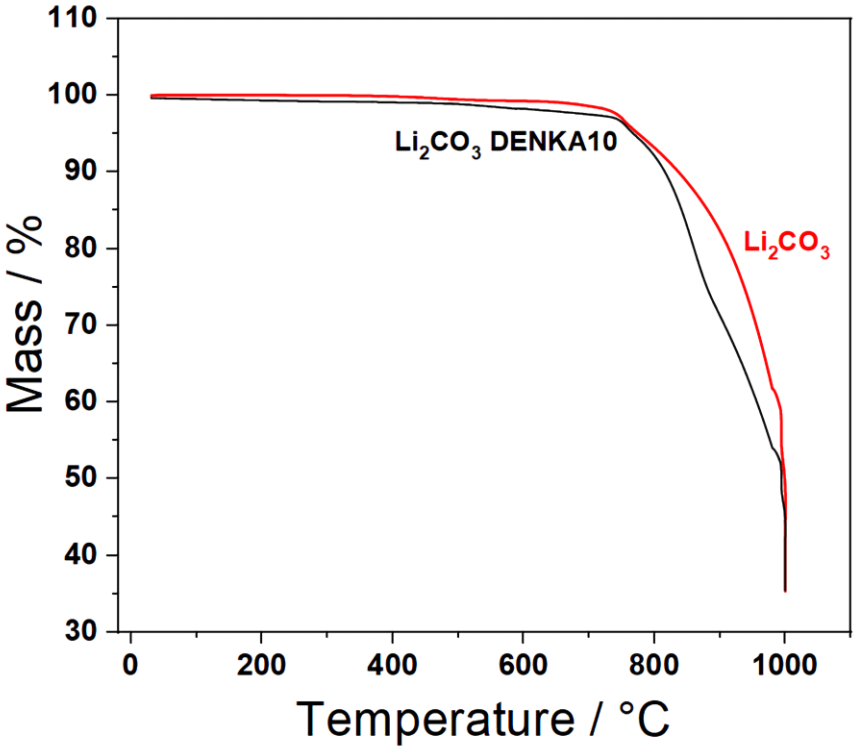

Figure 5.S1. TGA curves for Li_2CO_3 with and without addition of DENKA carbon, in the temperature range from RT to 1000 °C.

Table 5.S1. Average value of particle size from statistical analysis of SEM images

Sample	Average size / μm
Pristine	7.87 (± 3.69)
MAG10	5.88 (± 2.46)
MAG50	3.40 (± 1.52)
MAG100	3.47 (± 1.49)
DENKA10	3.98 (± 1.78)

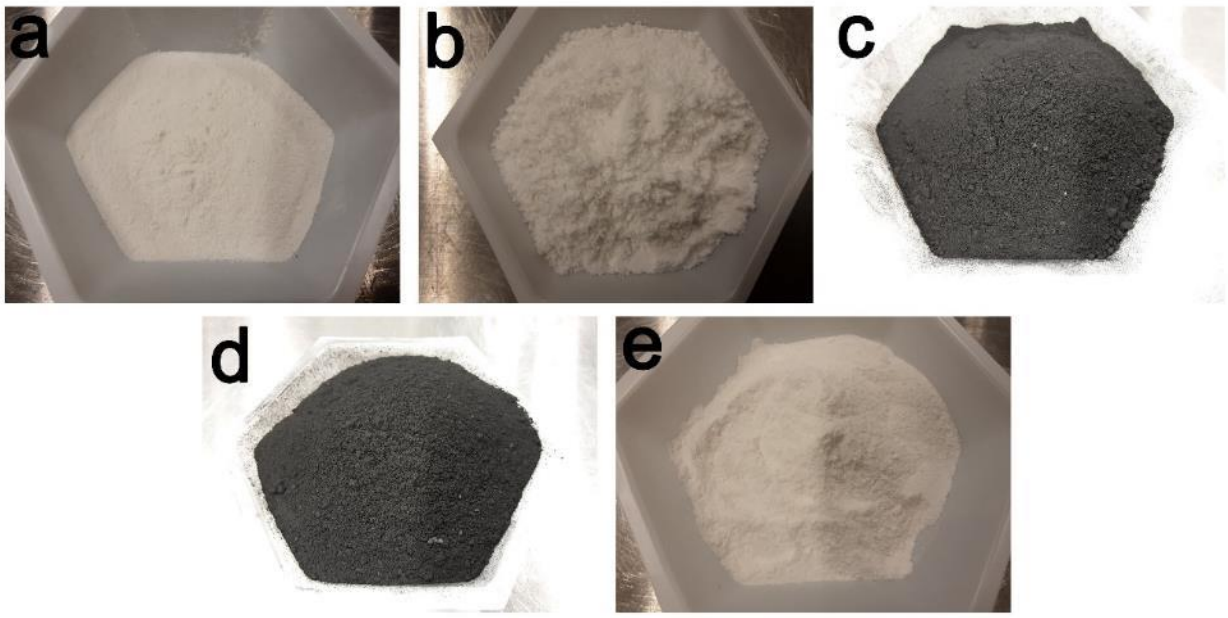

Figure 5. S2. Photographs of LLZO powders after first thermal treatment in Ar atmosphere for 3 h at 1000 °C. a) pristine; b) MAG10; c) MAG50; d) MAG100 and e) DENKA10.

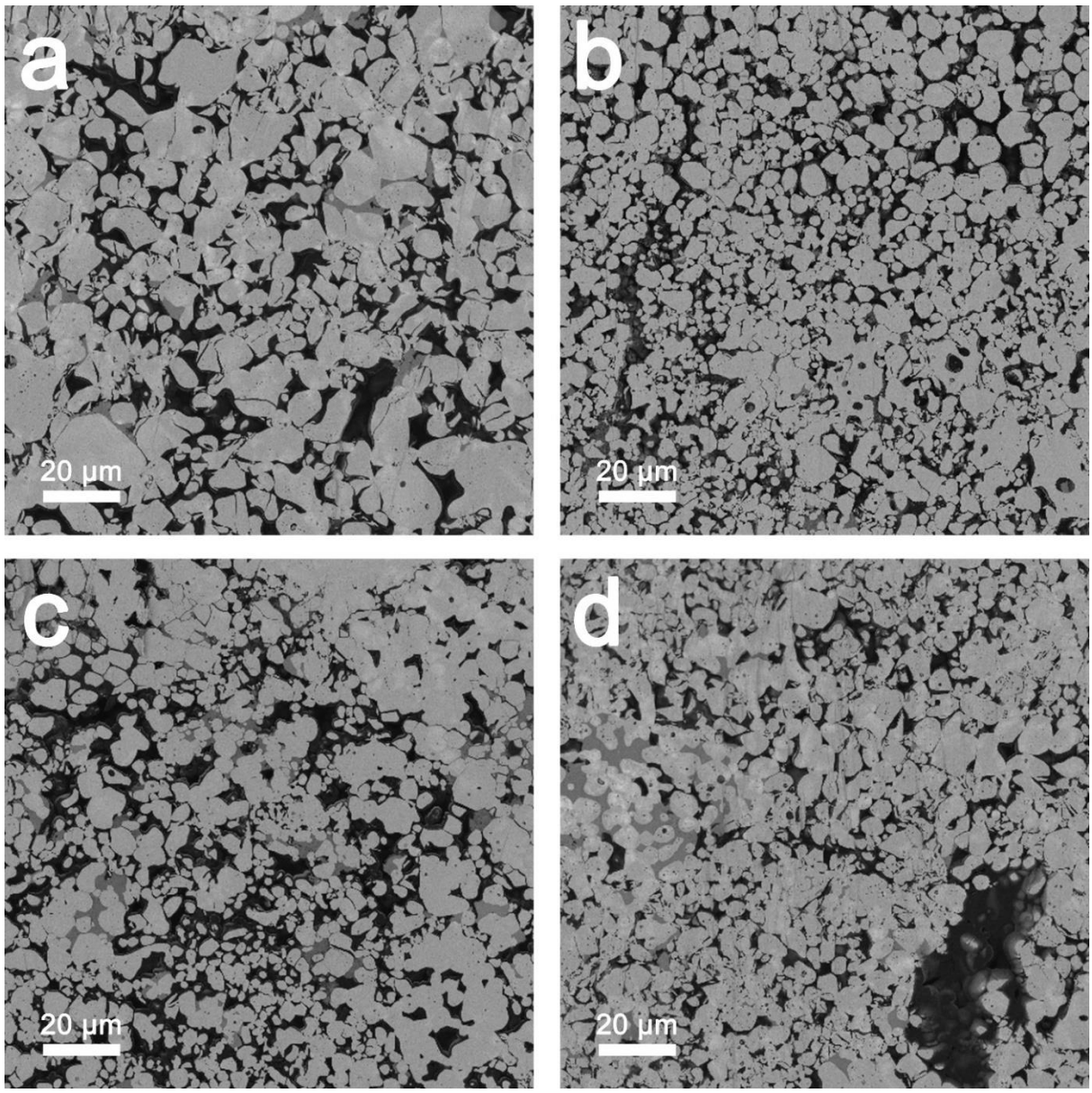

Figure 5.S3. Cross-section SEM images of Ga-LLZO pellets hot-pressed at 800 °C. a) pristine; b) MAG50; c) MAG100 and d) DENKA10.

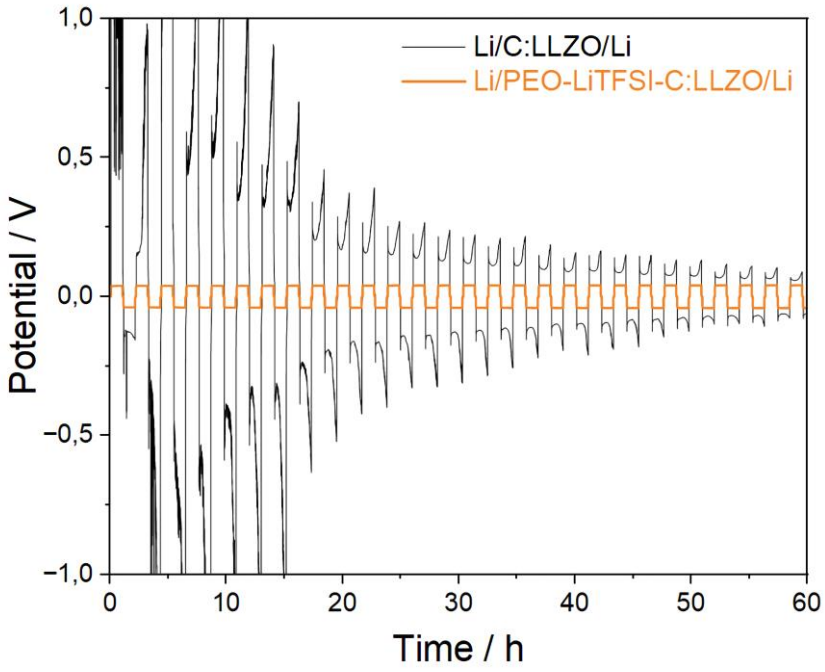

Figure 5.S4. Compared cycling profiles for Li/Li symmetrical cells containing LLZO (*C:LLZO*: LLZO-DENKA10)

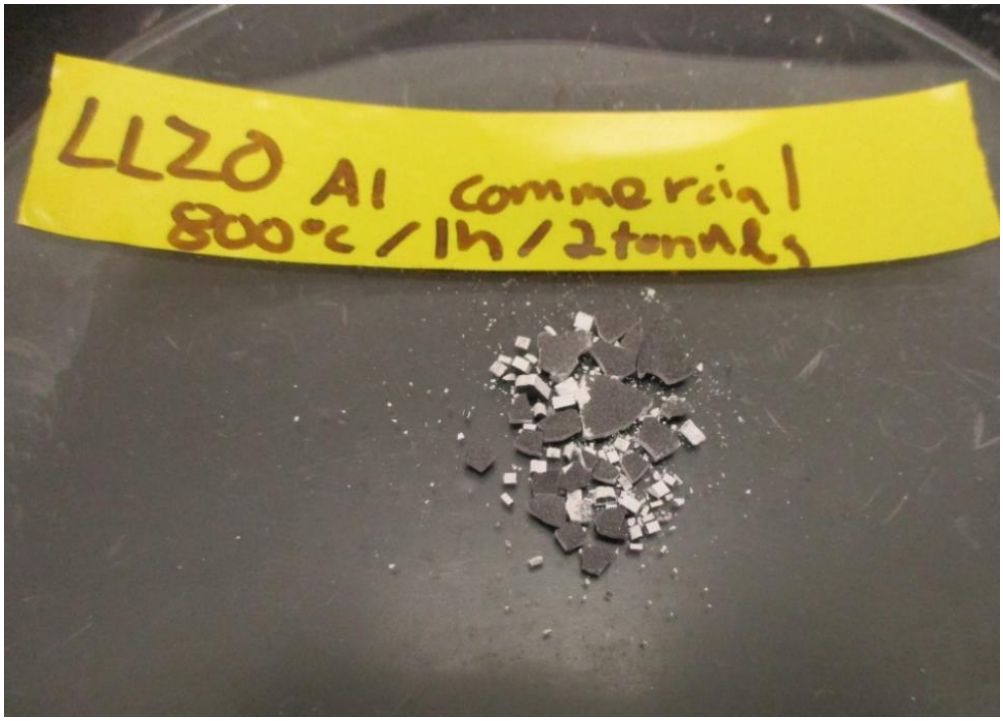

Figure 5.S5. Picture of the remains of a ceramic pellet of commercial Al-doped LLZO, after hot-pressing at 800 °C.

CHAPTER VI
HEXAVALENT IONS INSERTION IN GARNET $Li_7La_3Zr_2O_{12}$ TOWARD A LOW TEMPERATURE DENSIFICATION REACTION

6.1. Introduction

Chapter V is still centered on garnet LLZO, but in this study the role of sintering aid is hold by tellurium ions. Insertion of tellurium as a doping agent in LLZO has already been explored in the past, and the modified garnet reported remarkably high values of conductivity (over 10^{-3} S cm^{-1}). The cubic structure is positively influenced by the action of aliovalent doping, which leads to local distortions in the lattice and modifies the distribution of Li vacancies, improving ion conduction. Previous studies on tellurium doping, however, focused mainly on the electrochemical features and conductivity of the material, therefore in this investigation the action of the dopant in the densification process is the main topic. The goal of the study is to better comprehend how the introduction of dopants can act on the solid electrolytes on a more macroscopic scale, directly influencing the synthesis and reactivity of the material. The structural analysis unveils the differences in the formation mechanism between Te-free and Te-doped samples, revealing a faster formation of the cubic phase at lower temperatures for the sample using tellurium, with a direct mechanism and no presence of intermediates. A good balance in the insertion of dopants needs to be achieved, and diverse compositions with increasing Te content were subsequently investigated. In the same synthesis conditions at 750 °C, using even minimal quantities of Te in the mix generates a prevalent cubic phase, while the preparation without doping leads to an impure tetragonal phase. The beneficial consequences of elemental doping are confirmed by molecular calculations, which indicate an entropy stabilization for the doped phase leading to a lower synthesis temperature compared to the undoped product. A reduction in the average particle size is visible for increased tellurium content in the ceramic, and the results of Chapter IV pointed out a benefit in densification for a smaller-sized ceramic precursor; this can indicate an advantageous outcome for the sintering of Te-doped LLZO. Application of the hot-pressing method allowed a low temperature sintering of the electrolyte, achieving notable values of conductivity for

densification temperature between 600 and 700 °C. Most importantly, a direct comparison with commercial Al-doped and Ta-doped LLZO samples undergoing the same temperature treatment manifests a significant difference in conductivity, showing much higher values for the Te-doped samples, with an increase of more than one order of magnitude. The augmented sintering temperature reflects in an increased segregation of Te-rich phases in the pellets, which can have an impact in the final densification and the electrochemical performances as well.

Chapter published in ChemSusChem, **2023**, e202300399, 1-10

Author contributions: Daniele Campanella participated in the design of the study, the synthesis of the materials and the final assembly of the cells. He performed the XRD analysis, SEM analysis of the powders and electrochemical testing. He also gathered, analyzed, and interpreted the experimental data. He was responsible for the writing and the correction of the manuscript and the bibliographic research. Sylvio Savoie and Gabriel Girard aided in laboratory procedures for the synthesis of the materials. Wen Zhu participated in the *in situ* XRD testing and helped in the interpretation of the experimental data. Shirin Kaboli helped performing the cross-section SEM analysis of the samples and provided the experimental results of the tests. Abdelbast Guerfi, Martina Romio and Palanivel Molaiyan participated to the critical review and revision of the manuscript. Prof. Daniel Belanger supervised the research project and participated in designing the study. He was also involved in writing, critically reviewing, and revising the manuscript. Dr. Andrea Paolella supervised the study and was directly involved in the interpretation of the experimental data. He participated to the drafting, revising and submission of the manuscript.

6.2. Article 4: Hexavalent Ions Insertion in Garnet $Li_7La_3Zr_2O_{12}$ toward a Low Temperature Densification Reaction

Daniele Campanella[1,2], Wen Zhu[1], Gabriel Girard[1], Sylvio Savoie[1], Shirin Kaboli[1], Zimin Feng[1], Abdelbast Guerfi[1], Daniel Bélanger[2] and Andrea Paolella[3,4*]

[1]*Centre d'Excellence en Électrification des Transports et Stockage d'Energie (CEETSE), Hydro-Québec, Varennes, Québec J3X 1S1, Canada*

[2]*Université du Québec à Montréal (UQAM), Département de Chimie, 2101 Rue Jeanne-Mance, Montréal, Québec, H3C 3P8, Canada*

[3]*University of Vienna, Department of Inorganic Chemistry - Functional Materials, Währinger Straße 42,1090 Vienna, Austria*

[4]*Austrian Institute of Technology (AIT), Battery Tecnologies, Giefinggasse 2, 1210 Wien, Austria*

* Corresponding author: andrea.paolella@ait.ac.at

6.2.1 Abstract

Nowadays, solid electrolytes are considered the main alternative to conventional flammable liquid electrolytes in lithium batteries. The fabrication of these materials is however limited by the strict synthesis conditions, requiring high temperature which can negatively impact the final performances. In this work, we report a modification of garnet based $Li_7La_3Zr_2O_{12}$ (LLZO) and show that the incorporation of tellurium can accelerate the synthesis process by lowering the formation temperature of cubic LLZO at temperature below 700°C. Optimized synthesis at 750 °C showed a decrease in particle size and cell parameter for samples with higher amounts of Te. The LLZO Te0.25 material shows an ionic conductivity of 5.15×10^{-5} S cm^{-1} after hot-pressing at 700 °C that is orders of magnitude higher than commercial compositions with Ta or Al undergoing the same densification conditions, and the highest value at this densification temperature. Partial segregation of Te-rich phases occurs for high temperature densification. Our study shows the

advantages of Te insertion during the sintering process of LLZO garnet and demonstrates the achievement of highly ionically conductive LLZO with a low temperature treatment.

Keywords: Garnet solid electrolytes, ionic conductivity, hot-pressing, sintering process, LLZO

6.2.2 Introduction

The topic of energy storage has a critical importance in modern society. The rapid diffusion of portable electronic devices and the development of electric vehicles are leading to an increasing energy demand. Modern technologies moving past the traditional lithium-ion battery concept (Scrosati et al., 2011), such as Li-air or Li-S batteries, are steadily gaining attention due to their remarkable properties in terms of energy and power density (M. Armand & Tarascon, 2008; Varzi et al., 2020). Still, Li-metal batteries can be plagued by the problem of lithium dendrites (X. B. Cheng et al., 2017), which can lead to short circuiting of the battery and cause severe safety risks in the presence of flammable liquid electrolytes. In Li-air and Li-S systems, the phenomenon of electrolyte decomposition is a significant issue that seriously hinders the global performances and efficiencies of the system (G. Liu et al., 2021; Marangon et al., 2020). Because of these safety hitches, strong efforts have been made for the development of all-solid-state Li-ion batteries (ASSLIBs) (Fergus, 2010; Manthiram et al., 2017), replacing conventional graphite-based anode and flammable electrolyte with Li-metal anode and solid-state electrolyte (Manthiram et al., 2017). Among the families of materials investigated for this purpose we can find polymers (PEO-LiTFSI) (Q. Zhao et al., 2019), ceramics (e.g., garnets (C. Wang et al., 2020), perovskites (Inaguma et al., 1994), NaSICON (Anantharamulu et al., 2011; Jian et al., 2017), sulfides (Seymour et al., 2023) and halides (Campanella et al., 2021; Molaiyan et al., 2023)) and hybrids (ceramic-polymer composites) (J. Li et al., 2020; Wan et al., 2019). A good solid electrolyte should meet several requirements: a wide stability window against Li metal and high-voltage cathodes (Cavers et al., 2022; F. Han et al., 2016), a high room temperature ionic conductivity ($>10^{-3}$ S cm^{-1}) with low electronic conductivity (Gorai et al., 2021), a good chemical and thermal stability and good mechanical properties (Bedrov et al., 2017). Garnet-based solid-state electrolytes are one of the most promising solutions (Abouali et al., 2021; Thangadurai et al., 2014; X. Wang et al., 2020), due to their aptness in accommodating excess Li (Golozar et al., 2020), their remarkably high ionic

conductivities (Murugan et al., 2007; Thangadurai et al., 2003b; Thangadurai & Weppner, 2005a, 2005b), reaching 10^{-4} S cm^{-1}, and stability towards metallic Li, air and moisture (Thangadurai et al., 2003b; Thangadurai & Weppner, 2005a, 2005b). Moreover, their wide voltage stability window (up to 6 V) renders them compatible towards high-voltage cathodes (Thangadurai & Weppner, 2005b, 2005c).

$Li_7La_3Zr_2O_{12}$ (LLZO) has attracted a strong interest because of its high Li^+ ions content and occupancy of octahedral sites, which could increment Li-ion transport in the structure (Murugan et al., 2007). LLZO presents two different crystal polymorphs: a tetragonal phase (Space group: $I4_1/acd$) and cubic phase (Space group: $Ia\bar{3}d$). The two phases have the same stoichiometry and framework structure but a different distribution of Li^+ ions, which has a strong impact on the ionic diffusion mechanism and electrochemical performance (Bernstein et al., 2012). The material undergoes a tetragonal-to-cubic phase transition at high temperature (F. Chen et al., 2018) due to lithium loss (Paolella, Zhu, Bertoni, Savoie, et al., 2020), and the former exhibits an ionic conductivity ($\sim 10^{-6}$ S cm^{-1}) (Awaka et al., 2009) about two orders of magnitude lower than the latter ($\sim 10^{-4}$ S cm^{-1}) (Buschmann et al., 2011). Undoped LLZO tends to crystallize in the tetragonal phase at room temperature (Awaka et al., 2009), which has been found to be the most thermodynamically stable and is generally obtained via solid-state reactions at T ~ 1000 °C, whereas for the production of the cubic form with standard ceramic process higher temperature (above 1200 °C) are required. Ionic substitution has been proven to help decreasing the sintering temperature below 1100 °C and stabilize the cubic phase at room temperature (S. Cao et al., 2019a). The cubic phase is typically obtained with the introduction of doping elements together with the usual LLZO precursors. Partial replacement of Li with supervalent cations like Al (Geiger et al., 2011a), Ga (Wolfenstine et al., 2012) ,and Y (Deviannapoorani et al., 2016b) has been observed to increment the concentration of Li^+ vacancies in the structure (J. F. Wu et al., 2017), hence allowing to obtain a highly conductive cubic LLZO. Substitution of Zr(IV) with pentavalent cations, such as Ta (Logéat et al., 2012), Nb (Ishiguro et al., 2013) or Bi (Campanella, Krachkovskiy, et al., 2023; Schwanz et al., 2020), is another possible solution for stabilizing the cubic structure and improve Li^+ ions transport. Li et al. (Y. Li et al., 2015) showed that a partial doping with W (VI) on the Zr site has a positive effect on the densification of the material, resulting in high density and improved conductivity. Incorporating high-entropy cations within the structural scaffold can positively influence the distribution of site energies and, consequently, the

percolating transport of charge carriers, hence leading to a global improvement of the conductive properties (Y. Zeng et al., 2022). Ions such as Hf, Te, and rare earth elements may enhance the ionic conductivity of solid electrolytes of several orders of magnitude compared with the undoped materials (S.-K. Jung et al., 2022; Y. Zeng et al., 2022). Te-doped LLZO was successfully prepared via solid state reaction (Deviannapoorani et al., 2013) and presented a bulk conductivity of about 1.02 mS cm^{-1} at room temperature after high temperature sintering, whilst the simultaneous introduction of Te and Al stabilized the cubic phase and lowered the activation energy, at the expense of a lower ionic conductivity (4×10^{-4} S cm^{-1}) (D. Wang et al., 2014).

Hot-pressing has been often employed as a technique to improve the annealing process of ceramic materials and involves the concurrent application of uniaxial pressure and heat (David et al., 2015; Virkar et al., 1979). This allows a lower-temperature densification and shorter processing times and eventually leads to benefits such as a reduced loss of lithium, with positive effects on the ionic conductivity The purpose of this work is to investigate the effects of hot-pressing on Te-doped LLZO on its structural and electrochemical properties. Here, we report a series of $Li_{7-2x}La_3Zr_{2-x}Te_xO_{12}$ (x = 0.1, 0.25, 0.375, 0.5) compositions. The materials were prepared following a conventional solid-state synthesis. The evolution of crystal phases and the reaction mechanism were studied combining *in situ* and *ex situ* X-ray diffraction while scanning electron microscopy (SEM) was used to explore particle morphology and elemental distribution. Electrochemical investigations were eventually performed, allowing to evaluate the final ionic conductivity of the materials.

6.2.3 Experimental

A series of Te-doped lithium garnets with compositions $Li_{7-2x}La_3Zr_{2-x}Te_xO_{12}$ (x = 0.1, 0.25, 0.375, 0.5) were synthesized via conventional solid-state reaction. The samples are reported in the text as Te0.1, Te0.25, Te0.375 and Te0.5, respectively. The precursors LiOH (Sigma Aldrich, anhydrous powder, purity 99.9% trace metals basis) , La_2O_3 (Sigma Aldrich, powder, purity 99.99% trace metals basis), ZrO_2 (Sigma Aldrich, powder, 5 μm, purity 99% trace metals basis) and TeO_2 (Sigma Aldrich, powder, purity ≥99%) were mixed in stoichiometric amounts and ground using a Retsch PM-100 planetary ball mill in a 250 ml zirconia coated jar with 16 mm zirconia balls. A 10 wt.% excess of Li_2CO_3 was added to the mixture to make up for the loss of

lithium during the synthesis process. The materials were ground for 6 h at 400 rpm and calcined at 750 °C for 6 h. The resulting powder was subsequently hot-pressed under flowing Ar atmosphere. To avoid pellet gluing, the annealing took place in a 16 mm Si_3N_4 die with WC pistons, and carbon paper films were applied on both sides of the powder, to ensure a conductive coating for the pellet. The hot-press treatment was carried out at temperatures 600, 650 and 700 °C for 1 h under a pressure of 2 tons, with a temperature increment of 20°C per minute during the heating step. The LLZO phase formation was investigated via *in situ* X-ray diffraction with a Bruker D8 advance diffractometer equipped with an Anton Paar DHS 1100 domed hot stage, and it was performed on mixtures of LLZO precursors, both undoped and doped with Te (x = 0.25). The samples were heated to 855 °C at a rate of 30 °C/min and held at the temperature for 3 hours under air flow. The XRD spectra were collected every 6 min. The calcined powders were characterized by X-ray diffraction in a Rigaku Miniflex600 diffractometer at RT in a 2θ range from 10° to 100° with a step of 0,02° to determine the final phase of the materials. The surface morphology of the sintered powders was investigated by scanning electron microscopy (SEM) using a Hitachi FlexSEM1000 electronic microscope. SEM cross-section surfaces were set up with the help of an Ar Ion Milling IM4000 Plus (Hitachi, Japan) with an ion beam energy of 6 kV at a 30° rotation for 4 h and subsequently analyzed using a Lyra 3 (TESCAN) SEM equipped with an Oxford Instruments Energy-Dispersive Spectroscopy (EDS) detector. Electrochemical impedance spectroscopy (EIS) measurements were performed to evaluate the ionic conductivity, using a BioLogic VMP-300 potentiostat with frequency ranging from 1 Hz to 7×10^6 Hz, in a temperature interval between 25 and 80 °C for all samples.

6.2.4 Results and Discussion

6.2.4.1. Formation of LLZO followed by X-ray Diffraction

The evolution of LLZO phase following the incorporation of tellurium using *in situ* XRD is investigated to comprehend the reactivity of the precursors as shown in **Figure 6.1a**. The tellurium-free sample (black patterns) shows the evolution of synthesis intermediates $La_2Zr_2O_7$ and Li_2ZrO_3 in the temperature interval between 555 and 755 °C, following the reactions (1)

$$La_2O_3 + 2\ ZrO_2 \rightarrow La_2Zr_2O_7 \text{ and } Li_2O + ZrO_2 \rightarrow Li_2ZrO_3 \qquad (1)$$

The formation of the LLZO phase is first observed above 755 °C but the relative intensity of the peaks remains low until reaching higher temperature (>850°C). The formation mechanism is related to the reaction between the intermediates previously formed (possibly following the equation (2)

$$La_2Zr_2O_7 + Li_2ZrO_3 + Li_2O + La_2O_3 \rightarrow Li_7La_3Zr_2O_{12}\,[cubic] \qquad (2)$$

The XRD patterns display the peak of an unidentified phase around 22° during the heating steps which suddenly disappears upon reaching the hold temperature of 855 °C. On the other hand, the mixture of precursors containing Te (red patterns) exhibits a different behavior, manifesting the absence of the mixed phases during the heating segment. The evolution of the cubic LLZO phase follows directly from the synthesis precursors in the starting mix and its presence is firstly observed between 555 and 755 °C. Cubic LLZO becomes a major phase in the mix above 755 °C and the peaks related to the remaining unreacted phases of La_2O_3 steadily fade out during the high temperature hold, leaving an almost pure LLZO phase. The reaction supposedly undergoes a direct mechanism according to the equation (3)

$$1.5\ La_2O_3 + 2\ ZrO_2 + 3.5\ Li_2O \rightarrow c\text{-}Li_7La_3Zr_2O_{12} \qquad (3)$$

During the 3 hours hold time at 855 °C, the diffraction patterns for both samples show a main presence of the LLZO phase. The highlighted patterns in **Figure 6.1b**, show more visibly the relative intensity of the LLZO peaks in the heating step, confirming the more rapid evolution of the cubic product in the sample with Te incorporation. This result confirms the influence of tellurium in lowering the temperature formation of LLZO.

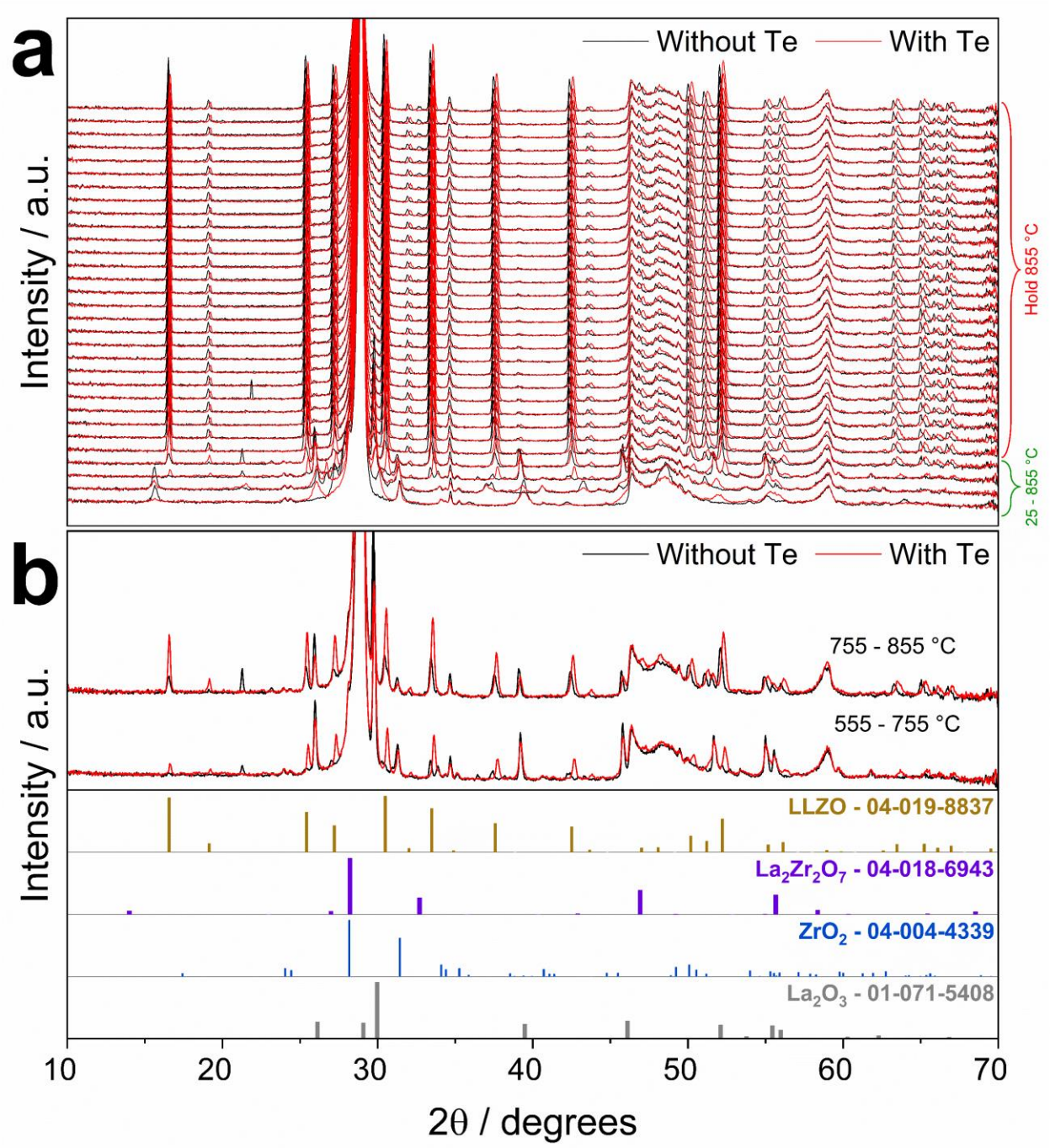

Figure 6.1. a) Compared evolution of in situ XRD patterns for precursors mix with and without Te addition during the heating process of LLZO precursors in a range of temperature from 25 to 855 °C and during the hold step; b) highlighted XRD patterns during the heating step (555–755 and 755–855°C) compared with the reference patterns for LLZO and synthesis intermediates.

6.2.4.2. Effect of Tellurium Content

To observe in more detail the direct effects of Te incorporation, powders with different tellurium amounts were prepared by increasing Te content $Li_{7-2x}La_3Zr_{2-x}Te_xO_{12}$ (x = 0.1, 0.25, 0.375, 0.5). The different compositions were synthesized with a single annealing step at 750 °C for 6 h, following a process already reported in literature (Deviannapoorani et al., 2013). An undoped sample was prepared following the same procedure as reference. The compared X-ray diffraction patterns for the resulting powders are reported in **Figure 6.2a**. The pattern for the undoped sample displays a singular behavior, showing the characteristic peaks of a tetragonal LLZO phase, such as the bicuspid peak at 2θ = 19.5°. This may indicate that the absence of tellurium in the precursor mix hampers the formation of the cubic phase for a low temperature synthesis process. This aspect is further confirmed by the XRD patterns for the different Te-doped compositions, all of which manifest the characteristic peaks of a cubic phase, without showing the typical peak splitting of the tetragonal phase (2θ = 19.5° and 30°). Such a display points out the proper crystallization of the expected cubic phase even for relatively low incorporation of tellurium in the structure. The samples with higher Te content (x = 0.25 and higher) revealed some identifying peaks corresponding to a secondary phase of lithium tellurate (Li_6TeO_6, $R\bar{3}$, ICDD 04-015-4293). In particular, the XRD patterns for x = 0.375 and x = 0.5 manifest intense peaks at 2θ = 21.1°, 33.8° and 50.9°. This could indicate a partial phase segregation in presence of exceedingly high tellurium content in the material, which can depend on the nature of the synthesis process itself as observed by the absence of corresponding peaks in the *in situ* patterns. Moreover, the XRD pattern for x = 0.5 shows an additional minor peak at 2θ = 34.9° indicating the presence of La_2O_3 impurities. The graph reports the values of the average crystallite size, and we can observe a general trend showing a decrease in size with the increment of Te content, with the significant exception of Te0.375 which shows the highest value of 418 Å. Scanning electron micrographs of the Te-doped powders (**Figures 5.2b-e**) revealed the typical rounded shape of LLZO particles and the images seem to display a slight but visible diminution in the surface particle size for the specimens with higher Te presence. A similar behavior has recently been observed by our group with the incorporation of graphite in LLZO (Campanella, Bertoni, et al., 2023).

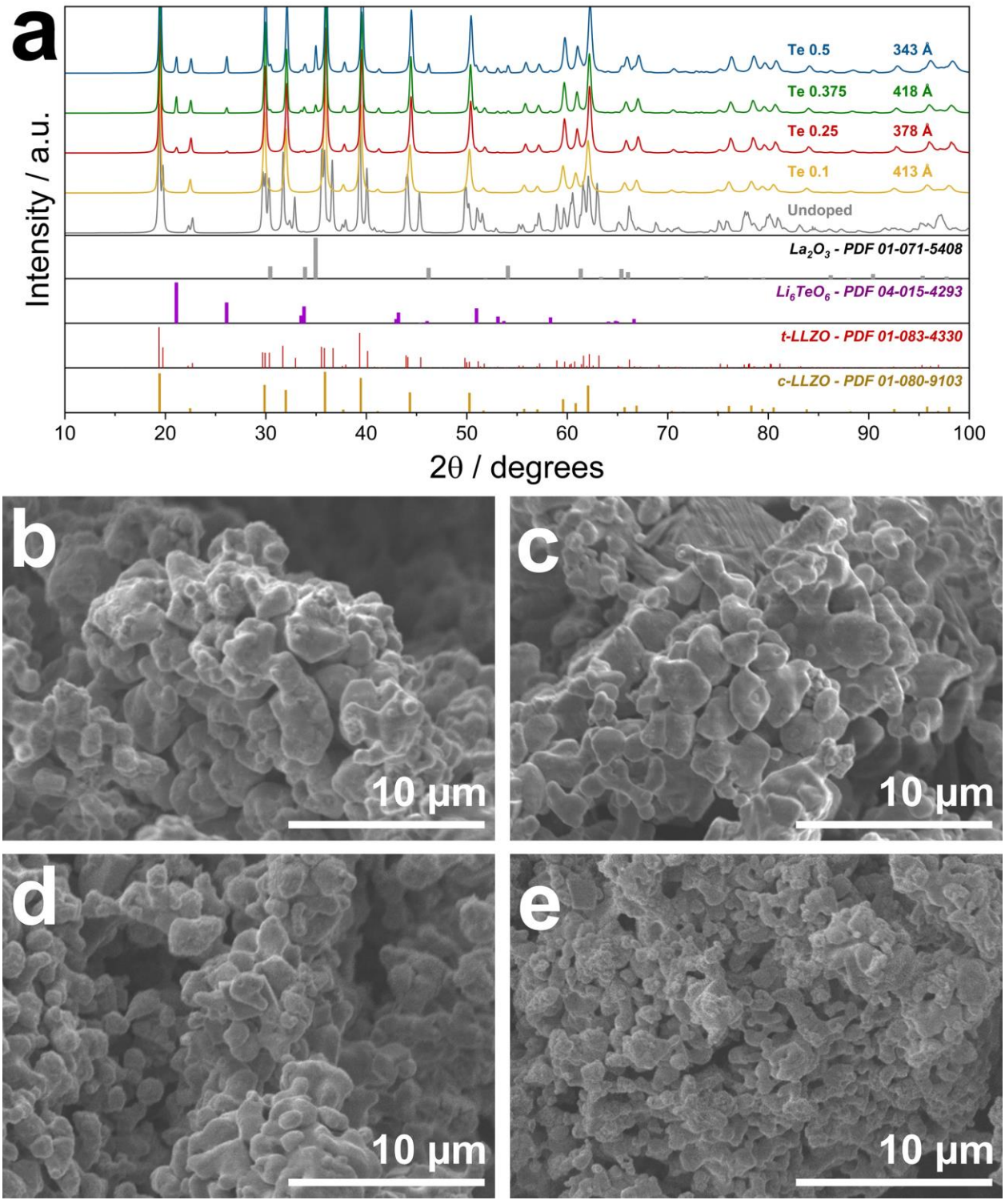

Figure 6.2. a) XRD patterns for powders of with different Te content, annealed at 750 °C for 6 h, compared with the PDF cards. The image reports the value of the average crystallite size for the Te-doped samples; b-e) SEM images for the synthesized powders with different carbon content: b) Te 0.1, c) Te 0.25, d) Te 0.375 and e) Te 0.5.

The calculated lattice parameters of all $Li_{7-2x}La_3Zr_{2-x}Te_xO_{12}$ compositions are found in the table reported in **Table 6.1**. The continuous decrease in the value of cell parameters, going from 12.9921 Å for x = 0.1 to 12.9585 Å for x = 0.5, is in accordance with previous literature results (Deviannapoorani et al., 2013; El-Shinawi et al., 2017). A possible reason for this phenomenon may be found in the diminution in Li content along with the concurrent substitution of large Zr^{4+} cations (r = 0.72 Å) with much smaller Te^{6+} ions (r = 0.56 Å). The results of the XRD analysis therefore confirm the successful formation of a cubic LLZO after a low temperature sintering for all stoichiometries due to the partial introduction of Te in the garnet structure. The XRD reports the average crystallite size, and we can observe a general trend showing a decrease in size with the increment of Te content, with the significant exception of Te0.375 which shows the highest value of 418 Å.

Table 6.1. Calculated lattice parameters for the Te-doped LLZO samples

x_{Te}	a (Å)
0.1	12.9921
0.25	12.9822
0.375	12.9672
0.5	12.9585

6.2.4.3. Modelling

To better understand the influence of tellurium on cubic structure stability of LLZO, modelling experiments were performed. These allowed to heuristically infer the impact from doping on the change of configurational entropy, and henceforth on the phase transition. For the pristine LLZO, there are 24 d-sites, 48 g-sites and 96 h-sites for 56 Li ions in a unit cell (F. Chen et al., 2018). Nevertheless, it is almost impossible for more than one Li^+ ions to simultaneously occupy two or all of the three adjacent h- and g-sites due to the strong Coulomb repulsion. Hence, the number of possible configurations is given by (4):

$$\Omega_{\text{pristine}} = \sum_{i=8}^{24} \binom{24}{i} \binom{48}{56-i} 3^{56-i} \approx 1.5696 \times 10^{34} \quad (4)$$

which gives an entropy of (5)

$$S_{\text{pristine}} = k_B \log \Omega_{\text{pristine}} \approx 6.79 \text{ meV/K} \quad (5)$$

When LLZO is doped with higher valence elements, the number of Li ions in a unit cell is reduced. In our case (**Figure 6.3**) with 48 Li ions in a unit cell, the number of possible configurations, and consequently the configurational entropy, increase, as stated by (6).

$$\Omega_{\text{doped}} = \sum_{i=0}^{24} \binom{24}{i} \binom{48}{48-i} 3^{48-i} \approx 1.3644 \times 10^{35} \quad (6)$$

and (7)

$$S_{\text{doped}} = k_B \log \Omega_{\text{doped}} \approx 6.97 \text{ meV/K} \quad (7)$$

In the tetragonal phase, however, the Li^+ ions do not have partial occupancy in the pristine LLZO. Although doping could create some Li^+ vacancies, the hopping energy barrier of 0.4 eV in tetragonal phase effectively makes the hopping of Li^+ ions a rare event, therefore tetragonal phases are safely considered to have zero configurational entropy. Generally, a phase with higher entropy is preferred at higher temperatures while a phase with lower entropy appears at lower temperature. Although doped LLZO does not always have tetragonal phases, it is still interesting to observe that, since the difference in (configurational) entropy between doped cubic phase and doped tetragonal phase is larger than that between the two pristine phases, the phase transition temperature of cubic to tetragonal is expected to be lower than that of the pristine LLZO, aside from other factors. In this regard, doping LLZO is beneficial to keeping it in its highly conducting cubic phase.

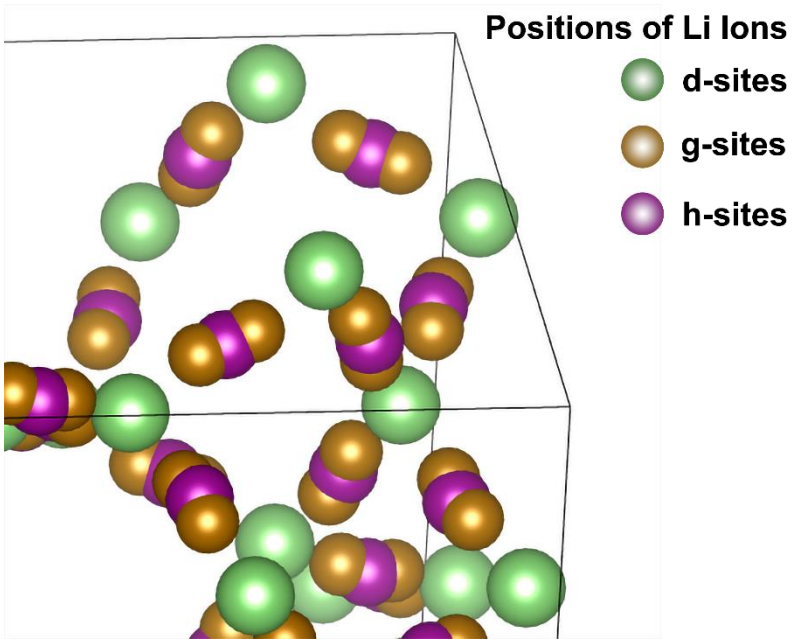

Figure 6.3. Distribution of Li ion sites in the cubic LLZO unit cell

6.2.4.4. Ionic Conductivity Measurements

To electrochemically evaluate the effect of Te incorporation on the total ionic conductivity of the garnet, the different samples were hot-pressed at different temperatures (600, 650 and 700 °C). Electrochemical impedance spectroscopy tests were subsequently performed on coin cells and the resulting pellets were sandwiched between stainless steel electrodes. The analyses took place in the temperature range from 20 to 80 °C and **Figure 6.4a** reports the resulting Nyquist plots collected at 20 °C for the pellets hot-pressed at 650 °C. The spectra show an important difference in the values of resistance for the materials, represented by the amplitude of the depressed semicircle. In particular, Te0.1 exhibits values of resistance of 4.5 kΩ at RT, about twice as large as the values for the samples with higher Te content while the lower value is reported for Te0.25 (x = 0.25). A subsequent data fitting of the Nyquist plots permitted to derive the values of ionic conductivity. The corresponding Arrhenius plots reported in **Figure 6.4b** show a similar behavior in the values of conductivity for all the different samples, for which an increase in the hot-pressing temperature is followed by an increment of the ionic conductivity. In contrast for the Te0.1 sample, the conductivities at different annealing temperatures are similar and, surprisingly, slightly higher for the pellet densified at 650 °C (1.76×10^{-5} S cm^{-1}) compared to the one treated at 700 °C (1.45×10^{-5} S cm^{-1}). This may indicate that the incorporation of low amounts ($x \leq 0.1$) of Te in the

structure does not have a significant impact on the final conductivity. On the other hand, the highest values are reported for the Te0.25 sample, showing a RT conductivity of 5.15×10^{-5} S cm^{-1} for Te 0.25 sintered at 700 °C, about 1.5 times higher than that of Te0.25 sintered at 600 °C (2.95×10^{-5} S cm^{-1}). In general, it can be observed that Te insertion can positively influence the stabilization of the cubic-LLZO phase during low temperature hot-pressing. To better understand the effects, a comparison between Te-LLZO and commercial samples of Al and Ta-doped LLZO was carried out. Te0.25 was chosen for the comparison due to its overall better performance. The results presented in **Figure 6.4c** show that the performance for Te-LLZO is much better than the ones for commercial LLZO treated at the same working conditions. Low temperature treatment does not help achieving good densification in commercial samples and this reflects in the average conductivity being astoundingly lower than that of Te-LLZO, about one order of magnitude lower for Ta-doped LLZO (6.70×10^{-6} vs. 5.15×10^{-5} S cm^{-1} for samples densified at 700 °C) and two orders of magnitude for Al-doped LLZO (3.05×10^{-7} vs. 5.15×10^{-5} S cm^{-1}). All ionic conductivity values are reported in **Table 6.2**.

The results further confirm the major influence of Te incorporation on the electrochemical performance of LLZO solid electrolyte and its advantages in improving the material densification at lower temperatures. In **Figure 6.4d,** the values of apparent density of the different Te-LLZO samples are reported. An irregular behavior of the density values is observed, and the samples generally exhibit lower values of density after densification at 700 °C, compared to 650 °C, with the exception of Te0.5. A precise evaluation of the effective values proves rather difficult because of the nature of the hot-pressing process itself. High temperature treatment in strict conditions often causes partial loss of material and the sintering of the pellets is affected, leading to inaccurate density values. In the graph we can however observe the highest values of density associated with Te0.25 sample, exceeding 90 % of the theoretical value (LLZO density = 5.1 g cm^{-3}), which reflect the better electrochemical performance of the specimen.

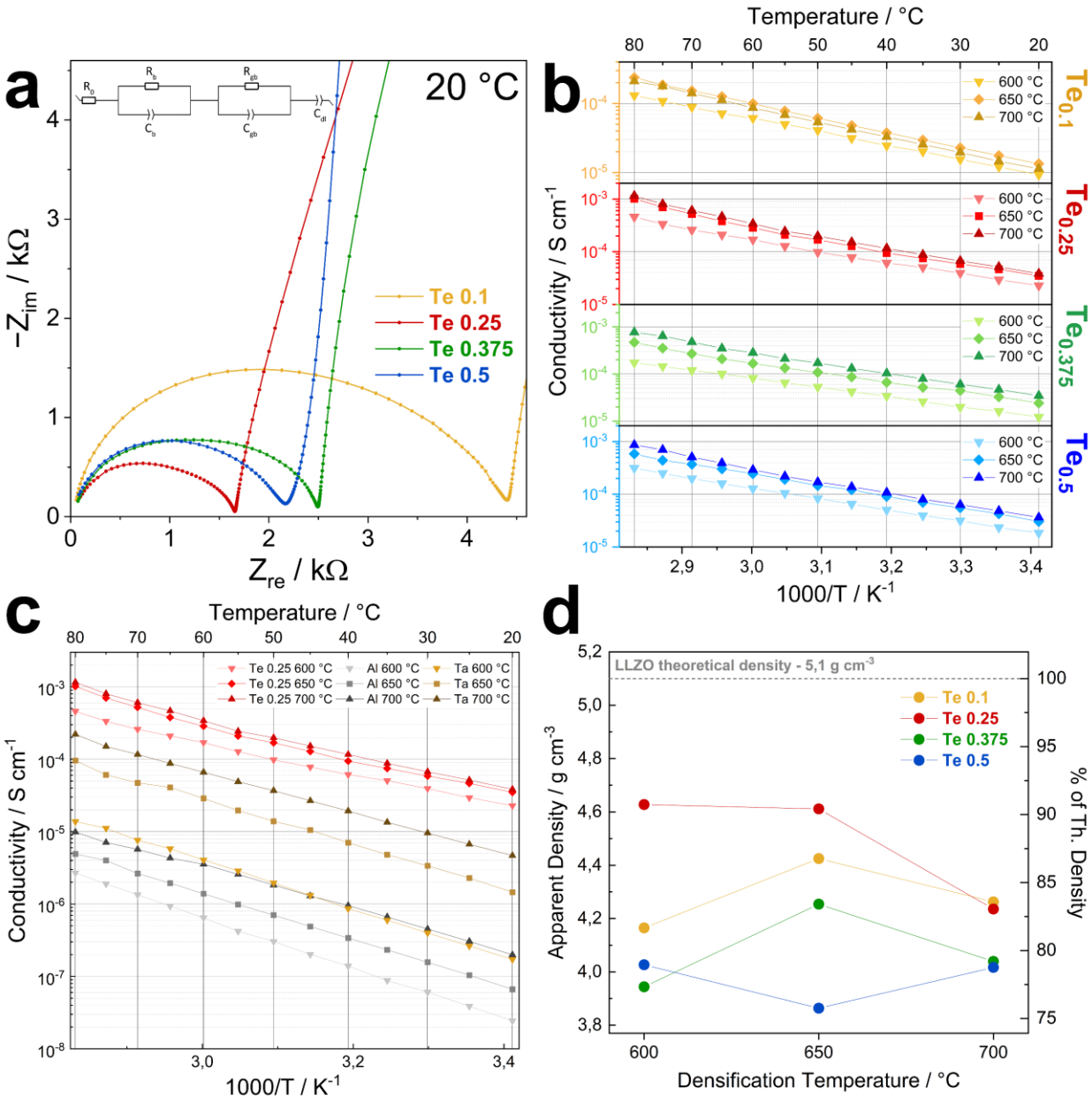

Figure 6.4. a) Nyquist plots of the impedance for different Te-doped LLZO densified at 650 °C samples measured at 20 °C. The image reports the equivalent circuit used for data fitting; b) Arrhenius plots of the total ionic conductivity of the different Te-doped LLZO samples densified at different temperatures in the temperature range from 20 to 80 °C. c) Compared Arrhenius plots of the total ionic conductivity of Te0.25 samples and commercial Al and Ta doped LLZO densified in the same working conditions; d) Graph of apparent density of Te-LLZO samples densified at different temperatures.

Table 6.2. Values of ionic conductivity at different temperatures of the different Te-doped LLZO samples, compared with commercial samples

T / °C	σ (25 °C) / S cm^{-1}					
	Te0.1	Te0.25	Te0.375	Te0.5	Al-LLZO	Ta-LLZO
600 °C	$1{,}21 \times 10^{-5}$	$2{,}95 \times 10^{-5}$	$1{,}61 \times 10^{-5}$	$2{,}33 \times 10^{-5}$	$3{,}88 \times 10^{-8}$	$2{,}64 \times 10^{-7}$
650 °C	$1{,}76 \times 10^{-5}$	$4{,}64 \times 10^{-5}$	$3{,}27 \times 10^{-5}$	$4{,}24 \times 10^{-5}$	$1{,}04 \times 10^{-7}$	$2{,}29 \times 10^{-6}$
700 °C	$1{,}45 \times 10^{-5}$	$5{,}15 \times 10^{-5}$	$4{,}66 \times 10^{-5}$	$4{,}83 \times 10^{-5}$	$3{,}05 \times 10^{-7}$	$6{,}70 \times 10^{-6}$

Figure 6.5a-c reports the SEM cross section images of Te0.25 pellets after hot-pressing along with the EDS mapping for the main elements. A more uniform distribution of the elements is observed for the sample densified at 600 °C (HP600), with the presence of small areas of Te segregation (**Figure 6.5a**). On the other hand, the elemental distribution for the pellets hot-pressed at higher temperature display wide spots with a significantly higher occurrence of Te and a lower concentration of La and Zr, which may indicate a higher degree of segregation of Te-rich phases after high temperature treatment. HP700 (**Figure 6.5c**) shows vast areas of Te segregation with almost absent presence of La and Zr, and these areas are reflected in the electron image showing large voids between the particles. The formation of separate phases abundant in Te may have a notable impact on the densification of the material. **Figure 6.5d** reports the XRD patterns of the powders of the different Te0.25 pellets after densification and the material manifests a similar pattern before and after hot-pressing. HP600 shows an additional peak at about 31° indicating the presence of carbon, possibly due to small traces of the carbon conductor used for annealing. The patterns show the absence of additional phases compared with the powder before hot-pressing, with the presence of the Te-rich secondary phase of Li_6TeO_6, which most likely constitutes the segregating phase observed in the EDS maps of **Figures 6.5a-c**. The formation of Li_6TeO_6 at the grains interphase is consistent with previous observations reported in literature for other dopants, such as aluminum or gallium (El Shinawi & Janek, 2013a; Zhuang et al., 2021).

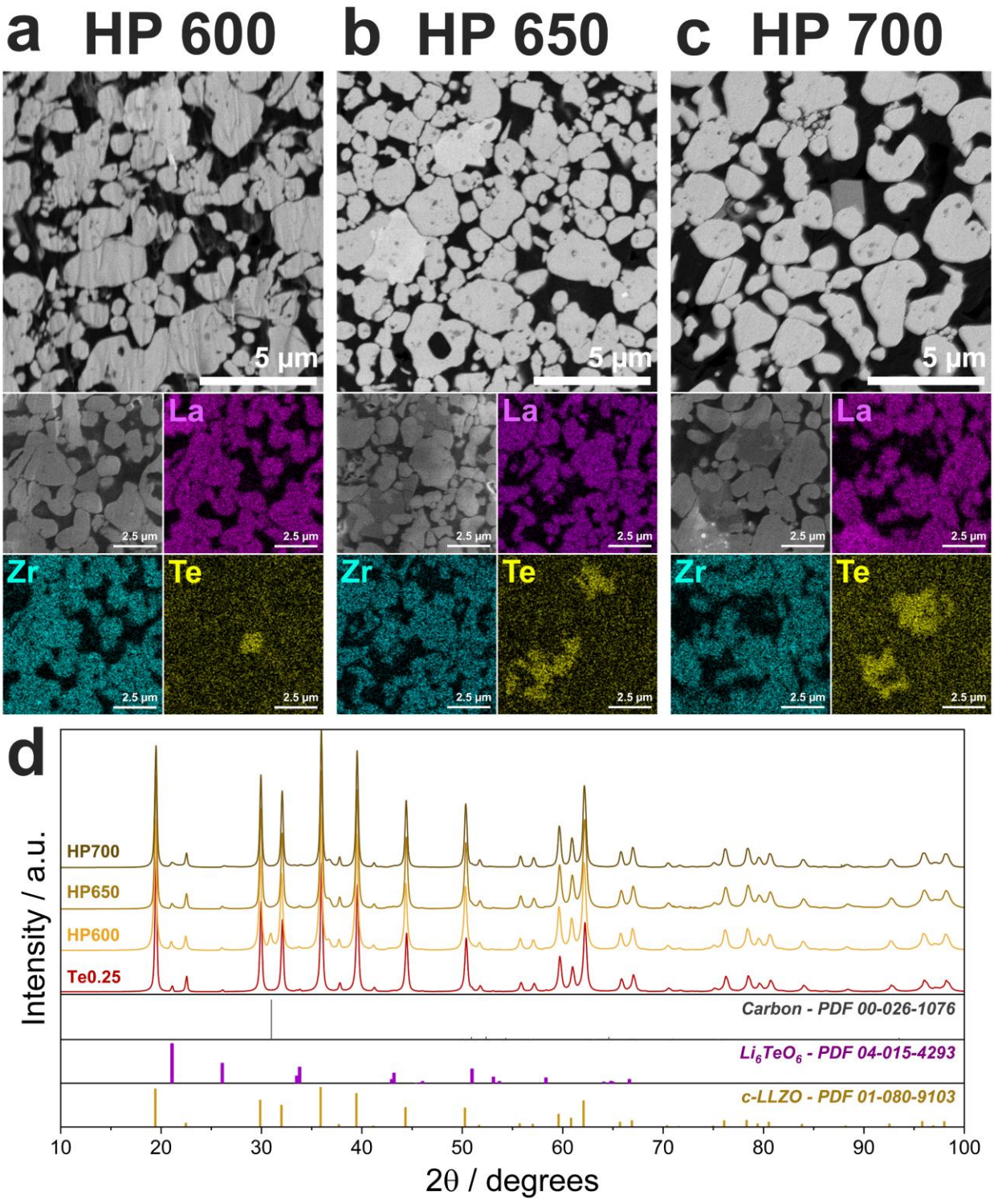

Figure 6.5. a-c) Cross section SEM images and EDS elemental mapping for La, Zr and Te of LLZO Te0.25 at different hot-pressing temperatures: a) 600 °C (HP600), b) 650 °C (HP650) and c) 700 °C (HP700); d) a) XRD patterns for the powders of hot-pressed LLZO Te0.25 pellets compared with the pristine powder before hot pressing.

6.2.5 Conclusions

In this work, we investigated the effects of tellurium insertion in the synthesis process of garnet LLZO prepared via solid-state reaction. Incorporation of Te affects the reaction mechanism of the electrolyte synthesis during the calcination, enabling the formation of cubic LLZO at lower temperatures. Even relatively low amounts of Te in the material have a positive impact in obtaining a cubic polymorph and tellurium incorporation helps stabilizing the structure and reducing the average particle size, possibly improving the densification of the ceramic electrolyte. Te-ions show a positive effect in the electrochemical properties of the material, as confirmed by electrochemical impedance spectroscopy. Te doped LLZO showed promising values of ionic conductivity after low-temperature hot-pressing, with the highest values of 5.15×10^{-5} S cm^{-1} reported for Te0.25 densified at 700 °C. This value is reported as the highest value achieved at this densification temperature, much higher than commercial Ta-doped or Al-doped LLZO densified in the same temperature and pressure conditions. The present work reports a promising method to obtain highly conductive LLZO at lower temperature and to improve the electrochemical properties of garnet solid electrolytes.

6.2.6 Conflict of Interest

The authors declare no conflict of interest.

6.2.7 Acknowledgements

The research was funded by Hydro-Québec's Center of Excellence in Transportation Electrification and Energy Storage, Varennes, Québec. D.C. and W.Z. thank Olivier Sioui-Latulippe of Polytechnique Montréal for his support in the *in situ* analysis. D.C. thanks Dr. Kim Chisu of CEETSE (Canada) for her suggestions. A.P. thanks Prof. Karim Zaghib of Concordia University (Canada) and Dr. Hendrix Demers of CEETSE (Canada) for their useful suggestions. D.C. acknowledges the financial support of Mitacs.

6.2.8 Abbreviations

LLZO, $Li_7La_3Zr_2O_{12}$; EDS Energy dispersion spectroscopy; EIS, Electrochemical impedance spectroscopy; SEM, Scanning electron microscopy; XRD, X-ray diffraction.

CHAPTER VII
GENERAL CONCLUSIONS

The quest for new-generation electrochemical energy storage systems has led to the development of solid-state batteries, which are considered a viable alternative to conventional lithium batteries and a chance to overcome the major limitations of current technologies. The physical features of the materials are crucial in establishing the final performances of the battery; for this reason, several families of materials have been explored as feasible candidates for applications in batteries and the most important of them are discussed in Chapter I. The content of this thesis focused in particular on the development and optimization of ceramic materials for applications as solid electrolytes in lithium batteries. The research was centered on inorganic oxides and, more in particular, on two main families of materials: NASICONs and garnets. NASICON structures typically display an improved stability to moisture and a large electrochemical stability window, along with a lower synthesis temperature with respect to other oxide compounds, but they show a lower total conductivity. On the other hand, garnet oxides show inferior reactivity towards metallic lithium, good mechanical resilience and a higher ionic conductivity than NASICONs, but they are more susceptible to moist atmosphere and display poor interfacial contact with electrodes. The synthesis conditions for garnets are more demanding as well, usually requiring very high temperatures to achieve a conductive phase. These materials were chosen in this thesis with the purpose of better understanding their properties and clarifying their behavior through experimental investigations. A common thread linking all the research activities described in the thesis is the application of the hot-pressing technique for the preparation of the materials. Use of hot-pressing is fairly common in the engineering of ceramic materials, allowing to achieve denser products with improved mechanical properties, but the use of this fabrication approach is not explored as much in the field of solid electrolytes, therefore this work deals with the issue in an original fashion.

The first results reported in Chapter II are the fabrication and characterization of ceramic pellets of NASICON-type $Li_{1.5}Al_{0.5}Ti_{1.5}(PO_4)_3$ (LATP). An in-depth structural investigation unveiled important information on the nature of the formation mechanism: *in situ* XRD analysis displayed a fast kinetics for the evolution of LATP structure, showing a first presence of the desired

phase at temperatures as low as 400 °C and a steady increase in the relative intensity up to a maximum observed at 700 °C. The LATP phase is stabilized upon cooling, but the resulting samples showed the presence of secondary phosphate phases, such as Li_3PO_4 and $Li_4P_2O_7$, as impurities. Optimization of the manufacturing process enabled the production of densified LATP samples via hot-pressing at 750 °C under inert atmosphere. A series of samples were synthesized at different temperatures and SEM observations were carried out to determine the powder microstructure: a lower annealing temperature (550 °C) led to powders with a higher amount of nanometric particles, whereas increasing the temperature to 950 °C saw the formation of larger micrometric grains. The finer microstructure of the low-temperature sample allowed a more facile sintering, due to the larger intrinsic surface area, producing ceramic pellets with a higher relative density. Conversely, the larger particles of the high-temperature sample slowed down the densification, leading to a prominent presence of pores and voids in the hot-pressed pellet. The best compromise between particle size and density was obtained after densification for a sample calcined at 700 °C, which exhibited the highest values of ionic conductivity (3.45×10^{-4} S cm^{-1}) evaluated by electrochemical impedance spectroscopy (EIS).

Analysis of the powders via XRD before hot-pressing revealed the presence of $AlPO_4$ impurities for the samples prepared at lower temperatures, further confirmed by ^{27}Al-NMR spectra showing a well-defined peak associated with the tetrahedral Al of $AlPO_4$. Calculation of the diffusion coefficients via PFG-NMR reveal higher values for the material synthesized at 950 °C, due to the faster Li^+ ion motion within the larger grains, but the poor densification has a negative impact on the final conductivity. The high porosity and the presence of voids reduce the contact area between the particles and creates longer diffusion paths, reflecting in a lower conductivity and a higher activation energy. Low-temperature powders present a lower diffusion coefficient with a strong influence of grain boundaries, but the improved contact given by the small-sized particles during densification is shown to overcome this issue and produce more conductive samples with a lower activation energy to ion transfer. Density functional theory (DFT) calculations were performed to inquire the stability of LATP with respect to high applied pressures and temperatures. The values of free energy point out an inevitable formation of $AlPO_4$ impurities after densification and indicate a less favorable evolution of the LATP phase with simple application of external pressure. The working conditions for the hot-pressing, however, make the enthalpy shift negligible in the economy of the reaction; a proper tuning of the sintering

temperature can reduce the impact of impurities, and a limited amount of these phases act as an inert filler, improving the densification and the ionic conductivity.

The modification of garnet materials is explored in the following chapters and, in particular, Chapter III is centered on the hot press-driven densification of $Li_5La_3Bi_2O_{12}$ (LLBO), which can be achieved at significantly lower temperature than other garnets such as $Li_7La_3Zr_2O_{12}$ (LLZO). Fabrication of the material was carried out via a solid-state route at 775 °C, followed by direct quenching at room temperature. This process involves a thermal shock of the ceramic and has been shown to stabilize the garnet structure at room temperature, allowing the production of smaller particles and improving the conductivity of the electrolyte. Different ceramic samples underwent densification in a temperature range from 550 to 650 °C and electrochemical impedance spectroscopy tests revealed the highest values of conductivity of 1.2×10^{-4} S cm^{-1} for the sample sintered at 600 °C. An ulterior increase in the sintering temperature (700 °C) led to a partial decomposition and the production of brittle pellets. Examination of the chemical affinity of LLBO towards metallic lithium presented an irreversible reaction at high potentials (> 5 V vs Li^+/Li), associated with the Bi^{3+}/Bi^{5+} redox process, but the material reports a long-term stability profile in a Li/Li symmetric cell. The metastable behavior of LLBO is explored and an increase in $LiLaO_2$ content is observed on parallel with an increment in sintering temperature from 650 to 700 °C. This behavior is confirmed by the EDS mappings, which point out a partial segregation of Bi rich phases with the increasing temperature, confirming the decomposition reaction of LLBO, whereas the elements are distributed homogeneously in the sample densified at 600 °C. DFT calculations confirmed the metastability of the garnet and indicated a more intense decomposition along with the increase in temperature, which can however be partially mitigated by increasing the external pressure, as shown by the higher calculated free energy values.

Following these observations, a subsequent investigation involved the use of LLBO as a sintering agent for garnet Ta-doped LLZO. Incorporation of small amounts of LLBO (<30 % wt.) is observed to improve the densification of the ceramic, leading to values of apparent density above 90% of the theoretical value. Samples with 5-10 % wt. of LLBO exhibited a notable increment in conductivity up to 1.5×10^{-4} S cm^{-1} after low-temperature sintering at 600 °C, about two orders of magnitude higher than pure LLZO undergoing the same thermal process (1×10^{-6} S cm^{-1}). Stability tests in symmetrical cells displayed a higher polarization compared with pure LLBO,

mainly due to the more resistive character of LLZO. Morphological characterization via SEM and EDS reported a limited segregation of Bi-rich phases dispersed throughout a LLZO bulk, with preservation of the cubic structures of both LLZO and LLBO. The ionic transport in the composite is determined via NMR analysis, which revealed values of diffusion coefficient for LLBO compatible with Li motion inside particles and at the grain boundaries; hence, an increment in densification temperature can promote a more intimate contact and diminish the grain boundary effect. The distribution of LLBO within LLZO can help keep the particles tighter and increase the density of the ceramic.

Chapters IV and V shift their attention to the thermal treatment of LLZO, dealing with the application of sintering agents and the structural stabilization of the electrolyte. In Chapter IV the role of additive was taken by carbonaceous materials, whose application is shown to directly influence the formation mechanism of the garnet phase. Observations by *in situ* XRD and TGA analysis demonstrate the effect of carbon supplements on decreasing the decomposition temperature of Li_2CO_3 precursor in the mix, from 750 to 680 °C, allowing for an improved reactivity of the coalescent mass and for a faster formation of garnet via a direct mechanism. In the presence of carbon, the desired phase is observed at temperatures as low as 720 °C and negligible presence of impurities. The incorporation of carbon activates the evolution of CO upon heating, with a more rapid generation of melted Li_2O at temperatures below those of formation of Li-free intermediates such as $La_2Zr_2O_7$. Carbon materials with diverse structures were employed, including graphitic carbons (MAG) and acetylene-black nanometric carbons (DENKA) and XRD observations revealed for all the different samples a pure cubic LLZO phase after thermal treatment in air atmosphere. However, a difference can be seen in the average crystal size, which is significantly smaller for the samples with the additives (10 to 20 % less) and shows an ever-increasing behavior with a higher carbon content. SEM analysis confirmed the results of the XRD, presenting a preserved morphology for LLZO particles and a decrement in particle size for samples with higher carbon content. A regular trend is observed for increased amounts of MAG carbon (from 10 % to 100 % wt. with respect of Li_2CO_3 precursor) but, surprisingly, a smaller incorporation of DENKA carbon, with a reduced particle dimension, has an influence comparable with larger quantities of MAG carbon. The distribution of distinct additives in the mix is proven then to have a different impact on the formation of the garnet particles and TEM images confirmed the supposition, displaying, for MAG carbon, a thin layer at the edges of the LLZO particles

obtained by graphite exfoliation during milling, and, for DENKA carbon, a homogeneous distribution of nanoparticles around the ceramic.

The results exposed in Chapter III demonstrated the effect of particle size on the densification of LLBO, and here a consistent behavior can be observed for LLZO. A smaller particle size obtained by carbon addition is definitely positive for enhancing pellet densification, as confirmed by cross-section images of sintered LLZO pellets which display a decrease in void spaces and a reduction in grain dimension for samples supplemented with carbon. The improved compactness is reflected on the electrochemical performances, reporting an increment in conductivity of about 40 % for samples with carbon compared with pristine LLZO (5.95×10^{-5} S cm^{-1} vs. 3.53×10^{-5} S cm^{-1}) after low-temperature sintering at 800 °C.

Finally, the experiences in Chapter V concern a different approach for the low-temperature densification of LLZO, involving elemental doping with tellurium. Structural substitution is a fairly common method for improving the performances of ceramic electrolytes, and the experiments aim at understanding the influence of doping on the evolution of LLZO itself. The addition of Te-ions in the lattice is shown to affect the reactivity of the precursors, inducing a variation in the formation mechanism with a direct reaction between the precursors. This reaction enables a faster formation of the LLZO phase at temperatures between 550 and 750 °C, compared with the undoped material where the reaction between intermediates retards the formation well above 750 °C. A series of Te-doped samples with different stoichiometries were prepared following a conventional solid-state synthesis at 750 °C. XRD compared analysis revealed a major cubic phase for all the compositions, whereas the undoped sample undergoing the same process displayed a tetragonal LLZO phase with presence of impurities. A partial segregation of Te-rich byproducts was detected for higher amounts of Te in the mix, as well as a decrement in the average particle size and a small but present decrease in the cell parameters. This is possibly due to the decrease in Li content in parallel with the replacement of large Zr^{4+} ions with smaller Te^{6+} ions. Molecular modelling and calculations ulteriorly confirmed the positive influence of doping in the stabilization of the cubic phase, following a variation in the configurational entropy between the cubic and tetragonal polymorphs in their pristine and doped compositions.

Low-temperature hot-pressing was subsequently undertaken on the doped samples in the temperature range from 600 to 700 °C, and the best values of ionic conductivity derived from EIS tests were reported for samples with 0.25 molar content of Te. The highest value of 5.95×10^{-5} S cm^{-1} was exhibited by the pellet sintered at 700 °C, and despite being definitely lower than the values reported in literature for Te-doped LLZO, it still remains the highest reported value for LLZO densified at such a low temperature. Moreover, the advantages of Te doping were confirmed by a comparison with commercial Al and Ta-doped samples. The synthesized Te-LLZO presented an increment in conductivity of more than one order of magnitude with respect to the commercial materials undergoing a similar low-temperature densification. EDS mapping allowed to observe a visible segregation of Te-abundant phases in the LLZO matrix following the hot-pressing treatment and the phenomenon is intensified with an increase in the sintering temperature.

Based on the results exposed in this thesis, some interesting questions remain open and can form the basis of future studies. Low-temperature densification of ceramic electrolytes has been proven possible and this can define a novel approach to solid-state synthesis, enabling less strict working conditions and reducing the time and the costs of the conventional electrolyte manufacturing. This method can be tested for other families of inorganic materials, such as perovskites or new superionic conductors, and their performance can be enhanced as well. The implementation of the distinct modifications, including elemental doping or additive supplement, combined with hot-pressing allows tailoring and simplify the fabrication process. Furthermore, the lower working temperature significantly decreases the risk of thermal decomposition and chemical deterioration of the electrolytes. Focusing on the materials explored in these studies, future experiments on LATP and NASICON materials can concern the incorporation of carbon additives like the ones employed for LLZO. This research can allow us to observe the behavior of the modified materials concerning low temperature synthesis and improved densification. A complete overhaul of the fabrication process, combining additives and dopants, can enable improved stability and performance. Reaching an even lower densification temperature is another future endeavor, which could be undertaken by varying the starting synthesis precursors or employing different sintering aids.

Given the promising results in adjusting the particle size of the products, an alternative modification can involve the use of liquid additives. Ionic liquids allow for the preparation of

composites with ceramics, reducing the effects of poor surface contact. A finer particle distribution in the product is desired for the liquids to imbue the ceramic bulk more homogeneously, increasing the interfacial contact even more. Interesting observations would regard the modified ion motion with presence of liquid conductive species. Interfacial modifications can decrease the area-specific resistance and allow a better ion transport. The modified structure can also limit even more the evolution of lithium dendrites, which can have negative effects on the cell performance even when using solid electrolytes.

A possible modification can concern the fabrication of ceramic electrolyte thin films, decreasing the volume of the solid electrolyte in the cell. The improved density given by the smaller particles is the perfect starting point for these attempts and it would be interesting to see if a similar approach could work for the engineering of thin layers. Another future prospect concerning this research can be related to the hot-pressing of a full cell comprising of both electrolyte and electrodes combined. This may prove a much more complicated challenge than the simple sintering of pellets since the control of interfacial contact is somehow difficult in the working conditions of hot-pressing. The possibility of reaction and decomposition between the different elements has to be considered as well. For this reason, in parallel with these studies, an effort should be undertaken in looking for new cathode chemistries showing improved compatibility with ceramic electrodes. Research on new electrodes can also incorporate alternative elements, reducing their cost and increasing their environmental compatibility.

The doctorate experience has given me a lot from a personal standpoint. It has broadened my horizons and given me a deeper knowledge about a field of study I was familiar with. It has helped me develop a working method and organizing my research in a more practical and efficient fashion. More practically, it provided me with a broad set of capabilities in the laboratory, including numerous techniques and characterization methods. During the hard times lived through the pandemic, this experience helped me become more resolute towards my goals and more positive in my capacities, making me hold on and carry on despite the hardships I have faced. Thanks to this experience I have become more confident about undertaking my future projects, so I should look positively at what comes next, wherever it may take me.

REFERENCES

Abe, M., & Uchino, K. (1974). X-ray study of the deficient perovskite La2/3TiO3. *Materials Research Bulletin*, *9*(2), 147–155. https://doi.org/10.1016/0025-5408(74)90194-9

Abouali, S., Yim, C.-H., Merati, A., Abu-Lebdeh, Y., & Thangadurai, V. (2021). Garnet-Based Solid-State Li Batteries: From Materials Design to Battery Architecture. *ACS Energy Letters*, *6*(5), 1920–1941. https://doi.org/10.1021/acsenergylett.1c00401

Adeli, P., Bazak, J. D., Huq, A., Goward, G. R., & Nazar, L. F. (2021). Influence of Aliovalent Cation Substitution and Mechanical Compression on Li-Ion Conductivity and Diffusivity in Argyrodite Solid Electrolytes. *Chemistry of Materials*, *33*(1), 146–157. https://doi.org/10.1021/acs.chemmater.0c03090

Adeli, P., Bazak, J. D., Park, K. H., Kochetkov, I., Huq, A., Goward, G. R., & Nazar, L. F. (2019). Boosting Solid-State Diffusivity and Conductivity in Lithium Superionic Argyrodites by Halide Substitution. *Angewandte Chemie - International Edition*, *58*(26), 8681–8686. https://doi.org/10.1002/anie.201814222

Ado, K., Saito, Y., Asai, T., Kageyama, H., & Nakamura, O. (1992). Li+-ion conductivity of Li1+xMxTi2−x(PO4)3 (M: Sc3+, Y3+). *Solid State Ionics*, *53–56*(PART 2), 723–727. https://doi.org/10.1016/0167-2738(92)90246-L

Agrawal, R. C., & Pandey, G. P. (2008). Solid polymer electrolytes: materials designing and all-solid-state battery applications: an overview. *Journal of Physics D: Applied Physics*, *41*(22), 223001. https://doi.org/10.1088/0022-3727/41/22/223001

Akridge, J. R., & Vourlis, H. (1986). Solid state batteries using vitreous solid electrolytes. *Solid State Ionics*, *18–19*(PART 2), 1082–1087. https://doi.org/10.1016/0167-2738(86)90313-9

Aktaş, S., Özkendir, O. M., Eker, Y. R., Ateş, Ş., Atav, Ü., Çelik, G., & Klysubun, W. (2019). Study of the local structure and electrical properties of gallium substituted LLZO electrolyte materials. *Journal of Alloys and Compounds*, *792*, 279–285. https://doi.org/10.1016/j.jallcom.2019.04.049

Alami, M., Brochu, R., Soubeyroux, J. L., Gravereau, P., Le Flem, G., & Hagenmuller, P. (1991). Structure and thermal expansion of LiGe2(PO4)3. *Journal of Solid State Chemistry*, *90*(2), 185–193. https://doi.org/10.1016/0022-4596(91)90134-4

Amaresh, S., Karthikeyan, K., Kim, K. J., Lee, Y. G., & Lee, Y. S. (2014). Aluminum based sulfide solid lithium ionic conductors for all solid state batteries. *Nanoscale*, *6*(12), 6661–6667. https://doi.org/10.1039/c4nr00804a

Anantharamulu, N., Koteswara Rao, K., Rambabu, G., Vijaya Kumar, B., Radha, V., & Vithal, M. (2011). A wide-ranging review on Nasicon type materials. In *Journal of Materials Science* (Vol. 46, Issue 9, pp. 2821–2837). https://doi.org/10.1007/s10853-011-5302-5

Anderman, M., Lundquist, J. T., Johnson, S. L., & Giovannoni, R. T. (1989). Rechargeable lithium-titanium disulphide cells of spirally-wound design. *Journal of Power Sources*, *26*(3–4), 309–312. https://doi.org/10.1016/0378-7753(89)80139-9

Aono, H., Sugimoto, E., Sadaoka, Y., Imanaka, N., & Adachi, G. (1990). Ionic Conductivity of Solid Electrolytes Based on Lithium Titanium Phosphate. *Journal of The Electrochemical Society*, *137*(4), 1023–1027. https://doi.org/10.1149/1.2086597

Aono, H., Sugimoto, E., Sadaoka, Y., Imanaka, N., & Adachi, G. (1992). Electrical Properties and Sinterability for Lithium Germanium Phosphate Li 1+ x M x Ge 2− x (PO 4) 3 , M = Al, Cr, Ga, Fe, Sc, and In Systems. *Bulletin of the Chemical Society of Japan*, *65*(8), 2200–2204. https://doi.org/10.1246/bcsj.65.2200

Aravindan, V., Gnanaraj, J., Madhavi, S., & Liu, H.-K. (2011). Lithium-Ion Conducting Electrolyte Salts for Lithium Batteries. *Chemistry - A European Journal*, *17*(51), 14326–14346. https://doi.org/10.1002/chem.201101486

Arbi, K., Bucheli, W., Jiménez, R., & Sanz, J. (2015). High lithium ion conducting solid electrolytes based on NASICON Li1+xAlxM2-x(PO4)3 materials (M = Ti, Ge and $0 \leq x \leq 0.5$). *Journal of the European Ceramic Society*, *35*(5), 1477–1484. https://doi.org/10.1016/j.jeurceramsoc.2014.11.023

Arbi, K., Lazarraga, M. G., Ben Hassen Chehimi, D., Ayadi-Trabelsi, M., Rojo, J. M., & Sanz, J. (2004). Lithium Mobility in Li 1.2 Ti 1.8 R 0.2 (PO 4) 3 Compounds (R = Al, Ga, Sc, In) as Followed by NMR and Impedance Spectroscopy. *Chemistry of Materials*, *16*(2), 255–262. https://doi.org/10.1021/cm030422i

Armand, M. (1983). Polymer solid electrolytes - an overview. *Solid State Ionics*, *9–10*(PART 2), 745–754. https://doi.org/10.1016/0167-2738(83)90083-8

Armand, M. B., Whittingham, M. S., & Huggins, R. A. (1972). The iron cyanide bronzes. *Materials Research Bulletin*, *7*(2), 101–107. https://doi.org/10.1016/0025-5408(72)90266-8

Armand, M., & Duclot, M. (1978). *Ionically and pref. electronically conductive electrode - comprising agglomerate of active electrode material and solid soln. of ionic cpd. in polymer pref. polyoxyalkylene* (Patent No. FR2442514A1). https://patents.google.com/patent/FR2442514A1/en

Armand, M., & Tarascon, J.-M. (2008). Building better batteries. *Nature*, *451*(7179), 652–657. https://doi.org/10.1038/451652a

Armand, M., & Touzain, P. (1977). Graphite intercalation compounds as cathode materials. *Materials Science and Engineering*, *31*(C), 319–329. https://doi.org/10.1016/0025-5416(77)90052-0

Aurbach, D., Gofer, Y., & Langzam, J. (1989). The Correlation Between Surface Chemistry, Surface Morphology, and Cycling Efficiency of Lithium Electrodes in a Few Polar Aprotic Systems. *Journal of The Electrochemical Society*, *136*(11), 3198–3205. https://doi.org/10.1149/1.2096425

Awaka, J., Kijima, N., Hayakawa, H., & Akimoto, J. (2009). Synthesis and structure analysis of tetragonal Li7La3Zr2O12 with the garnet-related type structure. *Journal of Solid State Chemistry*, *182*(8), 2046–2052. https://doi.org/10.1016/j.jssc.2009.05.020

Awaka, J., Kijima, N., Kataoka, K., Hayakawa, H., Ohshima, K. ichi, & Akimoto, J. (2010). Neutron powder diffraction study of tetragonal Li7La3Hf2O12 with the garnet-related type

structure. *Journal of Solid State Chemistry*, *183*(1), 180–185. https://doi.org/10.1016/j.jssc.2009.10.030

Azeez, F., & Fedkiw, P. S. (2010). Conductivity of libob-based electrolyte for lithium-ion batteries. *Journal of Power Sources*, *195*(22), 7627–7633. https://doi.org/10.1016/j.jpowsour.2010.06.021

Bedrov, D., Borodin, O., & Hooper, J. B. (2017). Li + Transport and Mechanical Properties of Model Solid Electrolyte Interphases (SEI): Insight from Atomistic Molecular Dynamics Simulations. *The Journal of Physical Chemistry C*, *121*(30), 16098–16109. https://doi.org/10.1021/acs.jpcc.7b04247

Bernstein, N., Johannes, M. D., & Hoang, K. (2012). Origin of the Structural Phase Transition in Li7La3Zr2O12. *Physical Review Letters*, *109*(20), 205702. https://doi.org/10.1103/PhysRevLett.109.205702

Berzelius, J. J. (1817). Ein neues mineralisches Alkali und ein neues Metall. *Journal Für Chemie Und Physik*, *21*(44–48).

Best, A. (2000). Stoichiometric changes in lithium conducting materials based on Li1+xAlxTi2−x(PO4)3: impedance, X-ray and NMR studies. *Solid State Ionics*, *136–137*(1–2), 339–344. https://doi.org/10.1016/S0167-2738(00)00493-8

Bintang, H. M., Lee, S., Shin, S., Kim, B. G., Jung, H.-G., Whang, D., & Lim, H.-D. (2021). Stabilization effect of solid-electrolyte interphase by electrolyte engineering for advanced Li-ion batteries. *Chemical Engineering Journal*, *424*(May), 130524. https://doi.org/10.1016/j.cej.2021.130524

Bosubabu, D., Sivaraj, J., Sampathkumar, R., & Ramesha, K. (2019). LAGP | Li Interface Modification through a Wetted Polypropylene Interlayer for Solid State Li-Ion and Li − S batteries. *ACS Applied Energy Materials*, *2*, 4118–4125. https://doi.org/10.1021/acsaem.9b00301

Braga, M. H., Ferreira, J. A., Stockhausen, V., Oliveira, J. E., & El-Azab, A. (2014). Novel Li3ClO based glasses with superionic properties for lithium batteries. *Journal of Materials Chemistry A*, *2*(15), 5470–5480. https://doi.org/10.1039/c3ta15087a

Braga, M. H. H., Grundish, N. S. S., Murchison, A. J. J., & Goodenough, J. B. B. (2017). *Alternative strategy for a safe rechargeable battery*. *10*(1), 331–336.

Brande, W. T. (1821). *A Manual of Chemistry* (2nd ed.). John Murray.

Brugge, R. H. (2018). *Garnet Ceramic Electrolytes for Lithium Ion Batteries*.

Buschmann, H., Dölle, J., Berendts, S., Kuhn, A., Bottke, P., Wilkening, M., Heitjans, P., Senyshyn, A., Ehrenberg, H., Lotnyk, A., Duppel, V., Kienle, L., & Janek, J. (2011). Structure and dynamics of the fast lithium ion conductor “li 7La3Zr2O12.” *Physical Chemistry Chemical Physics*, *13*(43), 19378–19392. https://doi.org/10.1039/c1cp22108f

Bushkova, O. V., Yaroslavtseva, T. V., & Dobrovolsky, Y. A. (2017). New lithium salts in electrolytes for lithium-ion batteries (Review). *Russian Journal of Electrochemistry*, *53*(7), 677–699. https://doi.org/10.1134/S1023193517070035

Campanella, D., Belanger, D., & Paolella, A. (2021). Beyond garnets, phosphates and phosphosulfides solid electrolytes: New ceramic perspectives for all solid lithium metal batteries. *Journal of Power Sources*, *482*(July 2020), 228949. https://doi.org/10.1016/j.jpowsour.2020.228949

Campanella, D., Bertoni, G., Zhu, W., Trudeau, M., Girard, G., Savoie, S., Clément, D., Guerfi, A., Vijh, A., George, C., Bélanger, D., & Paolella, A. (2023). Gram-scale carbothermic control of LLZO garnet solid electrolyte particle size. *Chemical Engineering Journal*, *457*(August 2022), 141349. https://doi.org/10.1016/j.cej.2023.141349

Campanella, D., Krachkovskiy, S., Bertoni, G., Gazzadi, G. C., Golozar, M., Kaboli, S., Savoie, S., Girard, G., Gheorghe Nita, A. C., Okhotnikov, K., Feng, Z., Guerfi, A., Vijh, A., Gauvin, R., Bélanger, D., & Paolella, A. (2023). Metastable properties of a garnet type Li 5 La 3 Bi 2 O 12 solid electrolyte towards low temperature pressure driven densification. *Journal of Materials Chemistry A*, *11*(1), 364–373. https://doi.org/10.1039/D2TA04259B

Cao, C., Li, Z.-B., Wang, X.-L., Zhao, X.-B., & Han, W.-Q. (2014). Recent Advances in Inorganic Solid Electrolytes for Lithium Batteries. *Frontiers in Energy Research*, *2*(JUN). https://doi.org/0.3389/fenrg.2014.00025

Cao, S., Song, S., Xiang, X., Hu, Q., Zhang, C., Xia, Z., Xu, Y., Zha, W., Li, J., Gonzale, P. M., Han, Y.-H., & Chen, F. (2019a). Modeling, Preparation, and Elemental Doping of Li7La3Zr2O12 Garnet-Type Solid Electrolytes: A Review. *Journal of the Korean Ceramic Society*, *56*(2), 111–129. https://doi.org/10.4191/kcers.2019.56.2.01

Cao, S., Song, S., Xiang, X., Hu, Q., Zhang, C., Xia, Z., Xu, Y., Zha, W., Li, J., Gonzale, P. M., Han, Y.-H. H., & Chen, F. (2019b). Modeling, Preparation, and Elemental Doping of Li7La3Zr2O12 Garnet-Type Solid Electrolytes: A Review. *Journal of the Korean Ceramic Society*, *56*(2), 111–129. https://doi.org/10.4191/kcers.2019.56.2.01

Cao, W., Lei, B., Shi, Y., Dong, T., Peng, P., Zheng, Y., & Jiang, F. (2020). Ponderation over the recent safety accidents of lithium-ion battery energy storage stations in South Korea. *Energy Storage Science and Technology*, *9*(5). https://doi.org/10.19799/j.cnki.2095-4239.2020.0127

Cao, W., Yang, Y., Deng, J., Li, Y., Cui, C., & Zhang, T. (2021). Localization of electrons within interlayer stabilizes NASICON-type solid-state electrolyte. *Materials Today Energy*, *22*, 100875. https://doi.org/10.1016/j.mtener.2021.100875

Cao, Z., Cao, X., Liu, X., He, W., Gao, Y., Liu, J., & Zeng, J. (2015). Effect of Sb-Ba codoping on the ionic conductivity of Li7La3Zr2O12 ceramic. *Ceramics International*, *41*(5), 6232–6236. https://doi.org/10.1016/j.ceramint.2015.01.030

Capuano, F., Croce, F., & Scrosati, B. (1991). Composite Polymer Electrolytes. *Journal of The Electrochemical Society*, *138*(7), 1918–1922. https://doi.org/10.1149/1.2085900

Catti, M. (1999). Lithium location in NASICON-type Li+ conductors by neutron diffraction. I. Triclinic α'-LiZr2(PO4)3. *Solid State Ionics*, *123*(1–4), 173–180. https://doi.org/10.1016/S0167-2738(99)00089-2

Catti, M., Sommariva, M., & Ibberson, R. M. (2007). Tetragonal superstructure and thermal

history of Li0.3La 0.567TiO3 (LLTO) solid electrolyte by neutron diffraction. *Journal of Materials Chemistry*, *17*(13), 1300–1307. https://doi.org/10.1039/b614345h

Cavers, H., Molaiyan, P., Abdollahifar, M., Lassi, U., & Kwade, A. (2022). Perspectives on Improving the Safety and Sustainability of High Voltage Lithium-Ion Batteries Through the Electrolyte and Separator Region. *Advanced Energy Materials*, *12*(23). https://doi.org/10.1002/aenm.202200147

Chandrasekaran, R., Koh, M., Ozhawa, Y., Aoyoma, H., & Nakajima, T. (2009). Electrochemical cell studies on fluorinated natural graphite in propylene carbonate electrolyte with difluoromethyl acetate (MFA) additive for low temperature lithium battery application. *Journal of Chemical Sciences*, *121*(3), 339–346. https://doi.org/10.1007/s12039-009-0039-2

Chawla, N. (2019). Recent advances in air-battery chemistries. *Materials Today Chemistry*, *12*, 324–331. https://doi.org/10.1016/j.mtchem.2019.03.006

Chen, C. H., & Amine, K. (2001). Ionic conductivity, lithium insertion and extraction of lanthanum lithium titanate. *Solid State Ionics*, *144*(1–2), 51–57. https://doi.org/10.1016/S0167-2738(01)00884-0

Chen, F., Li, J., Huang, Z., Yang, Y., Shen, Q., & Zhang, L. (2018). Origin of the Phase Transition in Lithium Garnets. *The Journal of Physical Chemistry C*, *122*(4), 1963–1972. https://doi.org/10.1021/acs.jpcc.7b10911

Chen, K., Huang, M., Shen, Y., Lin, Y., & Nan, C. W. (2013). Improving ionic conductivity of Li0.35La0.55TiO3 ceramics by introducing Li7La3Zr2O12 sol into the precursor powder. *Solid State Ionics*, *235*(3), 8–13. https://doi.org/10.1016/j.ssi.2013.01.007

Chen, L., Li, Y., Li, S. P., Fan, L. Z., Nan, C. W., & Goodenough, J. B. (2018). PEO/garnet composite electrolytes for solid-state lithium batteries: From "ceramic-in-polymer" to "polymer-in-ceramic." *Nano Energy*, *46*(December 2017), 176–184. https://doi.org/10.1016/j.nanoen.2017.12.037

Chen, R., Yao, C., Yang, Q., Pan, H., Yu, X., Zhang, K., & Li, H. (2021a). Enhancing the Thermal Stability of NASICON Solid Electrolyte Pellets against Metallic Lithium by Defect Modification. *ACS Applied Materials and Interfaces*, *13*(16), 18743–18749. https://doi.org/10.1021/acsami.1c01246

Chen, R., Yao, C., Yang, Q., Pan, H., Yu, X., Zhang, K., & Li, H. (2021b). Enhancing the Thermal Stability of NASICON Solid Electrolyte Pellets against Metallic Lithium by Defect Modification. *ACS Applied Materials & Interfaces*, *13*(16), 18743–18749. https://doi.org/10.1021/acsami.1c01246

Chen, Z., Kim, G. T., Kim, J. K., Zarrabeitia, M., Kuenzel, M., Liang, H. P., Geiger, D., Kaiser, U., & Passerini, S. (2021). Highly Stable Quasi-Solid-State Lithium Metal Batteries: Reinforced Li1.3Al0.3Ti1.7(PO4)3/Li Interface by a Protection Interlayer. *Advanced Energy Materials*, *11*(30). https://doi.org/10.1002/aenm.202101339

Chen, Z., Xu, W., & Jiang, Y. (2020). Investigation of the effect of dimethyl methylphosphonate (DMMP) on flame extinction limit of lithium-ion battery electrolyte solvents. *Fuel*,

270(January), 117423. https://doi.org/10.1016/j.fuel.2020.117423

Cheng, L., Chen, W., Kunz, M., Persson, K., Tamura, N., Chen, G., & Doeff, M. (2015). Effect of Surface Microstructure on Electrochemical Performance of Garnet Solid Electrolytes. *ACS Applied Materials & Interfaces*, *7*(3), 2073–2081. https://doi.org/10.1021/am508111r

Cheng, L., Park, J. S., Hou, H., Zorba, V., Chen, G., Richardson, T., Cabana, J., Russo, R., & Doeff, M. (2014). Effect of microstructure and surface impurity segregation on the electrical and electrochemical properties of dense Al-substituted Li7La 3Zr2O12. *Journal of Materials Chemistry A*, *2*(1), 172–181. https://doi.org/10.1039/c3ta13999a

Cheng, X. B., Zhang, R., Zhao, C. Z., & Zhang, Q. (2017). Toward Safe Lithium Metal Anode in Rechargeable Batteries: A Review. *Chemical Reviews*, *117*(15), 10403–10473. https://doi.org/10.1021/acs.chemrev.7b00115

Chowdari, B. V. R., Radhakrishnan, K., Thomas, K. A., & Subba Rao, G. V. (1989). Ionic conductivity studies on Li1−xM2−xM′xP3O12 (H = Hf, Zr; M′ = Ti, Nb). *Materials Research Bulletin*, *24*(2), 221–229. https://doi.org/10.1016/0025-5408(89)90129-3

Chung, H. T., Kim, J. G., & Kim, H. G. (1998). Dependence of the lithium ionic conductivity on the B-site ion substitution in (Li0.5La0.5)Ti1 - XMxO3 (M = Sn, Zr, Mn, Ge). *Solid State Ionics*, *107*(1–2), 153–160. https://doi.org/10.1016/s0167-2738(97)00525-0

Ciosek Högström, K., Lundgren, H., Wilken, S., Zavalis, T. G., Behm, M., Edström, K., Jacobsson, P., Johansson, P., & Lindbergh, G. (2014). Impact of the flame retardant additive triphenyl phosphate (TPP) on the performance of graphite/LiFePO4 cells in high power applications. *Journal of Power Sources*, *256*, 430–439. https://doi.org/10.1016/j.jpowsour.2014.01.022

Commarieu, B., Paolella, A., Daigle, J. C., & Zaghib, K. (2018). Toward high lithium conduction in solid polymer and polymer–ceramic batteries. *Current Opinion in Electrochemistry*, *9*, 56–63. https://doi.org/10.1016/j.coelec.2018.03.033

Conte, F. V. (2006). Battery and battery management for hybrid electric vehicles: a review. *E & i Elektrotechnik Und Informationstechnik*, *123*(10), 424–431. https://doi.org/10.1007/s00502-006-0383-6

Cortes, F. J. Q., Lewis, J. A., Tippens, J., Marchese, T. S., & McDowell, M. T. (2020). How Metallic Protection Layers Extend the Lifetime of NASICON-Based Solid-State Lithium Batteries. *Journal of The Electrochemical Society*, *167*(5), 050502. https://doi.org/10.1149/2.0032005jes

Croce, F., Appetecchi, G. B., Persi, L., & Scrosati, B. (1998). Nanocomposite polymer electrolytes for lithium batteries. *Nature*, *394*(6692), 456–458. https://doi.org/10.1038/28818

Cussen, E. J. (2006). The structure of lithium garnets: cation disorder and clustering in a new family of fast Li + conductors. *Chem. Commun.*, *4*, 412–413. https://doi.org/10.1039/B514640B

David, I. N., Thompson, T., Wolfenstine, J., Allen, J. L., & Sakamoto, J. (2015). Microstructure and Li-Ion Conductivity of Hot-Pressed Cubic Li 7 La 3 Zr 2 O 12. *Journal of the American*

Ceramic Society, *98*(4), 1209–1214. https://doi.org/10.1111/jace.13455

Dawson, J. A., Attari, T. S., Chen, H., Emge, S. P., Johnston, K. E., & Islam, M. S. (2018). Elucidating lithium-ion and proton dynamics in anti-perovskite solid electrolytes. *Energy & Environmental Science*, *11*(10), 2993–3002. https://doi.org/10.1039/C8EE00779A

Dawson, J. A., Canepa, P., Famprikis, T., Masquelier, C., & Islam, M. S. (2018). Atomic-Scale Influence of Grain Boundaries on Li-Ion Conduction in Solid Electrolytes for All-Solid-State Batteries. *Journal of the American Chemical Society*, *140*(1), 362–368. https://doi.org/10.1021/jacs.7b10593

Deiseroth, H. J., Kong, S. T., Eckert, H., Vannahme, J., Reiner, C., Zaiß, T., & Schlosser, M. (2008). Li6PS5X: A class of crystalline Li-rich solids with an unusually high Li+ mobility. *Angewandte Chemie - International Edition*, *47*(4), 755–758. https://doi.org/10.1002/anie.200703900

Delmas, C. (1992). Electrochemical and physical properties of the LixNi1-yCoyO2 phases. *Solid State Ionics*, *53–56*(PART 1), 370–375. https://doi.org/10.1016/0167-2738(92)90402-B

Deng, Y., Eames, C., Fleutot, B., David, R., Chotard, J. N., Suard, E., Masquelier, C., & Islam, M. S. (2017). Enhancing the Lithium Ion Conductivity in Lithium Superionic Conductor (LISICON) Solid Electrolytes through a Mixed Polyanion Effect. *ACS Applied Materials and Interfaces*, *9*(8), 7050–7058. https://doi.org/10.1021/acsami.6b14402

Deng, Y., Shang, S.-J., Mei, A., Lin, Y.-H., Liu, L.-Y., & Nan, C.-W. (2009). The preparation and conductivity properties of Li0.5La0.5TiO3/inactive second phase composites. *Journal of Alloys and Compounds*, *472*(1–2), 456–460. https://doi.org/10.1016/j.jallcom.2008.04.085

Deng, Z., Radhakrishnan, B., & Ong, S. P. (2015a). Rational composition optimization of the lithium-rich Li3OCl1- xBrx anti-perovskite superionic conductors. *Chemistry of Materials*, *27*(10), 3749–3755. https://doi.org/10.1021/acs.chemmater.5b00988

Deng, Z., Radhakrishnan, B., & Ong, S. P. (2015b). Rational composition optimization of the lithium-rich Li3OCl1- xBrx anti-perovskite superionic conductors. *Chemistry of Materials*, *27*(10), 3749–3755. https://doi.org/10.1021/acs.chemmater.5b00988

Deviannapoorani, C., Dhivya, L., Ramakumar, S., & Murugan, R. (2013). Lithium ion transport properties of high conductive tellurium substituted Li7La3Zr2O12 cubic lithium garnets. *Journal of Power Sources*, *240*, 18–25. https://doi.org/10.1016/j.jpowsour.2013.03.166

Deviannapoorani, C., Ramakumar, S., Janani, N., & Murugan, R. (2015). Synthesis of lithium garnets from La2Zr2O7 pyrochlore. *Solid State Ionics*, *283*, 123–130. https://doi.org/10.1016/j.ssi.2015.10.006

Deviannapoorani, C., Shankar, L. S., Ramakumar, S., & Murugan, R. (2016a). Investigation on lithium ion conductivity and structural stability of yttrium-substituted Li7La3Zr2O12. *Ionics*, *22*(8), 1281–1289. https://doi.org/10.1007/s11581-016-1674-5

Deviannapoorani, C., Shankar, L. S., Ramakumar, S., & Murugan, R. (2016b). Investigation on lithium ion conductivity and structural stability of yttrium-substituted Li7La3Zr2O12. *Ionics*, *22*(8), 1281–1289. https://doi.org/10.1007/s11581-016-1674-5

DeWees, R., & Wang, H. (2019). Synthesis and Properties of NaSICON-type LATP and LAGP Solid Electrolytes. *ChemSusChem*, *12*(16), 3713–3725. https://doi.org/10.1002/cssc.201900725

Di Lecce, D., Verrelli, R., & Hassoun, J. (2017). Lithium-ion batteries for sustainable energy storage: Recent advances towards new cell configurations. In *Green Chemistry* (Vol. 19, Issue 15, pp. 3442–3467). Royal Society of Chemistry. https://doi.org/10.1039/c7gc01328k

Dominko, R., Gaberscek, M., Bele, M., Mihailovic, D., & Jamnik, J. (2007). Carbon nanocoatings on active materials for Li-ion batteries. *Journal of the European Ceramic Society*, *27*(2–3), 909–913. https://doi.org/10.1016/j.jeurceramsoc.2006.04.133

Dondelinger, M., Swanson, J., Nasymov, G., Jahnke, C., Qiao, Q., Wu, J., Widener, C., Numan-Al-Mobin, A. M., & Smirnova, A. (2019). Electrochemical stability of lithium halide electrolyte with antiperovskite crystal structure. *Electrochimica Acta*, *306*, 498–505. https://doi.org/10.1016/j.electacta.2019.03.074

Doughty, D., & Roth, E. P. (2012). A General Discussion of Li Ion Battery Safety. *Electrochemical Society Interface*, *21*(2), 37–44. https://doi.org/10.1149/2.F03122if

Doux, J. M., Nguyen, H., Tan, D. H. S., Banerjee, A., Wang, X., Wu, E. A., Jo, C., Yang, H., & Meng, Y. S. (2020). Stack Pressure Considerations for Room-Temperature All-Solid-State Lithium Metal Batteries. *Advanced Energy Materials*, *10*(1), 1–6. https://doi.org/10.1002/aenm.201903253

Duan, H., Yin, Y. X., Shi, Y., Wang, P. F., Zhang, X. D., Yang, C. P., Shi, J. L., Wen, R., Guo, Y. G., & Wan, L. J. (2018). Dendrite-Free Li-Metal Battery Enabled by a Thin Asymmetric Solid Electrolyte with Engineered Layers. *Journal of the American Chemical Society*, *140*(1), 82–85. https://doi.org/10.1021/jacs.7b10864

Dumon, A., Huang, M., Shen, Y., & Nan, C. W. (2013). High Li ion conductivity in strontium doped Li7La 3Zr2O12 garnet. *Solid State Ionics*, *243*, 36–41. https://doi.org/10.1016/j.ssi.2013.04.016

El-Shinawi, H., Paterson, G. W., MacLaren, D. A., Cussen, E. J., & Corr, S. A. (2017). Low-temperature densification of Al-doped Li7La3Zr2O12: a reliable and controllable synthesis of fast-ion conducting garnets. *Journal of Materials Chemistry A*, *5*(1), 319–329. https://doi.org/10.1039/c6ta06961d

El Shinawi, H., & Janek, J. (2013a). Stabilization of cubic lithium-stuffed garnets of the type "li 7La3Zr2O12" by addition of gallium. *Journal of Power Sources*, *225*, 13–19. https://doi.org/10.1016/j.jpowsour.2012.09.111

El Shinawi, H., & Janek, J. (2013b). Stabilization of cubic lithium-stuffed garnets of the type "Li7La3Zr2O12" by addition of gallium. *Journal of Power Sources*, *225*, 13–19. https://doi.org/10.1016/j.jpowsour.2012.09.111

Emly, A., Kioupakis, E., & Van Der Ven, A. (2013). Phase stability and transport mechanisms in antiperovskite Li 3OCl and Li3OBr superionic conductors. *Chemistry of Materials*, *25*(23), 4663–4670. https://doi.org/10.1021/cm4016222

EPA. (n.d.). *Overview of Greenhouse Gases*. https://www.epa.gov/ghgemissions/overview-

greenhouse-gases

Epp, V., Ma, Q., Hammer, E. M., Tietz, F., & Wilkening, M. (2015). Very fast bulk Li ion diffusivity in crystalline Li1.5Al0.5Ti1.5(PO4)3 as seen using NMR relaxometry. *Physical Chemistry Chemical Physics*, *17*(48), 32115–32121. https://doi.org/10.1039/c5cp05337d

Famprikis, T., Canepa, P., Dawson, J. A., Islam, M. S., & Masquelier, C. (2019). Fundamentals of inorganic solid-state electrolytes for batteries. *Nature Materials*, *18*(12), 1278–1291. https://doi.org/10.1038/s41563-019-0431-3

Fan, L., Wei, S., Li, S., Li, Q., & Lu, Y. (2018). Recent Progress of the Solid-State Electrolytes for High-Energy Metal-Based Batteries. *Advanced Energy Materials*, *8*(11), 1702657. https://doi.org/10.1002/aenm.201702657

Fan, X., Wang, Z., Cai, T., Yang, Y., Wu, H., Cao, S., Yang, Z., & Zhang, W. (2021). An integrated highly stable anode enabled by carbon nanotube-reinforced all-carbon binder for enhanced performance in lithium-ion battery. *Carbon*, *182*, 749–757. https://doi.org/10.1016/j.carbon.2021.06.065

Feng, J. K., Sun, X. J., Ai, X. P., Cao, Y. L., & Yang, H. X. (2008). Dimethyl methyl phosphate: A new nonflammable electrolyte solvent for lithium-ion batteries. *Journal of Power Sources*, *184*(2), 570–573. https://doi.org/10.1016/j.jpowsour.2008.02.006

Feng, W., Yang, P., Dong, X., & Xia, Y. (2022). A Low Temperature Soldered All Ceramic Lithium Battery. *ACS Applied Materials & Interfaces*, *14*(1), 1149–1156. https://doi.org/10.1021/acsami.1c21332

Ferg, E., Gummow, R. J., de Kock, A., & Thackeray, M. M. (1994). Spinel Anodes for Lithium-Ion Batteries. *Journal of The Electrochemical Society*, *141*(11), L147–L150. https://doi.org/10.1149/1.2059324

Fergus, J. W. (2010). Ceramic and polymeric solid electrolytes for lithium-ion batteries. *Journal of Power Sources*, *195*(15), 4554–4569. https://doi.org/10.1016/j.jpowsour.2010.01.076

Fouassier, C., Matejka, G., Reau, J.-M., & Hagenmuller, P. (1973). Sur de nouveaux bronzes oxygénés de formule NaχCoO2 (χ1). Le système cobalt-oxygène-sodium. *Journal of Solid State Chemistry*, *6*(4), 532–537. https://doi.org/10.1016/S0022-4596(73)80011-8

Fourquet, J. L., Duroy, H., & Crosnier-Lopez, M. P. (1996). Structural and Microstructural Studies of the Series La2/3−xLi3x□1/3−2xTiO3. *Journal of Solid State Chemistry*, *127*(2), 283–294. https://doi.org/10.1006/jssc.1996.0385

Fox, J. (2023). *ASEAN Economic Outlook 2023*. ASEANbriefing. https://www.aseanbriefing.com/news/asean-economic-outlook-2023/#theaseangrowthstoryHeader

Francis, C., Louey, R., Sammut, K., & Best, A. S. (2018). Thermal Stability of Pyrrolidinium-FSI Ionic Liquid Electrolyte and Lithium-Ion Electrodes at Elevated Temperatures. *Journal of The Electrochemical Society*, *165*(7), A1204–A1221. https://doi.org/10.1149/2.0281807jes

Fredenhagen, K., & Cadenbach, G. (1926). Die Bindung von Kalium durch Kohlenstoff.

Zeitschrift Für Anorganische Und Allgemeine Chemie, *158*(1), 249–263. https://doi.org/10.1002/zaac.19261580122

Fu, K. (Kelvin), Gong, Y., Liu, B., Zhu, Y., Xu, S., Yao, Y., Luo, W., Wang, C., Lacey, S. D., Dai, J., Chen, Y., Mo, Y., Wachsman, E., & Hu, L. (2017). Toward garnet electrolyte–based Li metal batteries: An ultrathin, highly effective, artificial solid-state electrolyte/metallic Li interface. *Science Advances*, *3*(4). https://doi.org/10.1126/sciadv.1601659

Gai, J., Zhao, E., Ma, F., Sun, D., Ma, X., Jin, Y., Wu, Q., & Cui, Y. (2018). Improving the Li-ion conductivity and air stability of cubic Li7La3Zr2O12 by the co-doping of Nb, Y on the Zr site. *Journal of the European Ceramic Society*, *38*(4), 1673–1678. https://doi.org/10.1016/j.jeurceramsoc.2017.12.002

Gamble, F. R., Osiecki, J. H., Cais, M., Pisharody, R., DiSalvo, F. J., & Geballe, T. H. (1971). Intercalation Complexes of Lewis Bases and Layered Sulfides: A Large Class of New Superconductors. *Science*, *174*(4008), 493–497. https://doi.org/10.1126/science.174.4008.493

Gao, Y. X., Wang, X. P., Wang, W. G., Zhuang, Z., Zhang, D. M., & Fang, Q. F. (2010). Synthesis, ionic conductivity, and chemical compatibility of garnet-like lithium ionic conductor Li5La3Bi2O12. *Solid State Ionics*, *181*(31–32), 1415–1419. https://doi.org/10.1016/j.ssi.2010.08.012

Gao, Z., Sun, H., Fu, L., Ye, F., Zhang, Y., Luo, W., & Huang, Y. (2018). Promises, Challenges, and Recent Progress of Inorganic Solid-State Electrolytes for All-Solid-State Lithium Batteries. *Advanced Materials*, *30*(17), 1705702. https://doi.org/10.1002/adma.201705702

Geiger, C. A., Alekseev, E., Lazic, B., Fisch, M., Armbruster, T., Langner, R., Fechtelkord, M., Kim, N., Pettke, T., & Weppner, W. (2011a). Crystal Chemistry and Stability of "Li 7 La 3 Zr 2 O 12 " Garnet: A Fast Lithium-Ion Conductor. *Inorganic Chemistry*, *50*(3), 1089–1097. https://doi.org/10.1021/ic101914e

Geiger, C. A., Alekseev, E., Lazic, B., Fisch, M., Armbruster, T., Langner, R., Fechtelkord, M., Kim, N., Pettke, T., & Weppner, W. (2011b). Crystal Chemistry and Stability of "Li7La3Zr2O12" Garnet: A Fast Lithium-Ion Conductor. *Inorganic Chemistry*, *50*(3), 1089–1097. https://doi.org/10.1021/ic101914e

Giarola, M., Sanson, A., Tietz, F., Pristat, S., Dashjav, E., Rettenwander, D., Redhammer, G. J., & Mariotto, G. (2017). Structure and Vibrational Dynamics of NASICON-Type LiTi 2 (PO 4) 3. *The Journal of Physical Chemistry C*, *121*(7), 3697–3706. https://doi.org/10.1021/acs.jpcc.6b11067

Golozar, M., Paolella, A., Demers, H., Savoie, S., Girard, G., Delaporte, N., Gauvin, R., Guerfi, A., Lorrmann, H., & Zaghib, K. (2020). Direct observation of lithium metal dendrites with ceramic solid electrolyte. *Scientific Reports*, *10*(1), 1–11. https://doi.org/10.1038/s41598-020-75456-0

Goodenough, J. B., Hong, H. .-P., & Kafalas, J. A. (1976). Fast Na+-ion transport in skeleton structures. *Materials Research Bulletin*, *11*(2), 203–220. https://doi.org/10.1016/0025-5408(76)90077-5

Goodenough, J. B., Mizushima, K., & Wiseman, P. J. (1976). Electrochemical cell and method of making ion conductors for said cell (Patent No. EP0017400B1). In *European Patent Office* (EP0017400B1).

Gorai, P., Famprikis, T., Singh, B., Stevanović, V., & Canepa, P. (2021). Devil is in the Defects: Electronic Conductivity in Solid Electrolytes. *Chemistry of Materials*, *33*(18), 7484–7498. https://doi.org/10.1021/acs.chemmater.1c02345

Greco, A., Jiang, X., & Cao, D. (2015). An investigation of lithium-ion battery thermal management using paraffin/porous-graphite-matrix composite. *Journal of Power Sources*, *278*, 50–68. https://doi.org/10.1016/j.jpowsour.2014.12.027

Guerard, D., & Herold, A. (1975). Intercalation of lithium into graphite and other carbons. *Carbon*, *13*(4), 337–345. https://doi.org/10.1016/0008-6223(75)90040-8

Haber, F. (1905). *Thermodynamik technischer Gasreaktionen*. https://www.ptonline.com/articles/how-to-get-better-mfi-results

Han, F., Zhu, Y., He, X., Mo, Y., & Wang, C. (2016). Electrochemical Stability of Li 10 GeP 2 S 12 and Li 7 La 3 Zr 2 O 12 Solid Electrolytes. *Advanced Energy Materials*, *6*(8), 1501590. https://doi.org/10.1002/aenm.201501590

Han, K. S., Bazak, J. D., Chen, Y., Graham, T. R., Washton, N. M., Hu, J. Z., Murugesan, V., & Mueller, K. T. (2021). Pulsed Field Gradient Nuclear Magnetic Resonance and Diffusion Analysis in Battery Research. *Chemistry of Materials*, *33*(22), 8562–8590. https://doi.org/10.1021/acs.chemmater.1c02891

Han, M., Zheng, D., Song, P., & Ding, Y. (2021). Theoretical study on fluoroethylene carbonate as an additive for the electrolyte of lithium ion batteries. *Chemical Physics Letters*, *771*(January), 138538. https://doi.org/10.1016/j.cplett.2021.138538

Han, X., Gong, Y., Fu, K. (Kelvin), He, X., Hitz, G. T., Dai, J., Pearse, A., Liu, B., Wang, H., Rubloff, G., Mo, Y., Thangadurai, V., Wachsman, E. D., & Hu, L. (2017). Negating interfacial impedance in garnet-based solid-state Li metal batteries. *Nature Materials*, *16*(5), 572–579. https://doi.org/10.1038/nmat4821

Hanghofer, I., Redhammer, G. J., Rohde, S., Hanzu, I., Senyshyn, A., Wilkening, H. M. R., & Rettenwander, D. (2018). Untangling the Structure and Dynamics of Lithium-Rich Anti-Perovskites Envisaged as Solid Electrolytes for Batteries. *Chemistry of Materials*, *30*(22), 8134–8144. https://doi.org/10.1021/acs.chemmater.8b02568

Hannan, M. A., Lipu, M. S. H., Hussain, A., & Mohamed, A. (2017). A review of lithium-ion battery state of charge estimation and management system in electric vehicle applications: Challenges and recommendations. *Renewable and Sustainable Energy Reviews*, *78*(May), 834–854. https://doi.org/10.1016/j.rser.2017.05.001

Harada, M., Takeda, H., Suzuki, S., Nakano, K., Tanibata, N., Nakayama, M., Karasuyama, M., & Takeuchi, I. (2020). Bayesian-optimization-guided experimental search of NASICON-type solid electrolytes for all-solid-state Li-ion batteries. *Journal of Materials Chemistry A*, *8*(30), 15103–15109. https://doi.org/10.1039/d0ta04441e

Haregewoin, A. M., Wotango, A. S., & Hwang, B. J. (2016). Electrolyte additives for lithium ion

battery electrodes: Progress and perspectives. *Energy and Environmental Science*, *9*(6), 1955–1988. https://doi.org/10.1039/c6ee00123h

Harris, S. J., Timmons, A., & Pitz, W. J. (2009). A combustion chemistry analysis of carbonate solvents used in Li-ion batteries. *Journal of Power Sources*, *193*(2), 855–858. https://doi.org/10.1016/j.jpowsour.2009.04.030

Harris, W. S. (1958). *ELECTROCHEMICAL STUDIES IN CYCLIC ESTERS*. https://doi.org/10.2172/4305596

Hartmann, P., Leichtweiss, T., Busche, M. R., Schneider, M., Reich, M., Sann, J., Adelhelm, P., & Janek, J. (2013). Degradation of NASICON-type materials in contact with lithium metal: Formation of mixed conducting interphases (MCI) on solid electrolytes. *Journal of Physical Chemistry C*, *117*(41), 21064–21074. https://doi.org/10.1021/jp4051275

Hayamizu, K., & Seki, S. (2017). Long-range Li ion diffusion in NASICON-type Li1.5Al0.5Ge1.5(PO4)3 (LAGP) studied by 7Li pulsed-gradient spin-echo NMR. *Physical Chemistry Chemical Physics*, *19*(34), 23483–23491. https://doi.org/10.1039/c7cp03647g

Hayashi, A., Muramatsu, H., Ohtomo, T., Hama, S., & Tatsumisago, M. (2014). Improved chemical stability and cyclability in Li2S–P2S5–P2O5–ZnO composite electrolytes for all-solid-state rechargeable lithium batteries. *Journal of Alloys and Compounds*, *591*, 247–250. https://doi.org/10.1016/j.jallcom.2013.12.191

Hayashi, A., Yamashita, H., Tatsumisago, M., & Minami, T. (2002). Characterization of Li2S–SiS2–LixMOy (M=Si, P, Ge) amorphous solid electrolytes prepared by melt-quenching and mechanical milling. *Solid State Ionics*, *148*(3–4), 381–389. https://doi.org/10.1016/S0167-2738(02)00077-2

He, L., Sun, Q., Chen, C., Oh, J. A. S., Sun, J., Li, M., Tu, W., Zhou, H., Zeng, K., & Lu, L. (2019). Failure Mechanism and Interface Engineering for NASICON-Structured All-Solid-State Lithium Metal Batteries. *ACS Applied Materials and Interfaces*, *11*(23), 20895–20904. https://doi.org/10.1021/acsami.9b05516

He, L. X., & Yoo, H. I. (2003). Effects of B-site ion (M) substitution on the ionic conductivity of (Li3xLa2/3-x)1+y/2(MyTi1-y)O3 (M = Al, Cr). *Electrochimica Acta*, *48*(10), 1357–1366. https://doi.org/10.1016/S0013-4686(02)00848-4

Hong, H. .-P. (1976). Crystal structures and crystal chemistry in the system Na1+xZr2SixP3−xO12. *Materials Research Bulletin*, *11*(2), 173–182. https://doi.org/10.1016/0025-5408(76)90073-8

Hong, H. Y. P. (1978). Crystal structure and ionic conductivity of Li14Zn(GeO4)4 and other new Li+ superionic conductors. *Materials Research Bulletin*, *13*(2), 117–124. https://doi.org/10.1016/0025-5408(78)90075-2

Hopkins, G. M. (1889). Secondary Battery. *Scientific American*, *61*(2), US4668595A. https://doi.org/10.1038/scientificamerican07131889-22

Hradecky, S. (2013). Accident: ANA B788 near Takamatsu on Jan 16th 2013, battery problem and burning smell on board. *The Aviation Herald*. http://avherald.com/h?article=45c377c5&opt=0

Hu, Y.-S. (2016). Batteries: Getting solid. *Nature Energy*, *1*(4), 16042. https://doi.org/10.1038/nenergy.2016.42

Huang, M., Dumon, A., & Nan, C. W. (2012). Effect of Si, in and Ge doping on high ionic conductivity of Li 7La 3Zr 2O 12. *Electrochemistry Communications*, *21*(1), 62–64. https://doi.org/10.1016/j.elecom.2012.04.032

Huang, W., Cheng, L., Hori, S., Suzuki, K., Yonemura, M., Hirayama, M., & Kanno, R. (2020). Ionic Conduction Mechanism of a Lithium Superionic Argyrodite in the Li-Al-Si-S-O System. *Materials Advances*, *1*(3), 334–340. https://doi.org/10.1039/d0ma00115e

Huang, W., Yoshino, K., Hori, S., Suzuki, K., Yonemura, M., Hirayama, M., & Kanno, R. (2019). Superionic lithium conductor with a cubic argyrodite-type structure in the Li–Al–Si–S system. *Journal of Solid State Chemistry*, *270*(October 2018), 487–492. https://doi.org/10.1016/j.jssc.2018.12.015

Huang, Z., Chen, L., Huang, B., Xu, B., Shao, G., Wang, H., Li, Y., & Wang, C.-A. (2020). Enhanced Performance of Li 6.4 La 3 Zr 1.4 Ta 0.6 O 12 Solid Electrolyte by the Regulation of Grain and Grain Boundary Phases. *ACS Applied Materials & Interfaces*, *12*(50), 56118–56125. https://doi.org/10.1021/acsami.0c18674

Huang, Z., Liu, K., Chen, L., Lu, Y., Li, Y., & Wang, C.-A. (2017). Sintering behavior of garnet-type Li 6.4 La 3 Zr 1.4 Ta 0.6 O 12 in Li 2 CO 3 atmosphere and its electrochemical property. *International Journal of Applied Ceramic Technology*, *14*(5), 921–927. https://doi.org/10.1111/ijac.12735

Huo, H., Luo, J., Thangadurai, V., Guo, X., Nan, C. W., & Sun, X. (2020). Li2CO3: A Critical Issue for Developing Solid Garnet Batteries. *ACS Energy Letters*, *5*(1), 252–262. https://doi.org/10.1021/acsenergylett.9b02401

Hyung, Y. E., Vissers, D. R., & Amine, K. (2003). Flame-retardant additives for lithium-ion batteries. *Journal of Power Sources*, *119–121*, 383–387. https://doi.org/10.1016/S0378-7753(03)00225-8

IEA. (2021). Key World Energy Statistics 2021 – Statistics Report. In *IEA Publications*. https://www.iea.org/reports/key-world-energy-statistics-2021

Il'ina, E. A., Pershina, S. V., Antonov, B. D., Pankratov, A. A., & Vovkotrub, E. G. (2018). The influence of the glass additive Li2O-B2O3-SiO2 on the phase composition, conductivity, and microstructure of the Li7La3Zr2O12. *Journal of Alloys and Compounds*, *765*, 841–847. https://doi.org/10.1016/j.jallcom.2018.06.154

Inaguma, Y., Chen, L., Itoh, M., & Nakamura, T. (1994). Candidate compounds with perovskite structure for high lithium ionic conductivity. *Solid State Ionics*, *70–71*(PART 1), 196–202. https://doi.org/10.1016/0167-2738(94)90309-3

Inaguma, Y., Katsumata, T., Itoh, M., & Morii, Y. (2002). Crystal Structure of a Lithium Ion-Conducting Perovskite La2/3−xLi3xTiO3 (x=0.05). *Journal of Solid State Chemistry*, *166*(1), 67–72. https://doi.org/10.1006/jssc.2002.9560

Inaguma, Y., Katsumata, T., Itoh, M., Morii, Y., & Tsurui, T. (2006). Structural investigations of migration pathways in lithium ion-conducting La2/3−Li3TiO3 perovskites. *Solid State*

Ionics, *177*(35–36), 3037–3044. https://doi.org/10.1016/j.ssi.2006.08.012

Inaguma, Y., Liquan, C., Itoh, M., Nakamura, T., Uchida, T., Ikuta, H., & Wakihara, M. (1993). High ionic conductivity in lithium lanthanum titanate. *Solid State Communications*, *86*(10), 689–693. https://doi.org/10.1016/0038-1098(93)90841-A

Inaguma, Y., Matsui, Y., Yu, J., Shan, Y.-J., Nakamura, T., & Itoh, M. (1997). Effect of substitution and pressure on lithium ion conductivity in perovskites Ln12Li12TiO3 (Ln= La, Pr, Nd and Sm). *Journal of Physics and Chemistry of Solids*, *58*(6), 843–852. https://doi.org/10.1016/S0022-3697(96)00226-0

IPCC. (2022). Climate Change 2022 - Mitigation of Climate Change. In *Cambridge University Press* (Issue 1).

Ishiguro, K., Nakata, Y., Matsui, M., Uechi, I., Takeda, Y., Yamamoto, O., & Imanishi, N. (2013). Stability of Nb-Doped Cubic Li7La3Zr2O12 with Lithium Metal. *Journal of The Electrochemical Society*, *160*(10), A1690–A1693. https://doi.org/10.1149/2.036310jes

Jaguemont, J., Boulon, L., & Dubé, Y. (2016). A comprehensive review of lithium-ion batteries used in hybrid and electric vehicles at cold temperatures. *Applied Energy*, *164*, 99–114. https://doi.org/10.1016/j.apenergy.2015.11.034

Jalem, R., Rushton, M., Manalastas, W., Nakayama, M., Kasuga, T., Kilner, J. A., Grimes, R. W., & Kasuga, ro. (2015). *Effects of Gallium Doping in Garnet-Type Li 7 La 3 Zr 2 O 12 Solid Electrolytes Effects of Gallium Doping in Garnet-Type Li 7 La 3 Zr 2 O 12 Solid Electrolytes 2*.

Jalem, R., Yamamoto, Y., Shiiba, H., Nakayama, M., Munakata, H., Kasuga, T., & Kanamura, K. (2013). Concerted Migration Mechanism in the Li Ion Dynamics of Garnet-Type Li 7 La 3 Zr 2 O 12. *Chemistry of Materials*, *25*(3), 425–430. https://doi.org/10.1021/cm303542x

Janani, N., Deviannapoorani, C., Dhivya, L., & Murugan, R. (2014). Influence of sintering additives on densification and Li + conductivity of Al doped Li 7 La 3 Zr 2 O 12 lithium garnet. *RSC Adv.*, *4*(93), 51228–51238. https://doi.org/10.1039/C4RA08674K

Janek, J., & Zeier, W. G. (2016). A solid future for battery development. *Nature Energy*, *1*(9), 16141. https://doi.org/10.1038/nenergy.2016.141

Jasinki, R. (1969). *High Energy Battery Systems Based on Propylene Carbonate*.

Javed, M. A., Ahola, S., Håkansson, P., Mankinen, O., Aslam, M. K., Filippov, A., Shah, F. U., Glavatskih, S., Antzutkin, O. N., & Telkki, V. V. (2017). Structure and dynamics elucidation of ionic liquids using multidimensional Laplace NMR. *Chemical Communications*, *53*(80), 11056–11059. https://doi.org/10.1039/c7cc05493a

Jian, Z., Hu, Y. S., Ji, X., & Chen, W. (2017). NASICON-Structured Materials for Energy Storage. *Advanced Materials*, *29*(20). https://doi.org/10.1002/adma.201601925

Jiang, J., Fortier, H., Reimers, J. N., & Dahn, J. R. (2004). Thermal Stability of 18650 Size Li-Ion Cells Containing LiBOB Electrolyte Salt. *Journal of The Electrochemical Society*, *151*(4), A609. https://doi.org/10.1149/1.1667520

Jung, S.-K., Gwon, H., Kim, H., Yoon, G., Shin, D., Hong, J., Jung, C., & Kim, J.-S. (2022). Unlocking the hidden chemical space in cubic-phase garnet solid electrolyte for efficient quasi-all-solid-state lithium batteries. *Nature Communications*, *13*(1), 7638. https://doi.org/10.1038/s41467-022-35287-1

Jung, Y.-C., Lee, S.-M., Choi, J.-H., Jang, S. S., & Kim, D.-W. (2015). All Solid-State Lithium Batteries Assembled with Hybrid Solid Electrolytes. *Journal of The Electrochemical Society*, *162*(4), A704–A710. https://doi.org/10.1149/2.0731504jes

Kahlaoui, R., Arbi, K., Sobrados, I., Jimenez, R., Sanz, J., & Ternane, R. (2017). Cation Miscibility and Lithium Mobility in NASICON Li1+xTi2-xScx(PO4)3 ($0 \leq x \leq 0.5$) Series: A Combined NMR and Impedance Study. *Inorganic Chemistry*, *56*(3), 1216–1224. https://doi.org/10.1021/acs.inorgchem.6b02274

Kaib, T., Haddadpour, S., Kapitein, M., Bron, P., Schröder, C., Eckert, H., Roling, B., & Dehnen, S. (2012). New lithium chalcogenidotetrelates, LiChT: Synthesis and characterization of the Li +-conducting tetralithium ortho-sulfidostannate Li 4SnS 4. *Chemistry of Materials*, *24*(11), 2211–2219. https://doi.org/10.1021/cm3011315

Kamaya, N., Homma, K., Yamakawa, Y., Hirayama, M., Kanno, R., Yonemura, M., Kamiyama, T., Kato, Y., Hama, S., Kawamoto, K., & Mitsui, A. (2011). A lithium superionic conductor. *Nature Materials*, *10*(9), 682–686. https://doi.org/10.1038/nmat3066

Kammampata, S. P., Basappa, R. H., Ito, T., Yamada, H., & Thangadurai, V. (2019). Microstructural and Electrochemical Properties of Alkaline Earth Metal-Doped Li Garnet-Type Solid Electrolytes Prepared by Solid-State Sintering and Spark Plasma Sintering Methods [Research-article]. *ACS Applied Energy Materials*, *2*(3), 1765–1773. https://doi.org/10.1021/acsaem.8b01899

Kanno, R., Hata, T., Kawamoto, Y., & Irie, M. (2000). Synthesis of a new lithium ionic conductor, thio-LISICON–lithium germanium sulfide system. *Solid State Ionics*, *130*(1–2), 97–104. https://doi.org/10.1016/S0167-2738(00)00277-0

Kanno, R., & Murayama, M. (2001). Lithium Ionic Conductor Thio-LISICON: The Li_2S-GeS_2-P_2S_5 System. *Journal of The Electrochemical Society*, *148*(7), A742. https://doi.org/10.1149/1.1379028

Kasper, H. M. (1969). A new series of rare earth garnets Ln3+3M2Li+3O12(M = Te, W). *Inorganic Chemistry*, *8*(4), 1000–1002. https://doi.org/10.1021/ic50074a058

Kato, Y., Hori, S., Saito, T., Suzuki, K., Hirayama, M., Mitsui, A., Yonemura, M., Iba, H., & Kanno, R. (2016). High-power all-solid-state batteries using sulfide superionic conductors. *Nature Energy*, *1*(4), 16030. https://doi.org/10.1038/nenergy.2016.30

Katsumata, T., Inaguma, Y., & Itoh, M. (1998). New perovskite-type lithium ion conductors, La M Li1−3−NbO3 (M=Ag and Na). *Solid State Ionics*, *113–115*, 465–469. https://doi.org/10.1016/S0167-2738(98)00311-7

Katsumata, T., Matsui, Y., Inaguma, Y., & Itoh, M. (1996). Influence of site percolation and local distortion on lithium ion conductivity in perovskite-type oxides La0.55Li0.35 − K TiO3 and La0.55Li0.35TiO3-KMO3 (M = Nb and Ta). *Solid State Ionics*, *86–88*(PART 1),

165–169. https://doi.org/10.1016/0167-2738(96)00116-6

Kawai, H., & Kuwano, J. (1994). Lithium Ion Conductivity of A-Site Deficient Perovskite Solid Solution La0.67 − x Li3x TiO3. *Journal of The Electrochemical Society*, *141*(7), L78–L79. https://doi.org/10.1149/1.2055043

Kawamura, T., Kimura, A., Egashira, M., Okada, S., & Yamaki, J.-I. (2002). Thermal stability of alkyl carbonate mixed-solvent electrolytes for lithium ion cells. *Journal of Power Sources*, *104*(2), 260–264. https://doi.org/10.1016/S0378-7753(01)00960-0

Kazyak, E., Garcia-Mendez, R., LePage, W. S., Sharafi, A., Davis, A. L., Sanchez, A. J., Chen, K. H., Haslam, C., Sakamoto, J., & Dasgupta, N. P. (2020). Li Penetration in Ceramic Solid Electrolytes: Operando Microscopy Analysis of Morphology, Propagation, and Reversibility. *Matter*, *2*(4), 1025–1048. https://doi.org/10.1016/j.matt.2020.02.008

Khurana, R., Schaefer, J. L., Archer, L. A., & Coates, G. W. (2014). Suppression of lithium dendrite growth using cross-linked polyethylene/poly(ethylene oxide) electrolytes: A new approach for practical lithium-metal polymer batteries. *Journal of the American Chemical Society*, *136*(20), 7395–7402. https://doi.org/10.1021/ja502133j

Kim, J.-W., & Lee, H.-G. (2001). Thermal and carbothermic decomposition of Na2CO3 and Li2CO3. *Metallurgical and Materials Transactions B*, *32*(1), 17–24. https://doi.org/10.1007/s11663-001-0003-0

Kim, Y., Kim, D., Bliem, R., Vardar, G., Waluyo, I., Hunt, A., Wright, J. T., Katsoudas, J. P., & Yildiz, B. (2020). Thermally driven interfacial degradation between Li7La3Zr2O12 electrolyte and LiNi0.6Mn0.2Co0.2O2 cathode. *Chemistry of Materials*, *32*(22), 9531–9541. https://doi.org/10.1021/acs.chemmater.0c02261

Kotobuki, M. (2017). *Garnet-type Li Ion Conductive Ceramics and its Application for All-solid-state Li Batteries* (Vol. 12, pp. 164–184). https://doi.org/10.21741/9781945291272-7

Kotobuki, M., Lei, H., Chen, Y., Song, S., Xu, C., Hu, N., Molenda, J., & Lu, L. (2019). Preparation of thin solid electrolyte by hot-pressing and diamond wire slicing. *RSC Advances*, *9*(21), 11670–11675. https://doi.org/10.1039/C9RA00711C

Kraft, M. A., Culver, S. P., Calderon, M., Böcher, F., Krauskopf, T., Senyshyn, A., Dietrich, C., Zevalkink, A., Janek, J., & Zeier, W. G. (2017). Influence of Lattice Polarizability on the Ionic Conductivity in the Lithium Superionic Argyrodites Li 6 PS 5 X (X = Cl, Br, I). *Journal of the American Chemical Society*, *139*(31), 10909–10918. https://doi.org/10.1021/jacs.7b06327

Kraft, M. A., Ohno, S., Zinkevich, T., Koerver, R., Culver, S. P., Fuchs, T., Senyshyn, A., Indris, S., Morgan, B. J., & Zeier, W. G. (2018). Inducing High Ionic Conductivity in the Lithium Superionic Argyrodites Li6+xP1-xGexS5I for All-Solid-State Batteries [Research-article]. *Journal of the American Chemical Society*, *140*(47), 16330–16339. https://doi.org/10.1021/jacs.8b10282

Kresse, G., & Furthmüller, J. (1996). Efficient iterative schemes for ab initio total-energy calculations using a plane-wave basis set. *Physical Review B*, *54*(16), 11169–11186. https://doi.org/10.1103/PhysRevB.54.11169

Kuo, D. H., Lo, R., Hsueh, T. H., Jan, D. J., & Su, C. H. (2019). LiSnOS/gel polymer hybrid electrolyte for the safer and performance-enhanced solid-state LiCoO2/Li lithium-ion battery. *Journal of Power Sources*, *429*(October 2018), 89–96. https://doi.org/10.1016/j.jpowsour.2019.05.010

Kwak, H., Park, K. H., Han, D., Nam, K. W., Kim, H., & Jung, Y. S. (2020). Li+ conduction in air-stable Sb-Substituted Li4SnS4 for all-solid-state Li-Ion batteries. *Journal of Power Sources*, *446*, 227338. https://doi.org/10.1016/j.jpowsour.2019.227338

Kwon, N., Mouck-Makanda, D., & Fromm, K. (2018). A Review: Carbon Additives in LiMnPO4- and LiCoO2-Based Cathode Composites for Lithium Ion Batteries. *Batteries*, *4*(4), 50. https://doi.org/10.3390/batteries4040050

La Monaca, A., Zhu, W., Feng, Z., Bertoni, G., Campanella, D., Girard, G., Savoie, S., Nita, A. G., Clement, D., Demers, H., Vijh, A., Rosei, F., & Paolella, A. (2022). Influence of Rutile and Anatase TiO2 Precursors on the Synthesis of a Li1.5Al0.5Ti1.5(PO4)3 Electrolyte for Solid-State Lithium Batteries. *Journal of The Electrochemical Society*, *169*(4), 040515. https://doi.org/10.1149/1945-7111/ac6325

Lang, B., Ziebarth, B., & Elsässer, C. (2015). Lithium Ion Conduction in LiTi 2 (PO 4) 3 and Related Compounds Based on the NASICON Structure: A First-Principles Study. *Chemistry of Materials*, *27*(14), 5040–5048. https://doi.org/10.1021/acs.chemmater.5b01582

Larminie, J., & Lowry, J. (2012). *Electric Vehicle Technology Explained* (2nd ed.). Wiley. http://site.ebrary.com.vlib.interchange.at/lib/stategov/detail.action?docID=10579519&p00=electric+vehicle+technology+explained

Lazzari, M., & Scrosati, B. (1980). A Cyclable Lithium Organic Electrolyte Cell Based on Two Intercalation Electrodes. *Journal of The Electrochemical Society*, *127*(3), 773–774. https://doi.org/10.1149/1.2129753

Leblanc-Soreau, A., Danot, M., Trichet, L., & Rouxel, J. (1974). Les intercalaires Ax Ti S2 et Ax Zr S2. Structure et liaisons. (A = Li, Na, K, Rb, Cs). *Materials Research Bulletin*, *9*(2), 191–197. https://doi.org/10.1016/0025-5408(74)90198-6

Lee, S. J., Bae, J. J., & Son, J. T. (2019). Structural and Electrical Effects of Y-doped Li0.33La0.56−xYxTiO3 Solid Electrolytes on All-Solid-State Lithium Ion Batteries. *Journal of the Korean Physical Society*, *74*(1), 73–77. https://doi.org/10.3938/jkps.74.73

Lee, W., Lyon, C. K., Seo, J., Lopez-Hallman, R., Leng, Y., Wang, C., Hickner, M. A., Randall, C. A., & Gomez, E. D. (2019). Ceramic–Salt Composite Electrolytes from Cold Sintering. *Advanced Functional Materials*, *29*(20), 1807872. https://doi.org/10.1002/adfm.201807872

Lewis, G. N., & Keyes, F. G. (1913). THE POTENTIAL OF THE LITHIUM ELECTRODE. *Journal of the American Chemical Society*, *35*(4), 340–344. https://doi.org/10.1021/ja02193a004

Li, C., Liu, Y., He, J., & Brinkman, K. S. (2017). Ga-substituted Li7La3Zr2O12: An investigation based on grain coarsening in garnet-type lithium ion conductors. *Journal of Alloys and Compounds*, *695*, 3744–3752. https://doi.org/10.1016/j.jallcom.2016.11.277

Li, J., Ma, C., Chi, M., Liang, C., & Dudney, N. J. (2015). Solid Electrolyte: the Key for High-Voltage Lithium Batteries. *Advanced Energy Materials*, *5*(4), 1401408. https://doi.org/10.1002/aenm.201401408

Li, J., Zhu, K., Yao, Z., Qian, G., Zhang, J., Yan, K., & Wang, J. (2020). A promising composite solid electrolyte incorporating LLZO into PEO/PVDF matrix for all-solid-state lithium-ion batteries. *Ionics*, *26*(3), 1101–1108. https://doi.org/10.1007/s11581-019-03320-x

Li, N., Weng, Z., Wang, Y., Li, F., Cheng, H. M., & Zhou, H. (2014). An aqueous dissolved polysulfide cathode for lithium-sulfur batteries. *Energy and Environmental Science*, *7*(10), 3307–3312. https://doi.org/10.1039/c4ee01717j

Li, S., Zhu, J., Wang, Y., Howard, J. W., Lü, X., Li, Y., Kumar, R. S., Wang, L., Daemen, L. L., & Zhao, Y. (2016). Reaction mechanism studies towards effective fabrication of lithium-rich anti-perovskites Li3OX (X = Cl, Br). *Solid State Ionics*, *284*, 14–19. https://doi.org/10.1016/j.ssi.2015.11.027

Li, W., Dahn, J. R., & Wainwright, D. S. (1994). Rechargeable Lithium Batteries with Aqueous Electrolytes. *Science*, *264*(5162), 1115–1118. https://doi.org/10.1126/science.264.5162.1115

Li, Y., Wang, Z., Cao, Y., Du, F., Chen, C., Cui, Z., & Guo, X. (2015). W-Doped Li7La3Zr2O12 Ceramic Electrolytes for Solid State Li-ion Batteries. *Electrochimica Acta*, *180*, 37–42. https://doi.org/10.1016/j.electacta.2015.08.046

Li, Y., Wang, Z., Li, C., Cao, Y., & Guo, X. (2014). Densification and ionic-conduction improvement of lithium garnet solid electrolytes by flowing oxygen sintering. *Journal of Power Sources*, *248*, 642–646. https://doi.org/10.1016/j.jpowsour.2013.09.140

Li, Y., Xu, B., Xu, H., Duan, H., Lü, X., Xin, S., Zhou, W., Xue, L., Fu, G., Manthiram, A., & Goodenough, J. B. (2017). Hybrid Polymer/Garnet Electrolyte with a Small Interfacial Resistance for Lithium-Ion Batteries. *Angewandte Chemie International Edition*, *56*(3), 753–756. https://doi.org/10.1002/anie.201608924

Li, Y., Yang, T., Wu, W., Cao, Z., He, W., Gao, Y., Liu, J., & Li, G. (2018). Effect of Al-Mo codoping on the structure and ionic conductivity of sol-gel derived Li7La3Zr2O12 ceramics. *Ionics*, *24*(11), 3305–3315. https://doi.org/10.1007/s11581-018-2497-3

Li, Y., Zhou, W., Xin, S., Li, S., Zhu, J., Xujie, L., Cui, Z., Jia, Q., Zhou, J., Zhao, Y., & Goodenough, J. B. (2016). Fluorine-Doped Antiperovskite Electrolyte for All-Solid-State Lithium-Ion Batteries. *Angewandte Chemie International Edition*, *55*(34), 9965–9968. https://doi.org/10.1002/anie.201604554

Li, Z., Li, A., Zhang, H. H., Lin, R., Jin, T., Cheng, Q., Xiao, X., Lee, W.-K. W. K., Ge, M., Zhang, H. H., Zangiabadi, A., Waluyo, I., Hunt, A., Zhai, H., Borovilas, J. J. J., Wang, P., Yang, X. Q. X.-Q., Chuan, X., & Yang, Y. (2020). Interfacial engineering for stabilizing polymer electrolytes with 4V cathodes in lithium metal batteries at elevated temperature. *Nano Energy*, *72*(March), 104655. https://doi.org/10.1016/j.nanoen.2020.104655

Liang, C. C. (1973). Conduction Characteristics of the Lithium Iodide-Aluminum Oxide Solid Electrolytes. *Journal of The Electrochemical Society*, *120*(10), 1289.

https://doi.org/10.1149/1.2403248

Lin, D., Yuen, P. Y., Liu, Y., Liu, W., Liu, N., Dauskardt, R. H., & Cui, Y. (2018). A Silica-Aerogel-Reinforced Composite Polymer Electrolyte with High Ionic Conductivity and High Modulus. *Advanced Materials*, *30*(32), 1–8. https://doi.org/10.1002/adma.201802661

Lisbona, D., & Snee, T. (2011). A review of hazards associated with primary lithium and lithium-ion batteries. *Process Safety and Environmental Protection*, *89*(6), 434–442. https://doi.org/10.1016/j.psep.2011.06.022

Liu, C., Wang, H.-R., Long, T., Ma, Q., Ning, P., Dong, X.-R., Zhou, C.-S., Wu, X.-W., & Zeng, X.-X. (2022). Borosilicate Glass-Enabled Antifracture NASICON Solid Electrolytes for Lithium-Metal Batteries. *ACS Applied Energy Materials*, *5*(3), 3734–3740. https://doi.org/10.1021/acsaem.2c00180

Liu, G., Sun, Q., Li, Q., Zhang, J., & Ming, J. (2021). Electrolyte Issues in Lithium-Sulfur Batteries: Development, Prospect, and Challenges. *Energy and Fuels*, *35*(13), 10405–10427. https://doi.org/10.1021/acs.energyfuels.1c00990

Liu, J., Liu, T., Pu, Y., Guan, M., Tang, Z., Ding, F., Xu, Z., & Li, Y. (2017). Facile synthesis of NASICON-type Li1.3Al0.3Ti1.7(PO4)3 solid electrolyte and its application for enhanced cyclic performance in lithium ion batteries through the introduction of an artificial Li3PO4 SEI layer. *RSC Advances*, *7*(74), 46545–46552. https://doi.org/10.1039/c7ra09335g

Liu, J., Xu, C., Chen, Z., Ni, S., & Shen, Z. X. (2018). Progress in aqueous rechargeable batteries. *Green Energy and Environment*, *3*(1), 20–41. https://doi.org/10.1016/j.gee.2017.10.001

Liu, M., Li, X., Wang, X., Yu, R., Chen, M., Lu, Q., Lu, B., Shu, H., & Yang, X. (2018). Facile synthesis and electrochemical properties of high lithium ionic conductivity Li1.7Al0.3Ti1.7Si0.4P2.6O12 ceramic solid electrolyte. *Journal of Alloys and Compounds*, *756*, 103–110. https://doi.org/10.1016/j.jallcom.2018.04.333

Liu, W., Lin, D., Sun, J., Zhou, G., & Cui, Y. (2016). Improved Lithium Ionic Conductivity in Composite Polymer Electrolytes with Oxide-Ion Conducting Nanowires. *ACS Nano*, *10*(12), 11407–11413. https://doi.org/10.1021/acsnano.6b06797

Liu, Y., Li, C., Li, B., Song, H., Cheng, Z., Chen, M., He, P., & Zhou, H. (2018). Germanium Thin Film Protected Lithium Aluminum Germanium Phosphate for Solid-State Li Batteries. *Advanced Energy Materials*, *8*(16), 1–7. https://doi.org/10.1002/aenm.201702374

Liu, Y., Liu, J., Sun, Q., Wang, D., Adair, K. R., Liang, J., Zhang, C., Zhang, L., Lu, S., Huang, H., Song, X., & Sun, X. (2019). Insight into the Microstructure and Ionic Conductivity of Cold Sintered NASICON Solid Electrolyte for Solid-State Batteries [Research-article]. *ACS Applied Materials & Interfaces*, *11*(31), 27890–27896. https://doi.org/10.1021/acsami.9b08132

Liu, Y., Sun, Q., Zhao, Y., Wang, B., Kaghazchi, P., Adair, K. R., Li, R., Zhang, C., Liu, J., Kuo, L. Y., Hu, Y., Sham, T. K., Zhang, L., Yang, R., Lu, S., Song, X., & Sun, X. (2018). Stabilizing the Interface of NASICON Solid Electrolyte against Li Metal with Atomic Layer Deposition. *ACS Applied Materials and Interfaces*, *10*(37), 31240–31248.

https://doi.org/10.1021/acsami.8b06366

Logéat, A., Köhler, T., Eisele, U., Stiaszny, B., Harzer, A., Tovar, M., Senyshyn, A., Ehrenberg, H., & Kozinsky, B. (2012). From order to disorder: The structure of lithium-conducting garnets Li 7 - XLa 3Ta xZr 2 - xO 12 (x = 0-2). *Solid State Ionics*, *206*, 33–38. https://doi.org/10.1016/j.ssi.2011.10.023

Losch, P., Huang, W., Goodman, E. D., Wrasman, C. J., Holm, A., Riscoe, A. R., Schwalbe, J. A., & Cargnello, M. (2019). Colloidal nanocrystals for heterogeneous catalysis. *Nano Today*, *24*, 15–47. https://doi.org/10.1016/j.nantod.2018.12.002

Losilla, E. R., Aranda, M. A. G., Martínez-Lara, M., & Bruque, S. (1997). Reversible Triclinic-Rhombohedral Phase Transition in LiHf2(PO4)3: Crystal Structures from Neutron Powder Diffraction. *Chemistry of Materials*, *9*(7), 1678–1685. https://doi.org/10.1021/cm970078n

Lu, W., Xue, M., & Zhang, C. (2021). Modified Li7La3Zr2O12 (LLZO) and LLZO-polymer composites for solid-state lithium batteries. *Energy Storage Materials*, *39*(April), 108–129. https://doi.org/10.1016/j.ensm.2021.04.016

Lu, X., Wang, R., Zhang, F., & Li, J. (2020). The influence of phosphorous source on the properties of NASICON lithium-ion conductor Li1.3Al0.3Ti1.7(PO4)3. *Solid State Ionics*, *354*(July), 115417. https://doi.org/10.1016/j.ssi.2020.115417

Lu, Z., Liu, J., & Ciucci, F. (2020). Superionic conduction in low-dimensional-networked anti-perovskites. *Energy Storage Materials*, *28*(November 2019), 146–152. https://doi.org/10.1016/j.ensm.2020.03.005

Ma, C., Chen, K., Liang, C., Nan, C. W., Ishikawa, R., More, K., & Chi, M. (2014). Atomic-scale origin of the large grain-boundary resistance in perovskite Li-ion-conducting solid electrolytes. *Energy and Environmental Science*, *7*(5), 1638–1642. https://doi.org/10.1039/c4ee00382a

Ma, F., Zhao, E., Zhu, S., Yan, W., Sun, D., Jin, Y., & Nan, C. (2016). Preparation and evaluation of high lithium ion conductivity Li1.3Al0.3Ti1.7(PO4)3 solid electrolyte obtained using a new solution method. *Solid State Ionics*, *295*, 7–12. https://doi.org/10.1016/j.ssi.2016.07.010

Ma, Z., Xue, H. G., & Guo, S. P. (2018). Recent achievements on sulfide-type solid electrolytes: crystal structures and electrochemical performance. In *Journal of Materials Science* (Vol. 53, Issue 6, pp. 3927–3938). Springer New York LLC. https://doi.org/10.1007/s10853-017-1827-6

Maldonado-Manso, P., Losilla, E. R., Martínez-Lara, M., Aranda, M. A. G., Bruque, S., Mouahid, F. E., & Zahir, M. (2003). High Lithium Ionic Conductivity in the Li 1+ x Al x Ge y Ti 2 - x - y (PO 4) 3 NASICON Series. *Chemistry of Materials*, *15*(9), 1879–1885. https://doi.org/10.1021/cm021717j

Manthiram, A., & Goodenough, J. B. (1989). Lithium insertion into Fe2(SO4)3 frameworks. *Journal of Power Sources*, *26*(3–4), 403–408. https://doi.org/10.1016/0378-7753(89)80153-3

Manthiram, A., Yu, X., & Wang, S. (2017). Lithium battery chemistries enabled by solid-state

electrolytes. *Nature Reviews Materials*, *2*(4), 1–16. https://doi.org/10.1038/natrevmats.2016.103

Marangon, V., Hernandez-Rentero, C., Levchenko, S., Bianchini, G., Spagnolo, D., Caballero, A., Morales, J., & Hassoun, J. (2020). Lithium-Oxygen Battery Exploiting Highly Concentrated Glyme-Based Electrolytes. *ACS Applied Energy Materials*, *3*(12), 12263–12275. https://doi.org/10.1021/acsaem.0c02331

Meesala, Y., Liao, Y.-K. K., Jena, A., Yang, N.-H. H., Pang, W. K., Hu, S.-F. F., Chang, H., Liu, C.-E. E., Liao, S.-C. C., Chen, J.-M. M., Guo, X., & Liu, R.-S. S. (2019). An efficient multi-doping strategy to enhance Li-ion conductivity in the garnet-type solid electrolyte Li7La3Zr2O12. *Journal of Materials Chemistry A*, *7*(14), 8589–8601. https://doi.org/10.1039/c9ta00417c

Mei, A., Wang, X.-L., Feng, Y.-C., Zhao, S.-J., Li, G.-L., Geng, H.-X., Lin, Y.-H., & Nan, C.-W. (2008). Enhanced ionic transport in lithium lanthanum titanium oxide solid state electrolyte by introducing silica. *Solid State Ionics*, *179*(39), 2255–2259. https://doi.org/10.1016/j.ssi.2008.08.013

Mercier, R., Malugani, J.-P., Fahys, B., & Robert, G. (1981). Superionic conduction in Li 2 S - P 2 S 5 - LiI - glasses. *Solid State Ionics*, *5*(C), 663–666. https://doi.org/10.1016/0167-2738(81)90341-6

Messurier, D. Le, Petkov, V., Martin, S. W., Kim, Y., & Ren, Y. (2009). Three-dimensional structure of fast ion conducting 0.5Li2S + 0.5[(1 - x)GeS2 + xGeO2] glasses from high-energy X-ray diffraction and reverse Monte Carlo simulations. *Journal of Non-Crystalline Solids*, *355*(7), 430–437. https://doi.org/10.1016/j.jnoncrysol.2009.01.006

Miara, L. J., Richards, W. D., Wang, Y. E., & Ceder, G. (2015). First-Principles Studies on Cation Dopants and Electrolyte|Cathode Interphases for Lithium Garnets. *Chemistry of Materials*, *27*(11), 4040–4047. https://doi.org/10.1021/acs.chemmater.5b01023

Milian Pila, C. R., Cappe, E. P., Mohallem, N. D. S., Alves, O. L., Aguilar Frutis, M. A., Sánchez-Ramírez, N., Torresi, R. M., León Ramírez, H., & Laffita, Y. M. (2019). Effect of the LLTO nanoparticles on the conducting properties of PEO-based solid electrolyte. *Solid State Sciences*, *88*, 41–47. https://doi.org/10.1016/j.solidstatesciences.2018.10.014

Min, X., Xiao, J., Fang, M., Wang, W., Zhao, Y., Liu, Y., Abdelkader, A. M., Xi, K., Kumar, R. V., & Huang, Z. (2021). Potassium-ion batteries: Outlook on present and future technologies. *Energy and Environmental Science*, *14*(4), 2186–2243. https://doi.org/10.1039/d0ee02917c

Minami, K., Mizuno, F., Hayashi, A., & Tatsumisago, M. (2007). Lithium ion conductivity of the Li2S–P2S5 glass-based electrolytes prepared by the melt quenching method. *Solid State Ionics*, *178*(11–12), 837–841. https://doi.org/10.1016/j.ssi.2007.03.001

Mizushima, K., Jones, P. C., Wiseman, P. J., & Goodenough, J. B. (1980). LixCoO2 (0<x<-1): A new cathode material for batteries of high energy density. *Materials Research Bulletin*, *15*(6), 783–789. https://doi.org/10.1016/0025-5408(80)90012-4

Molaiyan, P., Mailhiot, S. E., Voges, K., Kantola, A. M., Hu, T., Michalowski, P., Kwade, A.,

Telkki, V. V., & Lassi, U. (2023). Investigation of the structure and ionic conductivity of a Li3InCl6 modified by dry room annealing for solid-state Li-ion battery applications. *Materials and Design*, *227*, 111690. https://doi.org/10.1016/j.matdes.2023.111690

Mouta, R., Melo, M. Á. B., Diniz, E. M., & Paschoal, C. W. A. (2014). Concentration of charge carriers, migration, and stability in Li3OCl solid electrolytes. *Chemistry of Materials*, *26*(24), 7137–7144. https://doi.org/10.1021/cm503717e

Murphy, D. W., & Trumbore, F. A. (1976). The Chemistry of TiS3 and NbSe3 Cathodes. *Journal of The Electrochemical Society*, *123*(7), 960–964. https://doi.org/10.1149/1.2133012

Murugan, R., Ramakumar, S., & Janani, N. (2011). High conductive yttrium doped Li7La3Zr2O12 cubic lithium garnet. *Electrochemistry Communications*, *13*(12), 1373–1375. https://doi.org/10.1016/j.elecom.2011.08.014

Murugan, R., Thangadurai, V., & Weppner, W. (2007). Fast Lithium Ion Conduction in Garnet-Type Li7La3Zr2O12. *Angewandte Chemie International Edition*, *46*(41), 7778–7781. https://doi.org/10.1002/anie.200701144

Nam, N. D., Park, I. J., & Kim, J. G. (2012). Triethyl and tributyl phosphite as flame-retarding additives in Li-ion batteries. *Metals and Materials International*, *18*(1), 189–196. https://doi.org/10.1007/s12540-012-0025-y

Nan, C.-W., Fan, L., Lin, Y., & Cai, Q. (2003). Enhanced Ionic Conductivity of Polymer Electrolytes Containing Nanocomposite SiO2 Particles. *Physical Review Letters*, *91*(26), 266104. https://doi.org/10.1103/PhysRevLett.91.266104

Nayak, P. K., Yang, L., Brehm, W., & Adelhelm, P. (2018). From Lithium-Ion to Sodium-Ion Batteries: Advantages, Challenges, and Surprises. *Angewandte Chemie - International Edition*, *57*(1), 102–120. https://doi.org/10.1002/anie.201703772

Ni, J. E., Case, E. D., Sakamoto, J. S., Rangasamy, E., & Wolfenstine, J. B. (2012). Room temperature elastic moduli and Vickers hardness of hot-pressed LLZO cubic garnet. *Journal of Materials Science*, *47*(23), 7978–7985. https://doi.org/10.1007/s10853-012-6687-5

O' Neill, J. (2001). *Building Better Global Economic BRICs*. *November 2001*.

O' Neill, J. (2021). *Is the Emerging World Still Emerging?* International Monetary Fund. https://www.imf.org/external/pubs/ft/fandd/2021/06/jim-oneill-revisits-brics-emerging-markets.htm

Oh, S. M., Oh, S. W., Yoon, C. S., Scrosati, B., Amine, K., & Sun, Y. K. (2010). High-performance carbon-LiMnPO4 nanocomposite cathode for lithium batteries. *Advanced Functional Materials*, *20*(19), 3260–3265. https://doi.org/10.1002/adfm.201000469

Ohno, S., Helm, B., Fuchs, T., Dewald, G., Kraft, M. A., Culver, S. P., Senyshyn, A., & Zeier, W. G. (2019). Further Evidence for Energy Landscape Flattening in the Superionic Argyrodites Li6+ xP1- xMxS5I (M = Si, Ge, Sn) [Research-article]. *Chemistry of Materials*, *31*(13), 4936–4944. https://doi.org/10.1021/acs.chemmater.9b01857

Ohta, S., Kobayashi, T., & Asaoka, T. (2011). High lithium ionic conductivity in the garnet-type

oxide Li7-X La3(Zr2-X, NbX)O12 (X = 0-2). *Journal of Power Sources*, *196*(6), 3342–3345. https://doi.org/10.1016/j.jpowsour.2010.11.089

Ohta, S., Seki, J., Yagi, Y., Kihira, Y., Tani, T., & Asaoka, T. (2014). Co-sinterable lithium garnet-type oxide electrolyte with cathode for all-solid-state lithium ion battery. *Journal of Power Sources*, *265*, 40–44. https://doi.org/10.1016/j.jpowsour.2014.04.065

Okhotnikov, K., Charpentier, T., & Cadars, S. (2016). Supercell program: a combinatorial structure-generation approach for the local-level modeling of atomic substitutions and partial occupancies in crystals. *Journal of Cheminformatics*, *8*(1), 17. https://doi.org/10.1186/s13321-016-0129-3

Ooura, Y., MacHida, N., Naito, M., & Shigematsu, T. (2012). Electrochemical properties of the amorphous solid electrolytes in the system Li 2S-Al 2S 3-P 2S 5. *Solid State Ionics*, *225*, 350–353. https://doi.org/10.1016/j.ssi.2012.03.003

Ouyang, D., Chen, M., Liu, J., Wei, R., Weng, J., & Wang, J. (2018). Investigation of a commercial lithium-ion battery under overcharge/over-discharge failure conditions. *RSC Advances*, *8*(58), 33414–33424. https://doi.org/10.1039/C8RA05564E

Owens, B. B. (2000). Solid state electrolytes: Overview of materials and applications during the last third of the Twentieth Century. *Journal of Power Sources*, *90*(1), 2–8. https://doi.org/10.1016/S0378-7753(00)00436-5

Padhi, A. K., Nanjundaswamy, K. S., & Goodenough, J. B. (1997). Phospho-olivines as Positive-Electrode Materials for Rechargeable Lithium Batteries. *Journal of The Electrochemical Society*, *144*(4), 1188–1194. https://doi.org/10.1149/1.1837571

Paolella, A., Savoie, S., Gariepy, V., Zhu, W., Guerfi, A., & Zaghib, K. (2021). *Ceramics, methods for the production thereof and uses of same* (Patent No. US 2021/0147299 A1). https://patents.google.com/patent/US20210147299A1/en

Paolella, A., Zhu, W., Bertoni, G., Perea, A., Demers, H., Savoie, S., Girard, G., Delaporte, N., Guerfi, A., Rumpel, M. M., Lorrmann, H., Demopoulos, G. P., & Zaghib, K. (2020a). Toward an All-Ceramic Cathode–Electrolyte Interface with Low-Temperature Pressed NASICON Li 1.5 Al 0.5 Ge 1.5 (PO 4) 3 Electrolyte. *Advanced Materials Interfaces*, *7*(12), 2000164. https://doi.org/10.1002/admi.202000164

Paolella, A., Zhu, W., Bertoni, G., Perea, A., Demers, H., Savoie, S., Girard, G., Delaporte, N., Guerfi, A., Rumpel, M. M., Lorrmann, H., Demopoulos, G. P., & Zaghib, K. (2020b). Toward an All-Ceramic Cathode–Electrolyte Interface with Low-Temperature Pressed NASICON Li1.5Al0.5Ge1.5(PO4)3 Electrolyte. *Advanced Materials Interfaces*, *7*(12), 2000164. https://doi.org/10.1002/admi.202000164

Paolella, A., Zhu, W., Bertoni, G., Savoie, S., Feng, Z., Demers, H., Gariepy, V., Girard, G., Rivard, E., Delaporte, N., Guerfi, A., Lorrmann, H., George, C., & Zaghib, K. (2020). Discovering the Influence of Lithium Loss on Garnet Li 7 La 3 Zr 2 O 12 Electrolyte Phase Stability. *ACS Applied Energy Materials*, *3*(4), 3415–3424. https://doi.org/10.1021/acsaem.9b02401

Paolella, A., Zhu, W., Xu, G. L., La Monaca, A., Savoie, S., Girard, G., Vijh, A., Demers, H.,

Perea, A., Delaporte, N., Guerfi, A., Liu, X., Ren, Y., Sun, C. J., Lu, J., Amine, K., & Zaghib, K. (2020). Understanding the Reactivity of a Thin Li1.5Al0.5Ge1.5(PO4)3 Solid-State Electrolyte toward Metallic Lithium Anode. *Advanced Energy Materials*, *10*(32), 1–7. https://doi.org/10.1002/aenm.202001497

Papakyriakou, M., Lu, M., Liu, Y., Liu, Z., Chen, H., McDowell, M. T., & Xia, S. (2021). Mechanical behavior of inorganic lithium-conducting solid electrolytes. *Journal of Power Sources*, *516*(July). https://doi.org/10.1016/j.jpowsour.2021.230672

París, M. A., Martínez-Juárez, A., Rojo, J. M., & Sanz, J. (1996). Lithium mobility in the NASICON-type compound LiTi2(PO4)3 by nuclear magnetic resonance and impedance spectroscopies. *Journal of Physics Condensed Matter*, *8*(29), 5355–5366. https://doi.org/10.1088/0953-8984/8/29/011

Pecher, O., Kong, S. T., Goebel, T., Nickel, V., Weichert, K., Reiner, C., Deiseroth, H. J., Maier, J., Haarmann, F., & Zahn, D. (2010). Atomistic characterisation of Li+ mobility and conductivity in Li7-xPS6-xix argyrodites from molecular dynamics simulations, solid-state NMR, and impedance spectroscopy. *Chemistry - A European Journal*, *16*(28), 8347–8354. https://doi.org/10.1002/chem.201000501

Peng, H., Xiao, L., Cao, Y., & Luan, X. (2015). Synthesis and ionic conductivity of Li6La3BiSnO12 with cubic garnet-type structure via solid-state reaction. *Journal of Central South University*, *22*(8), 2883–2886. https://doi.org/10.1007/s11771-015-2821-2

Peng, H., Xie, H., & Goodenough, J. B. (2012). Use of B2O3 to improve Li+-ion transport in LiTi2(PO4)3-based ceramics. *Journal of Power Sources*, *197*, 310–313. https://doi.org/10.1016/j.jpowsour.2011.09.046

Peng, H., Zhang, Y., Li, L., & Feng, L. (2017a). Effect of quenching method on Li ion conductivity of Li5La3Bi2O12 solid state electrolyte. *Solid State Ionics*, *304*, 71–74. https://doi.org/10.1016/j.ssi.2017.03.030

Peng, H., Zhang, Y., Li, L., & Feng, L. (2017b). Effect of quenching method on Li ion conductivity of Li5La3Bi2O12 solid state electrolyte. *Solid State Ionics*, *304*, 71–74. https://doi.org/10.1016/j.ssi.2017.03.030

Percival, J., Kendrick, E., & Slater, P. R. (2008). Synthesis and conductivities of the garnet-related Li ion conductors, Li5Ln3Sb2O12 (Ln=La, Pr, Nd, Sm, Eu). *Solid State Ionics*, *179*(27–32), 1666–1669. https://doi.org/10.1016/j.ssi.2008.01.002

Percival, J., Kendrick, E., Smith, R. I., & Slater, P. R. (2009). Cation ordering in Li containing garnets: Synthesis and structural characterisation of the tetragonal system, Li7La3Sn 2O12. *Dalton Transactions*, *26*, 5177–5181. https://doi.org/10.1039/b907331k

Perdew, J. P., Burke, K., & Ernzerhof, M. (1996). Generalized Gradient Approximation Made Simple. *Physical Review Letters*, *77*(18), 3865–3868. https://doi.org/10.1103/PhysRevLett.77.3865

Pershina, S. V., Il'Ina, E. A., & Reznitskikh, O. G. (2017). Phase Composition, Density, and Ionic Conductivity of the Li7La3Zr2O12-Based Composites with LiPO3 Glass Addition. *Inorganic Chemistry*, *56*(16), 9880–9891. https://doi.org/10.1021/acs.inorgchem.7b01379

Pervez, S. A., Kim, G., Vinayan, B. P., Cambaz, M. A., Kuenzel, M., Hekmatfar, M., Fichtner, M., & Passerini, S. (2020). Overcoming the Interfacial Limitations Imposed by the Solid–Solid Interface in Solid-State Batteries Using Ionic Liquid-Based Interlayers. *Small*, *16*(14). https://doi.org/10.1002/smll.202000279

Ping, P., Wang, Q., Sun, J., Xiang, H., & Chen, C. (2010). Thermal Stabilities of Some Lithium Salts and Their Electrolyte Solutions With and Without Contact to a $LiFePO_4$ Electrode. *Journal of The Electrochemical Society*, *157*(11), A1170. https://doi.org/10.1149/1.3473789

Pogosova, M., Krasnikova, I., Sergeev, A., Zhugayevych, A., & Stevenson, K. (2020). Correlating structure and transport properties in pristine and environmentally-aged superionic conductors based on Li1.3Al0.3Ti1.7(PO4)3 ceramics. *Journal of Power Sources*, *448*(July 2019), 227367. https://doi.org/10.1016/j.jpowsour.2019.227367

Price, W. S. (1998). Pulsed-field gradient nuclear magnetic resonance as a tool for studying translational diffusion: Part II. Experimental aspects. *Concepts in Magnetic Resonance*, *10*(4), 197–237. https://doi.org/10.1002/(SICI)1099-0534(1998)10:4<197::AID-CMR1>3.0.CO;2-S

Py, M. A., & Haering, R. R. (1983). STRUCTURAL DESTABILIZATION INDUCED BY LITHIUM INTERCALATION IN MoS2 AND RELATED COMPOUNDS. *Canadian Journal of Physics*, *61*(1), 76–84. https://doi.org/10.1139/p83-013

Qiu, Y., & Jiang, F. (2022). A review on passive and active strategies of enhancing the safety of lithium-ion batteries. *International Journal of Heat and Mass Transfer*, *184*, 122288. https://doi.org/10.1016/j.ijheatmasstransfer.2021.122288

Qui, D. T., Hamdoune, S., Soubeyroux, J. L., & Prince, E. (1988). Neutron powder diffraction study of solid solution Li1+xTi2−xInxP3O12. *Journal of Solid State Chemistry*, *72*(2), 309–315. https://doi.org/10.1016/0022-4596(88)90034-5

Raju, M. M., Altayran, F., Johnson, M., Wang, D., & Zhang, Q. (2021). Crystal Structure and Preparation of Li7La3Zr2O12 (LLZO) Solid-State Electrolyte and Doping Impacts on the Conductivity: An Overview. *Electrochem*, *2*(3), 390–414. https://doi.org/10.3390/electrochem2030026

Ramström, O. (2019). The Nobel Prize in Chemistry 2019 - Scientific background. *The Royal Swedish Academy of Sciences*, *50005*, 0–13. https://www.nobelprize.org/prizes/chemistry/2019/advanced-information/

Rangasamy, E., Wolfenstine, J., & Sakamoto, J. (2012). The role of Al and Li concentration on the formation of cubic garnet solid electrolyte of nominal composition Li7La3Zr2O12. *Solid State Ionics*, *206*, 28–32. https://doi.org/10.1016/j.ssi.2011.10.022

Rao, G. V. S., & Tsang, J. C. (1974). Electrolysis method of intercalation of layered transition metal dichalcogenides. *Materials Research Bulletin*, *9*(7), 921–926. https://doi.org/10.1016/0025-5408(74)90171-8

Rao, R. P., & Adams, S. (2011). Studies of lithium argyrodite solid electrolytes for all-solid-state batteries. *Physica Status Solidi (A)*, *208*(8), 1804–1807. https://doi.org/10.1002/pssa.201001117

Rawlence, M., Filippin, A. N., Wäckerlin, A., Lin, T.-Y., Cuervo-Reyes, E., Remhof, A., Battaglia, C., Rupp, J. L. M., & Buecheler, S. (2018). Effect of Gallium Substitution on Lithium-Ion Conductivity and Phase Evolution in Sputtered Li 7–3 x Ga x La 3 Zr 2 O 12 Thin Films. *ACS Applied Materials & Interfaces*, *10*(16), 13720–13728. https://doi.org/10.1021/acsami.8b03163

Reddy, M. V., Mauger, A., Julien, C. M., Paolella, A., & Zaghib, K. (2020). Brief History of Early Lithium-Battery Development. *Materials*, *13*(8), 1884. https://doi.org/10.3390/ma13081884

Rettenwander, D., Redhammer, G., Preishuber-Pflügl, F., Cheng, L., Miara, L., Wagner, R., Welzl, A., Suard, E., Doeff, M. M., Wilkening, M., Fleig, J., & Amthauer, G. (2016). Structural and Electrochemical Consequences of Al and Ga Cosubstitution in Li7La3Zr2O12 Solid Electrolytes. *Chemistry of Materials*, *28*(7), 2384–2392. https://doi.org/10.1021/acs.chemmater.6b00579

Ribes, M., Barrau, B., & Souquet, J. . (1980). Sulfide glasses: Glass forming region, structure and ionic conduction of glasses in Na2S-XS2 (X=Si; Ge), Na2S-P2S5 and Li2S-GeS2 systems. *Journal of Non-Crystalline Solids*, *38–39*(PART 1), 271–276. https://doi.org/10.1016/0022-3093(80)90430-5

Richards, W. D., Miara, L. J., Wang, Y., Kim, J. C., & Ceder, G. (2016). Interface Stability in Solid-State Batteries. *Chemistry of Materials*, *28*(1), 266–273. https://doi.org/10.1021/acs.chemmater.5b04082

Roser, M., & Rodés-Guirao, L. (2014). *Future Population Growth*. https://ourworldindata.org/future-population-growth

Sadigov, R. (2022). Rapid Growth of the World Population and Its Socioeconomic Results. *Scientific World Journal*, *2022*(1930). https://doi.org/10.1155/2022/8110229

Safanama, D., Damiano, D., Rao, R. P., & Adams, S. (2014). Lithium conducting solid electrolyte Li1 + xAl xGe2 - X(PO4)3 membrane for aqueous lithium air battery. *Solid State Ionics*, *262*, 211–215. https://doi.org/10.1016/j.ssi.2013.11.031

Sahraei, E., Campbell, J., & Wierzbicki, T. (2012). Modeling and short circuit detection of 18650 Li-ion cells under mechanical abuse conditions. *Journal of Power Sources*, *220*, 360–372. https://doi.org/10.1016/j.jpowsour.2012.07.057

Sahu, G., Lin, Z., Li, J., Liu, Z., Dudney, N., & Liang, C. (2014). Air-stable, high-conduction solid electrolytes of arsenic-substituted Li4SnS4. *Energy and Environmental Science*, *7*(3), 1053–1058. https://doi.org/10.1039/c3ee43357a

Salimkhani, H., Yurum, A., & Gursel, S. A. (2021). A glance at the influence of different dopant elements on Li7La3Zr2O12 garnets. *Ionics*, *27*(9), 3673–3698. https://doi.org/10.1007/s11581-021-04152-4

Savaresi, A. (2016). The Paris Agreement: a new beginning? *Journal of Energy & Natural Resources Law*, *34*(1), 16–26. https://doi.org/10.1080/02646811.2016.1133983

Schlem, R., Ghidiu, M., Culver, S. P., Hansen, A. L., & Zeier, W. G. (2020). Changing the Static and Dynamic Lattice Effects for the Improvement of the Ionic Transport Properties within

the Argyrodite Li6PS5- xSexI. *ACS Applied Energy Materials*, *3*(1), 9–18. https://doi.org/10.1021/acsaem.9b01794

Schultz, C., Vedder, S., Winter, M., & Nowak, S. (2016). Investigation of the decomposition of organic solvent-based lithium ion battery electrolytes with liquid chromatography-mass spectrometry. *Spectroscopy Europe*, *28*(5), 21–24. https://www.spectroscopyeurope.com/article/investigation-decomposition-organic-solvent-based-lithium-ion-battery-electrolytes-liquid

Schwanz, D. K., Villa, A., Balasubramanian, M., Helfrecht, B., & Marinero, E. E. (2020). Bi aliovalent substitution in Li 7 La 3 Zr 2 O 12 garnets: Structural and ionic conductivity effects. *AIP Advances*, *10*(3), 035204. https://doi.org/10.1063/1.5141764

Scrosati, B. (1992). Lithium Rocking Chair Batteries: An Old Concept? *Journal of The Electrochemical Society*, *139*(10), 2776–2781. https://doi.org/10.1149/1.2068978

Scrosati, B., Hassoun, J., & Sun, Y.-K. (2011). Lithium-ion batteries. A look into the future. *Energy & Environmental Science*, *4*(9), 3287. https://doi.org/10.1039/c1ee01388b

Sebastian, L., & Gopalakrishnan, J. (2003). Lithium ion mobility in metal oxides: a materials chemistry perspectiveBased on a lecture delivered at the international symposium "Materials for Energy: Batteries and Fuel Cells", November 2002, Madrid, Spain. *Journal of Materials Chemistry*, *13*(3), 433–441. https://doi.org/10.1039/b211367h

Seymour, I. D., Quérel, E., Brugge, R. H., Pesci, F. M., & Aguadero, A. (2023). Understanding and Engineering Interfacial Adhesion in Solid-State Batteries with Metallic Anodes. *ChemSusChem*. https://doi.org/10.1002/cssc.202202215

Shah, R., Mittal, V., Matsil, E., & Rosenkranz, A. (2021). Magnesium-ion batteries for electric vehicles: Current trends and future perspectives. *Advances in Mechanical Engineering*, *13*(3), 168781402110033. https://doi.org/10.1177/16878140211003398

Shannon, R. D., Taylor, B. E., English, A. D., & Berzins, T. (1977). NEW Li SOLID ELECTROLYTES. In *International Symposium on Solid Ionic and Ionic-Electronic Conductors* (Vol. 24, Issue 2427, pp. 783–796). Elsevier. https://doi.org/10.1016/B978-0-08-021592-1.50024-6

Shao, Y., Wang, H., Gong, Z., Wang, D., Zheng, B., Zhu, J., Lu, Y., Hu, Y.-S., Guo, X., Li, H., Huang, X., Yang, Y., Nan, C.-W., & Chen, L. (2018). Drawing a Soft Interface: An Effective Interfacial Modification Strategy for Garnet-Type Solid-State Li Batteries [Rapid-communication]. *ACS Energy Letters*, *3*(6), 1212–1218. https://doi.org/10.1021/acsenergylett.8b00453

Sharafi, A., Kazyak, E., Davis, A. L., Yu, S., Thompson, T., Siegel, D. J., Dasgupta, N. P., & Sakamoto, J. (2017). Surface Chemistry Mechanism of Ultra-Low Interfacial Resistance in the Solid-State Electrolyte Li7La3Zr2O12. *Chemistry of Materials*, *29*(18), 7961–7968. https://doi.org/10.1021/acs.chemmater.7b03002

Shen, X., Liu, H., Cheng, X.-B., Yan, C., & Huang, J.-Q. (2018). Beyond lithium ion batteries: Higher energy density battery systems based on lithium metal anodes. *Energy Storage Materials*, *12*(December 2017), 161–175. https://doi.org/10.1016/j.ensm.2017.12.002

Simon, F. J., Hanauer, M., Henss, A., Richter, F. H., & Janek, J. (2019). Properties of the Interphase Formed between Argyrodite-Type Li6PS5Cl and Polymer-Based PEO10:LiTFSI. *ACS Applied Materials and Interfaces*, *11*(45), 42186–42196. https://doi.org/10.1021/acsami.9b14506

Sloop, S. E., Pugh, J. K., Wang, S., Kerr, J. B., & Kinoshita, K. (2001). Chemical Reactivity of PF_5 and $LiPF_6$ in Ethylene Carbonate/Dimethyl Carbonate Solutions. *Electrochemical and Solid-State Letters*, *4*(4), A42. https://doi.org/10.1149/1.1353158

Smil, V. (2000). *Feeding the World*. The MIT Press. https://doi.org/10.7551/mitpress/2977.001.0001

Soman, S., Iwai, Y., Kawamura, J., & Kulkarni, A. (2012). Crystalline phase content and ionic conductivity correlation in LATP glass-ceramic. *Journal of Solid State Electrochemistry*, *16*(5), 1761–1766. https://doi.org/10.1007/s10008-011-1592-4

Song, H., Wang, S., Song, X., Wang, J., Jiang, K., Huang, S., Han, M., Xu, J., He, P., Chen, K., & Zhou, H. (2020). Solar-driven all-solid-state lithium-air batteries operating at extreme low temperatures. *Energy and Environmental Science*, *13*(4), 1205–1211. https://doi.org/10.1039/c9ee04039k

Song, S., Kotobuki, M., Zheng, F., Xu, C., Wang, Y., Li, W. D. Z., Hu, N., & Lu, L. (2017). Roles of Alkaline Earth Ions in Garnet-Type Superionic Conductors. *ChemElectroChem*, *4*(2), 266–271. https://doi.org/10.1002/celc.201600639

Spotnitz, R., & Franklin, J. (2003). Abuse behavior of high-power, lithium-ion cells. *Journal of Power Sources*, *113*(1), 81–100. https://doi.org/10.1016/S0378-7753(02)00488-3

Subianto, S., Mistry, M. K., Choudhury, N. R., Dutta, N. K., & Knott, R. (2009). Composite polymer electrolyte containing ionic liquid and functionalized polyhedral oligomeric silsesquioxanes for anhydrous PEM applications. *ACS Applied Materials and Interfaces*, *1*(6), 1173–1182. https://doi.org/10.1021/am900020w

Sun, H., Kang, S., & Cui, L. (2023). Prospects of LLZO type solid electrolyte: From material design to battery application. *Chemical Engineering Journal*, *454*(P3), 140375. https://doi.org/10.1016/j.cej.2022.140375

Takahashi, T., Yamamoto, O., Yamada, S., & Hayashi, S. (1979). Solid-State Ionics: High Copper Ion Conductivity of the System CuCl - CuI - RbCl. *Journal of The Electrochemical Society*, *126*(10), 1654–1658. https://doi.org/10.1149/1.2128770

Tambelli, C. C., Bloise, A. C., Rosário, A. V., Pereira, E. C., Magon, C. J., & Donoso, J. P. (2002). Characterisation of PEO-Al2O3 composite polymer electrolytes. *Electrochimica Acta*, *47*(11), 1677–1682. https://doi.org/10.1016/S0013-4686(01)00900-8

Tang, Y., Zhang, Q., Luo, Z., Liu, P., & Lu, A. (2017). Effects of Li 2 O-Al 2 O 3 -SiO 2 system glass on the microstructure and ionic conductivity of Li 7 La 3 Zr 2 O 12 solid electrolyte. *Materials Letters*, *193*, 251–254. https://doi.org/10.1016/j.matlet.2017.01.134

Tao, Y., Chen, S., Liu, D., Peng, G., Yao, X., & Xu, X. (2016). Lithium Superionic Conducting Oxysulfide Solid Electrolyte with Excellent Stability against Lithium Metal for All-Solid-State Cells. *Journal of The Electrochemical Society*, *163*(2), A96–A101.

https://doi.org/10.1149/2.0311602jes

Tarascon, J.-M., & Armand, M. (2001). Issues and challenges facing rechargeable lithium batteries. *Nature*, *414*(6861), 359–367. https://doi.org/10.1038/35104644

Tarascon, J. M., & Guyomard, D. (1994). New electrolyte compositions stable over the 0 to 5 V voltage range and compatible with the Li1+xMn2O4/carbon Li-ion cells. *Solid State Ionics*, *69*(3–4), 293–305. https://doi.org/10.1016/0167-2738(94)90418-9

Tenhaeff, W. E., Rangasamy, E., Wang, Y., Sokolov, A. P., Wolfenstine, J., Sakamoto, J., & Dudney, N. J. (2014). Resolving the Grain Boundary and Lattice Impedance of Hot-Pressed Li7La3Zr2O12 Garnet Electrolytes. *ChemElectroChem*, *1*(2), 375–378. https://doi.org/10.1002/celc.201300022

Terada, N. (2001). Development of lithium batteries for energy storage and EV applications. *Journal of Power Sources*, *100*(1–2), 80–92. https://doi.org/10.1016/S0378-7753(01)00885-0

Thackeray, M. M., Johnson, P. J., de Picciotto, L. A., Bruce, P. G., & Goodenough, J. B. (1984). Electrochemical extraction of lithium from LiMn2O4. *Materials Research Bulletin*, *19*(2), 179–187. https://doi.org/10.1016/0025-5408(84)90088-6

Thangadurai, V., Kaack, H., & Weppner, W. J. F. (2003a). Novel Fast Lithium Ion Conduction in Garnet-Type Li5La3M2O12 (M: Nb, Ta). *ChemInform*, *34*(27), 437–440. https://doi.org/10.1002/chin.200327009

Thangadurai, V., Kaack, H., & Weppner, W. J. F. (2003b). Novel Fast Lithium Ion Conduction in Garnet-Type Li 5 La 3 M 2 O 12 (M = Nb, Ta). *Journal of the American Ceramic Society*, *86*(3), 437–440. https://doi.org/10.1111/j.1151-2916.2003.tb03318.x

Thangadurai, V., Narayanan, S., & Pinzaru, D. (2014). Garnet-type solid-state fast Li ion conductors for Li batteries: critical review. *Chemical Society Reviews*, *43*(13), 4714. https://doi.org/10.1039/c4cs00020j

Thangadurai, V., & Weppner, W. (2000). Effect of B-site substitution of (Li,La)TiO3 perovskites by Di-, tri-, tetra- and hexavalent metal ions on the lithium ion conductivity. *Ionics*, *6*(1–2), 70–77. https://doi.org/10.1007/BF02375549

Thangadurai, V., & Weppner, W. (2005a). Li6ALa2Ta2O12 (A=Sr, Ba): Novel garnet-like oxides for fast lithium ion conduction. *Advanced Functional Materials*, *15*(1), 107–112. https://doi.org/10.1002/adfm.200400044

Thangadurai, V., & Weppner, W. (2005b). Li6ALa2Nb2O12 (A = Ca, Sr, Ba): A new class of fast lithium ion conductors with garnet-like structure. *Journal of the American Ceramic Society*, *88*(2), 411–418. https://doi.org/10.1111/j.1551-2916.2005.00060.x

Thangadurai, V., & Weppner, W. (2005c). Investigations on electrical conductivity and chemical compatibility between fast lithium ion conducting garnet-like Li6BaLa2Ta2O12 and lithium battery cathodes. *Journal of Power Sources*, *142*(1–2), 339–344. https://doi.org/10.1016/j.jpowsour.2004.11.001

Thangadurai, V., & Weppner, W. (2006). Effect of sintering on the ionic conductivity of garnet-

related structure Li5La3Nb2O12 and In- and K-doped Li5La3Nb2O12. *Journal of Solid State Chemistry*, *179*(4), 974–984. https://doi.org/10.1016/j.jssc.2005.12.025

The Royal Swedish Academy of Sciences. (2019). The Nobel Prize in Chemistry 2019. In *Press release, Nobel Prize, Chemie 2019* (Issue Press Release).

Thokchom, J. S., Gupta, N., & Kumar, B. (2008). Superionic Conductivity in a Lithium Aluminum Germanium Phosphate Glass–Ceramic. *Journal of The Electrochemical Society*, *155*(12), A915. https://doi.org/10.1149/1.2988731

Thompson, T., Wolfenstine, J., Allen, J. L., Johannes, M., Huq, A., David, I. N., & Sakamoto, J. (2014). Tetragonal vs. cubic phase stability in Al-free Ta doped Li 7La3Zr2O12 (LLZO). *Journal of Materials Chemistry A*, *2*(33), 13431–13436. https://doi.org/10.1039/c4ta02099e

Titirici, M. M. (2021). Sustainable Batteries—Quo Vadis? *Advanced Energy Materials*, *11*(10), 1–11. https://doi.org/10.1002/aenm.202003700

Togo, A., & Tanaka, I. (2015). First principles phonon calculations in materials science. *Scripta Materialia*, *108*, 1–5. https://doi.org/10.1016/j.scriptamat.2015.07.021

Tolganbek, N., Mentbayeva, A., Uzakbaiuly, B., Kanamura, K., & Bakenov, Z. (2020). Li1+xAlxTi2−x (PO4)3, NASICON-type solid electrolyte fabrication with different methods. *Materials Today: Proceedings*, *25*(January), 97–100. https://doi.org/10.1016/j.matpr.2019.12.279

Tsai, C. L., Roddatis, V., Chandran, C. V., Ma, Q., Uhlenbruck, S., Bram, M., Heitjans, P., & Guillon, O. (2016). Li7La3Zr2O12 Interface Modification for Li Dendrite Prevention. *ACS Applied Materials and Interfaces*, *8*(16), 10617–10626. https://doi.org/10.1021/acsami.6b00831

Tubandt, C., & Lorenz, E. (1914). Molekularzustand und elektrisches Leitvermögen kristallisierter Salze. *Zeitschrift Für Physikalische Chemie*, *87U*(1), 513–542. https://doi.org/10.1515/zpch-1914-8737

UN. (n.d.). *Day of Eight Billion*. https://www.un.org/en/dayof8billion

UNFCCC. (2015). ADOPTION OF THE PARIS AGREEMENT. *FCCC/CP/2015/L.9/Rev.1*.

Van Bavel, J. (2013). The world population explosion: causes, backgrounds and -projections for the future. *Facts, Views & Vision in ObGyn*, *5*(4), 281–291. http://www.ncbi.nlm.nih.gov/pubmed/24753956%0Ahttp://www.pubmedcentral.nih.gov/articlerender.fcgi?artid=PMC3987379

Vardar, G., Bowman, W. J., Lu, Q., Wang, J., Chater, R. J., Aguadero, A., Seibert, R., Terry, J., Hunt, A., Waluyo, I., Fong, D. D., Jarry, A., Crumlin, E. J., Hellstrom, S. L., Chiang, Y.-M., & Yildiz, B. (2018). Structure, Chemistry, and Charge Transfer Resistance of the Interface between Li 7 La 3 Zr 2 O 12 Electrolyte and LiCoO 2 Cathode. *Chemistry of Materials*, *30*(18), 6259–6276. https://doi.org/10.1021/acs.chemmater.8b01713

Varzi, A., Thanner, K., Scipioni, R., Di Lecce, D., Hassoun, J., Dörfler, S., Altheus, H., Kaskel, S., Prehal, C., & Freunberger, S. A. (2020). Current status and future perspectives of lithium metal batteries. *Journal of Power Sources*, *480*.

https://doi.org/10.1016/j.jpowsour.2020.228803

Virkar, A. V., Ketcham, T. D., & Gordon, R. S. (1979). Hot pressing of lithia-stabilized β″-alumina. *Ceramurgia International*, *5*(2), 66–69. https://doi.org/10.1016/0390-5519(79)90031-0

Viswanathan, V. V., Choi, D., Wang, D., Xu, W., Towne, S., Williford, R. E., Zhang, J.-G., Liu, J., & Yang, Z. (2010). Effect of entropy change of lithium intercalation in cathodes and anodes on Li-ion battery thermal management. *Journal of Power Sources*, *195*(11), 3720–3729. https://doi.org/10.1016/j.jpowsour.2009.11.103

Wagner, R., Redhammer, G. J., Rettenwander, D., Senyshyn, A., Schmidt, W., Wilkening, M., & Amthauer, G. (2016). Crystal Structure of Garnet-Related Li-Ion Conductor Li 7–3 x Ga x La 3 Zr 2 O 12 : Fast Li-Ion Conduction Caused by a Different Cubic Modification? *Chemistry of Materials*, *28*(6), 1861–1871. https://doi.org/10.1021/acs.chemmater.6b00038

Wagner, R., Redhammer, G. J., Rettenwander, D., Tippelt, G., Welzl, A., Taibl, S., Fleig, J., Franz, A., Lottermoser, W., & Amthauer, G. (2016). Fast Li-Ion-Conducting Garnet-Related Li7-3xFexLa3Zr2O12 with Uncommon I4-3d Structure. *Chemistry of Materials*, *28*(16), 5943–5951. https://doi.org/10.1021/acs.chemmater.6b02516

Wakefield, E. H. (1994). *History of the Electric Automobile*.

Wan, Z., Lei, D., Yang, W., Liu, C., Shi, K., Hao, X., Shen, L., Lv, W., Li, B., Yang, Q. H., Kang, F., & He, Y. B. (2019). Low Resistance–Integrated All-Solid-State Battery Achieved by Li7La3Zr2O12 Nanowire Upgrading Polyethylene Oxide (PEO) Composite Electrolyte and PEO Cathode Binder. *Advanced Functional Materials*, *29*(1), 1–10. https://doi.org/10.1002/adfm.201805301

Wang, C., Fu, K., Kammampata, S. P., McOwen, D. W., Samson, A. J., Zhang, L., Hitz, G. T., Nolan, A. M., Wachsman, E. D., Mo, Y., Thangadurai, V., & Hu, L. (2020). Garnet-Type Solid-State Electrolytes: Materials, Interfaces, and Batteries. *Chemical Reviews*, *120*(10), 4257–4300. https://doi.org/10.1021/acs.chemrev.9b00427

Wang, C., Sun, Q., Liu, Y., Zhao, Y., Li, X., Lin, X., Banis, M. N., Li, M., Li, W., Adair, K. R., Wang, D., Liang, J., Li, R., Zhang, L., Yang, R., Lu, S., & Sun, X. (2018). Boosting the performance of lithium batteries with solid-liquid hybrid electrolytes: Interfacial properties and effects of liquid electrolytes. *Nano Energy*, *48*(March), 35–43. https://doi.org/10.1016/j.nanoen.2018.03.020

Wang, D., Zhong, G., Dolotko, O., Li, Y., McDonald, M. J., Mi, J., Fu, R., & Yang, Y. (2014). The synergistic effects of Al and Te on the structure and Li + -mobility of garnet-type solid electrolytes. *Journal of Materials Chemistry A*, *2*(47), 20271–20279. https://doi.org/10.1039/C4TA03591G

Wang, G. X., Yao, P., Bradhurst, D. H., Dou, S. X., & Liu, H. K. (2000). Structure characteristics and lithium ionic conductivity of La(0.57−2x/3)SrxLi0.3TiO3 perovskites. *Journal of Materials Science*, *5*, 4289–4291. https://doi.org/10.1023/A:1004876100938

Wang, H., Zhu, Y., Kim, S. C., Pei, A., Li, Y., Boyle, D. T., Wang, H., Zhang, Z., Ye, Y., Huang, W., Liu, Y., Xu, J., Li, J., Liu, F., & Cui, Y. (2020). Underpotential lithium plating

on graphite anodes caused by temperature heterogeneity. *Proceedings of the National Academy of Sciences*, *117*(47), 29453–29461. https://doi.org/10.1073/pnas.2009221117

Wang, J., Purewal, J., Liu, P., Hicks-Garner, J., Soukazian, S., Sherman, E., Sorenson, A., Vu, L., Tataria, H., & Verbrugge, M. W. (2014). Degradation of lithium ion batteries employing graphite negatives and nickel–cobalt–manganese oxide + spinel manganese oxide positives: Part 1, aging mechanisms and life estimation. *Journal of Power Sources*, *269*, 937–948. https://doi.org/10.1016/j.jpowsour.2014.07.030

Wang, J., Yamada, Y., Sodeyama, K., Watanabe, E., Takada, K., Tateyama, Y., & Yamada, A. (2018). Fire-extinguishing organic electrolytes for safe batteries. *Nature Energy*, *3*(1), 22–29. https://doi.org/10.1038/s41560-017-0033-8

Wang, Q., Jiang, L., Yu, Y., & Sun, J. (2019). Progress of enhancing the safety of lithium ion battery from the electrolyte aspect. *Nano Energy*, *55*(October 2018), 93–114. https://doi.org/10.1016/j.nanoen.2018.10.035

Wang, Q., Ping, P., Zhao, X., Chu, G., Sun, J., & Chen, C. (2012). Thermal runaway caused fire and explosion of lithium ion battery. *Journal of Power Sources*, *208*, 210–224. https://doi.org/10.1016/j.jpowsour.2012.02.038

Wang, X., Sun, Z., Zhao, Y., Li, J., Zhang, Y., & Zhang, Z. (2020). Na4Mn9O18 nanowires wrapped by reduced graphene oxide as efficient sulfur host material for lithium/sulfur batteries. *Journal of Solid State Electrochemistry*, *24*(1), 111–119. https://doi.org/10.1007/s10008-019-04478-0

Wang, Y., Richards, W. D., Ong, S. P., Miara, L. J., Kim, J. C., Mo, Y., & Ceder, G. (2015). Design principles for solid-state lithium superionic conductors. *Nature Materials*, *14*(10), 1026–1031. https://doi.org/10.1038/nmat4369

Wang, Y., Yan, P., Xiao, J., Lu, X., Zhang, J. G., & Sprenkle, V. L. (2016). Effect of Al2O3 on the sintering of garnet-type Li6.5La3Zr1.5Ta0.5O12. *Solid State Ionics*, *294*, 108–115. https://doi.org/10.1016/j.ssi.2016.06.013

Webber, A. (1991). Conductivity and Viscosity of Solutions of LiCF3 SO 3, Li (CF 3 SO 2) 2 N , and Their Mixtures. *Journal of The Electrochemical Society*, *138*(9), 2586–2590. https://doi.org/10.1149/1.2087287

Weiss, M., Ruess, R., Kasnatscheew, J., Levartovsky, Y., Levy, N. R., Minnmann, P., Stolz, L., Waldmann, T., Wohlfahrt-Mehrens, M., Aurbach, D., Winter, M., Ein-Eli, Y., & Janek, J. (2021). Fast Charging of Lithium-Ion Batteries: A Review of Materials Aspects. *Advanced Energy Materials*, *11*(33), 2101126. https://doi.org/10.1002/aenm.202101126

Wenzel, S., Randau, S., Leichtweiß, T., Weber, D. A., Sann, J., Zeier, W. G., & Janek, J. (2016). Direct Observation of the Interfacial Instability of the Fast Ionic Conductor Li10GeP2S12 at the Lithium Metal Anode. *Chemistry of Materials*, *28*(7), 2400–2407. https://doi.org/10.1021/acs.chemmater.6b00610

Whittingham, M. S. (1976). Electrical Energy Storage and Intercalation Chemistry. *Science*, *192*(4244), 1126–1127. https://doi.org/10.1126/science.192.4244.1126

Whittingham, M. S. (1977). *Chalcogenide battery* (Patent No. US4009052A).

Wolfenstine, J., Ratchford, J., Rangasamy, E., Sakamoto, J., & Allen, J. L. (2012). Synthesis and high Li-ion conductivity of Ga-stabilized cubic Li7La3Zr2O12. *Materials Chemistry and Physics*, *134*(2–3), 571–575. https://doi.org/10.1016/j.matchemphys.2012.03.054

Wong, S., Newman, P. J., Best, A. S., Nairn, K. M., Macfarlane, D. R., & Forsyth, M. (1998). Towards elucidating microscopic structural changes in Li-ion conductors Li1+yTi2−yAly[PO4]3 and Li1+yTi2−yAly[PO4]3−x [MO4]x(M=V and Nb): X-ray and27Al and31P NMR studies. *Journal of Materials Chemistry*, *8*(10), 2199–2203. https://doi.org/10.1039/a802752h

Wu, J. F., Chen, E. Y., Yu, Y., Liu, L., Wu, Y., Pang, W. K., Peterson, V. K., & Guo, X. (2017). Gallium-doped Li7La3Zr2O12 garnet-type electrolytes with high lithium-ion conductivity. *ACS Applied Materials and Interfaces*, *9*(2), 1542–1552. https://doi.org/10.1021/acsami.6b13902

Wu, N., Chien, P.-H., Li, Y., Dolocan, A., Xu, H., Xu, B., Grundish, N. S., Jin, H., Hu, Y.-Y., & Goodenough, J. B. (2020). Fast Li + Conduction Mechanism and Interfacial Chemistry of a NASICON/Polymer Composite Electrolyte. *Journal of the American Chemical Society*, *142*(5), 2497–2505. https://doi.org/10.1021/jacs.9b12233

Xiang, X., Chen, F., Shen, Q., Zhang, L., & Chen, C. (2019). Effect of the lithium ion concentration on the lithium ion conductivity of Ga-doped LLZO. *Materials Research Express*, *6*(8), 085546. https://doi.org/10.1088/2053-1591/ab2799

Xie, D., Chen, S., Zhang, Z., Ren, J., Yao, L., Wu, L., Yao, X., & Xu, X. (2018). High ion conductive Sb2O5-doped B-Li3PS4 with excellent stability against Li for all-solid-state lithium batteries. *Journal of Power Sources*, *389*, 140–147. https://doi.org/10.1016/j.jpowsour.2018.04.021

Xu, B., Li, W., Duan, H., Wang, H., Guo, Y., Li, H., & Liu, H. (2017). Li3PO4-added garnet-type Li6.5La3Zr1.5Ta0.5O12 for Li-dendrite suppression. *Journal of Power Sources*, *354*, 68–73. https://doi.org/10.1016/j.jpowsour.2017.04.026

Xu, K. (2004). Nonaqueous Liquid Electrolytes for Lithium-Based Rechargeable Batteries. *Chemical Reviews*, *104*(10), 4303–4418. https://doi.org/10.1021/cr030203g

Xu, K., Ding, M. S., Zhang, S., Allen, J. L., & Jow, T. R. (2002). An Attempt to Formulate Nonflammable Lithium Ion Electrolytes with Alkyl Phosphates and Phosphazenes. *Journal of The Electrochemical Society*, *149*(5), A622. https://doi.org/10.1149/1.1467946

Xu, K., Zhang, S., Poese, B. A., & Jow, T. R. (2002). Lithium Bis(oxalato)borate Stabilizes Graphite Anode in Propylene Carbonate. *Electrochemical and Solid-State Letters*, *5*(11), A259. https://doi.org/10.1149/1.1510322

Xu, K., Zhang, S. S., Lee, U., Allen, J. L., & Jow, T. R. (2005). LiBOB: Is it an alternative salt for lithium ion chemistry? *Journal of Power Sources*, *146*(1–2), 79–85. https://doi.org/10.1016/j.jpowsour.2005.03.153

Xu, L., Li, J., Deng, W., Shuai, H., Li, S., Xu, Z., Li, J., Hou, H., Peng, H., Zou, G., & Ji, X. (2021). Garnet Solid Electrolyte for Advanced All-Solid-State Li Batteries. *Advanced Energy Materials*, *11*(2), 2000648. https://doi.org/10.1002/aenm.202000648

Xu, P., Tan, D. H. S., & Chen, Z. (2021). Emerging trends in sustainable battery chemistries. *Trends in Chemistry*, *3*(8), 620–630. https://doi.org/10.1016/j.trechm.2021.04.007

Xuefu, S., Nemori, H., Mitsuoka, S., Xu, P., Matsui, M., Takeda, Y., Yamamoto, O., & Imanishi, N. (2016). High Lithium-Ion-Conducting NASICON-Type Li1+xAlxGeyTi2−x−y(PO4)3 Solid Electrolyte. *Frontiers in Energy Research*, *4*(APR), 2–10. https://doi.org/10.3389/fenrg.2016.00012

Yan, G., Nonemacher, J. F., Zheng, H., Finsterbusch, M., Malzbender, J., & Krüger, M. (2019). An investigation on strength distribution, subcritical crack growth and lifetime of the lithium-ion conductor Li7La3Zr2O12. *Journal of Materials Science*, *54*(7), 5671–5681. https://doi.org/10.1007/s10853-018-03251-4

Yang, C., Fu, K., Zhang, Y., Hitz, E., & Hu, L. (2017). Protected Lithium-Metal Anodes in Batteries: From Liquid to Solid. In *Advanced Materials* (Vol. 29, Issue 36). Wiley-VCH Verlag. https://doi.org/10.1002/adma.201701169

Yang, T., Li, Y., Wu, W., Cao, Z., He, W., Gao, Y., Liu, J., & Li, G. (2018). The synergistic effect of dual substitution of Al and Sb on structure and ionic conductivity of Li7La3Zr2O12 ceramic. *Ceramics International*, *44*(2), 1538–1544. https://doi.org/10.1016/j.ceramint.2017.10.072

Yang, Y., Xiong, J., Lai, S., Zhou, R., Zhao, M., Geng, H., Zhang, Y., Fang, Y., Li, C., & Zhao, J. (2019). Vinyl Ethylene Carbonate as an Effective SEI-Forming Additive in Carbonate-Based Electrolyte for Lithium-Metal Anodes. *ACS Applied Materials & Interfaces*, *11*(6), 6118–6125. https://doi.org/10.1021/acsami.8b20706

Yang, Z., Tang, B., Xie, Z., & Zhou, Z. (2021). NASICON-Type Na 3 Zr 2 Si 2 PO 12 Solid-State Electrolytes for Sodium Batteries. *ChemElectroChem*, *8*(6), 1035–1047. https://doi.org/10.1002/celc.202001527

Yang, Z., Yuan, H., Zhou, C., Wu, Y., Tang, W., Sang, S., & Liu, H. (2020). Facile interfacial adhesion enabled LATP-based solid-state lithium metal battery. *Chemical Engineering Journal*, *392*. https://doi.org/10.1016/j.cej.2019.123650

Yao, P., Yu, H., Ding, Z., Liu, Y., Lu, J., Lavorgna, M., Wu, J., & Liu, X. (2019). Review on Polymer-Based Composite Electrolytes for Lithium Batteries. *Frontiers in Chemistry*, *7*(August), 1–17. https://doi.org/10.3389/fchem.2019.00522

Yashima, M., Itoh, M., Inaguma, Y., & Morii, Y. (2005a). Crystal structure and diffusion path in the fast lithium-ion conductor La0.62Li0.16TiO3. *Journal of the American Chemical Society*, *127*(10), 3491–3495. https://doi.org/10.1021/ja0449224

Yashima, M., Itoh, M., Inaguma, Y., & Morii, Y. (2005b). Crystal Structure and Diffusion Path in the Fast Lithium-Ion Conductor La 0.62 Li 0.16 TiO 3. *Journal of the American Chemical Society*, *127*(10), 3491–3495. https://doi.org/10.1021/ja0449224

Yazami, R., & Touzain, P. (1983). A reversible graphite-lithium negative electrode for electrochemical generators. *Journal of Power Sources*, *9*(3), 365–371. https://doi.org/10.1016/0378-7753(83)87040-2

Yoshiasa, A., Sakamoto, D., Okudera, H., Sugahara, M., Ota, K., & Nakatsuka, A. (2005).

Electrical conductivities and conduction mechanisms of perovskite-type Na1-xKxMgF3 (x=0, 0.1, 1) and KZnF3. *Zeitschrift Fur Anorganische Und Allgemeine Chemie*, *631*(2–3), 502–506. https://doi.org/10.1002/zaac.200400358

Yu, C., Choi, J., Anandan, V., & Kim, J. (2020). High-Temperature Chemical Stability of Li1.4Al0.4Ti1.6(PO4)3 Solid Electrolyte with Various Cathode Materials for Solid-State Batteries. *Journal of Physical Chemistry C*, *124*, 14963–12971. https://doi.org/10.1021/acs.jpcc.0c01698

Yu, C., Ganapathy, S., Eck, E. R. H. V., Wang, H., Basak, S., Li, Z., & Wagemaker, M. (2017). Accessing the bottleneck in all-solid state batteries, lithium-ion transport over the solid-electrolyte-electrode interface. *Nature Communications*, *8*(1), 1–9. https://doi.org/10.1038/s41467-017-01187-y

Yu, C., Li, Y., Li, W., Adair, K. R., Zhao, F., Willans, M., Liang, J., Zhao, Y., Wang, C., Deng, S., Li, R., Huang, H., Lu, S., Sham, T.-K., Huang, Y., & Sun, X. (2020). Enabling ultrafast ionic conductivity in Br-based lithium argyrodite electrolytes for solid-state batteries with different anodes. *Energy Storage Materials*, *30*(March), 238–249. https://doi.org/10.1016/j.ensm.2020.04.014

Yu, J., Liu, Q., Hu, X., Wang, S., Wu, J., Liang, B., Han, C., Kang, F., & Li, B. (2022). Smart construction of multifunctional Li1.5Al0.5Ge1.5(PO4)3|Li intermediate interfaces for solid-state batteries. *Energy Storage Materials*, *46*(September 2021), 68–75. https://doi.org/10.1016/j.ensm.2021.12.043

Yu, K., Jin, L., Li, Y., Liu, G., Wei, X., & Yan, Y. (2019). Structure and conductivity of perovskite Li0.355La0.35Sr0.3Ti0.995M0.005O3 (M = Al, Co and In) ceramics. *Ceramics International*, *45*(18), 23941–23947. https://doi.org/10.1016/j.ceramint.2019.08.012

Yu, T., Yang, X., Yang, R., Bai, X., Xu, G., Zhao, S., Duan, Y., Wu, Y., & Wang, J. (2021). Progress and perspectives on typical inorganic solid-state electrolytes. *Journal of Alloys and Compounds*, *885*, 161013. https://doi.org/10.1016/j.jallcom.2021.161013

Yu, X., Chen, R., Gan, L., Li, H., & Chen, L. (2022). Battery Safety: From Lithium-Ion to Solid-State Batteries. *Engineering*. https://doi.org/10.1016/j.eng.2022.06.022

Yubuchi, S., Uematsu, M., Deguchi, M., Hayashi, A., & Tatsumisago, M. (2018). Lithium-Ion-Conducting Argyrodite-Type Li6PS5X (X = Cl, Br, I) Solid Electrolytes Prepared by a Liquid-Phase Technique Using Ethanol as a Solvent. *ACS Applied Energy Materials*, *1*(8), 3622–3629. https://doi.org/10.1021/acsaem.8b00280

Zeng, Y., Ouyang, B., Liu, J., Byeon, Y., Cai, Z., Miara, L. J., Wang, Y., & Ceder, G. (2022). High-entropy mechanism to boost ionic conductivity. *Science*, *378*(6626), 1320–1324. https://doi.org/10.1126/science.abq1346

Zeng, Z., Murugesan, V., Han, K. S., Jiang, X., Cao, Y., Xiao, L., Ai, X., Yang, H., Zhang, J. G., Sushko, M. L., & Liu, J. (2018). Non-flammable electrolytes with high salt-to-solvent ratios for Li-ion and Li-metal batteries. *Nature Energy*, *3*(8), 674–681. https://doi.org/10.1038/s41560-018-0196-y

Zhai, H., Xu, P., Ning, M., Cheng, Q., Mandal, J., & Yang, Y. (2017). A Flexible Solid

Composite Electrolyte with Vertically Aligned and Connected Ion-Conducting Nanoparticles for Lithium Batteries. *Nano Letters*, *17*(5), 3182–3187. https://doi.org/10.1021/acs.nanolett.7b00715

Zhang, H., Jin, M., Xiong, Y., Lim, B., & Xia, Y. (2013). Shape-Controlled Synthesis of Pd Nanocrystals and Their Catalytic Applications. *Accounts of Chemical Research*, *46*(8), 1783–1794. https://doi.org/10.1021/ar300209w

Zhang, H., Liu, X., Qi, Y., & Liu, V. (2013). On the La2/3−xLi3xTiO3/Al2O3 composite solid-electrolyte for Li-ion conduction. *Journal of Alloys and Compounds*, *577*, 57–63. https://doi.org/10.1016/j.jallcom.2013.04.195

Zhang, M., Takahashi, K., Uechi, I., Takeda, Y., Yamamoto, O., Im, D., Lee, D. J., Chi, B., Pu, J., Li, J., & Imanishi, N. (2013). Water-stable lithium anode with Li1.4Al0.4Ge 1.6(PO4)3-TiO2 sheet prepared by tape casting method for lithium-air batteries. *Journal of Power Sources*, *235*, 117–121. https://doi.org/10.1016/j.jpowsour.2013.01.167

Zhang, Q., Liu, K., Ding, F., & Liu, X. (2017). Recent advances in solid polymer electrolytes for lithium batteries. *Nano Research*, *10*(12), 4139–4174. https://doi.org/10.1007/s12274-017-1763-4

Zhang, S., Zhao, H., Wang, J., Xu, T., Zhang, K., & Du, Z. (2020). Enhanced densification and ionic conductivity of Li-garnet electrolyte: Efficient Li2CO3 elimination and fast grain-boundary transport construction. *Chemical Engineering Journal*, *393*(December 2019), 124797. https://doi.org/10.1016/j.cej.2020.124797

Zhang, Y., Zhao, Y., & Chen, C. (2013). Ab initio study of the stabilities of and mechanism of superionic transport in lithium-rich antiperovskites. *Physical Review B*, *87*(13), 134303. https://doi.org/10.1103/PhysRevB.87.134303

Zhang, Y., Zheng, Z., Liu, X., Chi, M., & Wang, Y. (2019). Fundamental Relationship of Microstructure and Ionic Conductivity of Amorphous LLTO as Solid Electrolyte Material. *Journal of The Electrochemical Society*, *166*(4), A515–A520. https://doi.org/10.1149/2.0161904jes

Zhang, Z., Chen, S., Yang, J., Wang, J., Yao, L., Yao, X., Cui, P., & Xu, X. (2018). Interface Re-Engineering of Li10GeP2S12 Electrolyte and Lithium anode for All-Solid-State Lithium Batteries with Ultralong Cycle Life. *ACS Applied Materials and Interfaces*, *10*(3), 2556–2565. https://doi.org/10.1021/acsami.7b16176

Zhang, Z., Shao, Y., Lotsch, B., Hu, Y.-S., Li, H., Janek, J., Nazar, L. F., Nan, C.-W., Maier, J., Armand, M., & Chen, L. (2018). New horizons for inorganic solid state ion conductors. *Energy & Environmental Science*, *11*(8), 1945–1976. https://doi.org/10.1039/C8EE01053F

Zhao, L., Pan, H.-L., Hu, Y.-S., Li, H., & Chen, L.-Q. (2012). Spinel lithium titanate (Li 4 Ti 5 O 12) as novel anode material for room-temperature sodium-ion battery. *Chinese Physics B*, *21*(2), 028201. https://doi.org/10.1088/1674-1056/21/2/028201

Zhao, N., Khokhar, W., Bi, Z., Shi, C., Guo, X., Fan, L. Z., & Nan, C. W. (2019). Solid Garnet Batteries. *Joule*, *3*(5), 1190–1199. https://doi.org/10.1016/j.joule.2019.03.019

Zhao, Q., Liu, X., Stalin, S., Khan, K., & Archer, L. A. (2019). Solid-state polymer electrolytes

with in-built fast interfacial transport for secondary lithium batteries. *Nature Energy*, *4*(5), 365–373. https://doi.org/10.1038/s41560-019-0349-7

Zhao, Y., & Daemen, L. L. (2012). Superionic Conductivity in Lithium-Rich Anti-Perovskites. *Journal of the American Chemical Society*, *134*(36), 15042–15047. https://doi.org/10.1021/ja305709z

Zheng, C., Ruan, Y., Su, J., Song, Z., Xiu, T., Jin, J., Badding, M. E., & Wen, Z. (2021). Grain boundary modification in garnet electrolyte to suppress lithium dendrite growth. *Chemical Engineering Journal*, *411*(October 2020), 128508. https://doi.org/10.1016/j.cej.2021.128508

Zheng, F., Kotobuki, M., Song, S., Lai, M. O., & Lu, L. (2018). Review on solid electrolytes for all-solid-state lithium-ion batteries. *Journal of Power Sources*, *389*, 198–213. https://doi.org/10.1016/j.jpowsour.2018.04.022

Zheng, J., Dang, H., Feng, X., Chien, P. H., & Hu, Y. Y. (2017). Li-ion transport in a representative ceramic-polymer-plasticizer composite electrolyte: Li7La3Zr2O12-polyethylene oxide-tetraethylene glycol dimethyl ether. *Journal of Materials Chemistry A*, *5*(35), 18457–18463. https://doi.org/10.1039/c7ta05832b

Zheng, J., & Hu, Y.-Y. (2018). New Insights into the Compositional Dependence of Li-Ion Transport in Polymer–Ceramic Composite Electrolytes. *ACS Applied Materials & Interfaces*, *10*(4), 4113–4120. https://doi.org/10.1021/acsami.7b17301

Zheng, Z., Fang, H., Liu, Z., & Wang, Y. (2015). A Fundamental Stability Study for Amorphous LiLaTiO3 Solid Electrolyte. *Journal of The Electrochemical Society*, *162*(1), A244–A248. https://doi.org/10.1149/2.0011503jes

Zhong, H., Sang, L., Ding, F., Song, J., & Mai, Y. (2018). Conformation of lithium-aluminium alloy interphase-layer on lithium metal anode used for solid state batteries. *Electrochimica Acta*, *277*, 268–275. https://doi.org/10.1016/j.electacta.2018.04.191

Zhou, D., Tkacheva, A., Tang, X., Sun, B., Shanmukaraj, D., Li, P., Zhang, F., Armand, M., & Wang, G. (2019). Stable Conversion Chemistry-Based Lithium Metal Batteries Enabled by Hierarchical Multifunctional Polymer Electrolytes with Near-Single Ion Conduction. *Angewandte Chemie - International Edition*, *58*(18), 6001–6006. https://doi.org/10.1002/anie.201901582

Zhou, L., Park, K. H., Sun, X., Lalère, F., Adermann, T., Hartmann, P., & Nazar, L. F. (2019). Solvent-Engineered Design of Argyrodite Li 6 PS 5 X (X = Cl, Br, I) Solid Electrolytes with High Ionic Conductivity. *ACS Energy Letters*, *4*(1), 265–270. https://doi.org/10.1021/acsenergylett.8b01997

Zhou, P., Wang, J., Cheng, F., Li, F., & Chen, J. (2016). A solid lithium superionic conductor Li11AlP2S12 with a thio-LISICON analogous structure. *Chemical Communications*, *52*(36), 6091–6094. https://doi.org/10.1039/c6cc02131j

Zhou, W., Wang, S., Li, Y., Xin, S., Manthiram, A., & Goodenough, J. B. (2016). Plating a Dendrite-Free Lithium Anode with a Polymer/Ceramic/Polymer Sandwich Electrolyte. *Journal of the American Chemical Society*, *138*(30), 9385–9388.

https://doi.org/10.1021/jacs.6b05341

Zhou, X. (2021). Why the socialist element of China's market economy is important. *South China Morning Post*. https://www.scmp.com/economy/china-economy/article/3131151/why-socialist-element-chinas-market-economy-important

Zhu, J., Li, S., Zhang, Y., Howard, J. W., Lü, X., Li, Y., Wang, Y., Kumar, R. S., Wang, L., & Zhao, Y. (2016). Enhanced ionic conductivity with Li7O2Br3 phase in Li3OBr anti-perovskite solid electrolyte. *Applied Physics Letters*, *109*(10). https://doi.org/10.1063/1.4962437

Zhu, J., Xiang, Y., Zhao, J., Wang, H., Li, Y., Zheng, B., He, H., Zhang, Z., Huang, J., & Yang, Y. (2022). Insights into the local structure, microstructure and ionic conductivity of silicon doped NASICON-type solid electrolyte Li1.3Al0.3Ti1.7P3O12. *Energy Storage Materials*, *44*(September 2021), 190–196. https://doi.org/10.1016/j.ensm.2021.10.003

Zhu, J., Zhao, J., Xiang, Y., Lin, M., Wang, H., Zheng, B., He, H., Wu, Q., Huang, J. Y., & Yang, Y. (2020). Chemomechanical Failure Mechanism Study in NASICON-Type Li1.3Al0.3Ti1.7(PO4)3Solid-State Lithium Batteries. *Chemistry of Materials*, *32*(12), 4998–5008. https://doi.org/10.1021/acs.chemmater.9b05295

Zhuang, L., Huang, X., Lu, Y., Tang, J., Zhou, Y., Ao, X., Yang, Y., & Tian, B. (2021). Phase transformation and grain-boundary segregation in Al-Doped Li7La3Zr2O12 ceramics. *Ceramics International*, *47*(16), 22768–22775. https://doi.org/10.1016/j.ceramint.2021.04.295